POLITECNICO DI TORINO
Repository ISTITUZIONALE

Mesoscopic Numerical Methods for Reactive Flows: Lattice Boltzmann Method and Beyond

Original
Mesoscopic Numerical Methods for Reactive Flows: Lattice Boltzmann Method and Beyond / DI RIENZO, ANTONIO FABIO. - (2012). [10.6092/polito/porto/2497051]

Availability:
This version is available at: 11583/2497051 since:

Publisher:
Politecnico di Torino

Published
DOI:10.6092/polito/porto/2497051

Terms of use:
Altro tipo di accesso

This article is made available under terms and conditions as specified in the corresponding bibliographic description in the repository

Publisher copyright

(Article begins on next page)

05 May 2023

Mesoscopic numerical methods for reactive flows: lattice Boltzmann method and beyond

PhD Dissertation

Antonio Fabio Di Rienzo

March 18, 2012

Advisors: Prof. P. Asinari , Dr. E. Chiavazzo

Energy Department, Politecnico di Torino

Abstract

Reactive flows are ubiquitous in several energy systems: internal combustion engines, industrial burners, gas turbine combustors. Numerical modeling of reactive flows is a key tool for the development of such systems. However, computational combustion is a challenging task per se. It generally includes different coupled physical and chemical processes. A single model can come to deal with simultaneous processes: turbulent mixing, multi-phase fluid-dynamics, radiative heat transfer, and chemical kinetics. It is required not only of mathematically representing these processes and coupling them to each other, but also of being numerical efficient. In some applications, the numerical model needs to be able to deal with different length scales. For instance, a continuum approach to reactive flows in porous media burners is not adequate: processes occurring at the pore-scale are not taken into account properly. It is therefore fundamental to have numerical methods able to capture phenomena at the microscopic scales and incorporate the effects in the macroscopic scale.

The lattice Boltzmann method (LBM), a relatively new numerical method in computational fluid-dynamics (CFD), summarizes the requirements of numerical efficiency and potential to relate micro-and macro-scale. However, despite these features and the recent developments, application of LBM to combustion problems is limited and hence further improvements are required. In this thesis, we explore the suitability of LBM for combustion problems and extend its capabilities.

The first key-issue in modeling reactive flows is represented by the fact that the model has to be able to handle the significant density and temperature changes that are tipically encountered in combustion. A recently proposed LBM model for compressible thermal flows is extended to simulate reactive flows at the low Mach number regime. This thermal model is coupled with the mass conservation equations of the chemical species. Also in this case a model able to deal with compressibility effects is derived. To this purpose, we propose a new scheme for solving the reaction-diffusion equations of chemical species where compressibility is accounted for by simply modifying the equilibrium distribution function and the relaxation frequency of models already available in the literature. This extension enables one to apply LBM to a wide range of combustion phenomena, which were not properly adressed so far. The effectiveness of this approach is proved by simulating combustion of hydrogen/air mixtures in a mesoscale channel. Validation against reference numerical solution in the continuum limit are also presented.

An adequate treatment of thermal radiation is important to develop a mathematical model of combustion systems. In fact, combustion incorporates also radiation process, which tends to plays a significant role if high temperatures (and solid opaque particles) are involved. In the thesis a LBM model for radiation is presented. The scheme is derived from the radiative transfer equation for a participating medium,

assuming isotropic scattering and radiative equilibrium condition. The azimuthal angle is discretized according to the lattice velocities on the computational plane, whereas an additional component of the discrete velocity normal to the plane is introduced to discretize the polar angle. The radiative LBM is used to solve a two-dimensional square enclosure bechmark problem. Validation of the model is carried out by investigating the effects of the spatial and angular discretizations and extinction coefficient on the solution. To this purpose, LBM results are compared against reference solutions obtained by means of standard Finite Volume Method (FVM). Extensive error analysis and the order of convergence of the scheme are also reported in the thesis.

In order to extend the capabilities of LBM and make it more efficient in the simulation of reactive flows, in this thesis a new formulation is presented, referred to as Link-wise Artificial Compressibility Method (LW-ACM). The Artificial Compressibility Method (ACM) is (link-wise) formulated by a finite set of discrete directions (links) on a regular Cartesian grid, in analogy with LBM. The main advantage is the possibility of exploiting well established technologies originally developed for LBM and classical computational fluid dynamics, with special emphasis on finite differences, at the cost of minor changes. For instance, wall boundaries not aligned with the background Cartesian mesh can be taken into account by tracing the intersections of each link with the wall (analogously to LBM technology). LW-ACM requires no high-order moments beyond hydrodynamics (often referred to as *ghost* moments) and no kinetic expansion. Like finite difference schemes, only standard Taylor expansion is needed for analyzing consistency. Preliminary efforts towards optimal implementations have shown that LW-ACM is capable of similar computational speed as optimized (BGK-) LBM. In addition, the memory demand is significantly smaller than (BGK-) LBM. Two- and three-dimensional benchmarks are investigated, and an extensive comparative study between solutions obtained through FVM. Numerical evidences suggest that LW-ACM represents an excellent alternative in terms of simplicity, stability and accuracy.

Acknowledgements

Robert Louis Stevenson (1850-1894) used to say:

There are no foreign lands. It is the traveler only who is foreign.

The last three years of PhD did represente to me a fascinating and wearing journey towards new territories. Distant and undiscovered lands were travelled and many people were met on the route. Some of them more than others deserve a special thank.

First of all, I would like to express my gratitude to Prof. Pietro Asinari and Dr. Eliodoro Chiavazzo for their support in quality of scientific advisors and for the useful discussions. Part of this work could not be possible without their invaluable help.

I also wish to acknowledge Dr. John Mantzaras and Dr. Nikolaos Prasianakis, for offering me the chance to spend a period at the Combustion Research Lab at the Paul Scherrer Institut (CH), where part of this work was carried out.

I owe a special thank to my very close friends. Mentioning them will never be enough to express my gratitude.

Last but not least, I am in debt to my parents Domenico and Rita as well as my brother Luca for their endless love. They have been and will aways be the compass of my life and the force in bad moments.

Contents

NOMENCLATURE

a	atom radius
c	speed of light, lattice sound speed, specific heat
f	distribution function
g	distribution function, external acceleration
h	enthalpy, height
$\mathbf{j}$	momentum
n	normal direction
p	pressure
q	normalized distance
$\mathbf{q}$	heat flux
r	radius
s	MRT parameters
t	time
$\mathbf{s}$	geometric distance
t	time
u	flow velocity along x-direction, internal energy
$\mathbf{v}$	lattice velocity
v	flow velocity along y-direction
w	flow velocity along z-direction, lattice weights
$\mathbf{x}$	spatial coordinates
x	x-coordinate, size parameter
y	y-coordinate
z	z-coordinate

A	pre-exponential factor
Br	Brinkmann number
D	mass diffusivity
E	total kinetic energy, activation energy
Ec	Eckert number
G	volumetric absorption
I	radiative intensity
Kn	Knudsen number
L	length
Le	Lewis number
Ma	Mach number
N	number of mesh points
Pr	Prandtl number
Q	number of lattice velocities, scattering efficiency
Q_h	energy source terms
Q_Y	species source terms
R	reaction rate
Re	Reynolds number
S	radiative source term, line strength

T	temperature
$\mathcal{T}$	torque
U	reference velocity
V	volume, diffusion velocity, magnitude of lattice velocity,
W	weights of quadrature formula, molecular weight
Y	species mass fraction
Z	enstrophy

Greek symbols

α	thermal diffusivity
β	extinction coefficient
γ	polar angle
δ	azimuthal angle
ε	energy shell constant
κ	thermal conductivity
κ_a	absorption coefficient
κ_P	Planck mean absorption coefficient
κ_R	Rosseland mean absorption coefficient
λ	wavenumber
μ	dynamic viscosity
ν	kinematic viscosity
ξ	bulk viscosity, species mass fraction distribution function
ρ	density
σ	Stefan-Boltzmann constant $= 5.67 \times 10^{-8} \mathrm{W/m^2K}$
σ_s	scattering coefficient
τ	relaxation time
ψ	stream function, dimensionless heat flux
ω	relaxation frequency
$\dot{\omega}$	molar concentration reaction rate
Δt	time step
Δx	mesh spacing
$\mathbf{\Pi}$	stress tensor
Φ	correction term of energy equation
Ψ	dimensionless total heat flux, correction term of momentum equation
Ω	computational domain, solid angle

Superscripts

$*$	modified
$\wedge$	dimesionless
(e)	equilibrium
in	inlet
o	odd
out	outlet
post	post-collisional

s	sensible
T	transposition

Subscripts

0	reference value, mean value
b	boundary, black body
e	outer
i	azimuthal direction, node label in x-direction, inner, lattice direction
j	polar direction, node label in y-direction
k	k-th chemical species
p	costant pressure
t	thermal, iteration step
v	costant volume
x, y, z	space directions
w	wall
BB	bounce-back
L	lid
R	radiative
Ref	reference solution
θ	angular direction

Symbols

$\perp$	perpendicular
$\|\|$	parallel

ABBREVIATIONS

ACE	Artificial Compressibility Equation
ACM	Artificial Compressibility Method
BE	Boltzmann Equation
BGK	Bhatnagar-Groos-Krook
CFD	Computational Fluid Dynamics
CSE	Common Subexpression Elimination
DOM	Discrete Ordinate Method
DTM	Discrete Transfer Method
FD	Finite Difference
FVM	Finite Volume Method
GPGPU	General-Purpose computing on Graphics Processing Units
INSE	Incompressible Navier-Stokes Equations
LB	Lattice Boltzmann
LBGK	Lattice Bhatnagar-Groos-Krook

LBM	Lattice Boltzmann Method
LKS	Lattice Kinetic Scheme
LW	Link-Wise
MD	Molecular Dynamics
MLUPS	Million Fluid Lattice cell Updates Per Second
MOC	Method Of Characteristics
MRT	Multiple Relaxation Time
RTE	Radiative Transfer Equation

Chapter 1

Introduction

A man of genius makes no
mistakes; his errors are volitional
and are the portals of discovery.

James Joyce (1882-1941)

1.1 Motivations

In the recent years, the lattice Boltzmann method (LBM) has been developed as an alternative numerical scheme for the simulation of fluid flows, and proved to be successful especially in case of complex boundaries. Unlike conventional numerical scheme for computational fluid-dynamics (CFD) based on the discretization of macroscopic continuum equations, LBM is derived from simplified kinetic models, and it solves the time evolution of the particle distribution function, which obeys target macroscopic equations. Hydrodynamic quantities can be computed as moments of the distribution function. The use of kinetic methods for the description of macroscopic fluid flows is made possible by the following reasons: (i) macroscopic dynamics of the fluids is the result of interaction of microscopic particles, and (ii) the macroscopic dynamics is not sensitive to the underlying details in microscopic physics.

The key focus of LBM is the averaged macroscopic behavior and, from this point of view, it can be regarded as an alternative tool to classical solvers of partial differential equations. LBM has some relevant features that distinguish if from classical numerical methods:

a. The advection term of LBM is linear, which contrasts with the nonlinear advection terms in other approaches based on the macroscopic equations for fluid-dynamics;

b. The pressure of LBM is computed using the equation of state. On the contrary, in classical CFD approaches, the pressure satisfies the Poisson equation. This is typical of the Artificial Compressibility Method;

c. LBM uses a minimal set of microscopic velocities, whereas in kinetic theory the Discrete Velocity Method (DVM) uses more velocities, but real informations beyond hydrodynamics. This feature of LBM implies that the transformation from the particle distribution function to hydrodynamic variables, which are usually the main concern, is greatly simplified.

In some applications, such as flow through porous media [4], where the reliability of the results is of key importance, the best way would be to solve a micro-scale model and then calculate the macro-scale quantities directly from it. In fact, the micro-scale formulation allows one to better focus on details which cannot be caught by macroscopic models. On the other side, micro-scale models can be limited to few applications if the computational resources are limited. Through LBM, it is actually possible to formulate problems which can be numerically solved by means of limited resources. Moreover, the link between micro- and macro-scale is readily available. For this reason, LBM is also referred to as *mesoscopic* approach.

LBM has been originally proposed as an alternative numerical solver for isothermal non-reactive Navier-Stokes equations. Over the last two decades, LBM has been greatly improved in order to address a larger range of engineering problems. LBM has offered a promising approach for investigating pore-scale phenomena involving reacting flow in porous media [53, 80, 84]. Fig. 1.1 illustrates the schematic of a porous media (PM) burner. This application meets the requirements of developing advanced combustion systems with high energy efficiency and low polluntants emission. The heat recovery serves to heat the porous layer in the pre-heat zone. This process makes combustion more efficient, and reduces the possibility of formation of polluntants, such as NO_x or CO. The development of such energy system requires suitable mathematical models, in order to describe processes like flows in porous media, radiative heat transfer or combustion.

The fluid flow in porous media highly influence the heat and mass transfer phenomena. In the past years, flow in porous media has been intensively studied from both experimental and numerical points of view. Three scales are involved: the pore-scale, the representative elementary volume (REV) and the device scale. The REV is defined as the smallest volume over which a measurement can be made that will yield a value representative of the whole. Below REV, the parameter is not defined and the material can not be treated as a continuum. The REV scale is smaller than the domain scale, but larger than the pore scale. Usually, the flow in porous media is studied by means of semi-empirical models based on the volume-averaging at the REV

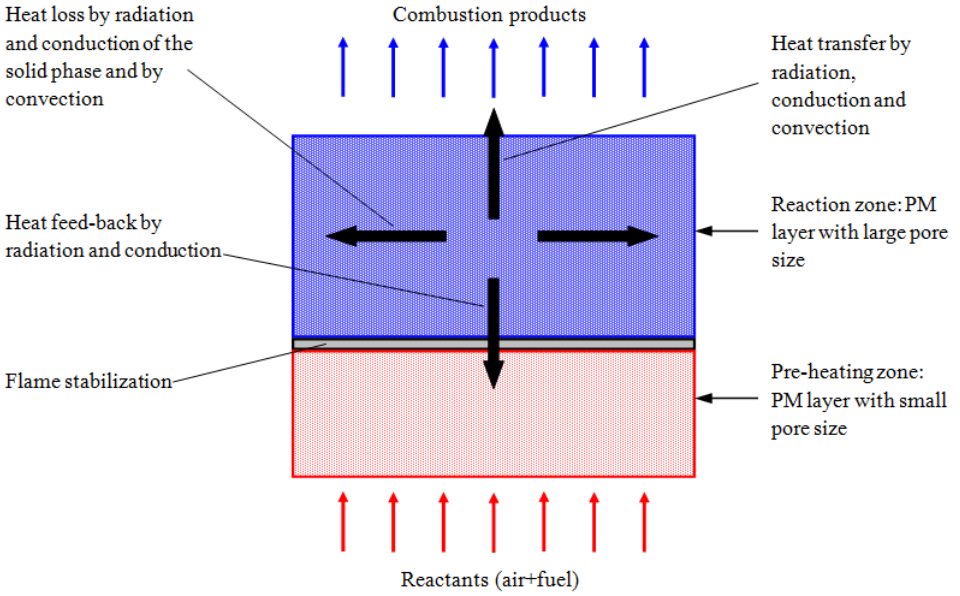

Figure 1.1: Schematic of two layers PM burner: major heat transfer modes are highlighted.

scale. On the contrary, if studies are carried out at the level of the pore-scale, detailed local informations of the flow can be obtained and used to study macroscopic relations. The pore-scale simulations can be of great help to the evaluation of constitutive laws for key parameters, e.g. permeability, dispersivity of reactants and tortuosity. However, the method at the pore-scale needs detailed geometric informations, and if the size of the computational domain is too large, the simulation becomes too demanding. Thus, the numerical tool has to be able not only (i) to simulate properly the pore-scale phenomena, but also (ii) to be numerically efficient. LBM revealed suitable to simulate systems at the pore-scale. Moreover, LBM is also characterized by a simple implementation in complex geometries and does not involve global operations, but only nearest neighbor interactions, which makes the method particularly suited for parallel calculations.

In this thesis, we will not focus on numerical modeling of flows in porous media. Instead a great consideration is dedicated to exploring the capabilities of LBM to simulate the other processes capitalized by the PM burner. More in particular, this thesis aims at investigating and extending LBM to the description of reactive flows. In fact, despite the last decade has witnessed a significant improvement in describing various problems (e.g. flows in porous media and shallow waters, magnetic and electric fields, thermal flows), applications of LBM to combustion is still limited. In principle, once lattice Boltzmann models can properly account for large temperature variation and mixing, extension to reactive flows essentially involves adding

appropriate source terms in the species equations to account for the reaction rate. However, no reactive lattice Boltzann model has been proposed so far that capitalizes on the latest developments [39]. One reason is that the original lattice Boltzmann formulation recovers consistently Navier-Stokes equations in the incompressible limit, where the density is (approximately) constant, whereas the numerical model has to deal with compressibility effects which originate from the heat release due to chemical reactions. Compressibility effects must be taken into account both in the Navier-Stokes-Fourier equations and the transport equation of each chemical species.

The first model for combustion simulation was proposed in [103], assuming fast chemistry and cold flames with weak heat release. As a consequence, large density variation was not allowed in the model. In [110] a model for reactive flows based on the classical incompressible LBM formulation [117] was presented, assuming that flow field is not affected by chemical reactions, though. The first lattice Boltzmann model able to handle density variations was proposed by Filippova et al. in [35] and [36]. It was derived by modifying the equilibrium populations so that the model behaves like a weak-compressible solver in the macroscopic limit. In order to correct the strain tensor, a term containing gradients of the density is added to the expression for the equilibrium distribution function. The coupling among continuity, momentum and energy equations is achieved by introducing an additional factor to the rest particle, so to model temporal changes of the density. In this way the simplicity of the LBM algorithm got somehow lost. In [88, 89], LBM has been extended to simulate compressible thermal flows on standard lattices and proved to be a good candidate for simulating reactive flows. However, further improvements are still required to make LBM suitable for combustion problems. Basic models for the solution of the transport equation of the chemical species [22] relevead to be inadequate for large density ratios.[1]

Combustion generally incorporates also radiation process, which tends to be important if high temperatures and participating media are involved. An adeguate treatment of thermal radiation is of key importance to develop a mathematical model of the combustion system. Despite several models have been proposed in the literature [1, 18, 27, 37, 57, 65, 75, 76, 77, 78, 99], however efficient solution of the radiative transfer equation (RTE) still represents a challenging task. Unlike conduction and convection modes of heat transfer which depend on spatial and temporal dimensions, an analysis of radiation involves additional three dimensions, i.e, two angular dimensions (polar and azimuthal angles) and one spectral dimension. This makes problems difficult to analyze. In a conduction-convection and radiation problem,

[1] A. F. Di Rienzo, P. Asinari, E. Chiavazzo, N. I. Prasianakis, J. Mantzaras, *Lattice Boltzmann model for reactive flows in combustion*, Europhys. Letters, 2012 (accepted).

it is the computation of radiative component that is the most time consuming one. This excessive computational time in the evaluation of radiative information is for the reason that, apart from covering all the spatial grid points in the solution domain, radiative intensities at every grid point need to be traced from their points of origin in the enclosure to the grid point under consideration. At every grid point, intensities are spanned over the whole spherical space. Recently, a different approach has been proposed by Asinari et al. [9], where LBM is directly used to solve the radiative heat transfer in a participating medium. Due to its kinetic nature, the RTE can be easily formulated according to the LBM formalism: unlike traditional LBM, the intensity, which is the unknown of the problem, is already a particle (phonon) distribution function. The numerical implementation is very simple and it is particularly suitable for complex geometries. The reason is twofold: the intensities at every grid point are automatically traced from their points of origin at the solid walls and the data structures for radiation can be the same of those for fluid flow. These advantages make promising the application of this approach to porous media, for instance. However, the radiative LBM needs further improvements, concerning the angular discetization. In [9], the polar angle was not discretized, spoiling the accuracy of the method with respect of standard Finite Volume Method (FVM) radiation solvers. This issue will be addressed in this dissertation.[2]

LBM shares similarities with the Artificial Compressibility Method (ACM). Asymptotic analysis of the updating rule of LBM derives the artificial compressibility equations (ACE), where momentum equations are the same of the incompressible Navier-Stokes equations and an artificial continuity equation with the pressure time derivative. Taking advantage of these similarities, in [81] the ACM was revived as a high-order accurate numerical method (fourth-order in space and second-order in time) for incompressible Navier-Stokes equations, even for transient simulations, linking the compressibility with the mesh spacing. The stability of the revived ACM has been further enhanced in [82]. However, it is also worth to stress out the differences between LBM and the revived ACM. The latter deals only with macroscopic variables, which represents an advantage in case of inlet and outlet boundary conditions. On the other side, due to its pseudo-kinetic origin, LBM works with a larger set of unknowns, including the so-called *ghost* variables, beyond the hydrodynamic variables, differently from ACM, which focuses only on macroscopic quantities. The ghost variables are unessential as long as the continuum limit is the main concern and they can also be responsible of numerical instabilities [30]. Furthemore, it is not clear how to optimally design these ghost quantities. The lattice kinetic scheme (LKS) [49] can be re-

[2] A. F. Di Rienzo, P. Asinari, R. Borchiellini, S. C. Mishra, *Improved angular discretization and error analysis of the lattice Boltzmann method for solving radiative heat transfer in a participating medium*, Int. Journ. Num. Meth. Heat & Fluid Flow, 21(5):640-662, 2011.

garded as a first attempt to overcome this limitation of LBM. The main idea of LKS is that the updating of the particle distribution function is ruled only by the hydrodynamic variables through the local equilibrium, which solely depends on macroscopic quantities. On the other side, LKS is able to deal only with a fixed value of the kinematic viscosity, and thus the relaxation frequency becomes no longer a tunable parameter, like in standard LBM. However, the underlying idea of LKS can be the starting point for futher developments of LBM.
Another key point is represented by the techniques used in case of complex boundaries. In general, ACM can use different meshing techniques. It is possible to use either Cartesian structured meshes, recursively refined like in LBM, or unstructured body-fitted meshes. In this latter case, advanced algorithms are required in order to have high quality meshes. They usually imply an additional computational overhead and may not convege to an acceptable solution. If Cartesian meshes are used, issues arise in case of wall treatment, which depends on the dimensionality of the problem, i.e. wall boundaty conditions in 2D are different than 3D. Thanks to its link-wise formulation, LBM can overcome this limitation and the same interpolation techniques are used for any orientations of the wall with respect to the lattice as well in any dimensions.
In this thesis, we present a novel formulation of the ACM, retaining the key features of LBM. In particular, (i) ACM is link-wise reformulated and (ii) ghost moments of traditional LBM are removed, by making the updating rule of the distribution function depend on the local equilibrium. This new formulation will be referred to as Link-wise Artificial Compressiblity Method (LW-ACM).[3]

1.2 Outline of the thesis

The thesis is organized as follows:

Chapter 2 The basics of LBM are briefly overviewed. Starting from the Boltzmann equation with Bhatnagar-Gross-Krook (BGK) approximation, the LBM numerical scheme is derived. Asymptotic analysis techniques are reported and the Navier-Stokes system of equations in the incompressible limit is recovered. The existence of multiple time scales, typical of kinetic-based approaches, is pointed out studying a simple one-dimensional heat diffusion equation. A quick overview of techiques for boundary conditions in LBM are also reported. Special attention is devoted to highlight the capability of LBM to deal in a very easy way with complex geometries, but its limitations are also stressed, especially in the case of more general boundaries.

[3] P. Asinari, T. Ohwada, E. Chiavazzo, A. F. Di Rienzo, *Link-wise Artificial Compressibility Method*, Jour. Comp. Phys, 2012 (accepted).

Chapter 3 We propose a general lattice Boltzmann model for reactive flow simulations at the low Mach number regime, which is suitable to accomodate significant density changes. A recent LBM model [88, 89] for compressible thermal flows is extended to combustion applications. In order to overcome the limitations of basic models, we also propose a new simple scheme for the solution of the governing equation of the chemical species, in order to account for compressibility effects. Validation of the proposed model is provided simulating combustion of a global chemical step for hydrogen/air mixtures in a mesoscale channel. Comparisons against reference numerical solutions in the continuum limit are presented.

Chapter 4 We present some improvements to the lattice Boltzmann scheme in [9] for solving radiative heat transfer in an absorbing, emitting and scattering medium. The full derivation of the radiative LBM from the RTE is provided, under the assumptions of isotropic scattering and radiative equilibrium conditions. Azimuthal angle is discretized according to the lattice velocities on the computational plane, while, concerning the polar angle, an additional component of the discrete velocity normal to the plane is introduced. Radiative LB scheme is used to solve a 2-D square enclosure benchmark problem. Results of the LBM scheme are compared with a reference solution obtained through a standard Finite Volume Method. Validation of the model is performed by investigating the effects of spatial and angular discretizations, and extinction coefficient on the solution. Error analysis and the order of convergence of the scheme are also reported.

Chapter 5 The Link-wise Artificial Compressibility Method is presented. The Artificial Compressibility Method (ACM) for the incompressible Navier-Stokes equations is (link-wise) reformulated by a finite set of discrete directions (links) on a regular Cartesian mesh, in analogy with the Lattice Boltzmann Method (LBM). The main features of ACM are summarized, for sake of completeness, and the additional advantages due to a link-wise formulation are stressed out. Two- and three-dimensional benchmarks are investigated, and an extensive comparative study between the present approach and state of the art methods from the literature is carried out.

Chapter 6 The conclusions of the thesis are drawn, and possible future works are outlined.

Chapter 2

Lattice Boltzmann method

> He who would learn to fly one day must first learn to stand and walk and run and climb and dance; one cannot fly into flying.
>
> *Friedrich Nietzsche (1844-1900)*

2.1 Introduction

A fluid is a system made of a large number of interacting particles. In principle, this system can be described by classical mechanics, taking into account the interaction of each particle with the others as done in Molecular Dynamics (MD) simulations. This approach, despite its simplicity, leads to a considerable number of equations, so that it easily becomes computationally intractable. On the other side, the macroscopic description reduces this complexity by dealing with macroscopic quantities which are averaged, at each time step, locally in space. This approach is possible as long as the number of particles is very large, in such a way that the mean distance between particle pairs is small with respect to the characteristic length of the system. For instance, this simpler approach cannot be applied in the case of rarefied gases, where the mean distance between particles can be even larger than the container of the fluid. In general, the Knudsen number $Kn = \ell_m / L$, the ratio of the fluid mean free path ℓ_m and the characteristic length of the macroscopic flow L, is usually involved in a criterion in determining if the continuum assumption can be used for describing the fluid flow. For example, the continuum approximation is considered valid in the regime of very small Knudsen number, usually $Kn \leq 10^{-2}$. According to the value of the Knudsen number, flow regimes can be classified as follows:

- **Hydrodynamic regime** ($Kn \leq 0.01$). It is very well described by the Navier-Stokes-Fourier equations (NSFE). Above this values, gases are called *rarefied* gases.
- **Slip flow regime** ($0.01 \leq Kn \leq 0.1$). It can still be described by NSFE, but the equations must be supplied with boundary conditions in order to take into account velocity slip and temperature jumps at the walls.
- **Transition regime** ($0.1 \leq Kn \leq 10$). NSFE fail: the gas must be described in greater detail, or by extended hydrodynamic equations (e.g. Burnett and super-Burnett equations). Extensions are tipically obtained with expressions for the stress tensor and heat flux containing higher-order (often non-linear) terms in the velocity and temperature gradients.
- **Free molecular flow** ($Kn \geq 10$). It is dominated by particle-wall interactions, and collision between the particles do not play an important role anymore. In this case kinetic theory is no longer valid and MD is usually employed.

Since some issues arise considering either equation of continuum fluid dynamics or particle dynamics, a different model is needed. Kinetic theory represents an alternative to both of them. A microscopic description of the fluid is still possible, but it is carried out statically, by solving evolution equations of particle distribution functions. The macroscopic quantities delivered by macroscopic models can be obtained by suitable moments of the distribution function itself.

2.2 BGK equation

The Boltzmann equation (BE) is the fundamental mathematical model of kinetic theory. It describes the time evolution of the distribution function of gas molecules, which is function of time, space coordinates and particle velocity [7]. The Bhatnagar-Gross-Krook (BGK) [11] model equation highly simplifies the description of the collision operator and thus, the relaxation process towards the equilibrium state. The BGK approximation retains the main features of the full Boltzmann equation. However, this simplification leads to some shortcomings. For instance, the BGK equation recovers the wrong Prandtl number and some corrections have to be introduced [3, 88, 89]. In this chapter we will consider isothermal incompressible flows, so that the problem of recovering the wrong thermal diffusivity can be neglected.

In absence of external body forces, the dimensionless form of the BGK Boltzmann equation reads:

$$\frac{\partial F}{\partial \hat{t}} + \hat{\mathbf{e}} \cdot \frac{\partial F}{\partial \hat{\mathbf{x}}} = \omega \left(F^{(e)} - F \right), \tag{2.1}$$

where the right-hand side of the equation represents the collision term with the BGK approximation and it models the change in the distribution function F due to particle interations. In Eq. (2.1), $F(\hat{\mathbf{x}}, \hat{\mathbf{e}}, \hat{t})$ is the particle distribution function, $\hat{\mathbf{x}}$ and $\hat{t}$ are the dimensionless space coordinates and $\hat{\mathbf{e}}$ is the particle velocity; ω is the characteristic frequency of collision processes; $F^{(e)}$ is the equilibrium distribution function defined as:

$$F^{(e)} = \rho \left(\frac{3}{2\pi}\right)^{D/2} \exp\left[-\frac{3\left(\hat{\mathbf{e}} - \mathbf{u}\right)^2}{2}\right], \tag{2.2}$$

where

$$\rho = \langle\langle F \rangle\rangle, \qquad \rho\mathbf{u} = \langle\langle \hat{\mathbf{e}}\, F \rangle\rangle, \tag{2.3}$$

and

$$\langle\langle \cdot \rangle\rangle = \int_{-\infty}^{+\infty} \cdot \prod_{m=1}^{D} d\hat{\mathbf{e}}_m, \tag{2.4}$$

where ρ and $\mathbf{u}$ are the dimensionless mass density and the dimensionless macroscopic flow velocity, respectively, and D is the number of dimensions. In this chapter, we consider the two dimensional case, i.e. $D = 2$.

2.3 Lattice BGK equation

The discrete models of the BGK equation can be obtained assuming that particles are allowed to move with a finite number of velocities. In the evolution equation, the distribution function is linked to a discrete set of admissible microscopic velocities, referred to as *lattice* velocities. It is basically the same idea of the Discrete Velocity Method (DVM) in kinetic theory. By accounting for this discrete set of velocities, the lattice BGK (LBGK) equation can be derived from Eq. (2.1). The dimensionless LBGK equation is written as (in the absence of external body forces):

$$\frac{\partial f_i}{\partial \hat{t}} + \hat{\mathbf{v}}_i \cdot \frac{\partial f_i}{\partial \hat{\mathbf{x}}} = \omega \left(f_i^{(e)} - f_i\right), \tag{2.5}$$

where f_i and $f_i^{(e)}$ are the discrete distribution function and the discrete equilibrium distribution function, respectively; $\hat{\mathbf{v}}_i$ is the dimensionless lattice velocity, such that $\hat{\mathbf{v}}_i \in \mathbf{Q}$, where $\mathbf{Q}$ is the set of permitted velocities, or *lattice*. The lattice BGK models proposed by Qian et al. [90] are the basic models for LBM. According to the standard terminology, LBM schemes are denoted by DdQq, meaning that q particle ensembles move on d-dimensional lattice. In Fig. 2.1, popular lattices for (a) 1D, (b) 2D and (c) 3D simulations are depicted. In Table 2.1 discrete velocities and lattice weights commonly used for the D1Q3, D2Q9 and D3Q19 models are reported. For the D2Q9 model,

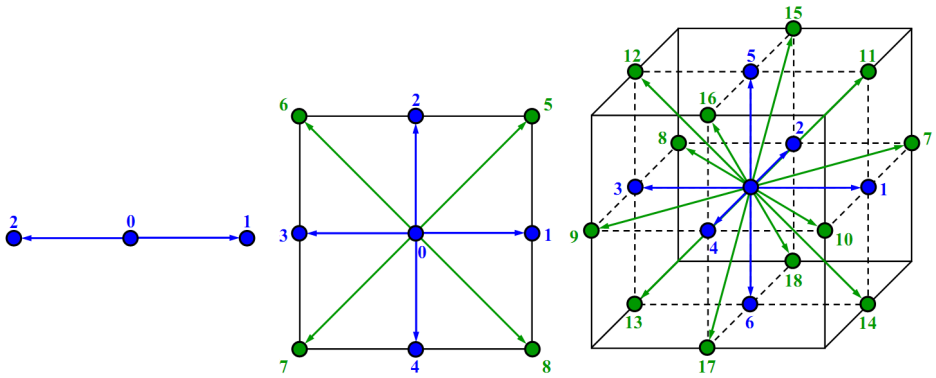

(a) (b) (c)

Figure 2.1: Schematics of (a) D1Q3 (b) D2Q9 and (c) D3Q19 lattices.

Table 2.1: Lattice velocities and weights for the D1Q3, D2Q9 and D3Q19 LBM models.

	$\hat{\mathbf{v}}_i$	w_i
D1Q3	$\{0, 1, -1\}$	$\left\{\frac{2}{3}, \frac{1}{6}, \frac{1}{6}\right\}$
D1Q9	$\{(0,0)$ $(1,0), (0,1), (-1,0), (0,-1)$ $(1,1), (-1,1), (-1,-1), (1,-1)\}$	$\left\{\frac{4}{9},\right.$ $\frac{1}{9},$ $\left.\frac{1}{36}\right\}$
D3Q19	$\{(0,0,0)$ $(1,0,0), (0,1,0), (-1,0,0), (0,-1,0), (0,0,1), (0,0,-1)$ $(1,1,0), (-1,1,0), (-1,-1,0), (1,-1,0)$ $(1,0,1), (-1,0,1), (-1,0,-1), (1,0,-1)$ $(0,1,1), (0,-1,1), (0,-1,-1), (0,1,-1)\}$	$\left\{\frac{1}{3},\right.$ $\frac{1}{18},$ $\frac{1}{36},$ $\frac{1}{36},$ $\left.\frac{1}{36}\right\}$

the i-th equilibrium distribution function reads:

$$f_i^{(e)} = w_i \rho \left[1 + 3\hat{\mathbf{v}}_i \cdot \mathbf{u} + \frac{9}{2} \left(\hat{\mathbf{v}} \cdot \mathbf{u} \right)^2 - \frac{3}{2} \mathbf{u}^2 \right], \tag{2.6}$$

where w_i are the lattice weights, listed in Table 2.1. More explicitely, the complete set of equilibria are:

$$f^{(e)} = \begin{bmatrix} 4/9\rho - 2/3\rho \left(u^2 + v^2 \right) \\ 1/9\rho + 1/6\rho \left(2u^2 + 2u - v^2 \right) \\ 1/9\rho + 1/6\rho \left(2v^2 + 2v - u^2 \right) \\ 1/9\rho - 1/6\rho \left(-2u^2 + 2u + v^2 \right) \\ 1/9\rho - 1/6\rho \left(-2v^2 + 2v + u^2 \right) \\ 1/36\rho + 1/12\rho \left(u^2 + 3uv + u + v + v^2 \right) \\ 1/36\rho + 1/12\rho \left(u^2 - 3uv - u + v + v^2 \right) \\ 1/36\rho + 1/12\rho \left(u^2 + 3uv - u - v + v^2 \right) \\ 1/36\rho + 1/12\rho \left(u^2 - 3uv + u - v + v^2 \right) \end{bmatrix}, \tag{2.7}$$

where u and v are the x and y components of the velocity field $\mathbf{u}$. For isothermal flow, density and momentum are the only conserved statistical moments, defined as:

$$\rho = \langle 1, f_i \rangle = \left\langle 1, f_i^{(e)} \right\rangle, \qquad \rho \mathbf{u} = \langle \hat{\mathbf{v}}_i, f_i \rangle = \left\langle \hat{\mathbf{v}}_i, f_i^{(e)} \right\rangle, \tag{2.8}$$

where the operator $\langle \cdot, \cdot \rangle$ involves a sum on the lattice velocities, namely

$$\left\langle A_{i,j,\ldots,q}, B_{m,n,\ldots,q} \right\rangle = \sum_{q=0}^{Q-1} A_{i,j,\ldots,q}, B_{m,n,\ldots,q} \tag{2.9}$$

In general, it is possible to compute all the other statistical moments at the equilibrium. For this purpose, let us define the transformation matrix $M = \left[1; \hat{\mathrm{v}}_x; \hat{\mathrm{v}}_y; \hat{\mathrm{v}}_x^2; \hat{\mathrm{v}}_y^2; \hat{\mathrm{v}}_x \hat{\mathrm{v}}_y; \hat{\mathrm{v}}_x \hat{\mathrm{v}}_y^2; \hat{\mathrm{v}}_x^2 \hat{\mathrm{v}}_y; \hat{\mathrm{v}}_x^2 \hat{\mathrm{v}}_y^2 \right]$. The equilibrium moments are then defined as:

$$\left\langle M f^{(e)} \right\rangle = \begin{bmatrix} \rho \\ \rho u \\ \rho v \\ p + \rho u^2 \\ p + \rho v^2 \\ \rho u v \\ \rho u / 3 \\ \rho v / 3 \\ p/3 + \rho/3 \left(u^2 + v^2 \right) \end{bmatrix}. \tag{2.10}$$

Table 2.2: Conversion table from lattice to physical units in case of diffusive scaling, i.e. $\Delta x = \varepsilon$ and $\Delta t = \varepsilon^2$ with $\varepsilon = \Delta x/L = 1/N$ and N the number of mesh points along one axis. Quantities in lattice units are readily computed in the code, but they are mesh-dependent. Corresponding quantities in physical units are mesh-independent and can be computed during post-processing. In the text, in case of ambiguity, quantities in physical units are denoted by overbar.

Quantity	Lattice units	Physical units
Pressure	$p = 1/3 \sum_i f_i$	$\bar{p} = (p - p_0)/\varepsilon^2$
Velocity	$\mathbf{u} = \sum_i \hat{\mathbf{v}}_i f_i / \sum_i f_i$	$\bar{\mathbf{u}} = \mathbf{u}/\varepsilon$
Force by Eqs. (5.42, 5.43)	$\mathcal{F} = \sum_{i \in \mathsf{S}} \hat{\mathbf{v}}_i \mathbf{p}_i$	$\Delta\bar{\mathcal{F}} = (\mathcal{F} - \mathcal{F}_0)/\varepsilon^2$
Torque by Eqs. (5.53, 5.54)	$\mathcal{T} = \sum_{i \in \mathsf{S}} (\hat{\mathbf{x}} - \hat{\mathbf{x}}_c) \times \mathbf{p}_i$	$\bar{\mathcal{T}} = \mathcal{T}$
Temperature	$T = \sum_i g_i$	$\bar{T} = T$

2.4 Physical and lattice units

Before proceeding further, it is worth to make the following considerations. In particular, we want to stress that in LBM it is important to consider a proper post-processing of the numerical results. Post-processing depends on the adopted scaling. In particular, in this section we refer to the diffusive scaling, which relates the Mach number to the mesh size: $Ma = O(\varepsilon)$.

We notice that, for instance, the velocity field $\mathbf{u} = \sum_i \hat{\mathbf{v}}_i f_i / \sum_i f_i$ is mesh-dependent: $\mathbf{u} = \mathbf{u}(\varepsilon)$, with $\mathbf{u}$ going to zero as the mesh spacing ε vanishes. As a result, $\mathbf{u}$ is not the proper choice for describing the velocity field of incompressible flows. To this aim, instead, the quantity $\bar{\mathbf{u}} = \mathbf{u}/\varepsilon$ is adopted due to mesh-independence. Similar considerations apply also to other fields. For consistency with the LBM literature, in this work, the units of quantities directly based on f_i are referred to as *lattice units*, while units of the corresponding mesh-independent quantities are termed *physical units*, denoted by overbar.

For the sake of clarity, the complete set of formulas for converting units of all relevant variables are reported in Table 2.2.

2.5 Hydrodynamic limit of LBGK equation: Truncated moment system

Eq. (2.5) provides a tool to compute the time evolution of the discrete distribution functions f_i. Since the hydrodynamic quantities, e.g. mass density and the macroscopic flow velocity, are moments of f_i in the lattice velocity

space, their time evolution is automatically described. However, it is fundamental to check if the model properly recovers the target equations in the macroscopic limit, i.e. the incompressible Navier-Stokes equations (INSE). In other words, a connection between LBGK and macroscopic equations of fluid dynamics needs to be established. For this purpose, classical expansion techniques such as Hilbert or Chapman-Enskog are often used. In this section we describe a simple asymptotic analysis based on the Grad moment system in order to derive the macroscopic system of equations corresponding to Eq. (2.5). This method is based on the Hilbert expansion. It differs from Chapman-Enskog expansion which is described in Section 2.8.

The diffusive scaling [51, 52] is here employed. The unit of space coordinate and the one of time variable in Eq.(2.5) are the mean free path l_c and the mean collision time t_c, respectively. Since they are not appropriate for the flow field in the continuum limit, we define the characteristic length scale as L and the characteristic flow speed as U. For the continuum and incompressible limits $l_c \ll L$ and $U \ll c = l_c/t_c$ hold. The dimensionless space coordinate and time in Eq.(2.5) are defined as:

$$\mathbf{x} = (l_c/L)\,\hat{\mathbf{x}}, \qquad\qquad t = (Ut_c/L)\,\hat{t}, \tag{2.11}$$

We define a small parameters ε as $\varepsilon = l_c/L$ (i.e. the Knudsen number), such that $x_i = \varepsilon\hat{x}_i$. Moreover if we also assume $\varepsilon = U/c$, then $t = \varepsilon^2\,\hat{t}$ and $Ma = O(\varepsilon)$. Eq. (2.5) is rewritten as:

$$\varepsilon^2\frac{\partial f_i}{\partial t} + \varepsilon\hat{\mathbf{v}}_i \cdot \frac{\partial f_i}{\partial \mathbf{x}} = \omega\left(f_i^{(e)} - f_i\right). \tag{2.12}$$

In this section ω is regarded as a constant of the order of unity, i.e. $\omega \sim O(1)$. This means that ω does not depend on ε in the diffusive scaling. In next section, it will be shown that ω becomes a tunable parameter in LBM models.

We use the following notations for the non-conserved equilibrium moments

$$\Pi^{(e)}_{xx\cdots x\,yy\cdots y}(\overbrace{xx\cdots x}^{n\text{ times}},\overbrace{yy\cdots y}^{m\text{ times}}) = \left\langle \hat{\mathrm{v}}_x^n\hat{\mathrm{v}}_y^m f^{(e)}\right\rangle, \tag{2.13}$$

and for the non-conserved generic moments

$$\Pi_{xx\cdots x\,yy\cdots y}(\overbrace{xx\cdots x}^{n\text{ times}},\overbrace{yy\cdots y}^{m\text{ times}}) = \left\langle \hat{\mathrm{v}}_x^n\hat{\mathrm{v}}_y^m f\right\rangle. \tag{2.14}$$

In the incompressible limit, the density can be assumed as $\rho = \rho_0 + \delta\rho$, where ρ_0 is an arbitrary constant and $\delta\rho$ is the denisty fluctuation of the order of $O\left(Ma^2\right) = O\left(\varepsilon^2\right)$, because of the diffusive scaling. Similarly, for

the pressure we can assume $p = p_0 + \varepsilon^2 \bar{p}$ Moreover, because of the low Mach number limit, $\bar{\mathbf{u}} = \varepsilon \mathbf{u}$ and then (2.10) is recast as:

$$\left\langle M f^{(e)} \right\rangle = \begin{bmatrix} \rho \\ \rho u \\ \rho v \\ \Pi_{xx}^{(e)} \\ \Pi_{yy}^{(e)} \\ \Pi_{xy}^{(e)} \\ \Pi_{xyy}^{(e)} \\ \Pi_{xxy}^{(e)} \\ \Pi_{xxyy}^{(e)} \end{bmatrix} = \begin{bmatrix} \rho_0 + \varepsilon^2 \bar{\rho} \\ \varepsilon \left(\rho_0 + \varepsilon^2 \bar{\rho}\right) \bar{u} \\ \varepsilon \left(\rho_0 + \varepsilon^2 \bar{\rho}\right) \bar{v} \\ \left(p_0 + \varepsilon^2 \bar{p}\right) \varepsilon^2 \left(\rho_0 + \varepsilon^2 \bar{\rho}\right) \bar{u}^2 \\ \left(p_0 + \varepsilon^2 \bar{p}\right) \varepsilon^2 \left(\rho_0 + \varepsilon^2 \bar{\rho}\right) \bar{v}^2 \\ \varepsilon^2 \left(\rho_0 + \varepsilon^2 \bar{\rho}\right) \bar{u}\bar{v} \\ \frac{1}{3} \varepsilon \left(\rho_0 + \varepsilon^2 \bar{\rho}\right) \bar{u} \\ \frac{1}{3} \varepsilon \left(\rho_0 + \varepsilon^2 \bar{\rho}\right) \bar{v} \\ \frac{1}{3} \left(p_0 + \varepsilon^2 \bar{p}\right) + \frac{1}{3} \varepsilon^2 \left(\rho_0 + \varepsilon^2 \bar{\rho}\right) \left(\bar{u}^2 + \bar{v}^2\right) \end{bmatrix}. \tag{2.15}$$

Property 1. The following equivalences hold for the considered D2Q9:

$$\hat{\mathrm{v}}_x^3 = \hat{\mathrm{v}}_x \qquad \hat{\mathrm{v}}_y^3 = \hat{\mathrm{v}}_y \ , \tag{2.16}$$

and consequently, $\Pi_{xxx} = \Pi_x = \varepsilon \bar{u}$ and $\Pi_{yyy} = \Pi_y = \varepsilon \bar{v}$.

Property 2. The diffusive scaling assumes that the system is close to the local equilibrium. Hence, we can write:

$$\Pi_{xx\cdots x\, yy\cdots y} = O\left(\Pi_{xx\cdots x\, yy\cdots y}^{(e)}\right) \qquad \frac{\partial \Pi_{xx\cdots x\, yy\cdots y}}{\partial \alpha} = O\left(\frac{\partial \Pi_{xx\cdots x\, yy\cdots y}^{(e)}}{\partial \alpha}\right), \tag{2.17}$$

where $\alpha = t, \mathbf{x}$. In general, whatever scaling we adopt, the leading term describing the dynamics of any moments, in the limiting case of $Kn \ll 1$, will always be the one of the corresponding equilibrium moment.

The system of moments corresponding to Eq. (2.12) is:

$$\varepsilon^2 \frac{\partial \rho}{\partial t} + \varepsilon \frac{\partial}{\partial x} (\rho u) + \varepsilon \frac{\partial}{\partial y} (\rho v) = 0, \tag{2.18a}$$

$$\varepsilon^2 \frac{\partial}{\partial t} (\rho u) + \varepsilon \frac{\partial \Pi_{xx}}{\partial x} + \varepsilon \frac{\partial \Pi_{xy}}{\partial y} = 0, \tag{2.18b}$$

$$\varepsilon^2 \frac{\partial}{\partial t} (\rho v) + \varepsilon \frac{\partial \Pi_{xy}}{\partial x} + \varepsilon \frac{\partial \Pi_{yy}}{\partial y} = 0, \tag{2.18c}$$

$$\varepsilon^2 \frac{\partial \Pi_{xx}}{\partial t} + \varepsilon \frac{\partial}{\partial x}(\rho u) + \varepsilon \frac{\partial \Pi_{xxy}}{\partial y} = \omega \left(p + \rho u^2 - \Pi_{xx}\right), \tag{2.18d}$$

$$\varepsilon^2 \frac{\partial \Pi_{yy}}{\partial t} + \varepsilon \frac{\partial \Pi_{xyy}}{\partial y} x + \varepsilon \frac{\partial}{\partial y}(\rho v) = \omega \left(p + \rho v^2 - \Pi_{yy}\right), \tag{2.18e}$$

$$\varepsilon^2 \frac{\partial \Pi_{xy}}{\partial t} + \varepsilon \frac{\partial \Pi_{xxy}}{\partial x} + \varepsilon \frac{\partial \Pi_{xyy}}{\partial y} = \omega \left(\rho u v - \Pi_{xy}\right), \tag{2.18f}$$

$$\varepsilon^2 \frac{\partial \Pi_{xyy}}{\partial t} + \varepsilon \frac{\partial \Pi_{xxyy}}{\partial x} + \varepsilon \frac{\partial \Pi_{xy}}{\partial y} = \omega \left(\frac{1}{3}\rho u - \Pi_{xyy}\right), \tag{2.18g}$$

$$\varepsilon^2 \frac{\partial \Pi_{xxy}}{\partial t} + \varepsilon \frac{\partial \Pi_{xy}}{\partial x} + \varepsilon \frac{\partial \Pi_{xxyy}}{\partial y} = \omega \left(\frac{1}{3}\rho v - \Pi_{xxy}\right), \tag{2.18h}$$

$$\varepsilon^2 \frac{\partial \Pi_{xxyy}}{\partial t} + \varepsilon \frac{\partial \Pi_{xyy}}{\partial x} + \varepsilon \frac{\partial \Pi_{xxy}}{\partial y} = \omega \left(\frac{1}{3}p + \frac{1}{3}\rho\left(u^2 + v^2\right) - \Pi_{xxyy}\right). \tag{2.18i}$$

It is worth to stress that Eqs. (2.18a-2.18i) form a closed system or, in other words, a discrete set of Q lattice velocities is enough to ensure a closure of the moment system, since only Q independent moment equations exist.

According to (2.15), from Eq. (2.18a) we get:

$$\boxed{\nabla \cdot \bar{\mathbf{u}} = -\varepsilon^2 \frac{1}{\rho_0} \frac{\partial \bar{\rho}}{\partial t} = O\left(\varepsilon^2\right)}, \tag{2.19}$$

which means that the divergence-free consition of the velocity field is recovered if $O(\varepsilon^2)$ terms are neglected, namely ε is small enough.

Recalling the property given by Eq. (2.17)

$$\frac{\partial \Pi_{\alpha\beta}}{\partial x_\beta} = O\left(\varepsilon^2\right), \qquad \frac{\partial \Pi_{\alpha\beta\gamma}}{\partial x_\gamma} = O\left(\varepsilon\right), \qquad \frac{\partial \Pi_{\alpha\beta\gamma\delta}}{\partial x_\delta} = O\left(\varepsilon^2\right), \tag{2.20}$$

we have:

$$\Pi_{xxy} = \frac{1}{3}\varepsilon \rho_0 \bar{v} + O\left(\varepsilon^3\right), \qquad \Pi_{xyy} = \frac{1}{3}\varepsilon \rho_0 \bar{u} + O\left(\varepsilon^3\right) \tag{2.21}$$

Using these expressions in Eq. (2.18d-2.18f) yields:

$$\varepsilon^2 \rho_0 \frac{\partial \bar{u}}{\partial x} + \frac{1}{3}\varepsilon^2 \rho_0 \frac{\partial \bar{v}}{\partial y} = \omega \left(p_0 + \varepsilon^2 \bar{p} + \varepsilon^2 \rho_0 \bar{u}^2 - \Pi_{xx}\right) + O\left(\varepsilon^4\right), \tag{2.22a}$$

$$\frac{1}{3}\varepsilon^2 \rho_0 \frac{\partial \bar{u}}{\partial x} + \varepsilon^2 \rho_0 \frac{\partial \bar{v}}{\partial y} = \omega \left(p_0 + \varepsilon^2 \bar{p} + \varepsilon^2 \rho_0 \bar{v}^2 - \Pi_{yy}\right) + O\left(\varepsilon^4\right), \tag{2.22b}$$

$$\frac{1}{3}\varepsilon^2\rho_0\frac{\partial\bar{v}}{\partial x}+\frac{1}{3}\varepsilon^2\rho_0\frac{\partial\bar{u}}{\partial y}=\omega\left(\varepsilon^2\rho_0\bar{u}\bar{v}-\Pi_{xy}\right)+O\left(\varepsilon^4\right). \tag{2.22c}$$

Introducing the last equations in Eqs. (2.18b) and (2.18c) leads to:

$$\boxed{\frac{\partial\bar{\mathbf{u}}}{\partial t}+\bar{\mathbf{u}}\cdot\nabla\bar{\mathbf{u}}+\nabla\bar{P}-\nu\nabla^2\bar{\mathbf{u}}=O\left(\varepsilon^2\right)}, \tag{2.23}$$

where $\bar{P}=\bar{p}/\rho_0$ is the total kinetic pressure, and $\nu=1/\left(3\omega\right)$. Eqs. (2.19) and (2.23) approximate the INSE with $O(\varepsilon^2)$ error. The term $\bar{\mathbf{u}}\cdot\nabla\bar{\mathbf{u}}$ in Eq. (2.23) represents the non-linear advective term in the Navier-Stokes equations, as opposed to the linear streaming operator $\hat{\mathbf{v}}_i\cdot\nabla f_i$ in Eq. (2.5).

2.6 Slow and fast modes decomposition

Before describing the lattice Boltzmann method, we want to point out some basic feature of a kinetic approach. As described in the previous section, one scale is enough for recovering INSE. On the contrary, to understand the dynamics of ghost modes (i.e modes beyond hydrodynamics), we need more scales. In order to discuss this point, a simple example is presented in this section. The macroscopic target equation is represented by the heat diffusion equation. For sake of simplicity, let us consider one dimensional domain in space and indefinite domain in time, i.e.$(x,t)\in[0,1]\times[0,\infty]$, and periodic boundary conditions.

2.6.1 Heat diffusion equation

The heat conduction equation in the real positive domain is given by:

$$\frac{\partial T}{\partial t}=\alpha\frac{\partial^2 T}{\partial x^2}, \tag{2.24}$$

where T is the temperature and α the thermal diffusivity. By means of the Fourier transform and antitransform, the temperature can be defined as follows:

$$T\left(x,t\right)=\int\int T\left(x,t\right)e^{-ikx}dxe^{ikx}dk=\int\mathbb{F}\left(T\left(x,t\right),k\right)e^{ikx}dk, \tag{2.25}$$

so that Eq. (2.24) can be rewritten as:

$$\frac{d}{dt}\mathbb{F}\left(T\left(x,t\right),k\right)=-\alpha k^2\mathbb{F}\left(T\left(x,t\right),k\right), \tag{2.26}$$

whose solution is:

$$\mathbb{F}\left(T\left(x,t\right),k\right)=\mathbb{F}\left(T\left(x,0\right),k\right)e^{-\alpha k^2 t}, \tag{2.27}$$

where $T(x,0) = T_0$ is the initial condition. Letting the initial condition be in the form $T_0 = \sin(k_0 x)$, using the definition of Fourier antitransform we recover the solution with respect to the physical temperature T:

$$T(x,t) = \mathbb{F}^{-1}\left(\mathbb{F}\left(T(x,t),k\right)\right) = T_0 e^{-\alpha k^2 t}. \tag{2.28}$$

The same solution can be alternately obtained by applying the Fourier transform to Eq. (2.24):

$$\frac{\partial}{\partial t}\mathbb{F}\left(T(x,t),k\right)e^{ikx} = \alpha\frac{\partial^2}{\partial x^2}\mathbb{F}\left(T(x,t),k\right)e^{ikx}. \tag{2.29}$$

Defining as $\Theta(k,x,t) = \mathbb{F}\left(T(x,t),k\right)\exp(ikx)$ yieds:

$$\frac{\partial\Theta}{\partial t} = \alpha\frac{\partial^2\Theta}{\partial x^2}. \tag{2.30}$$

Solution of Eq. (2.30) is:

$$\Theta(k,x,t) = F\left(\mathbb{T}(x,0),k\right)e^{(ikx+\lambda t)} = \Theta_0 e^{(ikx+\lambda t)}, \tag{2.31}$$

where $\Theta_0 = \mathbb{F}\left(T(x,0),k\right)$. Substituting Eq. (2.31) into Eq. (2.30) we have $\lambda = \alpha k^2 i$ and therefore

$$\Theta(k,x,t) = \Theta_0 e^{-\alpha k^2 t})e^{ikx} = \mathbb{F}\left(T(x,t),k\right))e^{ikx}. \tag{2.32}$$

Applying the definition of Fourier antitransform to Eq. (2.32), we can obtain the solution of Eq. (2.24):

$$T(x,t) = \mathbb{F}^{-1}\left(\Theta_0 e^{-\alpha k^2 t}\right). \tag{2.33}$$

2.6.2 Mesoscopic systems: Multiple time scales

The solution of Eq. (2.24) by means of a kinetic approach is well understood. Let us recall the model equation:

$$\varepsilon^2\frac{\partial f_i}{\partial t} + \varepsilon\hat{\mathrm{v}}_{xi}\cdot\frac{\partial f_i}{\partial x} = \omega\left(f_i^{(e)} - f_i\right). \tag{2.34}$$

We consider a simple D1Q3 model (Fig. 2.1a). It is based on three velocities $\hat{\mathrm{v}}_{xi} = [0,-1,1]$ and the equilibrium distribution function is $f_i^{(e)} = w_i T$, where the weights are $w_0 = 2/3$ and $w_{1,2} = 1/6$. T is the temperature, which is also the only conserved moment of this model. If we define the transformation matrix as $M = \left[1;\hat{\mathrm{v}}_x;\hat{\mathrm{v}}_x^2\right]$, the equilibrium moments are:

$$\left\langle M f_i^{(e)}\right\rangle = \begin{bmatrix} T \\ \Pi_x^{(e)} \\ \Pi_{xx}^{(e)} \end{bmatrix} = \begin{bmatrix} T \\ 0 \\ T/3 \end{bmatrix}. \tag{2.35}$$

Following the same procedure described in section 2.5, it is possible to show that this model actually recovers Eq. (2.24) in the macroscopic limit. The system of moments reads:

$$\varepsilon^2 \frac{\partial T}{\partial t} + \varepsilon \frac{\partial \Pi_x}{\partial x} = 0, \tag{2.36a}$$

$$\varepsilon^2 \frac{\partial \Pi_x}{\partial t} + \varepsilon \frac{\partial \Pi_{xx}}{\partial x} = -\omega \Pi_x, \tag{2.36b}$$

$$\varepsilon^2 \frac{\partial \Pi_{xx}}{\partial t} + \varepsilon \frac{\partial \Pi_x}{\partial x} = \omega \left(\frac{T}{3} - \Pi_{xx} \right), \tag{2.36c}$$

where we used the property $\hat{v}_x^3 = \hat{v}_x$. From Eq. (2.36c) we have:

$$\Pi_{xx} = \frac{T}{3} - \frac{\varepsilon}{\omega} \frac{\partial \Pi_x}{\partial x} + O\left(\varepsilon^2\right). \tag{2.37}$$

Substituting it into Eq. (2.36b) and differentiating with respect to space, it leads to:

$$\varepsilon^2 \frac{\partial}{\partial t} \frac{\partial \Pi_x}{\partial x} + \frac{\varepsilon}{3} \frac{\partial^2 T}{\partial x^2} - \frac{\varepsilon^2}{\omega} \frac{\partial^3 \Pi_x}{\partial x^3} = -\omega \frac{\partial \Pi_x}{\partial x} + O\left(\varepsilon^3\right). \tag{2.38}$$

$\partial_x \Pi_x$ can be derived from Eq. (2.36a) and therefore,

$$\frac{\partial T}{\partial t} - \alpha \frac{\partial^2 T}{\partial x^2} = O\left(\varepsilon^2\right), \tag{2.39}$$

where the thermal diffusivity is $\alpha = 1/(3\omega)$.

Let us now take into account also terms of order $O\left(\varepsilon^2\right)$ into Eq. (2.39):

$$3\alpha\varepsilon^2 \frac{\partial^2 T}{\partial t^2} + \frac{\partial T}{\partial t} - \alpha \frac{\partial^2 T}{\partial x^2} - 9\alpha^2 \frac{\partial}{\partial t} \frac{\partial^2 T}{\partial x^2} = 0. \tag{2.40}$$

We now apply the variable transformation given by Eq. (2.31) and find the following characteristic polynomial:

$$3\alpha\varepsilon^2 \lambda^2 - i\left(1 + 9\alpha^2 k^2\right)\lambda - \alpha k^2 = 0, \tag{2.41}$$

whose roots are:

$$\lambda_1 = i \frac{S + \sqrt{S^2 - 4\alpha^2\varepsilon^2 k^2}}{2\alpha\varepsilon^2}, \tag{2.42a}$$

$$\lambda_2 = i \frac{S - \sqrt{S^2 - 4\alpha^2\varepsilon^2 k^2}}{2\alpha\varepsilon^2}, \tag{2.42b}$$

where $S = 1 + 9\alpha^2 k^2$. Thus, the temperature in the complex domain is made of two contributions, i.e.

$$\Theta = \Theta_1 + \Theta_2 = \Theta_{01} e^{ikx} e^{i\lambda_1 t} + \Theta_{02} e^{ikx} e^{i\lambda_2 t}. \tag{2.43}$$

Let us investigate more in details these two contributions. We define $p^2\left(\varepsilon^2\right) = \alpha^2\varepsilon^2k^2/S^2$. The roots λ_1 and λ_2 can be rewritten as:

$$\lambda_1 = i\frac{\alpha k^2}{S}\left(\frac{1+\sqrt{1-4p^2}}{2p^2}\right), \tag{2.44a}$$

$$\lambda_2 = i\frac{\alpha k^2}{S}\left(\frac{1-\sqrt{1-4p^2}}{2p^2}\right). \tag{2.44b}$$

Their Taylor expansions with respect to p are:

$$\lambda_1 = i\frac{\alpha k^2}{Sp^2} - i\frac{\alpha k^2}{S} - i\frac{\alpha k^2}{S}p^2 + O\left(p^4\right), \tag{2.45a}$$

$$\lambda_2 = i\frac{\alpha k^2}{S} + i\frac{\alpha k^2}{S}p^2 + i\frac{\alpha k^2}{S}p^4 + O\left(p^6\right), \tag{2.45b}$$

such that:

$$e^{i\lambda_1 t} = e^{-C_1 t/\varepsilon^2}e^{C_2 t}e^{C_3\varepsilon^2 t} + O\left(\varepsilon^4\right) = e^{-C_1 t/\varepsilon^2 + C_2 t + C_3\varepsilon^2 t + O\left(\varepsilon^4\right)}, \tag{2.46a}$$

$$e^{i\lambda_2 t} = e^{-D_1 t}e^{-D_2\varepsilon^2 t}e^{-D_3\varepsilon^4 t} + O\left(\varepsilon^6\right) = e^{-D_1 t + D_2\varepsilon^2 t + D_3\varepsilon^4 t + O\left(\varepsilon^6\right)}. \tag{2.46b}$$

This shows that both Θ_1 and Θ_2 are function of time with multiple scale:

$$\Theta_1 = \Theta_1\left(t/\varepsilon^2, t, \varepsilon^2 t, \ldots\right), \tag{2.47a}$$

$$\Theta_2 = \Theta_2\left(t, \varepsilon^2 t, \ldots\right). \tag{2.47b}$$

It is possible to notice two main time scales: (1) *advective (fast) scale* t/ε^2, which disappears very quickly, and (2) *diffusive (slow) scale* t, which is the only one occuring in the macroscopic limit. In Fig.2.2, the comparison between the LBM solution and the analytical one is presented. Oscillations on the LBM solution must be ascribed to the advective scale. Thus, we can conclude that this kinetic model always comes with two different time scales, which both share the same spatial scale. This result will be used in Section 2.8 to analyze the BGK model for INSE.

2.7 Discretized lattice BGK equation

The starting point to derive the discretized BGK equation is the lattice BGK equation. Time and space derivatives on the left-hand side of Eq. (2.5) are discretized by means of finite-differences. Let us recall that $\Delta\hat{x} = \Delta x/Kn$

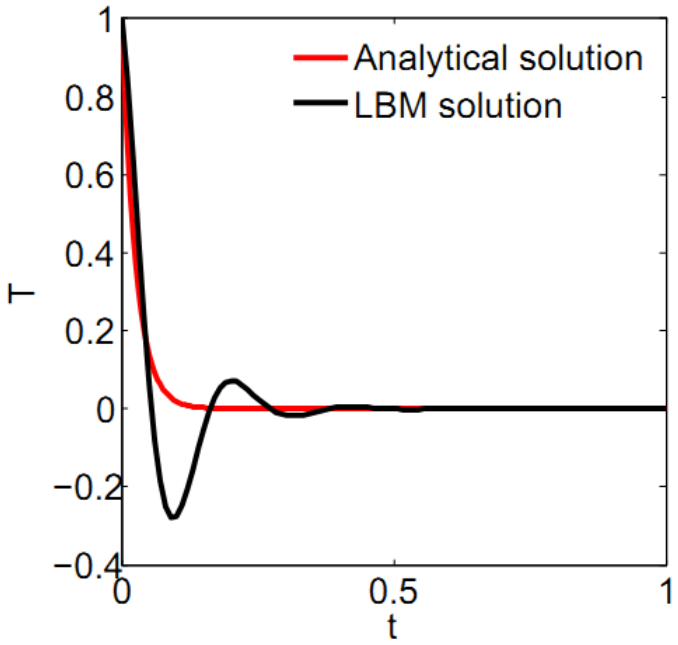

Figure 2.2: Effect of advective scale on the solution.

and $\Delta\hat{t} = \Delta t/(KnMa)$ (see (2.11)). If we set $\Delta\hat{t} = \Delta\hat{x} = 1$, hence $\Delta x = Kn = \varepsilon$ and $\Delta t = KnMa = \varepsilon^2$ represent the expansion parameters.

From Taylor expansion

$$f_i(\mathbf{x}, t+\Delta t) = f_i(\mathbf{x}, t) + \Delta t \frac{\partial}{\partial t} f_i(\mathbf{x}, t) + \frac{\Delta t^2}{2} \frac{\partial^2}{\partial t^2} f_i(\mathbf{x}, t) + \ldots, \tag{2.48}$$

we have a first-order forward-difference approximation (namely, forward Euler) for the time derivative:

$$\frac{\partial}{\partial t} f_i(\mathbf{x}, t) = \frac{f_i(\mathbf{x}, t+\Delta t) - f_i(\mathbf{x}, t)}{\Delta t} + O(\Delta t). \tag{2.49}$$

For the advective term, the method of characteristics (MOC) is applied. The lattice velocities $\hat{\mathbf{v}}_i$ define the upwind directions (characteristic lines), and also serve as links between the grid nodes of the lattice. The upwind treatement means that the information at time t and position $\mathbf{x}$ is propagated along the characteristics and, after a time step Δt, arrives at the position $\mathbf{x} + \hat{\mathbf{v}}_i \Delta t$. Thus,

$$\hat{\mathbf{v}}_i \frac{\partial}{\partial \mathbf{x}} f_i(\mathbf{x}, t) = \frac{f_i(\mathbf{x} + \hat{\mathbf{v}}_i \Delta t, t) - f_i(\mathbf{x}, t)}{\Delta t} + O\left(\hat{\mathbf{v}}_i^2 \Delta t\right). \tag{2.50}$$

From Eqs. (2.49) and (2.50) we can notice that for the left-hand side of Eq. (2.5) an upwind treatment is used. An upwind scheme is stable if the

Courant number C_o satisfies the Courant-Friedrichs-Lewy (CFL) condition. The mesh spacing in physical units is $\Delta x' = L\,\Delta x$, where L is the characteristic length scale. Similarly, the time step in physical units is $\Delta t' = U/L\,\Delta t$, where U is the characteristic flow speed. Therefore:

$$C_o = U\frac{\Delta t'}{\Delta x'} = Ma, \tag{2.51}$$

and the CFL condition is satisfied, since $Ma = O(\varepsilon) \ll 1$.

The discretized form of the lattice BGK equation can be rewritten as folllows:

$$f_i\left(\mathbf{x} + \hat{\mathbf{v}}_i\Delta t, t + \Delta t\right) = f_i\left(\mathbf{x}, t\right) + \omega\left[f_i^{(e)}\left(\mathbf{x}, t\right) - f_i\left(\mathbf{x}, t\right)\right], \tag{2.52}$$

or equivalently, in the dimensionless form as:

$$f_i\left(\hat{\mathbf{x}} + \hat{\mathbf{v}}_i, \hat{t} + 1\right) = f_i\left(\hat{\mathbf{x}}, \hat{t}\right) + \omega\left[f_i^{(e)}\left(\hat{\mathbf{x}}, \hat{t}\right) - f_i\left(\hat{\mathbf{x}}, \hat{t}\right)\right]. \tag{2.53}$$

Eq. (2.52) represents the LBM numerical equation in the standard formulation. Sterling and Chen [101] gave the following interpretation of Eq. (2.52):

> *This equation has a particular simple physical interpretation in which the collision term is evaluated locally and there is only one streaming step or "shift" operation per lattice velocity. This stream-and-collide particle interpretation is a result of the fully Lagrangian character of the equation for which the lattice spacing is the distance travelled by the particle during a time step.*

2.8 Hydrodynamic limit of LBM: Chapman-Enskog expansion

The derivation of Navier-Stokes equations and its transport coefficients from Eq. (2.52) can be accomplished by the Chapman-Enskog (CE) expansion [19, 20, 34, 16, 17]. The expansion parameter is the Knudsen number ε. For the distribution function, it is postulated that the numerical solution f_i from Eq. (2.52) depends on ε as follows:

$$f_i \approx A_\varepsilon = f_i^{(0)} + \varepsilon f_i^{(1)} + \varepsilon^2 f_i^{(2)} + \ldots + \varepsilon^m f_i^{(m)} = \sum_{n=0}^{\infty} \varepsilon^n f_i^{(n)}, \tag{2.54}$$

where the function A_ε is called *ansatz*. The symbol ε is here used in two different ways:

a. As small parameter ($\varepsilon \ll 1$) when expanding terms as power series;

b. To keep track of the orders of magnitude of various terms. In the final results, it will be dropped out by setting $\varepsilon = 1$.

The collision term in Eq. (2.52) is then expanded as follows:

$$\omega\left(f_i^{(e)} - f_i\right) = \omega\left(f_i^{(e)} - f_i^{(0)} - \varepsilon f_i^{(1)} - \varepsilon^2 f_i^{(2)} - \ldots\right). \tag{2.55}$$

CE expansion is combined with a multiple-timescale analysis. As remarked in section 2.6.2, a kinetic approach involves different time scales: the advective (fast) scale t_0 and the diffusive (slow) scale t_1. It is equivalent to assert that the distribution functions depend on two independent time variables instead of one: $f_i(\mathbf{x}, t) \rightarrow f_i(\mathbf{x}, t_0, t_1)$. Thus, the time derivative is expanded as:

$$\frac{\partial}{\partial \hat{t}} = \sum_{n=0}^{\infty} \varepsilon^n \frac{\partial}{\partial t_n}. \tag{2.56}$$

The spatial derivative is not subject to a multi-scale expansion, i.e. $\partial_{\hat{\mathbf{x}}} = \varepsilon \partial_{\mathbf{x}_1}$. Only one macroscopic scale is considered because advection and diffusion can be distinguished by their time scales but occur on similar spatial scales[109].

We assume the same scaling adopted in section 2.5. Eq. (2.52) is rewritten as:

$$f_i\left(\mathbf{x} + \varepsilon \hat{\mathbf{v}}_i, t + \varepsilon^2\right) = f_i(\mathbf{x}, t) + \omega\left[f_i^{(e)}(\mathbf{x}, t) - f_i(\mathbf{x}, t)\right]. \tag{2.57}$$

The left-hand side of Eq. (2.52) is Taylor expanded aroud $(\mathbf{x}, t)$ as:

$$f_i\left(\mathbf{x} + \varepsilon \hat{\mathbf{v}}_i, t + \varepsilon^2\right) = \sum_{n=0}^{\infty} \frac{\varepsilon^n}{n!} D_t^n f_i(\mathbf{x}, t), \tag{2.58}$$

where $D_t = (\partial_t + \hat{\mathbf{v}}_i \cdot \nabla)$. Introducing expansions given by Eqs. (2.54-2.56,2.58) in Eq. (3.8) and equating terms of the same order of ε, we derive the expressions for the distribution function coefficients $f_i^{(n)}$:

$$O\left(\varepsilon^0\right): \quad f_i^{(0)} = f_i^{(e)}, \tag{2.59a}$$

$$O\left(\varepsilon^1\right): \quad f_i^{(1)} = -\tau D_{t_0} f_i^{(0)}, \tag{2.59b}$$

$$O\left(\varepsilon^2\right): \quad f_i^{(2)} = -\tau\left[\frac{\partial}{\partial t_1} f_i^{(0)} + \left(\frac{2\tau - 1}{2\tau}\right) D_{t_0} f_i^{(1)}\right]. \tag{2.59c}$$

The distribution fuction is constrained by:

$$\sum_i f_i \begin{bmatrix} 1 \\ \hat{\mathbf{v}}_i \end{bmatrix} = \begin{bmatrix} \rho \\ \rho \mathbf{u} \end{bmatrix}, \tag{2.60a}$$

$$\sum_i f_i^{(n)} \begin{bmatrix} 1 \\ \hat{\mathbf{v}}_i \end{bmatrix} = 0, \qquad n > 0, \tag{2.60b}$$

where the equilibrium distribution function is given by Eq. (2.7).

2.8.1 Euler level

The moments of Eq. (2.59b) lead to the Euler system of equations:

$$\frac{\partial \rho}{\partial t_0} + \nabla \cdot (\rho \mathbf{u}) = 0, \tag{2.61a}$$

$$\frac{\partial}{\partial t_0} (\rho \mathbf{u}) + \nabla \cdot \mathbf{\Pi}^{(0)} = 0, \tag{2.61b}$$

where

$$\Pi^{(0)}_{\alpha\beta} = \sum_i \hat{\mathrm{v}}_{i,\alpha} \hat{\mathrm{v}}_{i,\beta} f_i^{(0)} = p\delta_{\alpha\beta} + \rho u_\alpha u_\beta \tag{2.62}$$

is the zeroth-order momentum flux tensor. Eq. (2.61b) is rewritten as:

$$\frac{\partial}{\partial t_0} (\rho \mathbf{u}) + \nabla \cdot \Big(\mathbf{u} \otimes (\rho \mathbf{u}) \Big) + \nabla p = 0. \tag{2.63}$$

It should be stressed out that in Eq. (2.61a) the divergent term is of the order of $O\left(\varepsilon^2\right)$, which makes the divergent term in Eq. (2.61b) be of the order of $O\left(\varepsilon^3\right)$.

2.8.2 Navier-Stokes level

The moments of Eq. (2.59c) lead to the following equations:

$$\frac{\partial \rho}{\partial t_1} = 0, \tag{2.64a}$$

$$\frac{\partial}{\partial t_1} (\rho \mathbf{u}) + \left(\frac{2\tau - 1}{2\tau} \right) \nabla \cdot \mathbf{\Pi}^{(1)} = 0, \tag{2.64b}$$

where $\Pi^{(1)}_{\alpha\beta} = \sum_i \hat{\mathrm{v}}_{i,\alpha} \hat{\mathrm{v}}_{i,\beta} f_i^{(1)}$ is the first-order momentum flux tensor, defined as:

$$\Pi_{\alpha\beta}{}^{(1)} \approx -\frac{1}{3}\tau \left[\frac{\partial}{\partial x_\alpha} (\rho u_\beta) + \frac{\partial}{\partial x_\beta} (\rho u_\alpha) \right], \tag{2.65}$$

where we neglected the term $O\left(\varepsilon^3\right)$. Therefore,

$$\nabla \cdot \mathbf{\Pi}^{(1)} = -\frac{1}{3}\tau \, \nabla^2 (\rho \mathbf{u}) + O\left(\varepsilon^3\right). \tag{2.66}$$

Eq. (2.64b) is rewritten as:

$$\frac{\partial}{\partial t_1} (\rho \mathbf{u}) - \frac{1}{3} \left(\tau - \frac{1}{2} \right) \nabla^2 (\rho \mathbf{u}) = O\left(\varepsilon^3\right), \tag{2.67}$$

Combining the zeroth and first order results, we recover Navier-Stokes equations in the incompressible limit:

$$\boxed{\nabla \cdot \mathbf{u} = -\varepsilon^2 \frac{1}{\rho_0} \frac{\partial \rho}{\partial t} = O\left(\varepsilon^2\right)}, \tag{2.68a}$$

$$\boxed{\frac{\partial \mathbf{u}}{\partial t} + \mathbf{u} \cdot \nabla \mathbf{u} + \nabla P - \nu \nabla^2 \mathbf{u} = O\left(\varepsilon^2\right)}, \tag{2.68b}$$

where the kinematic viscosity is defined as:

$$\nu = \frac{1}{3}\left(\frac{1}{\omega} - \frac{1}{2}\right). \tag{2.69}$$

Eqs. (2.68a) and (2.68b) are equivalent to Eqs. (2.19) and (2.23). It is worth to point out that here the viscosity differs from the one we obtained in section 2.5 in the term $1/2$. This difference is ascribed to forward Euler scheme, which requires a correction in the definition of the kinematic viscosity in order to truly recover INSE. Another difference is that Eqs. (2.19) and (2.23) are obtained by means of the Hilbert expansion, whereas Eqs. (2.68a) and (2.68b) by means of Chapman-Enskog expansion.

2.9 Boundary Conditions

> *To a certain degree, achieving self-consistent boundary conditions with a given accuracy is as important as developing numerical schemes themselves.*
> Chen at al. (1996)

As already pointed out in this thesis, LBM is characterized by the easiness to implement boundary conditions in complex geometries. Neverthless, general boundary conditions represents a critical aspect in LBM, since suitable models are required for the distribution function in such a way to recover the desired boundary conditions in terms of macroscopic variables. The desired values of the macroscopic moments needs to be converted in terms of constraints for the distribution function. From this point of view, traditional numerical methods, such as finite differences, offer simpler solutions, especially in case of general boundaries. In this section, we are not going to provide an exhaustive review about models for boundary conditions in LBM. We rather want to point out the suitabity of LBM for complex boudaries. Its limitations in case of general boundaries are also stressed out and possible remedies are suggested.

In general, there are four different types of boundary conditions [109]:

1. *Periodic* BC are often used, because they are very easy to code.

2. *Inflow* BC.
3. *Outflow* BC.
4. *Wall* BC apply to either moving or fixed solid bundaries (wall, obstacle). Slip BC belong to this category: the velocity component normal to the boundary and the normal derivative of the tangential component vanish ($u_n = 0$ and $\partial u_t/\partial n = 0$). Slip BC apply to solid boundaries where the frictional force adjacent to the wall is not resolved.

Hereafter, we brielfy review the most used methods to implement boundary conditions for incompressible LBGK models. For wall boundaries, bounce-back techiques for straight and curved boundaries are reviewed in such a way to show the suitability of LBM for complex geometries. For inflow and outlflow BC, Zou-He [116] methodology is described.

2.9.1 Wall boundary conditions

When solving Navier-Stokes equations, a solid wall is specified by imposing no-slip boundary conditions for the flow velocity $\mathbf{u}$ at the macroscopic level. From the point of view of LBM, the interaction between particle and boundary for no-slip boundary condition is modeled by means of *bounce-back*. After encountering a wall, a particle initially travelling along the direction $\mathbf{v}_i$ is backscattered on the opposite direction, $\mathbf{v}_{-i} = -\mathbf{v}_i$. The implementation of the bounce-back boundary condition can be formulated as:

$$\begin{aligned} \text{in-state}: &\quad f_0, f_1, f_2, f_3, f_4, f_5, f_6, f_7, f_8, \\ \text{out-state}: &\quad f_0, f_1, f_4, f_3, f_2, f_7, f_8, f_5, f_6, \end{aligned} \tag{2.70}$$

for a node on the bottom wall of a 2D channel (Fig 2.3). As depicted in Fig.

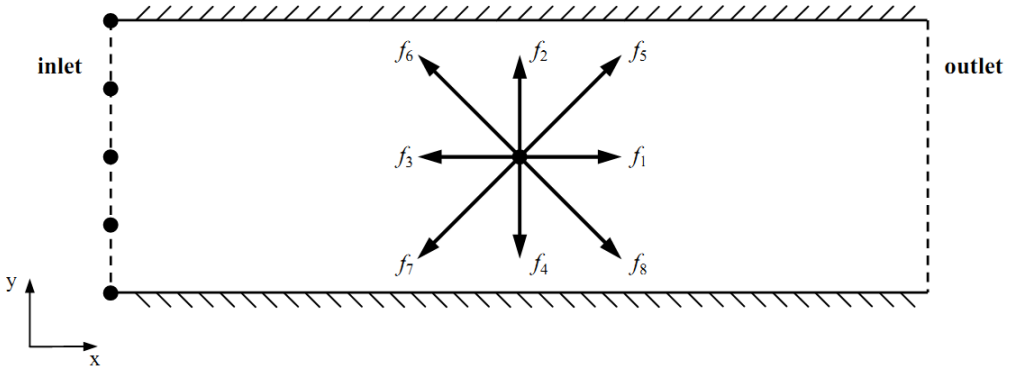

Figure 2.3: Schematic of a 2D channel.

2.4, there are two possible implementation of the bounce-back rule. In the first case (Fig. 2.4a), the solid nodes are exactly located onto the slid wall.

In this case, the bounce-back scheme has been proved to be only first-order accurate. An improvement of this method has been proposed in [115] (Fig. 2.4b): the wall-fluid interface is located halfway between the wall and the fluid nodes. This implementation of the bounce-back rule, often referred to as the *halfway* bounce-back, has been proved to be second-order accurate and consistent with LBM schemes.

The bounce-back is a very easy and effective technique, appropriate for simple boundaries made of straight lines. In dealing with complex geometries

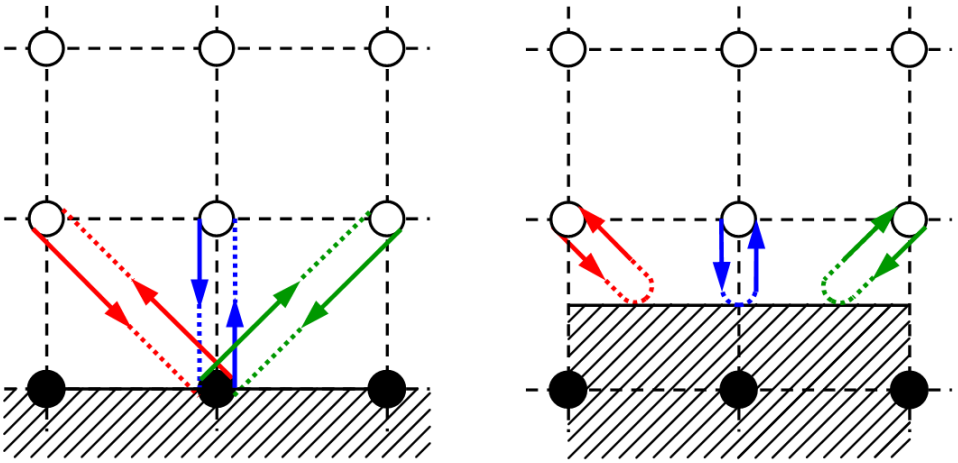

(a) (b)

Figure 2.4: Schematic description of (a) the standard bounce-back and (b) the halfway bounce-back boundary condition. The values of the distribution functions propagate along the directions indicated by the dotted lines at every time step. Blank and filled circles represent fluid nodes and wall nodes, respectively.

of arbitrary curvatures, one possible strategy in LBM is to make use of regular Cartesian grid and perform interpolations to keep track of the position of the boundary. Bounce-back is executed at the boundary location, which may be out of the lattice node of the Cartesian grid. In [12], the combination of the bounce-back and interpolations schemes leads to a model capable of dealing in a very easy way with boundaries of arbitrary geometry. In order to understand the methodology, let us consider the one-dimensional problem depicted in Fig. 2.5. Fluid nodes are on the left-hand side, with A being the last one before the wall, and B being the first solid node. The location of the wall in between lattice nodes is expressed as the fraction of the link in the fluid,

$$0 \leq q = \frac{|\mathbf{x}_C - \mathbf{x}_A|}{|\mathbf{x}_B - \mathbf{x}_A|} \leq 1 \tag{2.71}$$

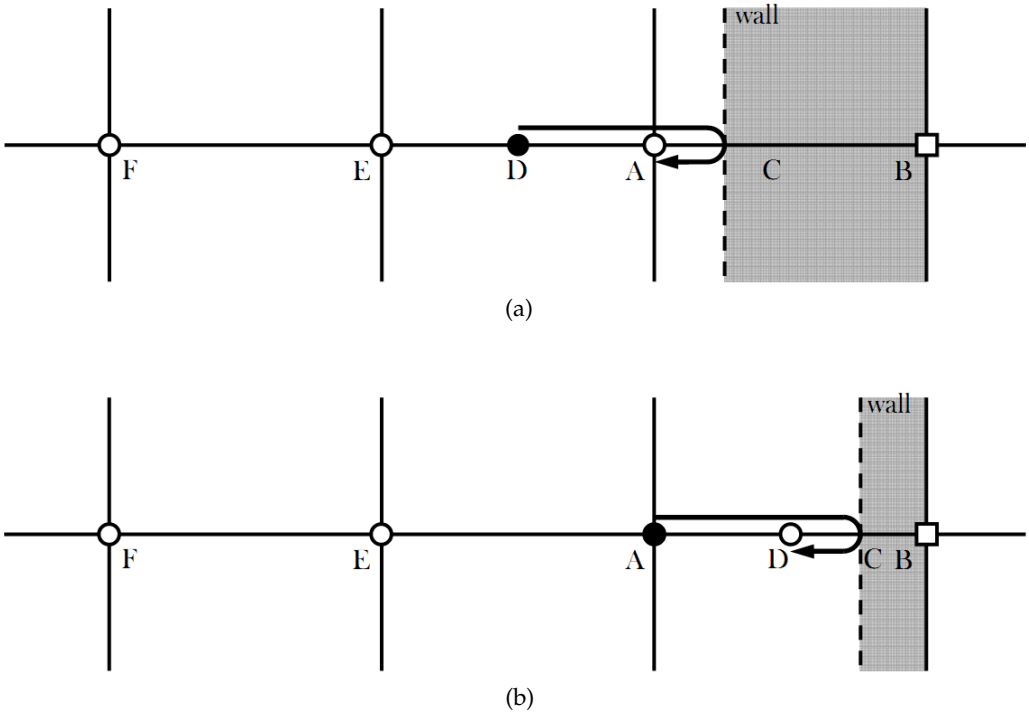

Figure 2.5: Details of the collision process for velocities of opposite directions [12]: (a) $q < 1/2$, (b) $q \geq 1/2$.

The particle leaving the node A is backscattered on the wall. After the collision step, the population particles at the node A with the reversed velocity $-\mathbf{v}_i$, is equal to the post-collision distribution function at the fictitious node D. The latter one is calculated by interpolating the values of the distribution function at the nodes A and E. Both linear and quadratic interpolation formulas can be used. Using linear interpolation, we have the following implementation:

$$\begin{aligned} q < \frac{1}{2}: \quad & f_{-i}\left(\hat{\mathbf{x}}, \hat{t}+1\right) = 2q f_i^*\left(\hat{\mathbf{x}}, \hat{t}\right) + (1-2q) f_i^*\left(\hat{\mathbf{x}} - \mathbf{v}_i, \hat{t}\right), \\ q \geq \frac{1}{2}: \quad & f_{-i}\left(\hat{\mathbf{x}}, \hat{t}+1\right) = \frac{1}{2q} f_i^*\left(\hat{\mathbf{x}}, \hat{t}\right) + \frac{2q-1}{2q} f_{-i}^*\left(\hat{\mathbf{x}}, \hat{t}\right), \end{aligned} \tag{2.72}$$

where $f_i^*(\hat{\mathbf{x}}, \hat{t})$ is the post-collision distribution function. It is worth to stress that this method mantains a regular Cartesian grid, but unlike "classical" bounce-back it works for geometries of arbitrary curvature. Differently from LBM, in traditional CFD non-uniform meshes and body-fitting operations are usually employed in order to match solid boundaries. Actually, it is possible to adopt interpolation techniques also in CFD. Interpolation is easier than body-fitting, but the former is less accurate than the latter. In the

present thesis, the methodology described in [12] is employed in Chapter 5 for the solution of fluid-wall interface in case of curved and moving walls and its effectiveness is highlighted.

2.9.2 Inflow and outflow boundary conditions

The boundary condition by Zou and He [116] is based on the idea of applying the bounce-back rule to non-equilibrum distribution functions. In order to illustrate the methodology, we consider the 2D channel in Fig. 2.3, where the D2Q9 lattice in Fig. 2.1b is used. The lattice velocities and the equilibriuim distribution function are given by Table 2.1 and Eq. (2.7), respectively. As an example, we take the case of a inlet node in Fig. 2.3. In some applications, it can be necessary to specify the value of the pressure or the velocity on inlet nodes. Let us suppose that the density (pressure) and the velocity component along y-direction have to be imposed at the inlet. After the streaming process, f_1, f_2, f_4, f_5 and f_8 are known, as well as $\rho = \rho_{in}$ and $v = 0$. We need to compute $\hat{u}_x$, and the distribution functions f_3, f_6 and f_7. From Eqs. (2.8), we can write the following system of equations:

$$f_3 + f_6 + f_7 = \rho_{in} - (f_0 + f_1 + f_2 + f_4 + f_5 + f_8)\,, \tag{2.73a}$$

$$f_3 + f_6 + f_7 = -\rho_{in} u + f_1 + f_5 + f_8, \tag{2.73b}$$

$$f_6 - f_7 = -f_2 + f_4 - f_5 + f_8. \tag{2.73c}$$

Consistency of Eqs. (2.73a) and (2.73b) gives the value of $\hat{u}_x$ at the inlet:

$$u = -1 + \frac{f_0 + f_2 + f_4 + 2\,(f_1 + f_5 + f_8)}{\rho_{in}}. \tag{2.74}$$

In order to determine f_3, f_6 and f_7, the bounce-back of the non-equilibrium part of the particle distribution normal to the boundary ($f_1 - f_1^{(e)} = f_3 - f_3^{(e)}$) is performed. Therefore,

$$f_3 = f_1 - \frac{2}{3}\rho_{in} u, \tag{2.75a}$$

$$f_6 = f_8 - \frac{1}{2}\,(f_2 - f_4) - \frac{1}{6}\rho_{in} u, \tag{2.75b}$$

$$f_7 = f_5 + \frac{1}{2}\,(f_2 - f_4) - \frac{1}{6}\rho_{in} u, \tag{2.75c}$$

Similar procedure can be applied also to the outlet nodes. The effect of specifying velocity at the inlet is similar to specifying pressure (density)

at the inlet, since both conditions will generate a density difference in the flow [116]. However, it is clear from the above description that LBM deals with general boundaries in a more complicated way that traditional methods (i.e. finite differences). This limitation of LBM arises from the fact that we always need to reconstruct the distribution function on the boundary nodes in order to have the desired values for the hydrodynamic variable. On the boundary nodes, in addition to the values of the hydrodynamic variables, conditions for the ghost moments must be provided as well. With the Link-wise Artificial Compressibility Method (see Chapter 5), this limitation is overcome, due to the fact that the updating of the distribution function is ruled only by the hydrodynamic variables, and thus, we can borrow simpler techniques from finite differences.

Chapter 3

Lattice Boltzmann model for reactive flows in combustion

3.1 Introduction

Lattice Boltzmann method (LBM) has become a very popular technique for simulating fluid flows [21, 45, 46, 47, 90, 102] in a variety of applications such as laminar, turbulent, thermal and multiphase flows and even beyond hydrodynamics, according to some authors [96]. Despite that, applications of LBM to combustion are still limited. One reason is that the original LBM formulation recoves Navier-Stokes equations in the incompressible limit, where the density is (approximately) constant. On the contrary, combustion problems exhibit significant density variations due to the heat release in chemical reactions. Therefore, consistent LBM models are requested to accurately recover the Navier-Stokes-Fourier equations, coupled to a transport equation for each chemical species. Hence, the numerical model is expected to behave macroscopically like a compressible solver, so as to account for large density and temperature variations.

The first model for combustion simulation was proposed by Succi at al. [103], assuming fast chemistry and cold flames with weak heat release. As a consequence, large density variation was not allowed in the model. Yamamoto et al. [110] presented a model for reactive flows based on the classical incompressible LBM formulation [117], under the quite restrictive assumption that the flow field is not affected by chemical reactions. Filippova and Hänel [35] proposed a scheme for modeling reactive flows at low Mach numbers able to handle density variation. In this model, continuity and momentum equations are solved by means of a modified Bhatnagar-Gross-Krook (BGK) scheme, coupled with finite difference schemes for the solution of energy and species equations. The LBM model was derived by modifying the equilibrium populations so that the model behaves like a weak-compressible solver in the macroscopic limit. In order to correct the strain tensor, a term

containing gradients of the density is added to the expression for the equilibrium distribution function. The coupling among continuity, momentum and energy equations is achieved by introducing an additional factor to the rest particle, so to model temporal changes of the density. Macroscopically, this model behaves like a weak-compressible solver. However, in this way the simplicity of the LBM algorithm is somehow lost. Chen et al. [22] overcame this limitation using the model proposed by Guo et al. [42] for the solution of the flow field. Neverthless, the LBM model for the species equation cannot properly account for compressibility effects.

In Ref. [3], a LBM model with energy conservation on standard lattices has been introduced. Unlike more traditional approaches, this model makes unnecessary the introduction of a separate population set for the energy field [44]. However, this (consistent) LBM model is still limited to weakly compressible flows and is not suitable to accurately simulate thermal flows with large density and temperature variations. In order to overcome this limitation, in Refs. [88] and [89], the consistent LBM has been extended to derive a model for simulating compressible thermal flows on standard lattices. The key *ingredient* is the introduction of correction terms into the kinetic Boltzmann-BGK equation, so that the Navier-Stokes-Fourier equations are accurately recovered. The same idea can be also found in [105]. Here, Navier-Stokes equation in the compressible limit are recovered by introducing spatial derivatives of the density in the equilibrium moments. The energy equation is modelled as an advection-diffusion equation and solved by means of finite differences. In principle a second distribution function can be used for the energy equation as well, provided that a model which takes into account large temperature variations is available. Thus, [105] cannot be used for combustion applications. On the contrary, the LBM scheme in [89] has been tested and validated in case of subsonic flows with large density and temperature variations, typically encountered in combustion. More specifically, by solving the benchmark problem in [106], this model proved to be able to handle temperature ratios larger than 10, and hence a good candidate for simulating reactive flows.

In this chapter, the suitability of the aforementioned compressible thermal model for the solution of combustion problems is investigated. To this purpose, without a lack of generality, we will not consider detailed chemistry, while a global chemical step for hydrogen/air reactive mixtures is used instead. The chapter is organized as follows. In Section 3.2, the governing equations for reactive flows at the low Mach number limit are recalled. In Section 3.3, the lattice Boltzmann method for simulating reactive flows is presented: the LBM schemes for the Navier-Stokes-Fourier and species equations are described. In Section 3.4, the proposed model is used for simulating a reactive flow in a *mesoscale* channel [85] and validated against a reference solution obtained by means of FLUENT [38]. In Section 3.5 conclu-

sions are drawn and future works outlined.

3.2 Governing Equations

In Chapter 2, LBM for the incompressible non-reactive Navier-Stokes was discussed. In this chapter, density variaitons are taken into account and the governing equations for reactive flows at low Mach number are the following [63]:

$$\partial_t \rho + \nabla \cdot (\rho \mathbf{u}) = 0, \tag{3.1a}$$

$$\partial_t (\rho \mathbf{u}) + \nabla \cdot (\rho \mathbf{u} \otimes \mathbf{u} + p\mathbf{I}) = \nabla \cdot \mathbf{\Pi} + \rho \sum_{k=1}^{N} Y_k \mathbf{f}_k, \tag{3.1b}$$

$$\partial_t (\rho h^s) + \nabla \cdot (\rho \mathbf{u} h^s + \mathbf{q}) = \frac{dp}{dt} + \mathbf{\Pi} : \nabla \mathbf{u} - \sum_{k=1}^{N} h_k^0 \dot{\omega}_k W_k + \rho \sum_{k=1}^{N} Y_k \mathbf{f_k} \cdot \mathbf{V}_k, \tag{3.1c}$$

$$\partial_t (\rho Y_k) + \nabla \cdot (\rho \mathbf{u} Y_k) - \nabla \cdot (\rho D_k \nabla Y_k) = \dot{\omega}_k W_k, \tag{3.1d}$$

where ρ is the mixture density, $\mathbf{u}$ the mass weighted velocity, p the pressure, $\mathbf{\Pi}$ the viscous tensor; $\mathbf{f}_k$ and $\mathbf{V}_k$ are the body force per unit mass and the diffusive velocity associated to the k-th species. $h^s = c_{p,k} T$ the sensible enthalpy, where T is the mixture temperature and $c_{p,k}$ the specific heat of the k-th species ($k = 1, ..., N$). D_k is the mass diffusivity of the k-th species. Fick's law applies to diffusion of chemical species. In principle, in case of more than two species, Maxwell-Stefan model should be used, instead [5, 6]. The mass fraction, the reaction rate, the molecular weight and the enthalpy of formation of the k-th species are denoted by Y_k, $\dot{\omega}_k$, W_k and h_k^0, respectively. In Eq. (3.1c) isobaric assumption has been used. The heat flux $\mathbf{q}$ includes heat conduction, heat diffusion by mass diffusion of the chemical species, thermal diffusion (Dufour effect), and radiative heat transfer. The heat flux is defines as follows:

$$\mathbf{q} = -\kappa \nabla T + \rho \sum_{k=1}^{N} h_k Y_k \mathbf{V}_k + RT \sum_{k=1}^{N} \sum_{j=1}^{N} \left(\frac{X_j D_{T,k}}{W_k D_{kj}} \right) (\mathbf{V}_k - \mathbf{V}_j) + \mathbf{q}_{rad}, \tag{3.2}$$

where κ is the thermal conductivity, R is the universal gas constant, X_j is the molar concentrations of species j, D_{kj} is the bunary mass diffusivity between species k and j, and $D_{T,k}$ is the thermal diffusion coefficient of species k. Detailed formulations for D_{kj} and $D_{T,k}$ can be found in several textbooks (see for example [55, 63]). $\mathbf{V}_k$ and $\mathbf{V}_j$ are the diffusion velocity of species k and j, respectively. If Fick's model using mixture-averaged transport coefficients is adopted, the diffusion velocity is given by:

$$X_k \mathbf{V}_k = -D_k^m \nabla X_k, \tag{3.3}$$

where D_k^m is the mixture-averaged mass diffusion coefficient for species k, defined as:

$$D_k^m = \frac{\kappa}{\rho c_p Le_k}, \tag{3.4}$$

where c_p is the mixture specific heat, and $Le_k = \alpha_k / D_k$ is the k-th species Lewis number, α_k being the thermal diffusivity of species k. $\mathbf{q}_{rad}$ in Eq. (3.2) represents the source term due to radiative contribution (see Chapter 4 and Appendix B).

In the following, we will neglect the body force $\mathbf{f}_k$ and only contribution of heat conduction is taken into account in the heat flux $\mathbf{q}$.

3.3 Lattice Boltzmann Method for reactive flows

The LBM formulation which recovers Eqs. (3.1a-3.1c) and Eq. (3.1d) in the macroscopic limit is given by the following kinetic equations with the BGK collision model:

$$\begin{aligned} g_i\left(\mathbf{x}+\hat{\mathbf{v}}_i\Delta t, t+\Delta t\right) = g_i\left(\mathbf{x},t\right) + \frac{2\Delta t}{\Delta t+2\tau}\left[f_i^{eq}\left(\mathbf{x},t\right) - g_i\left(\mathbf{x},t\right)\right] \\ + \frac{2\tau\Delta t}{\Delta t+2\tau}\left[\Psi_i\left(\mathbf{x},t\right) + \Phi_i\left(\mathbf{x},t\right)\right], \end{aligned} \tag{3.5}$$

$$\xi_{i,k}\left(\mathbf{x}+\hat{\mathbf{v}}_i\Delta t, t+\Delta t\right) = \xi_{i,k}\left(\mathbf{x},t\right) + \omega_k^{(*)}\left[\xi_{i,k}^{eq(*)}\left(\mathbf{x},t\right) - \xi_{i,k}\left(\mathbf{x},t\right)\right] + Q_{Y_k}. \tag{3.6}$$

ρ, $\mathbf{u}$ and T are computed as moments of g_i, while Y_k as moment of ξ_i. Hereafter, Eqs. (3.5) and (3.6) are described more in detail.

3.3.1 Thermal Lattice Boltzmann model

Eq. (3.5) is derived from the following lattice BGK equation (2.5), modified in such a way to recover the correct Navier-Stokes-Fourier equation [88]:

$$\frac{\partial f_i}{\partial \hat{t}} + \hat{\mathbf{v}}_i \cdot \frac{\partial f_i}{\partial \hat{\mathbf{x}}} = \omega\left(f_i^{(e)} - f_i\right) + \Psi_i + \Phi_i. \tag{3.7}$$

Differently from Eq. (2.5), we can note the presence of the two correction terms Ψ_i and Φ_i. The purpose of the former is to correct the momentum equation, whereas the latter corrects the energy equation [88]. The exact expressions for the correction terms is provided hereafter in this section.

Let us recall Eq. (2.52):

$$f_i\left(x+\hat{\mathbf{v}}_i\Delta t, t+\Delta t\right) = f_i\left(x,t\right) + \frac{1}{\tau}\left[f_i^{(e)}\left(x,t\right) - f_i\left(x,t\right)\right], \tag{3.8}$$

where $\tau = 1/\omega$. The above equation is integrated over the time step Δt as:

$$f_i\left(\mathbf{x}+\hat{\mathbf{v}}_i\Delta t, t+\Delta t\right) = f_i\left(x,t\right) + \int_t^{t+\Delta t} \frac{1}{\tau}\left[f_i^{(e)}\left(t^*\right) - f_i\left(t^*\right)\right] d\,t^* + \int_t^{t+\Delta t} \Psi_i\left(t^*\right) d\,t^* + \int_t^{t+\Delta t} \Phi_i\left(t^*\right) d\,t^*. \tag{3.9}$$

In order to avoid impliciteness, the following variable transformation is applied between the two set of distribution function f_i and g_i:

$$g_i = f_i + \frac{\Delta t}{2}\left[\left(f_i - f_i^{eq}\right) - \left(\Psi_i + \Phi_i\right)\right], \tag{3.10}$$

which leads back to Eq. (3.5), where the discretization in space is done as in standard lattice Boltzmann models (see Section 2.7). The equilibrium values are expressed as follows for the D2Q9 lattice [2, 54]:

$$f_i^{eq} = \rho \prod_{\alpha=x,y} \frac{\left(1-2\hat{\mathrm{v}}_{i,\alpha}^2\right)}{2^{\hat{\mathrm{v}}_{i,\alpha}^2}}\left[\left(\hat{\mathrm{v}}_{i,\alpha}^2 - 1\right) + \hat{\mathrm{v}}_{i,\alpha}u_\alpha + u_\alpha^2 + T\right], \tag{3.11}$$

where the lattice velocities are given by Table 2.1.

The correction terms Ψ and Φ are designed in such a way to properly recover the momentum and energy equations, respectively. They are defined as follows:

$$\Psi_i = \psi_{i,\alpha}\partial_\gamma P''_{a\gamma}, \quad \Phi_i = \varphi_i\left(\partial_\alpha(q'_\alpha + q''_\alpha) + Q_h\right), \tag{3.12}$$

where $\psi_{i,x} = 1/4\,[0,4,0,-4,0,-1,1,1,-1]$, $\psi_{i,y} = 1/4\,[0,0,4,0,-4,-1,-1,1,1]$ and $\varphi_i = 1/8\,[-12,4,4,4,4,-1,-1,-1,-1]$. $\partial_\gamma P''_{\alpha\gamma}$ is deviation from the momentum equation, while q'_α and q''_α are deviations from the energy equation, defined as:

$$\partial_\gamma P''_{\alpha\gamma} = -\frac{\tau}{2}\partial_\alpha\left[\partial_\alpha\left(\rho u_\alpha\left(1-3T\right) - \rho^2 u_\alpha^3\right) - \partial_\beta\left(\rho u_\beta\left(1-3T\right) - \rho'' u_\beta^3\right)\right], \tag{3.13}$$

$$q'_\alpha = \rho u_\alpha\left(1-3T\right) - \rho u_\alpha^3, \tag{3.14}$$

$$\begin{aligned} q''_\alpha = {} & \frac{4-\mathrm{Pr}}{\mathrm{Pr}}\tau\rho T\partial_\alpha T - \tau\left[3u_\alpha^2\partial_\alpha\left(\rho T\right) + 3\rho u_\alpha T\partial_\beta u_\beta - \frac{3}{2}\rho u_\alpha u_\beta\partial_\beta T\right] \\ & -\tau\left\{\left(1-3T\right)\left[\partial_\beta\left(\rho u_\alpha u_\beta\right) - \frac{1}{2}u_\alpha\partial_\beta\left(\rho u_\beta\right)\right]\right\} \\ & -\tau\left[2u_\alpha^3\partial_\beta\left(\rho u_\beta\right) + 3u_\alpha^2\partial_\beta\left(\rho u_\alpha u_\beta\right) + \frac{1}{2}u_\alpha\partial_\beta\left(\rho u_\beta^3\right)\right] \\ & +\tau\partial_\beta e''_{\alpha\beta}, \end{aligned} \tag{3.15}$$

where

$$e''_{\alpha\alpha} = \rho u_\alpha^2 + \rho u_\alpha^4, \quad e''_{\alpha\beta} = \rho^2 u_\alpha u_\beta u. \tag{3.16}$$

The terms $\partial_\gamma P''_{\alpha\gamma}$ and $\partial_\alpha(q'_\alpha + q''_\alpha)$ are evaluated using second-order accurate finite-difference scheme, as suggested in [88] and [89]. Q_h is the energy source, defined as:

$$Q_h = \frac{1}{h_0}\left(\sum_k h_k \dot{\omega}_k W_k\right). \tag{3.17}$$

The relaxation time τ is related to the dynamic viscosity and thermal conductivity as:

$$\mu = \tau\rho T, \quad \kappa = \frac{2}{\mathrm{Pr}}\tau\rho T. \tag{3.18}$$

The hydrodynamic moments are defined as:

$$\rho(f) = \sum_i g_i, \tag{3.19a}$$

$$j_\alpha(f) = \rho u_\alpha(f) = \sum_i \hat{\mathrm{v}}_{i,\alpha} g_i + \frac{\Delta t}{2}\partial_\gamma P''_{\alpha\gamma}, \tag{3.19b}$$

$$T(f) = \frac{1}{2\rho}\left[\sum_i \hat{\mathrm{v}}_i^2 g_i - \rho u^2 + \frac{\Delta t}{2}\partial_\alpha\left(q'_\alpha + q''_\alpha\right)\right], \tag{3.19c}$$

Detailed derivation of the above model and its implementation are provided in Refs. [88] and [89]. It is worth stressing that the model 3.5 is based on a fixed heat capacity $c_p = 2$ in LB units (due to a restriction on the ratio of specific heats, $\gamma = 2$, and non-dimensionalisation of the gas constant $\mathcal{R} = 1$ in LB units). Therefore, the present model for reactive flows inherits this same feature, whereas the latter limitation may be overcome in future works by additional properly designed correction terms.

3.3.2 Lattice Boltzmann model for species equation

Standard lattice Boltzmann models for combustion (e.g. [22]) emulate advection-diffusion-reaction equations by means of the following kinetic equation:

$$\xi_{i,k}(\mathbf{x} + \hat{\mathbf{v}}_i\Delta t, t + \Delta t) = \xi_{i,k}(\mathbf{x}, t) + \omega_k\left[\xi_{i,k}^{eq}(\mathbf{x}, t) - \xi_{i,k}(\mathbf{x}, t)\right] + Q_{Y_k}, \tag{3.20}$$

where $\xi_{i,k}$ and $\xi_{i,k}^{eq}$ are the distribution function and the equilibrium distribution functions for species k along the lattice direction i, respectively and ω_k is the relaxation frequency. Q_{Y_k} is the species source term defined as:

$$Q_{Y_k} = \dot{\omega}_k W_k. \tag{3.21}$$

Both D2Q9 and D2Q5 models can be used to recover the species transport equation. However, here for simplicity, we consider the D2Q5 models, where the equilibrium populations are defined as:

$$\xi_{i,k}^{eq} = w_i \rho Y_k \left[1 + 3 \frac{(\hat{\mathbf{v}}_i \cdot \mathbf{u})}{c} \right], \tag{3.22}$$

where the lattice weights are $w_0 = 1/3$, $w_i = 1/6$ $(i = 1, ..., 4)$ and the lattice velocities are $\hat{\mathbf{v}}_0 = (0, 0)$, $\hat{\mathbf{v}}_i = (\cos(i-1)\pi/2, \sin(i-1)\pi/2)$ $(i = 1, ..., 4)$. The moments corresponding to the equilibrium population (3.22) are:

$$\sum_{i=0}^{4} \xi_{i,k}^{eq} = \sum_{i=0}^{4} \xi_{i,k} = \rho Y_k, \tag{3.23a}$$

$$\sum_{i=0}^{4} \hat{\mathrm{v}}_{i,\alpha} \xi_{i,k}^{eq} = \rho Y_k u_\alpha, \tag{3.23b}$$

$$\sum_{i=0}^{4} \hat{\mathrm{v}}_{i,\alpha}^2 \xi_{i,k}^{eq} = \frac{1}{3} \rho Y_k. \tag{3.23c}$$

The relaxation frequency ω_k is related to the k-th species mass diffusivity D_k in Eq. (3.1d) as:

$$D_k = \frac{1}{3} \left(\frac{1}{\omega_k} - \frac{1}{2} \right). \tag{3.24}$$

Unfortunately the previous approach fails in case of large density gradients. To the best of our knowledgem, some models allow large density changes in the fluid flow, but neglect the corresponding feedback to the sepcies fields (e.g. see Section 3.2 in [22]).
Eq. (3.20)-(3.21) recover the species transport equation (3.1d) with a deviation term:

$$\nabla \cdot (D_k Y_k \nabla \rho), \tag{3.25}$$

which is activated in case of significant compressibility effects (i.e. large $\nabla\rho$). In order to remove the deviation term in the species equation, we can proceed by introducing a correction term to be approximated e.g. by means of finite difference formulas, consistently with the thermal model in Section 3.3.1. However, in the case of advection-diffusion equation it possible to follow an alternative strategy which relies only on LBM formulation. In fact, the deviation term (3.25) can be removed by modifying the equilibrium population and the relaxation frequency in order to enforce Eq. (3.20) to accurately recover Eq. (3.1d). This model represents the main contribution of this part of the thesis.

Deviation from Eq. (3.1d) stems from the second-order moment. In order to remove it, the first step is to modify the equilibrium distribution function as

follows:

$$\begin{aligned} \xi_{0,k}^{eq(*)} &= \rho Y_k \left(1 - \frac{2}{3}\varphi\right), \\ \xi_{1,\dots 4,k}^{eq(*)} &= \frac{1}{6}\rho Y_k \left(\varphi + 3\left(\hat{\mathbf{v}}_i \cdot \mathbf{u}\right)\right), \end{aligned} \tag{3.26}$$

where $\varphi = \rho^{(*)}/\rho$, $\rho^{(*)}$ is a fixed value for the entire domain at any time step, i.e. the minimum value of the density field. The moments corresponding to the modified equilibrium (3.29) are:

$$\sum_{i=0}^{4} \xi_{i,k}^{eq(*)} = \sum_{i=0}^{4} \xi_{i,k} = \rho Y_k, \tag{3.27a}$$

$$\sum_{i=0}^{4} \hat{\mathrm{v}}_{i,\alpha} \xi_{i,k}^{eq(*)} = \rho Y_k u_\alpha, \tag{3.27b}$$

$$\sum_{i=0}^{4} \hat{\mathrm{v}}_{i,\alpha}^2 \xi_{i,k}^{eq(*)} = \frac{1}{3}\rho^{(*)} Y_k. \tag{3.27c}$$

It should be noted that with respect to Eqs. (3.23), in the second-order moment the local density does not appear any longer. In this way, compressibility effects in the species equation are cancelled out.

The second step for recovering Eq. (3.1d) consists in redifining the relaxation frequency in Eq. (3.20). The following relation is proposed:

$$\omega_k^{(*)} = \frac{1}{\frac{1}{2} + \frac{1}{\varphi}\left(\frac{1}{\omega} - \frac{1}{2}\right)}, \tag{3.28}$$

such that, if $\varphi = 1$, $\omega_k^{(*)} = \omega_k$. With the suggested modification, Eq. (3.6) recovers Eq. (3.1d) in the macroscopic limit. It is clear from Eq. (3.28) that, for stability reasons, $\varphi < 1$. It is worth stressing that, in the proposed model, there is a single consistent density field which is the one coming from populations g_i 3.5, and can thus properly accomodate large density variations. Therefore here, compressibility is taken into account using the g_i populations for computing density, which is in turn adopted in both the equilibrium populations 3.29 and the relaxation frequency 3.28 (through φ).

Without a lack of generality, a minimal D2Q5 is used for the species transport equations (unlike the hydrodynamic part 3.5 which is based on a D2Q9 lattice). Such a choice is motivated by convenience in reducing the memory demand. This is particularly desirable in the case of detailed chemical kinetics, where a large number of species is tipically taken into account. However,

for the sake of completeness, we report below the equilibrium populations in the case a D2Q9 lattice is adopted for the species transport equations:

$$\begin{aligned}
\xi_{0,k}^{eq(*)} &= \frac{1}{9}\rho Y_k \left(9 - 5\varphi\right), \\
\xi_{1,\ldots 4,k}^{eq(*)} &= \frac{1}{9}\rho Y_k \left(\varphi + 3\left(\hat{\mathbf{v}}_i \cdot \mathbf{u}\right)\right), \\
\xi_{1,\ldots 4,k}^{eq(*)} &= \frac{1}{36}\rho Y_k \left(\varphi + 3\left(\hat{\mathbf{v}}_i \cdot \mathbf{u}\right)\right).
\end{aligned} \tag{3.29}$$

3.4 Numerical results

First, validation of the proposed LB model for the species transport equation is discussed in this section. The 1D non-dimensional form of Eq. (3.1d) at the steady-state for one species ($k = 1$) non-reacting flow with constant mass diffusivity is:

$$\rho' u_x' \frac{dY}{dx'} = \frac{D'}{ReSc} \frac{d}{dx'} \left(\rho' \frac{dY}{dx'}\right), \tag{3.30}$$

where $x' = x/L_0$, $\rho' = \rho/\rho_0$, $u_x' = u_x/u_0$ and $D' = D/\left(u_0 L_0\right)$, with 0 and $'$ denoting the reference and the non-dimensional quantities, respectively. Re and Sc are the Reynolds number and the Schmidt number. Defining $Z = dY/dx'$ and $\Lambda = \rho' Z$, Eq. (3.30) is rewritten as:

$$u_x' \Lambda = \frac{D'}{ReSc} \frac{d\Lambda}{dx'}. \tag{3.31}$$

Imposing $u_x' = 1/\Lambda$, the solution of Eq. (3.31) is:

$$\Lambda = x' \frac{ReSc}{D'} + \Lambda_0, \tag{3.32}$$

where Λ_0 is an arbitrary constant. The condition $d\left(\rho' u_x'\right)/dx' = 0$ is satisfied imposing $\rho' = \Lambda$, such that $Z = 1$. Thus, the analytical solution of Eq. (3.30) is:

$$Y_{an} = x' + Y_0, \tag{3.33}$$

which can be used to validate the porposed LB model for the species transport equation. Here, periodicity is assumed in the y -direction of a square domain, so as to reduce the problem to 1D. Analytical solution is imposed at the inlet ($x' = 0$) and the outlet ($x' = 1$) of the domain. The L^2 norm of deviation of numerical results from the exact solution are reported in Table 3.1, in case of diffusive scaling (i.e. $\delta t \sim \delta x^2$).

In order to validate the proposed LBM model for reactive flows, we consider combustion of stoichiometric premixed hydrogen/air reactive mixture between two parallel horizontal plates, with a fixed length-to-height aspect

δx	Error $L^2[Y]$	Slope
0.05	2.745521×10^{-2}	–
0.025	8.186644×10^{-3}	1.75
0.0125	2.495928×10^{-3}	1.71

Table 3.1: Convergence analysis of the LB model for the species equations in case of diffusive scaling ($\delta t \sim \delta x^2$).

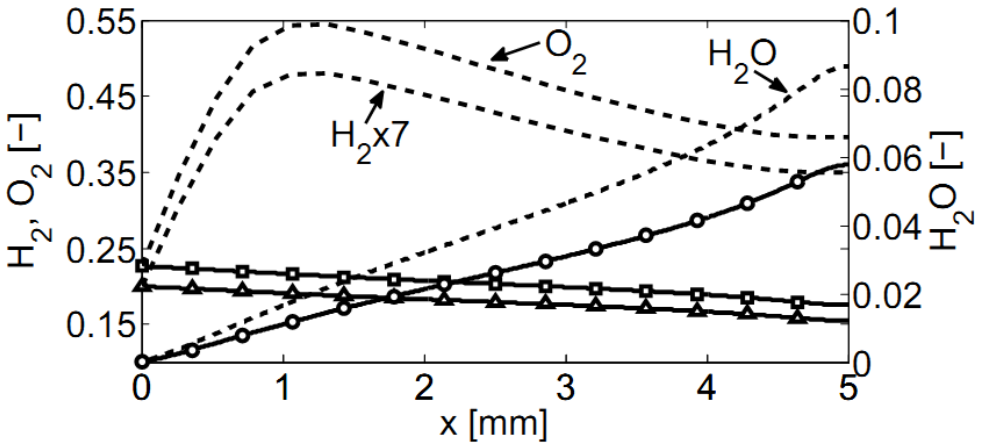

Figure 3.1: Species mass fractions along the channel walls predicted by basic model 3.22 (dashed-lines) are compared to those recovered by the proposed model (solid-lines). Symbols are the reference solution (circles H_2O, squares O_2, triangles H_2). Present application refers to Test 1.

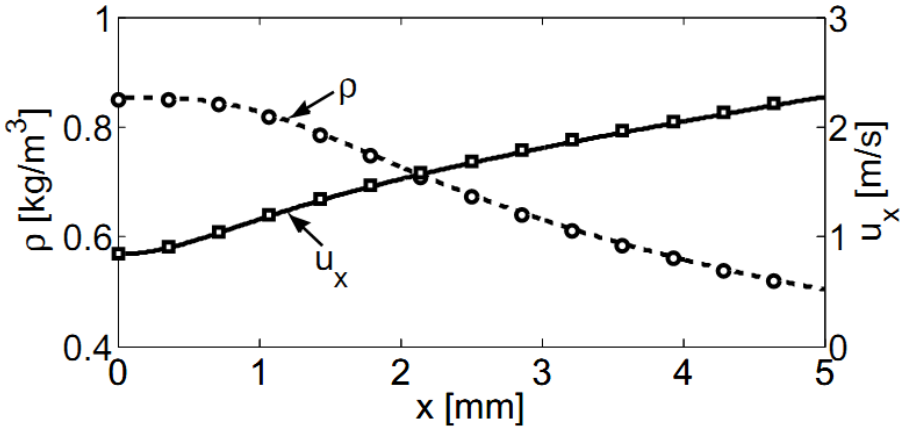

Figure 3.2: Test 1: Mixture density and x-velocity component along the horizontal plane of symmetry. Solid lines and symbols represent the LB and the reference solutions, respectively.

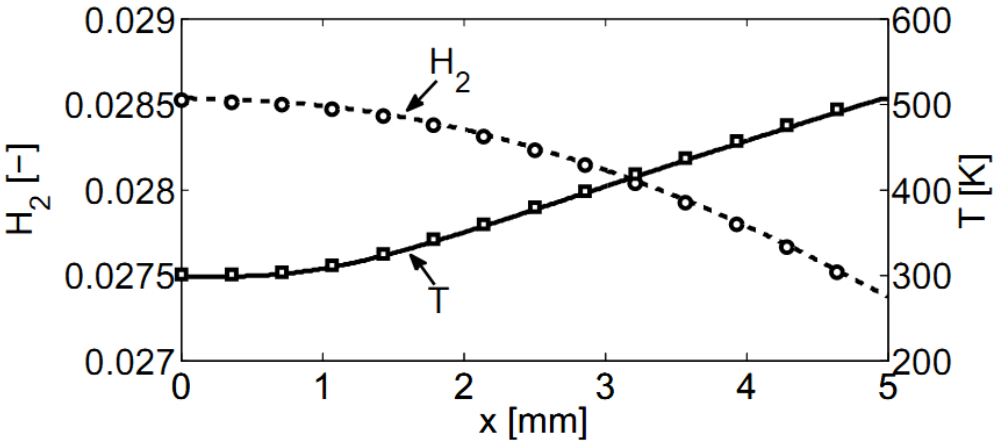

Figure 3.3: Test 1: Mixture temperature and H_2 mass fraction along the horizontal plane of symmetry. Solid lines and symbols represent the LB and the reference solutions, respectively.

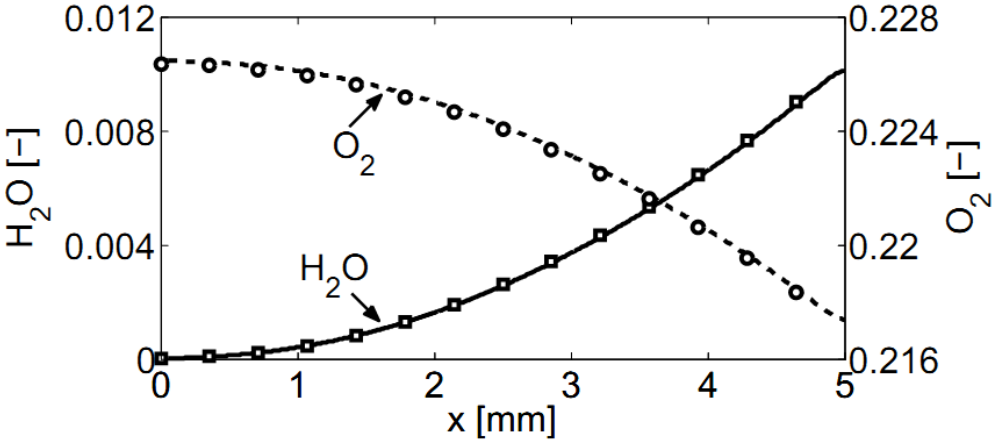

Figure 3.4: Test 1: H_2O and O_2 mass fractions along the horizontal plane of symmetry. Solid lines and symbols represent the LB and the reference solutions, respectively.

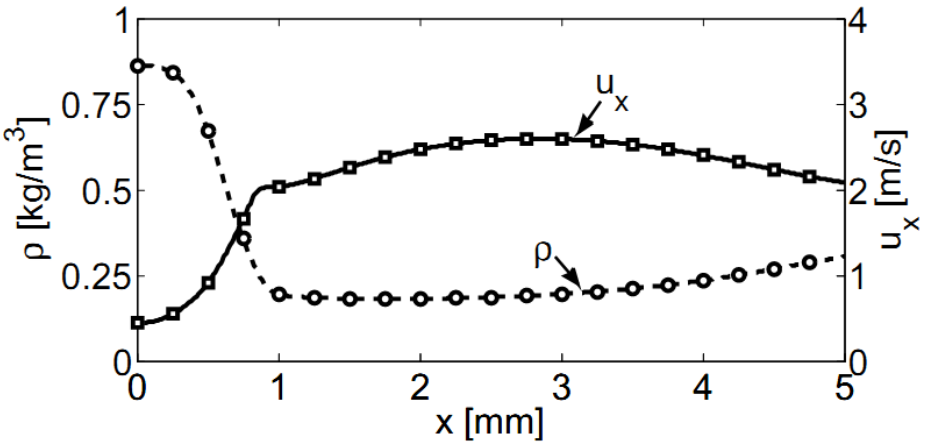

Figure 3.5: Test 2: Mixture density and x-velocity component along the horizontal plane of symmetry. Solid lines and symbols represent the LB and the reference solutions, respectively.

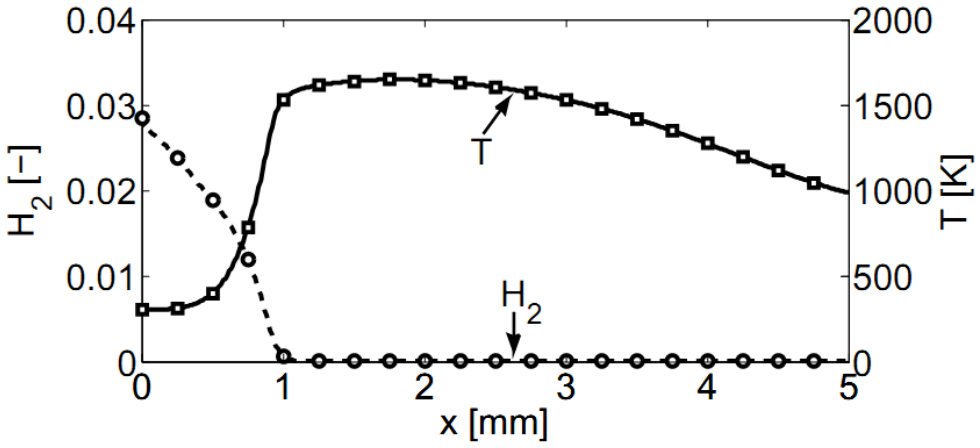

Figure 3.6: Test 2: Mixture temperature and H_2 mass fraction along the horizontal plane of symmetry. Solid lines and symbols represent the LB and the reference solutions, respectively.

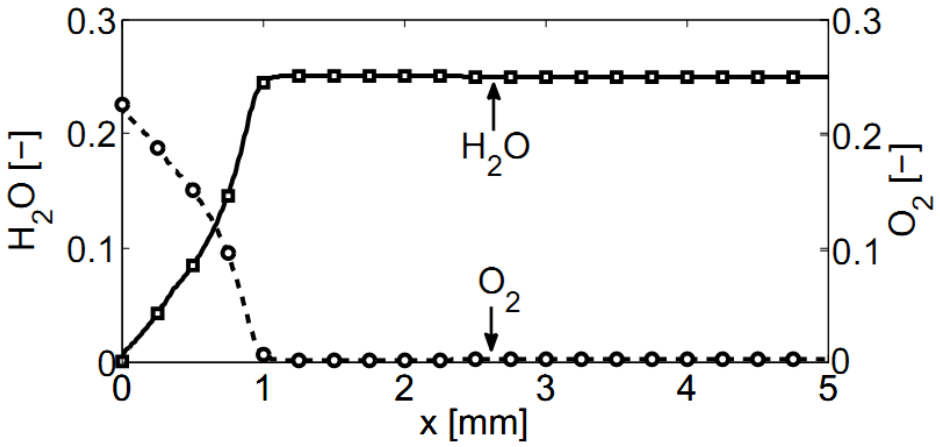

Figure 3.7: Test 2: H_2O and O_2 mass fractions along the horizontal plane of symmetry. Solid lines and symbols represent the LB and the reference solutions, respectively.

ratio, $L/h = 2.5$ and length $L = 5\,\text{mm}$. This domain is usually referred to as mesochannel. Ignition od the reactive mixture is produced ans sustained by heated walls. For fixed values of the channel height h and the wall temperature, different types of flames are observed, as function of the inlet velocity U_{in} [85]. In both cases, constant temperature $T_{in} = 300\,\text{K}$ is prescribed at the inflow, and a well premixed stoichiometric hydrogen-air mixture enters from the inlet. Along the channel walls, zero-flux for all species (e.g. chemically inert walls) and no-slip conditions for both velocity component are imposed. The wall temperature is prescribed via a hyperbolic tangent connecting fresh conditions up to the highest temperature $T_w = 960\,\text{K}$, according to $T(x) = S_1 \tanh(\beta x - \gamma) + (T_w - S_1)$, with $S_1 = 330\,\text{K}$, $\beta = 5$ and $\gamma = 4.2$. Such profile mimics heat losses at the channel inlet due to convective cooling of the cold incoming flow and radiative heat losses to the colder surroundings. At the outlet, atmospheric pressure and zero Neumann conditions are imposed. For the sake of simplicity, we assumed $D_k = D$ and $c_{p,k} = c_p$ for the mass diffusivity and specific heat of all chemical species.

The global reaction $H_2 + 1/2O_2 \rightarrow H_2O$ by Marinov et al. [70] is employed for the evaluation of the reaction rates in Eqs. (3.1c) and (3.1d):

$$R = A C_{H_2} C_{O_2}^{0.5} \exp\left(-\frac{E}{RT}\right), \tag{3.34}$$

with $A = 1.8 \times 10^{13}\ \text{mol}^{-0.5}\ \text{cm}^{1.5}\ \text{s}^{-1}$ and $E = 146.4\,\text{kJ/mol}$.

For validation purposes, solutions of the LBM scheme have been compared against solutions from FLUENT [38]. In this simulation we make use of $501(N_x) \times 201(N_y)$ regular lattice. Transport properties have been assumed

constant: the kinematic viscosity is ν=0.22 $\times 10^{-4}$ m^2/s, the mass diffusivity $D = 1.4 \times 10^{-4}$ m^2/s, the Prandtl number Pr = 0.465 and the Lewis number $Le = \alpha/D = 1/3$, where α is thermal diffusivity. Concerning the flow field, diffusive boundary conditions [2] are used for the walls, while equilibrium populations are imposed at the inlet and outlet as follows:

$$g_i^{in}(l=1,m) = f_i^{eq}\left(\frac{p(l=2,m)}{T^{in}}, \mathbf{u}^{in}, T^{in}\right), \tag{3.35}$$

$$\begin{aligned} g_i^{out}(l=N_x-1,m) = f_i^{eq}\Bigg[&\frac{p^{out}}{T(l=N_x-1,m)}, \mathbf{u}(l=N_x-1,m), \\ &T(l=N_x-1,m)\Bigg], \end{aligned} \tag{3.36}$$

where l and m label the nodes along x- and y- directions. p^{out} is the LB outlet pressure corresponding to $p = 1$ atm.

For the species equations, bounce-back is applied at the walls and equilibrium populations at the inlet and outlet as:

$$\xi_{i,k}^{in}(l=1,m) = \xi_{i,k}^{eq}\left(\rho^{in}Y_k^{in}, \mathbf{u}^{in}\right), \tag{3.37}$$

$$\xi_{i,k}^{out}(l=N_x,m) = \xi_{i,k}^{eq}\left[(\rho Y_k)^{out}), \mathbf{u}(l=N_x,m)\right] \tag{3.38}$$

where Y_k^{in} represents the mass fraction of the fresh mixture, while $\rho^{in} = p(l=2,m)/T^{in}$, $\mathbf{u}(l=N_x,m) = \mathbf{u}(l=N_x-1,m)$, and:

$$\begin{aligned} (\rho Y_k)^{out} = &\frac{3}{2}\rho(l=N_x-1,m)\,Y_k(l=N_x-1,m) \\ &-\frac{1}{2}\rho(l=N_x-3,m)\,Y_k(l=N_x-3,m). \end{aligned} \tag{3.39}$$

The proposed reactive LBM model is validated against reference solutions from FLUENT. In Figs. 3.2-3.7 the solutions of the test problem are presented. Comparisons between our results and the reference ones are reported at the steady state. Good agreement is demonstrated. In Figs. 3.2-3.4, the solutions for $U_{in} = 0.85$ m/s are presented. In this case, a longer channel is needed, in order to have complete fuel conversion. However, a smaller channel length has been chosen for validation purposes, so as to reduce the computational effort. In order to check the suitability of the model at larger temperature ratios in the bulk, the velocity at the inlet is reduced to $U_{in} = 0.48$ m/s. In this case, a closed symmetric flame is anchored at the vicinity of the inlet and fully converts the fuel within the channel (Figs.

3.5-3.7). In the test problems, the maximum relative difference between solutions are found to be: 2% for the density, 4.2% for the velocity, 5.7% for the temperature, and 3% for the chemical species.

In order to check the consistency of the LB scheme, we computed the following quantities for the H, O and N elements:

$$M_n = \int_0^h \sum_{k=1}^{N} \rho u_x Y_k c_{k,n} dy, \tag{3.40}$$

where $c_{k,n}$ is the number of atoms of the n-th element in the k-th species. Mass conservation is verified by measuring the previous quantities through the domain. For Test 1, $M_H = 8.01 \times 10^{-5} \pm 5 \times 10^{-6}$, $M_O = 6.42 \times 10^{-4} \pm 9.42 \times 10^{-6}$ and $M_N = 2.11 \times 10^{-3} \pm 3.96 \times 10^{-5}$. For Test 2, $M_H = 8.26 \times 10^{-5} \pm 1.73 \times 10^{-6}$, $M_O = 5.15 \times 10^{-5} \pm 7.4 \times 10^{-7}$ and $M_N = 3.17 \times 10^{-4} \pm 1.96 \times 10^{-9}$. We finally stress that mass conservation through (3.40) is accurate at the same level as FLUENT solution.

In general, the computational algorithm can be schematically summarized as follows:

1. At time step t, compute ρ, u_α and T from Eqs. (3.19a-3.19c), using $(\partial_\gamma P''_{\alpha,\gamma})^{t-1}$ and $(\partial_\alpha (q'_\alpha + q''_\alpha))^{t-1}$, evaluated at the previous time step; compute Y_k from Eq. (3.27a), $\rho^{(*)} = \min(\rho)$ and $\omega^{(*)}$ from Eq. (3.28).
2. Evaluate Q_h and Q_{Y_k}, using Eqs. (3.17) and (3.21).
3. Evaluate $(\partial_\gamma P''_{\alpha,\gamma})^t$ and $(\partial_\alpha \left(q'_\alpha + q''_\alpha\right))^t$, using ρ, u_α and T from 1; evaluate f^{eq} and ζ^{eq}.
4. Solve Eqs. (3.5) and (3.6).
5. Go back to step 1 until convergence.

3.5 Conclusions

In this chapter, we introduced a lattice Boltzmann scheme for simulating reactive flows at the low Mach number limit, on the basis of a recently proposed thermal model. The latter had to be coupled with mass conservation equations for the chemical species. Also in this case a model able to deal with compressibility effects was derived. To this purpose, we proposed a new scheme for solving the reaction-diffusion equation of chemical species, where compressibility effects are taken into account by modifying both the equilibrium distribution function and the relaxation frequency in the BGK collision term. This original idea can be extended to the compressible model in [105], so that also the energy equation can be solved by means of LBM in case of large temperature gradients.

The proposed LBM model has been validated against a commercial code in case of hydrogen/air reactive mixture. Instead of the detailed chemistry, a global chemical step mechanism has been used for simulating reactive flows in a mesochannel. Solutions of the proposed model are found to be in good agreement with the reference results, obtained in the continuum limit.

It is worth to recall that in this chapter, heat conduction is the only contribution to the heat flux $\mathbf{q}$. A more detailed description of combustion problems needs to take into account also heat diffusion by mass diffusion of chemical species, Dufour effect and radiative heat transfer. However, with regard to radiation, its negligibility is motivated by the fact that the size of the computational domain is too small to observe any radiative effect. In the next chapter, a lattice Boltzmann model for radiative heat transfer is discussed and the expression for $\mathbf{q}_{rad}$ is provided.

Chapter 4

Lattice Boltzmann method for solving radiative heat transfer

4.1 Introduction

Consideration of volumetric radiation (see $\mathbf{q}_{rad}$ in Eq. (3.1c)) is important in many high temperature thermal devices and processes [69, 100]. Design of boilers, furnaces, internal combustion engines and insulations are some of the systems which require a correct analysis of thermal radiation [69, 100]. Analysis of phase change process of semitransparent materials such as glass and semiconductor materials requires knowledge of the volumetric radiation [91, 94, 98, 111]. Correct estimates of volumetric radiation is also important in weather forecasting which relies on atmospheric radiation budget [40] and medium characterization of an optically participating medium like human tissue and laser surgery of a human organ [56, 83].

Radiative transport through a participating medium is a volumetric phenomenon [78, 99]. Unlike conduction and convection modes of heat transfer which depend on spatial and temporal dimensions, an analysis of radiation involves additional three dimensions, viz., two angular dimensions (polar and azimuthal angles) and one spectral dimension. A mandatory consideration of two angular dimensions in all problems except the simplest case of the planar geometry in which case radiation is azimuthally symmetric and thus it depends only on the planar angle, the problems are difficult to analyze. In a conduction-convection and radiation problem, it is the computation of radiative component that is the most time consuming one. This excessive computational time in the computation of radiative information is for the reason that apart from covering all the spatial grid points in the solution domain, intensities at every grid point need to be traced from their points of origin in the enclosure to the grid point under consideration. At every grid point, intensities are spanned over the whole spherical space. A method becomes computationally more and more expensive if for a given

number of control volumes, it requires more number of discrete directions.

The available numerical radiative transfer methods such as the flux method [78, 99], the zonal method [78, 99], the spherical harmonics method [78, 99], the discrete ordinates method (DOM) [37, 77], the discrete transfer method (DTM) [1, 27, 65], the collapsed dimension method [75] and the finite volume method (FVM) [18, 57, 76], in some form or the other, aim at minimizing the angular dependency of radiation in their formulations. Since the angular dependency cannot be fully eliminated, a method which is less prone to ray effect and is compatible to other CFD solvers such as the finite difference method (FDM) and the FVM for solving the combined mode problems in simple to complex geometry are the most desirable ones. Among the existing numerical radiative transfer methods, the FVM [18, 57, 76] is the most robust one. This is not only for the reason that the development of the FVM is the latest in the series, but for the very reason that it adopts the same principles of the FVM that has been widely used in the analysis of fluid flow and heat transfer problems. Further, unlike the DOM [37, 77], the FVM is fully conservative. In this, the ray effect is minimal. However, even with the FVM, radiation still remains a computationally expensive component. Therefore, search for a computationally more efficient method still continues.

Since in the LBM, processes are localized, it is well suited for a parallel architecture and the requirement of numerical efficiency can be fulfilled. In the recent past, the LBM has been applied to a large class of fluid flow and heat transfer problems [102]. Application of the LBM to solve energy equations, in particular by means of the so-called passive scalar approach [33, 44, 71, 97, 103, 107], has been known for quite some time. This has essentially been the simplest approach in which the temperature is treated as a passive scalar, which is diffused and moderately advected by the flow velocity. This particular approach has been adopted to analyze several thermal problems [33, 44, 71, 97, 103, 107] that involved computations of the density, velocity and temperature fields caused by convection and/or conduction heat transfer. Those studies, did not consider the effect of volumetric radiation which is an important component in high temperature applications.

Mishra and co-workers [28, 73, 74, 76, 79, 91] have applied the LBM to solve heat transfer problems involving thermal radiation. However, in such problems, the volumetric thermal radiation was always computed using the conventional numerical radiative transfer methods such as the DOM [37, 77], the DTM [1, 27, 65], the collapsed dimension method [75] and the FVM [18, 57, 76]. The previous studies [28, 73, 74, 76, 79, 91] have shown the superiority of the LBM over the FDM and the FVM to solve the energy equations of heat transfer problems involving thermal radiation. However, in none of the previous studies, the computation of radiative information, which is the main time consuming component, has been computed using the LBM, and

thus, the usage of the LBM for the analysis of radiative transport problems has not been investigated before. Further, in the combined mode problems studied in references [28, 73, 74, 76, 79, 91], the computational grids of the conventional radiation solvers such as the DTM [1, 27, 65], the DOM [37, 77], the FVM [18, 57, 76], etc., have always been different from the lattices of the LBM. Thus, the radiative information computed using these methods required to be interpolated to the lattice nodes that required an additional computational step.

Very recently a different approach has been proposed by Asinari et al. [9], where the LBM is directly used to solve the radiative heat transfer in a participating medium. Essentially the idea is to interpret the (transient) radiative transfer equation (RTE) as a kinetic equation for photons and consequently to solve it directly through the standard LBM formalism by a pseudo-time marching. The numerical implementation is very simple and it is particularly suitable for complex geometries. The reason is twofold: the intensities at every grid point are automatically traced from their points of origin at the solid walls and the data structures for radiation can be the same of those for fluid flow. These advantages make promising the application of this approach to porous media. However the accuracy of the method still needs to be investigated and further improved for making it competitive with standard FVM radiation solvers. This chapter aims to suggest simple but effective improvements to the method proposed in Ref. [9].

This chapter is organized as follows. In section 4.2, derivation of the radiative LBM scheme is described, including the improvements concerning the angular discretization of the radiative transfer equation. Moreover a detailed error analysis is carried out in order to point out the dependence of the numerical error on the discretization parameters. Section 4.3 reports the numerical results for the 2-D rectangular enclosure (both in terms of temperature field and radiative heat flux). In particular the complete simulation plan, the convergence study and the attempts to reduce the computational demand (the so–called thermalization of intensities out of the main simulation plane) are presented. Section 4.4 reports the concluding remarks. Finally, in Appendix A, a description of the Finite Volume procedure for radiative equation is given, and the numerical results obtained by standard FVM and used for comparison are also reported for sake of completeness. In Appendix B application of radiative LBM for combustion problems is presented, in order to provide the coupling with the combustion model in Chapter3.

4.2 Formulation

Let us consider a 2-D square enclosure. The participating medium bounded by the enclosure is assumed to be homogeneous, absorbing, emitting and scattering. All the boundaries are diffusive and gray: the source of radiation is the south wall at temperature T_s, while the other three boundaries are cold.
The starting point for deriving the LBM formulation is the Radiative Transfer Equation (RTE). In any direction **s** RTE reads:

$$\frac{dI}{ds} = \mathbf{s} \cdot \nabla I = -\beta I + \kappa_a I_b + \frac{\sigma_s}{4\pi} \int_{4\pi} I p \left(\Omega, \Omega^{'}\right) d\Omega^{'} \tag{4.1}$$

where I is the intensity, κ_a is the absorption coefficient, $I_b = (\sigma T^4)/\pi$ is the blackbody intensity, β is the extinction coefficient, σ_s is the scattering coefficient and p is the scattering phase function. s is the distance in the direction **s**, which is defined as:

$$\mathbf{s} = (\sin\gamma\cos\delta)\,\mathbf{i} + (\sin\gamma\sin\delta)\,\mathbf{j} + \cos\gamma\mathbf{k}, \tag{4.2}$$

where γ is the polar angle and δ is the azimuthal angle.

Since radiation is the only heat transfer mechanism under investigation, radiative equilibrium condition can be considered, so that $\nabla \cdot \mathbf{q}_R = 0$, where $\mathbf{q}_R$ is the radiative heat flux and its divergence is defined as follows:

$$\nabla \cdot \mathbf{q}_R = \kappa_a \left(4\pi I_b - G\right), \tag{4.3}$$

where $\nabla \cdot \mathbf{q}_R = \mathbf{q}_{rad}$ in Eq. (3.1c). Radiative equilibrium condition implies that the volumetric absorption G equals the volumetric emission $4\pi I_b$. If scattering is assumed isotropic ($p = 1$), Eq. (4.1) can be rewritten as:

$$\frac{dI}{ds} = \mathbf{s} \cdot \nabla I = \beta I + (\kappa_a + \sigma_s)\frac{G}{4\pi} = \beta\left(\frac{G}{4\pi} - I\right), \tag{4.4}$$

since the extinction coefficient $\beta = \kappa_a + \sigma_s$. For discrete directions, Eq. (4.4) is written as:

$$\frac{dI_{ij}}{ds} = \mathbf{s}_{ij} \cdot \nabla I ij = \beta\left(\frac{G}{4\pi} - I_{ij}\right), \tag{4.5}$$

where I_{ij} is the intensity evaluated along the i-th azimuthal direction and j-th polar direction.

In the LBM formulation proposed by Asinari et al. [9], isotropy in the polar direction is assumed and angular dependence of the intensity is only due to the azimuthal direction. Azimuthal angle is discretized (Fig. 4.1) by introducing a finite number of discrete velocities $\mathrm{v}_{\lambda,i}$ ($\lambda = x, y$), lying on the lattice, whose magnitude is given by:

$$|\mathrm{v}_i| = c\,\left(\sqrt{\mathrm{v}_{x,i}^2 + \mathrm{v}_{y,i}^2}\right), \tag{4.6}$$

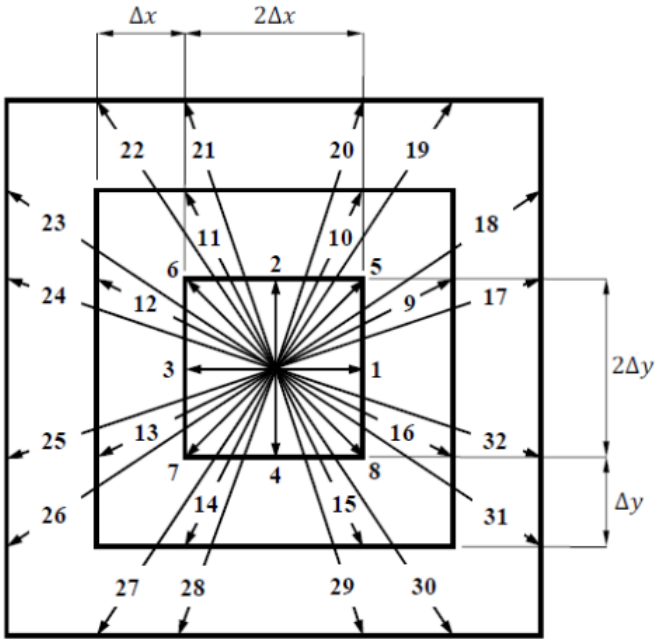

Figure 4.1: Schematic of the lattice: azimuthal angle discretization

where $c = \Delta x/\Delta t$. We may define the magnitude of the lattice velocities as $\mathrm{v}_i = \varepsilon_i c$, where ε_i is is a constant depending on the energy shell of the considered velocity. In Table 4.1, velocities for the D2Q32 lattice used in this work are given. Even though not discretizing the polar angle saves a lot of computations, this approximation may spoil the accuracy of the method, particularly in case of refined computational grids, where a sort of saturation of the numerical error appears [9]. Hence, in the present paper, a different solution is proposed and the polar angle γ ($0 \leq \gamma \leq \pi$) is discretized as well. In this paper discretization of the polar angle has been performed by introducing along the z-axis a velocity component $\mathrm{v}_{z,j}$ of the discrete lattice velocity, which has been designed in such a way that the projection on the lattice of the total velocity $\mathbf{V} = \left(\mathrm{v}_{x,i}, \mathrm{v}_{y,i}, \mathrm{v}_{z,j}\right)$ overlaps the velocity on the lattice $\mathrm{v}_{\lambda,i}$. Hence, $\mathrm{v}_{z,j}$ is defined as follows:

$$\mathrm{v}_{z,j} = \tan\left(\frac{\pi}{2} - \gamma_j\right)\mathrm{v}_i, \tag{4.7}$$

where γ_j is the discrete polar angle in the j-th direction, so that the magnitude of the total velocity is:

$$\mathrm{V}_{ij} = \sqrt{\mathrm{v}_{x,i}^2 + \mathrm{v}_{y,i}^2 + \mathrm{v}_{z,i}^2}. \tag{4.8}$$

The usual lattice Boltzmann numerical scheme is derived by applying the method of characteristics and forward Euler. Thus, the first task is to rewrite

Table 4.1: Lattice velocities for the D2Q32.

	$\hat{\mathrm{v}}_{xi} = \mathrm{v}_{xi}/c$	$\hat{\mathrm{v}}_{yi} = \mathrm{v}_{yi}/c$	v_i
$i = 1,3$	± 1	0	c
$i = 2,4$	0	± 1	c
$i = 5,6,7,8$	± 1	± 1	$\sqrt{2}c$
$i = 9,12$	± 2	1	$\sqrt{5}c$
$i = 13,16$	∓ 2	-1	$\sqrt{5}c$
$i = 10,11$	± 1	2	$\sqrt{5}c$
$i = 14,15$	∓ 1	-2	$\sqrt{5}c$
$i = 17,24$	± 3	1	$\sqrt{10}c$
$i = 25,32$	∓ 3	-1	$\sqrt{10}c$
$i = 18,23$	± 3	2	$\sqrt{13}c$
$i = 26,31$	∓ 3	-2	$\sqrt{13}c$
$i = 19,22$	± 2	3	$\sqrt{13}c$
$i = 27,30$	∓ 2	-3	$\sqrt{13}c$
$i = 20,21$	± 1	3	$\sqrt{10}c$
$i = 28,29$	± 1	-3	$\sqrt{10}c$

the RTE as a BGK equation in such a way that a Lagrangian derivative appears. Time dependence of the intensity is usually neglected in radiation problems because the speed of light is much faster than heat transfer phenomena. However, for the above mentioned reasons, it is convenient to consider a pseudo–transient equation as the starting point of the LBM formalism. The transient RTE reads:

$$\frac{1}{c}\frac{\partial I_{ij}}{\partial t} + \mathbf{s}_{ij} \cdot \nabla I_{ij} = \beta \left(\frac{G}{4\pi} - I_{ij} \right), \tag{4.9}$$

where c is the (fictitious) speed of light. Actually, the starting point for the derivation of the radiative LB scheme is Eq. (4.9), where we assume, along each discrete direction, the fictitious speed of light to be equal to the corresponding microscopic velocity $c = \mathrm{V}_{ij}$. If c is taken equal to the light speed, the term $c\Delta t \to \infty$ (see the left hand side in Eq. (4.13)), which makes the stencil involved in the streaming step very large. Choosing $c = \mathrm{V}_{ij}$, in the streaming step only the nodes belonging to the computational grid are taken into account and the stencil is the smallest as possible. Hence, from the LBM point of view, Eq. (4.9) rewrites as:

$$\frac{1}{\mathrm{V}_{ij}}\frac{\partial I_{ij}}{\partial t} + \mathbf{s}_{ij} \cdot \nabla I_{ij} = \beta \left(\frac{G}{4\pi} - I_{ij} \right). \tag{4.10}$$

Multiplying Eq. (4.10) by V_{ij} yields:

$$\frac{\partial I_{ij}}{\partial t} + \mathbf{V} \cdot \nabla I_{ij} = \frac{\partial I_{ij}}{\partial t} + \mathrm{v}_{x,i}\frac{\partial I_{ij}}{\partial x} + \mathrm{v}_{y,i}\frac{\partial I_{ij}}{\partial y} + \mathrm{v}_{z,i}\frac{\partial I_{ij}}{\partial z} = \mathrm{V}_{ij}\beta \left(\frac{G}{4\pi} - I_{ij} \right). \tag{4.11}$$

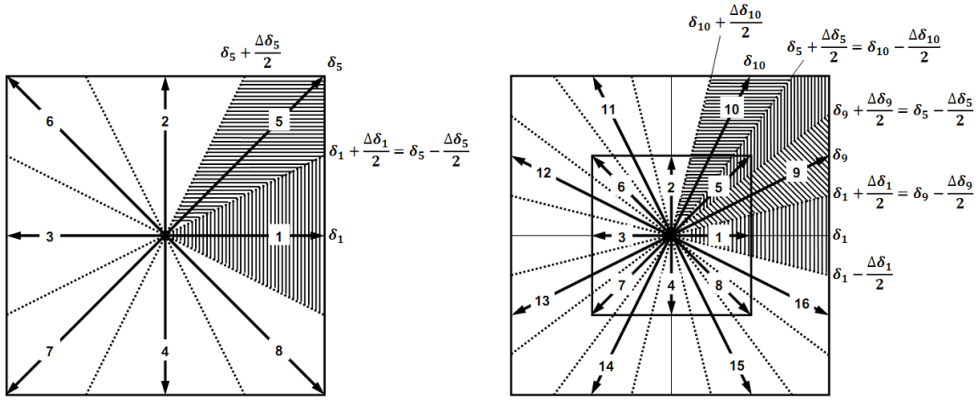

(a) (b)

Figure 4.2: Region of influence of the particle distribution function for the D2Q8 (a) and D2Q16 (b) lattices

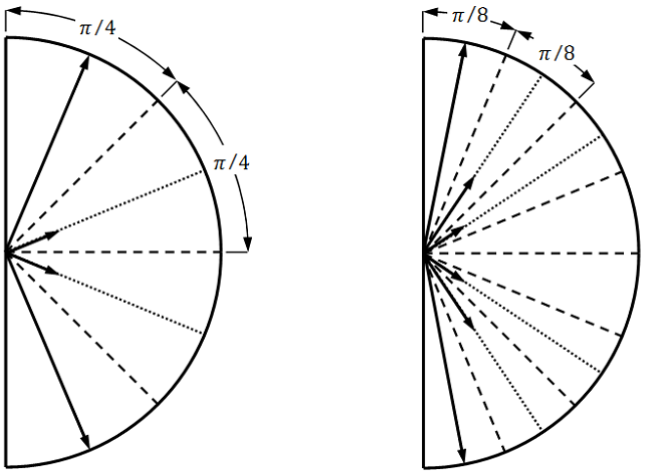

(a) (b)

Figure 4.3: Polar angle discretization for 4 (a) and 8 (b) subdivisions

Recalling that $\partial I_{ij}/\partial z = 0$ by definition of 2-D problem, one can rewrite the discrete Boltzmann equation for a 2-D radiative problem:

$$\frac{\partial I_{ij}}{\partial t} + \mathbf{v}_i \cdot \nabla I_{ij} = \frac{DI_{ij}}{Dt} = \mathrm{V}_{ij}\beta\left(\frac{G}{4\pi} - I_{ij}\right), \tag{4.12}$$

where $i = 1, ..., N_\delta$ and $j = 1, ..., N_\gamma$. N_δ and N_γ are the total number of discrete subdivisions for the azimuthal and polar angles, respectively. Eq. (4.12) is the RTE rewritten as a BGK equation and DI_{ij}/Dt represents the Lagrangian derivative.

In order to obtain the usual LBM formulation, applying the method of characteristics and forward Euler to Eq. (4.12) yields:

$$\frac{I_{ij}\left(\mathbf{x}_n+\mathbf{v}_i\Delta t,t+\Delta t\right)-I_{ij}\left(\mathbf{x}_n,t\right)}{\Delta t}=\omega_{ij}\left[I_{ij}^{eq}\left(\mathbf{x}_n,t\right)-I_{ij}\left(\mathbf{x}_n,t\right)\right] \\ +O\left(\Delta t\right)+O\left(\mathbf{v}_i\Delta t\right) \tag{4.13}$$

where the relaxation frequency $\omega_{ij}=\mathrm{V}_{ij}\beta$. According to LBM terminology, I_{ij} is the particle distribution function (PDF) and it is the carrier of the radiative energy. I_{ij}^{eq} is the equilibrium distribution function, defined as:

$$I_{ij}^{eq}=\frac{G}{4\pi}=\frac{1}{4\pi}\int_{\Omega=0}^{4\pi}I\left(\mathbf{x}_n,t,\delta,\gamma\right)d\Omega=\frac{1}{4\pi}\int_0^{2\pi}\int_0^{\pi}I\left(\mathbf{x}_n,t,\delta,\gamma\right)\sin\gamma\,d\delta\,d\gamma. \tag{4.14}$$

Integral in Eq. (4.14) is solved by means of quadrature schemes. Let us consider a portion of sphere of the size of $[\delta_i-(\Delta\delta_i)/2,\delta_i+(\Delta\delta_i)/2]$ and $\left[\gamma_j-(\Delta\gamma_j)/2,\gamma_j+(\Delta\gamma_j)/2\right]$ with regard to the azimuthal and polar directions, respectively. Taylor expanding the intensity around the value at the centroid of the infinitesimal region under consideration yields:

$$I\left(\mathbf{x}_n,t,\delta,\gamma\right)=I\left(\mathbf{x}_n,t,\delta_i,\gamma_j\right)+O\left(\max_i\left(\Delta\delta_i\right)\right)+O\left(\Delta\gamma\right), \tag{4.15}$$

and the integral over the same region is:

$$\begin{aligned}&\int_{\delta_i-\frac{\Delta\delta_i}{2}}^{\delta_i+\frac{\Delta\delta_i}{2}}\int_{\gamma_j-\frac{\Delta\gamma_j}{2}}^{\gamma_j+\frac{\Delta\gamma_j}{2}}I\left(\mathbf{x}_n,t,\delta,\gamma\right)\sin\gamma\,d\delta\,d\gamma=\\&\int_{\delta_i-\frac{\Delta\delta_i}{2}}^{\delta_i+\frac{\Delta\delta_i}{2}}\int_{\gamma_j-\frac{\Delta\gamma_j}{2}}^{\gamma_j+\frac{\Delta\gamma_j}{2}}I\left(\mathbf{x}_n,t,\delta_i,\gamma_j\right)\sin\gamma\,d\delta\,d\gamma+O\left(\max_i\left(\Delta\delta_i^2\right)\Delta\gamma\right)O\left(\max_i\left(\Delta\delta\right)\Delta\gamma^2\right)=\\&I_{ij}\int_{\delta_i-\frac{\Delta\delta_i}{2}}^{\delta_i+\frac{\Delta\delta_i}{2}}\int_{\gamma_j-\frac{\Delta\gamma_j}{2}}^{\gamma_j+\frac{\Delta\gamma_j}{2}}\sin\gamma\,d\delta\,d\gamma+O\left(\max_i\left(\Delta\delta_i^2\right)\Delta\gamma\right)O\left(\max_i\left(\Delta\delta\right)\Delta\gamma^2\right).\end{aligned} \tag{4.16}$$

If Eq. (4.16) is extended to the whole solid angle, the equilibrium PDF can

be computed as follows:

$$I_{ij}^{eq} = \frac{1}{4\pi}\int_0^{2\pi}\int_0^{\pi} I\left(\mathbf{x}_n, t, \delta, \gamma\right)\sin\gamma\, d\delta\, d\gamma = \sum_{i=1}^{N_\delta}\sum_{j=1}^{N_\gamma}\left[I_{ij}\int_{\delta_i-\Delta\delta_i/2}^{\delta_i+\Delta\delta_i/2}\int_{\gamma_j-\Delta\gamma_j/2}^{\gamma_j+\Delta\gamma_j/2}\frac{1}{4\pi}\sin\gamma\, d\delta\, d\gamma\right] + O\left(\max_i\left(\Delta\delta_i\right)\right) + O\left(\Delta\gamma\right) = \sum_{i=1}^{N_\delta}\sum_{j=1}^{N_\gamma} W_{ij}I_{ij} + + O\left(\max_i\left(\Delta\delta_i\right)\right) + O\left(\Delta\gamma\right), \tag{4.17}$$

where W_{ij} is the weight corresponding to the discrete directions i and j and is defined as:

$$W_{ij} = \frac{1}{4\pi}\int_{\delta_i-\frac{\Delta\delta_i}{2}}^{\delta_i+\frac{\Delta\delta_i}{2}}\int_{\gamma_j-\frac{\Delta\gamma_j}{2}}^{\gamma_j+\frac{\Delta\gamma_j}{2}}\sin\gamma\, d\delta\, d\gamma. \tag{4.18}$$

We want to stress the point that: a) the number of the weights W_{ij} has to be equal to the number of lattice velocities, b) discrete intensities has to be centered with respect to the portion of the sphere identified by the weight W_{ij} and c) the following condition must be verified:

$$\sum_{i=1}^{N_\delta}\sum_{j=1}^{N_\gamma} W_{ij} = 1. \tag{4.19}$$

Weights W_{ij} describe the region of influence of each of the discrete intensities. The regions of influence of the PDFs in the solution plane for D2Q8 and D2Q16 lattices are shown in Figs. 4.2a and 4.2b, respectively. If the D2Q8 lattice is used, then the sphere in the solution plane is subdivided into eight portions and, moreover, eight weights W_{ij} has to be computed. Discrete intensities are centered and condition given by Eq. (4.19) is satisfied if all directions are equally spaced (Fig. 4.2a) and the azimuthal angle is uniformly discretized ($\Delta\delta_i = \Delta\delta = \pi/4$). In D2Q16, 8 more directions are introduced keeping the D2Q8 lattice directions fixed. Similarly, the D2Q32 lattice is obtained by adding 16 more directions to the ones of the D2Q16 lattice. In the D2Q16 and D2Q32 lattices the regions of influence are evaluated by following the same procedure for the D2Q8 lattice, but in these cases the regions of influence are not equally spaced: $13\pi/90 \lesssim [\Delta\delta_i]_{D2Q16} \lesssim \pi/10$ and $2\pi/45 \lesssim [\Delta\delta_i]_{D2Q32} \lesssim 13\pi/90$. In the polar direction, due to the definition of the z-axis velocity component $v_{z,j}$, regions of influence of the PDFs are all equally spaced, as shown in Figs. 4.3a and 4.3b, in case of 4 and 8 subdivisions, respectively.

As usual in LBM, the algorithm to solve Eq. (4.10) is usually split into the collision and the streaming steps:

$$I_{ij}^{*}\left(\mathbf{x}_n, t\right) = I_{ij}\left(\mathbf{x}_n, t\right) + \frac{\Delta t}{\tau_{ij}}\left[I_{ij}^{eq}\left(\mathbf{x}_n, t\right) - I_{ij}\left(\mathbf{x}_n, t\right)\right], \tag{4.20}$$

$$I_{ij}\left(\mathbf{x}_n + \mathbf{v}_i\Delta t, t + \Delta t\right) = I_{ij}^{*}\left(\mathbf{x}_n, t\right). \tag{4.21}$$

Eqs. (4.20) and (4.21) provides the numerical solution for Eq. (4.12). The global numerical error can be determined by collecting the errors due to forward Euler and to the quadrature schemes given by Eq. (4.13) and Eq. (4.15) respectively:

$$\begin{aligned}\frac{I_{ij}\left(\mathbf{x}_n + \mathbf{v}_i\Delta t, t + \Delta t\right) - I_{ij}\left(\mathbf{x}_n, t\right)}{\Delta t} = \frac{1}{\tau_{ij}}\left[I_{ij}^{eq}\left(\mathbf{x}_n, t\right) - I_{ij}\left(\mathbf{x}_n, t\right)\right] + \\ O\left(\Delta t\right) + O\left(\mathbf{v}_i\Delta t\right) + \\ O\left(\max_i\left(\Delta\delta_i\right)\right) + O\left(\Delta\gamma\right).\end{aligned} \tag{4.22}$$

Recalling that $|\mathrm{v}_i| = \varepsilon_i c$ where ε_i is a constant depending on the energy shell of the considered velocity, and assuming $c = \Delta x/\Delta t$ as a constant (depending on the stability region), the global error becomes:

$$Err = O\Big(\left(1 + \varepsilon_i\right)\Delta x\Big) + O\left(\max_i\left(\Delta\delta_i\right)\right) + O\left(\Delta\gamma\right). \tag{4.23}$$

It is evident from the previous expression that the dependence of the global error on the discretization parameters is not trivial. In fact, improving the discretization of the azimuthal angle, i.e. reducing $\max_i(\Delta\delta_i)$, forces one to consider larger lattices, with larger energy shells, which usually spoil the accuracy of the advection step (because of larger ε_i). On the other hand, accurate advection step requires a compact computational stencil, i.e. few energy shells, but this makes quite rough the discretization of the azimuthal angle and consequently the computation of the collision step (by the definition of local equilibrium). With other words, because of the geometrical construction, the following relation holds $\varepsilon_i \propto 1/\max_i(\Delta\delta_i)$. Hence there is a tradeoff between the accuracy of the advection step and that of the collision step, which both affect the global error.

4.3 Numerical results

The proposed LB scheme has been applied to solve a 2-D square enclosure problem. In this work it has been assumed $X = Y = 1$ and uniform spatial discretization along both x and y directions, with $\Delta x = \Delta y$. In order to validate the LBM formulation, FVM results have been considered benchmark.

Table 4.2: Summary of the parameters adopted in the validation analysis.

$\beta = 2.0$	$\beta = 5.0$
$N_x = N_y = [40, 80, 160]$	$N_x = N_y = [100, 200, 400]$
$N_\delta = [8, 16, 32]$	$N_\delta = [8, 16, 32]$
$N_\gamma = [1, 4, 8, 16]$	$N_\gamma = [1, 4, 8, 16]$

Table 4.3: Summary of the parameters adopted in the convergence analysis.

$\beta = 2.0$	$\beta = 5.0$
$N_x = 40$, $N_\delta = 8$, $N_\gamma = 4$	$N_x = 10$, $N_\delta = 8$, $N_\gamma = 4$
$N_x = 80$, $N_\delta = 16$, $N_\gamma = 8$	$N_x = 200$, $N_\delta = 16$, $N_\gamma = 8$
$N_x = 160$, $N_\delta = 32$, $N_\gamma = 16$	$N_x = 400$, $N_\delta = 32$, $N_\gamma = 16$

Since both FVM and LBM are iterative methods, a convergence criterion is required: FVM and LBM solutions are assumed to converge when the maximum change in the incident radiation at any point is less than 10^{-10} between two successive iterations. Validation of the LBM formulation has been performed for several values of the spatial and angular discretizations and extinction coefficients, as shown in Table 4.2. Spatial discretization has been chosen in such a way that the Knudsen number is smaller than a threshold value that ensures stability of the LBM solution. In this work it has been chosen:

$$\mathrm{Kn} = \beta \Delta x \leq 0.05, \tag{4.24}$$

where $\Delta x = X/(N_x - 1)$ is the spatial grid length and N_x represents the number of nodes along x axis. The temperature of the participating medium is given by the following equation:

$$T = \left(\frac{G}{4\sigma} \right)^{1/4}, \tag{4.25}$$

where the volumetric absorption G is computed from Eq. (4.14). Fig. 4.4 shows the distribution of the temperature in the 2-D domain. Tables 4.4 shows the mean temperature T_m of the participating medium inside the enclosure

$$T_m = \frac{1}{XY} \int_0^X \int_0^Y T\,(x, y)\, dxdy, \tag{4.26}$$

which is related to the internal energy E_i as:

$$\mathrm{E}_i^* = \frac{\mathrm{E}_i}{c_v} = \frac{1}{XY} \int_0^X \int_0^Y T\,(x, y)\, dxdy = T_m, \tag{4.27}$$

if the specific heat at constant volume c_v of the medium assumes a constant value. In Appendix A the mean temperature T_m evaluated by means of a

Table 4.4: Mean temperature of the medium inside the enclosure.

		$\beta = 2.0$			$\beta = 5.0$		
		$N_x = 40$	$N_x = 80$	$N_x = 160$	$N_x = 100$	$N_x = 200$	$N_x = 400$
$N_\delta = 8$	$N_\gamma = 1$	0.63122	0.65742	0.67072	0.64538	0.65593	0.66123
	$N_\gamma = 4$	0.62774	0.62391	0.66718	0.64166	0.65223	0.65754
	$N_\gamma = 8$	0.62824	0.65442	0.66770	0.64204	0.65261	0.65793
	$N_\gamma = 16$	0.62832	0.65451	0.66779	0.64219	0.65276	0.65808
$N_\delta = 16$	$N_\gamma = 1$	0.62911	0.65528	0.66855	0.64364	0.65427	0.65962
	$N_\gamma = 4$	0.62542	0.65157	0.66484	0.63989	0.65054	0.65590
	$N_\gamma = 8$	0.62589	0.65204	0.66531	0.64017	0.65083	0.65619
	$N_\gamma = 16$	0.62595	0.65211	0.66537	0.64025	0.65092	0.65628
$N_\delta = 32$	$N_\gamma = 1$	0.62785	0.65440	0.66787	0.64298	0.65387	0.65935
	$N_\gamma = 4$	0.62404	0.65062	0.66410	0.63911	0.65006	0.65557
	$N_\gamma = 8$	0.62451	0.65107	0.66456	0.63934	0.65030	0.65581
	$N_\gamma = 16$	0.62455	0.62112	0.66461	0.63939	0.65035	0.65586

standard FVM code is reported in Table A.1. Overall radiative heat flux is

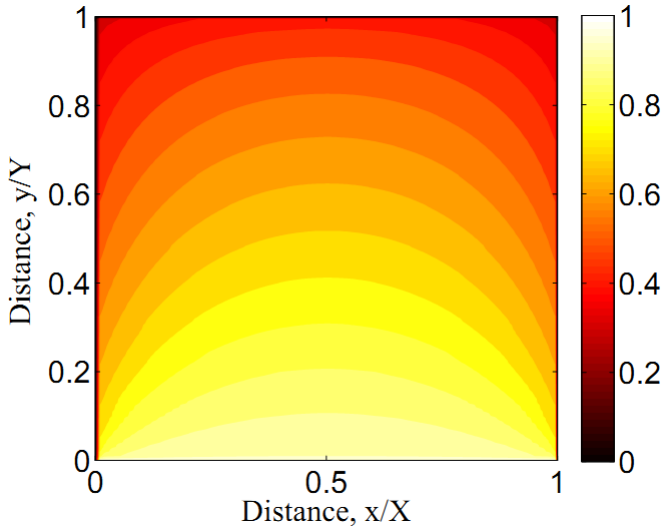

Figure 4.4: Distribution of the temperature in the square enclosure for $\beta = 5.0$.

computed from the following relation:

$$q_R = \int_0^{2\pi} \int_0^{\pi} I\,(\mathbf{n}\cdot\mathbf{s})\sin\gamma\, d\delta\, d\gamma. \tag{4.28}$$

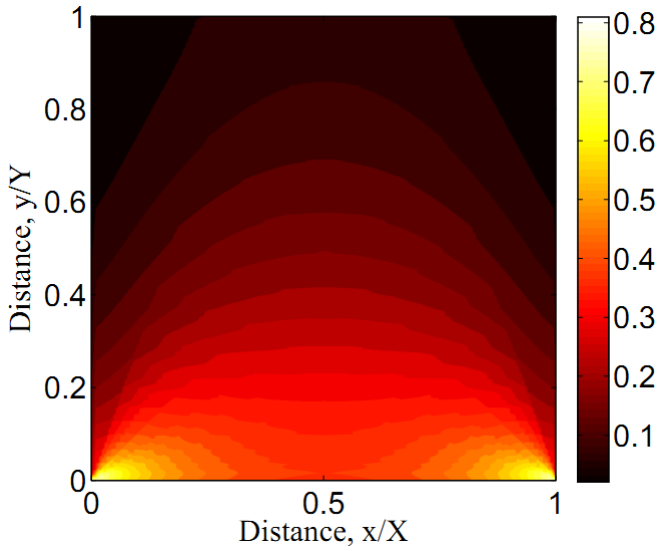

Figure 4.5: Distribution of dimensionless heat flux ψ_y in the square enclosure.

In the present work, we are interested in the heat flux normal to the south (hot) wall and thus, we define:

$$q_{Ry} = \int_0^{2\pi} \int_0^{\pi} I\left(\mathbf{x}_n, t, \delta, \gamma\right) \sin\delta \sin^2\gamma \, d\delta \, d\gamma, \tag{4.29}$$

as the heat flux along y faces of the enclosure. Applying the quadrature scheme already used in Eq. (4.17), Eq. (4.29) becomes:

$$q_{Ry} = \sum_{i=1}^{N_\delta} \sum_{j=1}^{N_\gamma} W_{ij}^{y} I_{ij}, \tag{4.30}$$

where the weights are given by:

$$W_{ij}^{y} = \int_{\gamma_j - \frac{\Delta\gamma_j}{2}}^{\gamma_j + \frac{\Delta\gamma_j}{2}} \sin^2\gamma \, d\gamma \int_{\delta_i - \frac{\Delta\delta_i}{2}}^{\delta_i + \frac{\Delta\delta_i}{2}} \sin\delta \, d\delta. \tag{4.31}$$

Fig. 4.5 shows the distribution of the dimensionless heat flux along the y direction:

$$\psi_y = \frac{q_{Ry}}{\sigma T_S^4}. \tag{4.32}$$

In Table 4.5 dimensionless total heat flux along the south wall is reported as function of the parameters of Table 4.2. Dimensionless total heat flux evaluated by means of FVM code is reported in Table A.2. The dimensionless

Table 4.5: Dimensionless total heat flux along the south wall.

		$\beta = 2.0$			$\beta = 5.0$		
		$N_x = 40$	$N_x = 80$	$N_x = 160$	$N_x = 100$	$N_x = 200$	$N_x = 400$
$N_\delta = 8$	$N_\gamma = 1$	0.67840	0.67316	0.67050	0.49908	0.49733	0.49645
	$N_\gamma = 4$	0.63746	0.63223	0.62961	0.45458	0.45328	0.45626
	$N_\gamma = 8$	0.64305	0.63775	0.63508	0.45930	0.45792	0.45722
	$N_\gamma = 16$	0.64412	0.63879	0.63612	0.46016	0.45876	0.45805
$N_\delta = 16$	$N_\gamma = 1$	0.71062	0.70430	0.70117	0.51616	0.51431	0.51338
	$N_\gamma = 4$	0.66572	0.65955	0.65649	0.46891	0.46763	0.46699
	$N_\gamma = 8$	0.67204	0.66575	0.66265	0.47415	0.47276	0.47208
	$N_\gamma = 16$	0.67333	0.66701	0.66389	0.47517	0.47376	0.47306
$N_\delta = 32$	$N_\gamma = 1$	0.72273	0.71421	0.71020	0.52166	0.51925	0.51808
	$N_\gamma = 4$	0.67688	0.66848	0.66451	0.47363	0.47186	0.47101
	$N_\gamma = 8$	0.68346	0.67492	0.67088	0.47906	0.47717	0.47626
	$N_\gamma = 16$	0.68481	0.67625	0.67220	0.48013	0.47822	0.47730

total heat flux at a given coordinate along the y axis is:

$$\Psi_{|y=y^*} = \int_0^X \psi_y\,(x,y)\,dx. \tag{4.33}$$

For the purpose of validation, since analytical solution is not available for a 2-D problem, LBM results must be compared with a numerical solution that could be considered as the reference one. In this work, LBM has been compared with the results obtained by the standard FVM. Validation analysis has been performed focusing on the dimensionless heat flux ψ_y. The error has been computed as follows:

$$\mathrm{Err} = \frac{\left\| \psi_{y_{FVM,Ref}} - \psi_{y_{LBM}} \right\|_2}{\left\| \psi_{y_{FVM,Ref}} \right\|_2}, \tag{4.34}$$

where $\|...\|_2$ indicates the Euclidean norm. In this work, the reference solution $\psi_{y_{FVM,Ref}}$ has been computed by means of a Richardson extrapolation of FVM results. In order to estimate the reference solution, the FVM dimensionless heat flux has been computed for the parameters shown in Table 4.6 and from which the Richardson extrapolation has been performed. In the application of Eq. (4.34), the reference solution has been interpolated in order to match the grid points of the LBM solution. A cubic interpolation is used for not affecting the measurement of the order of the present numerical method. For evaluating the order of convergence, let us recall Eq. (4.23). Contributions to the global error of the LBM scheme are given by the numerical approximation of the Lagrangian derivative of Eq. (4.12) and by the numerical approximation of the integrals over the solid angle. Eq.(4.23)

Table 4.6: Summary of the parameters adopted in the Richardson extrapolation.

$\beta = 2.0$	$\beta = 5.0$
$N_x = 80$, $N_\delta = 16$, $N_\gamma = 8$	$N_x = 200$, $N_\delta = 16$, $N_\gamma = 8$
$N_x = 160$, $N_\delta = 32$, $N_\gamma = 16$	$N_x = 400$, $N_\delta = 32$, $N_\gamma = 16$

suggests that the model is first order accurate with respect to either the spatial or the azimuthal angle or the polar angle discretizations, for lattices which are small enough to solve accurately the advection step. However in case of large lattices, the streaming step of the lattice velocities belonging to larger energy shells, inevitably leads to an accuracy spoil. This trend can be demonstrated if Δx, $\Delta\delta$ and $\Delta\gamma$ are scaled by the same ratio during the grid refinement. In this paper the order of convergence of the method is evaluated with regard to the values of discretization parameters given in Table 4.3.

Errors of the dimensionless heat flux are shown in Table 4.5, while the order of convergence can be evaluated from Table 4.8. It can be seen that the order of convergence of LBM model decreases moving from case B to case C: this is ascribed to the accuracy spoil in the computation of the advection step for large lattices (case C uses the D2Q32 lattice), as already pointed out in the previous section. Figs. 4.6 show the effects of different lattices on the intensity evaluated by means of the collision step (Eq.(4.20)) in the case of $\beta = 2$. In Figs. 4.6a-4.6c, LBM collision step intensity with $N_x = N_y = 40$, $N_\delta = [8, 16, 32]$ and $N_\gamma = 1$ has been compared with the intensity evaluated by means of standard FVM, with the same discretization parameters adopted for LBM. In Figs. 4.6d-4.6e LBM collision step solutions for three different lattices is compared with the FVM reference solution. The latter has been computed with $N_x = N_y = 160$, $N_\delta = [8, 16, 32]$ and $N_\gamma = 16$ and then interpolated to match the LBM resolution. Collision step solution gets closer to the FVM one as result of a more refined discretization of the azimuthal angle. Comparing results given in Table 4.8 and Figs. 4.6, the tradeoff between the collision and advection steps can be found for $N_\delta = 16$.

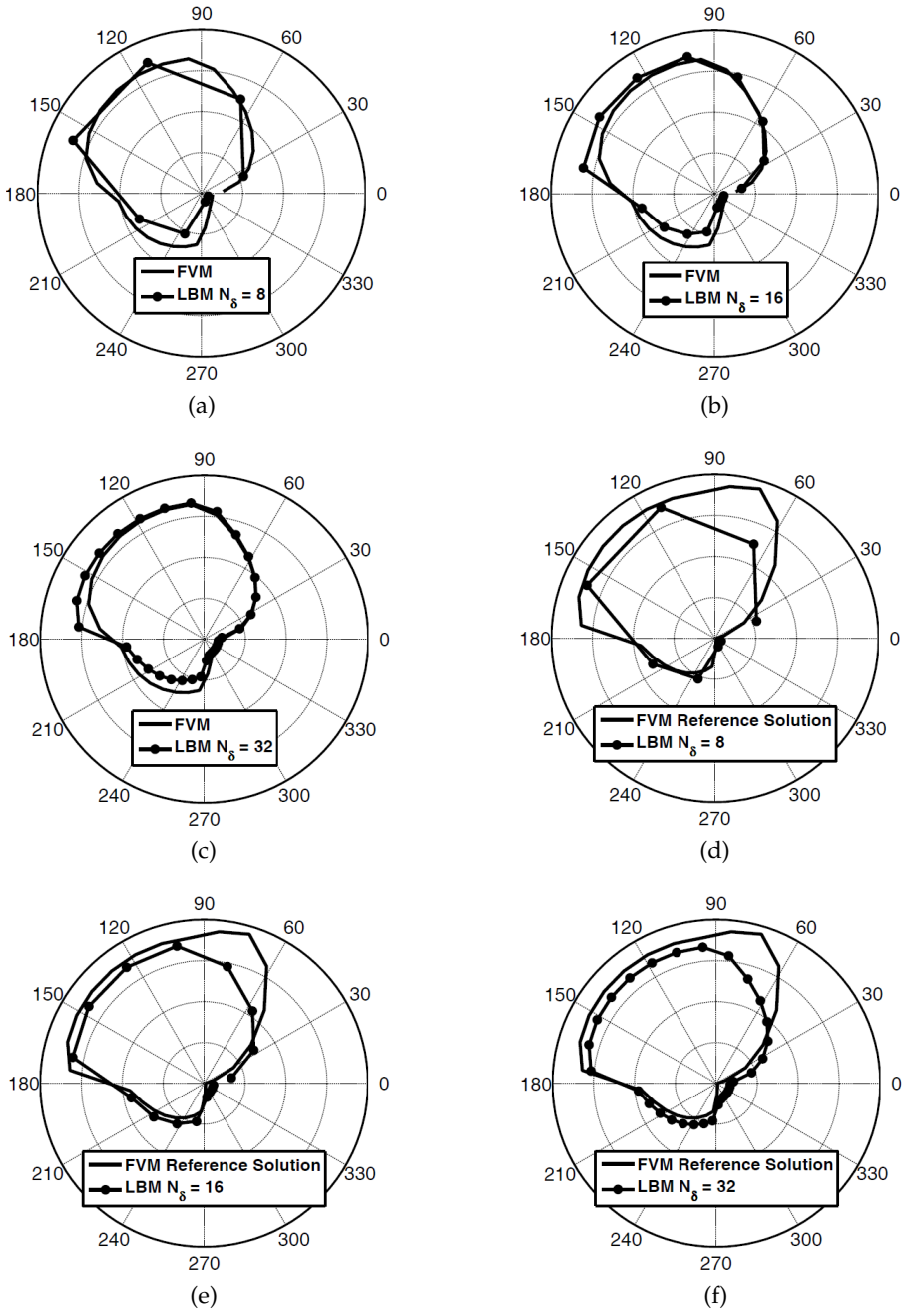

Figure 4.6: Effects of different lattices on the solution of the collision step: collision step intensity as function of the azimuthal angle. In Figs. 4.6a-4.6c LBM collision step is compared with the FVM solution obtained with the same discretization adopted for LBM; in Figs. 4.6d-4.6e LBM collision step is compared against the FVM reference solution.

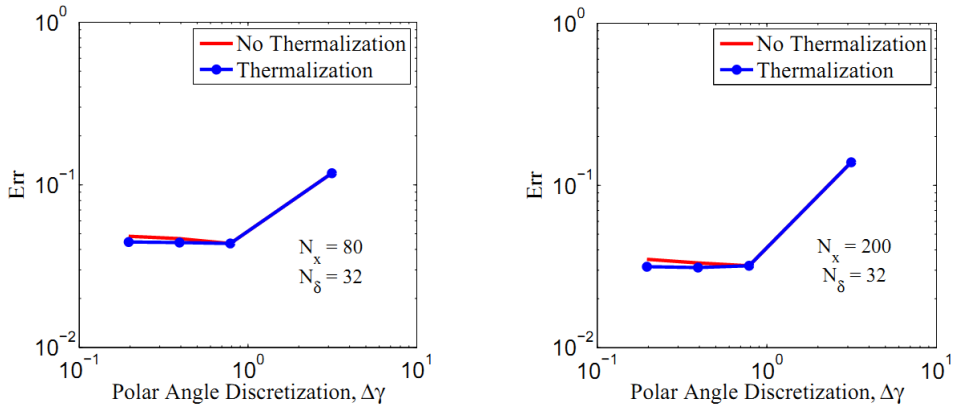

Figure 4.7: Error as function of the polar angle discretization for $\beta = 2.0$ (a) and $\beta = 5.0$ (b).

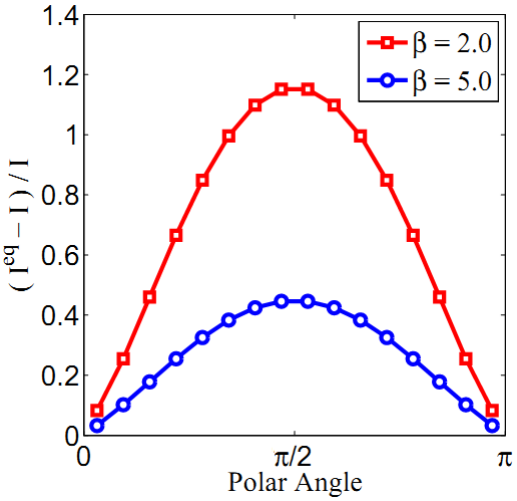

Figure 4.8: Comparison between PDF and the equilibrium PDF as function of the polar angle for $\beta = 2.0$ and $\beta = 5.0$.

Table 4.7: Errors of the dimensionless heat flux as function of the discretization and the extinction coefficients.

		$\beta = 2.0$			$\beta = 5.0$		
		$N_x = 40$	$N_x = 80$	$N_x = 160$	$N_x = 100$	$N_x = 200$	$N_x = 400$
$N_\delta = 8$	$N_\gamma = 1$	0.11378	0.10401	0.10199	0.11540	0.10530	0.10128
	$N_\gamma = 4$	0.07309	0.06552	0.06543	0.05540	0.05683	0.05958
	$N_\gamma = 8$	0.07178	0.06165	0.06050	0.04858	0.04564	0.04709
	$N_\gamma = 16$	0.07192	0.06137	0.06010	0.043375	0.04375	0.04480
$N_\delta = 16$	$N_\gamma = 1$	0.12217	0.10263	0.09490	0.12448	0.12448	0.11808
	$N_\gamma = 4$	0.04815	0.03249	0.03318	0.02720	0.02720	0.03086
	$N_\gamma = 8$	0.05394	0.03160	0.02844	0.02005	0.02005	0.01934
	$N_\gamma = 16$	0.05578	0.03253	0.02840	0.02064	0.02064	0.01844
$N_\delta = 32$	$N_\gamma = 1$	0.13391	0.10925	0.09863	0.13280	0.13280	0.12448
	$N_\gamma = 4$	0.05127	0.02314	0.02330	0.01898	0.01898	0.02250
	$N_\gamma = 8$	0.06009	0.02947	0.01930	0.01940	0.01940	0.01240
	$N_\gamma = 16$	0.06255	0.03165	0.01999	0.02145	0.02145	0.01295

The situation is even more critical for the polar discretization. In fact, from Table 4.7 one can notice that the error decreases as the spatial and azimuthal discretizations get more refined. The same trend does not show up for the polar discretization. Let us consider Figs 4.7a and 4.7b, where the error is plotted as function of the infinitesimal polar angle π/N_γ for $\beta = 2.0$ and $\beta = 5.0$. Subdivisions greater than $N_\gamma = 1$ produce more accurate solutions, even though the minimum error occurs for $N_\gamma = 4$. The larger the subdivisions in the polar direction, the closer the discrete polar angle γ_j gets to the upper and lower bounds of the polar angle γ: this makes intensity to move far outside from the 2-D lattice and it is like a fictitious increase in the free mean path of the radiation intensity. With other words, when the number of subdivisions of the polar angle increases, the magnitude V_{ij} of the lattice velocities for γ_j closest to 0 and π become very large and this produces accuracy spoil. For these directions, the relaxation time (fictitiously) increases and then the distribution function gets closer to the equilibrium distribution function, as shown in Fig. 4.8. This suggests another possible improvement. We enforce the intensities along j directions closer to the z-axis to be equal to the equilibrium values and we call this technique thermalization. In Figs.4.7a and 4.7b the effects of this thermalization process are shown for $N_\gamma = 8$ and $N_\gamma = 16$. Thermalization produces an improvement in the accuracy of the solution with respect to the case where thermalization is not applied (Table 4.9), even if the best accuracy still occurs for $N_\gamma = 4$. Results of Figs. 4.7 and 4.7b have been obtained by thermalizing intensities at $\gamma_j = [\pi/16, 15\pi/16]$ in case of 8 subdivisions and $\gamma_j = [\pi/32, 3\pi/32, 5\pi/32, 27\pi/32, 29\pi/32, 31\pi/32]$ in case of 16 subdivisions.

Table 4.8: Error and order of convergence of the LB scheme as function of the spatial discretization.

	Spatial Discretization	Error	Order
$\beta = 2.0$	**A.** $N_x = 40$, $N_\delta = 8$, $N_\gamma = 4$	0.07309	-
	B. $N_x = 80$, $N_\delta = 16$, $N_\gamma = 8$	0.03160	1.210
	C. $N_x = 160$, $N_\delta = 32$, $N_\gamma = 16$	0.01999	0.661
$\beta = 5.0$	**A.** $N_x = 100$, $N_\delta = 8$, $N_\gamma = 4$	0.05540	-
	B. $N_x = 200$, $N_\delta = 16$, $N_\gamma = 8$	0.02005	1.466
	C. $N_x = 400$, $N_\delta = 32$, $N_\gamma = 16$	0.01265	0.631

Table 4.9: Effects of thermalization on the accuracy for $\beta = 2.0$ and $\beta = 5.0$.

	$\beta = 2.0$, $N_x = 80$, $N_\delta = 32$		$\beta = 5.0$, $N_x = 200$, $N_\delta = 32$	
	$N_\gamma = 8$	$N_\gamma = 16$	$N_\gamma = 8$	$N_\gamma = 16$
No Thermalization	0.02947	0.03165	0.01940	0.02145
Thermalization	0.02807	0.02958	0.01837	0.01950

4.4 Conclusion

In this chapter, some improvements to the lattice Boltzmann method for solving radiative heat transfer in a participating medium, recently proposed by Asinari et al. [9], are presented and validated. In particular, the effects on the numerical solution produced by the discretization of the polar angle are systematically investigated. Essentially, uniform discretization of the polar angle is possible by defining an enlarged set of lattice velocities, with an additional component along the axis normal to the main simulation plane. In this way, the projection of the total velocity still belongs to the original computational lattice.

A preliminary validation of the model has been considered by solving a benchmark radiative transfer problem in a 2-D rectangular enclosure. The results of the dimensionless heat flux obtained by the proposed LB scheme have been compared with a reference solution by standard FVM. Simulations have been performed for several values of the spatial and angular discretizations and extinction coefficients, in order to find out the order of convergence of the scheme. The numerical results demonstrate that the proposed radiative LB scheme is (at most) first order accurate, in case of compact lattices, which still ensure enough accuracy in the advection of the radiation information.

With regard to the effects of the discretization of the polar angle, we showed that minimum error occurs for a given subdivision, which does not necessarily correspond to the most refined discretization. This means that greater subdivisions produce a spoil in the numerical accuracy, due to larger (ficti-

tious) mean free path of radiation. By means of a thermalization procedure, i.e. forcing the equilibrium values of some radiation intensities, a better accuracy can be achieved in case of large subdivisions of the polar angle.

Chapter 5

Link-wise Artificial Compressibility Method

5.1 Introduction

Chapters 3 and 4 provide a viable solution for the simulation of reactive flows within the framework of lattice Boltzmann methods. However, some difficulties emerge. Due to its pseudo-kinetic origin, LBM works with a larger set of unknowns, including the so-called *ghost* variables, beyond the hydrodynamics. This is different from traditional approaches in computational combustion, where the only unknowns are the macroscopic quantities. The ghost variables are not of relevant importance if the continuum limit is the main concern. Moreover, they can also lead to numerical instabilities, as pointed out in [30]. Other difficulties emerge when one deals with simple boundaries, such as in case of inlet and outlet: not only the known boundary conditions for the hydrodynamic variables need to be imposed, but also the boundary conditions for the ghost moments must be provided. Thus, a possible improvement of LBM would be to make the updating rule of the distribution function depend only on the local equilibrium, but retain its link-wise formulation. In this way, the limitation of LBM will be removed and the ability to easily deal with complex boundaries is preserved. While removing the ghost variables makes LBM closer to classical CFD approaches, the link-wise formulation allows to overcome the traditional limitations of Finite Volumes or Finite Elements with regard to complex geometries. In fact, despite a large variety of mesh generation techniques for numerical solvers of the fluid dynamics governing equations [64], addressing complex geometries remains a difficult duty. To this aim, several approaches were proposed for adapting computational grids to complex geometries by unstructured meshes. Generating unstructured meshes of high quality though, is a challenging computational task *per se*, which involves quite advanced algorithms (Rupperts algorithm, Chews second algorithm, Delaunay trian-

gulation, etc.) [64]. While those approaches simplify the treatment of boundaries, in turn, each of them introduces new difficulties such as extra terms in the equations, extra interpolations, larger computational molecules, and problems associated with the transfer of information across grid interfaces. The added complexity makes code development even more difficult and increases computation time [58], with an additional risk that those algorithms may not lead to an acceptable solution.

An alternative approach which has attracted an increasing interest in recent years makes use of Cartesian grids for all cells with the exception of those that present intersections with boundaries, which are thus truncated according to the shape of the boundary surface. The advantages of Cartesian grids can be retained for all cells in the bulk fluid, and a special treatment is only reserved to boundary cells. On the contrary, cells fully outside the flow can be simply ignored during computations [58]. In the literature, this approach is typically referred to as the "embedded boundary method", the "Cartesian grid method" or the "cut-cell method" [50, 68, 112, 113, 114]. Clearly, the challenging point is to make the method accurate in dealing with curved and planar boundaries transversal to the grid, even though such boundaries are conveniently approximated in a staircase fashion. More specifically, after determining the intersection between the Cartesian grid and a boundary, cells whose center lies in the fluid are reshaped by discarding their part belonging to the solid wall, while pieces of cut cells with the center in the solid are absorbed by neighboring cells [112]. This results in the formation of control-volumes which are trapezoidal in shape.

Classical approaches to the incompressible limit of Navier-Stokes equations require (a) dedicated techniques for solving a pressure Poisson equation in order to take advantage of the underlying structured nature of the mesh and thus speed-up convergence [112]. Moreover, (b) compact multi-dimensional polynomial interpolating functions are used for obtaining a second-order accurate approximation of the fluxes and gradients on the faces of the trapezoidal boundary cells from available neighboring cell-center values [112]. Recent developments to this also follows a similar approach [50, 68].

Both (a) the need of a dedicated solver for the pressure Poisson equation and (b) the use of compact multi-dimensional interpolations, can be overcome by the lattice Boltzmann method (LBM) [102], while preserving the main features of the Cartesian cut-cell method for mesh generation and boundary treatment. However, this comes at a price of dealing with specific features inherited from the kinetic theory of gases, which are unessential as far as the continuum description of incompressible Navier-Stokes equations is the only concern.

For this reason, we propose a novel formulation of the artificial compressibility method (ACM), which retains the convenient features of LBM, namely (a)

the artificial compressibility and (b) the link-wise formulation based on the theory of characteristics, but concurrently gets rid of unessential heritages of the kinetic theory of gases.

Similarities between LBM and ACM [26] are sometimes reminded in the literature. It is well known indeed that the Chapman-Enskog expansion of the LBM updating rule delivers the governing equation of ACM: the artificial compressibility equations (ACE). The latter consist of the same momentum equations as the incompressible Navier-Stokes equations (INSE), in addition to an artificial continuity equation including pressure time derivative. ACE can be also recovered by the more systematic expansion such as the Hilbert method under diffusive scaling [52].

The lattice kinetic scheme (LKS) [49] (a variant of LBM) also shows similarities with ACM at the level of computer programming, despite the fact that the former deals with distribution functions of gas molecules, while the latter only with hydrodynamic (macroscopic) variables.

For a special value of the relaxation parameter in the LBM updating rule, an updated value of the distribution function depends only on the previous equilibrium function at an arbitrary mesh point in the stencil. Since equilibria are in turn function of macroscopic variables only, the LKS updating rule can be immediately recognized as a kind of finite difference scheme, acting on hydrodynamic variables. As a result, the moment system of LKS delivers a variant of ACM. Recently, taking advantage of the similarities between LBM and ACM, the latter was reformulated as a high order accurate numerical method (fourth order in space and second order in time) [81].

Motivated by the common belief that an important reason of success of the LBM (in particular MRT-LBM [31]) is its remarkable robustness for simulating the various complex flows, the stability of the revived ACM has been further enhanced [82].

In this chapter, in an attempt of making ACM even more similar to LBM, we propose yet a new formulation of ACM referred to as link-wise ACM (LW-ACM) in the following text. For the sake of completeness, we summarize both the main features of the revived ACM [81, 82], still valid for the present LW-ACM, and the additional advantages due to a link-wise formulation.

1. ACM deals with macroscopic variables only, thus offering the opportunity of exploiting all the pre-existing finite-difference (FD) technologies: This is, for instance, a clear advantage when imposing inlet and outlet boundary conditions. On the contrary, LBM needs to account for ghost quantities which, though may not have direct impact on the hydrodynamic behavior, they can still be responsible of numerical instabilities [30]. Unfortunately, owing to nonlinearities, there are no clear and general recipes yet, on how to optimally design ghost quan-

tities with desired stability properties. As far as the popular compact stencils are concerned, such as D2Q9, D3Q15 and D3Q19 [90] with no special corrections, LBM ghost quantities remain numerical artifacts: Positive effects of such quantities for enhancing stability of usual FD schemes are still far from being clearly demonstrated. ACM fully overcomes this issue, focusing instead on the minimum set of information for incompressible fluid dynamics.

2. Similarly to LBM, ACM posses the ability of computing transient solutions of incompressible Navier-Stokes equations (INSE), without resorting to a Poisson equation for pressure. The underlying idea, directly inspired by the asymptotic analysis of LBM schemes, is to multiply the pressure time derivative of artificial continuity equation by a mesh-dependent parameter. In this way, the numerical Mach number, which is a mere numerical artifact for INSE (rigorously valid in the limit of vanishing Mach number) is linked to the mesh spacing. Higher accuracy than LBM schemes can be also achieved by exploiting the asymptotic behavior of the solution of the artificial compressibility equations for small Mach numbers [81].

3. ACM can use different meshing techniques. For example, it is possible to use simple lattice structures, namely Cartesian structured meshes, eventually recursively refined like those also used by LBM, or it can be even formulated in a finite-volume fashion including unstructured body-fitted meshes. In the latter case, the same comments discussed at the beginning of this section about the computational overhead for generating unstructured meshes hold as well. On the other hand, adopting simple lattice structures may be in some cases not so straightforward as in LBM: the wall treatment depends on the dimensionality of the problem (namely discriminating wall boundary conditions in 2D is different than in 3D). Previous problem can be overcome by LBM thanks to the link-wise formulation. A "link" is a generic direction identified by a discrete velocity of the lattice and coincides with one of the characteristics along which advection is performed (consistently with the method of characteristics - MOC). Such a numerical scheme based on a finite set of links can cope with a complex boundaries by (a) identifying the intersections of each link with the wall and (b) updating the variable corresponding to such a link by a local rule. The local rule is always the same and the intersections can be computed once for all during pre-processing. The previous procedure easily applies to any orientations of the wall with respect to the lattice, as well as to any dimensions. In this paper, the above advantages of LBM are made available to ACM.

4. ACM deals with the minimum number of fields describing incompress-

ible fluid dynamics: D+1, where D is the physical dimension of the problem. On the other hand, LBM deals with discrete distribution functions f_i, which are as many as the lattice velocities Q. LBM has thus a memory overhead due to: D+1<Q. Between these two sets of variables, there is a simple connection: Local equilibria $f_i^{(e)}$ (Q variables) can be computed by means of macroscopic quantities only (D+1 variables). Introducing a larger set of variables $f_i^{(e)}$ may seem a redundant and useless artifact. However, this work aims at demonstrating that formulating ACM in terms of $f_i^{(e)}$ offers advantages as well. In particular, as far as the updating rule of the algorithm is similar to LBM, it is possible (eventually with minor changes) to take advantage of most of LBM technology. For example, link-wise ACM can also be formulated in terms of local equilibrium $f_i^{(e)}$ and this enables a convenient treatment of complex moving boundaries typical of the LBM (see next). In conclusion, link-wise ACM has two possible (and fully equivalent) formulations: (a) in terms of macroscopic variables like standard ACM (capable of exploiting pre-existing FD technology) and (b) in terms of local equilibrium (capable of exploiting pre-existing LBM technology).

Before proceeding further with the discussion, it is worth to stress out that the formulation of the LW-ACM provided in this chapter is valid only in the incompressible limit. As remarked in Chapter 3, the numerical model must accomodate large density variations. Thus, the present formulation of LW-ACM is not suitable for combustion applications and suffers from the same limitations of [110], where significant deviations are found when compressiblity is taken into account. However, this was also the same starting point of LBM too.

The chapter is organized in sections as follow. The link-wise artificial compressibility algorithm for incompressible isothermal fluid dynamics is introduced. In Section 5.2.1, where some classical benchmarks are presented (isothermal Couette flow, generalized Green-Taylor vortex flow and Minion & Brown flow) as well. In Section 5.2.4 the link-wise wall boundary conditions are discussed, including moving and complex walls, and some numerical tests are presented (2D lid driven cavity flow, 3D diagonally driven cavity flow and Circular Couette flow). Finally, Section 6 reports some concluding remarks.

5.2 Link-wise Artificial Compressibility Method

5.2.1 The main algorithm: Link-wise and finite difference formulations

Link-wise formulation

The Boltzmann equation is the fundamental equation in kinetic theory of gases, describing time evolution of the distribution function of gas molecules as a function of time, space coordinates, and molecular velocity. The Bhatnagar-Gross-Krook (BGK) model equation inherits the main features of the original Boltzmann equation, with the fluid-dynamic description of the BGK solution for small Knudsen numbers being much simpler to obtain. Hence, owing to a remarkably less demanding effort, it come advantageous the employment of the BGK equation at the heart of kinetic methods for solving INSE. A well known drawback of the BGK equation is that the recovered Prandtl number is unity, while the original Boltzmann equation yields a value near to $2/3$. However, since most of the LBM schemes do not consider the energy equation, the issue of inaccurate thermal diffusivity can be often neglected. At the same time, it is allowed to employ the isothermal BGK with a constant collision frequency for this purpose [10]. Hence isothermal BGK will be our starting point in the following derivation. A crucial *ingredient* of any lattice Boltzmann scheme is a finite set of microscopic velocities, called lattice. The generic lattice velocity is identified by the subscript i, where $0 \leq i \leq Q-1$. The LBM simulates the time evolution of a weakly compressible gas flow in nearly continuum regime by solving a kinetic equation on the lattice and yields the solution of the incompressible Navier-Stokes equation as its leading order. Hence, the relaxation frequency in the BGK equation can be expressed as a function of the kinematic viscosity ν: In particular, the relaxation frequency is set equal to c^2/ν, where c is the lattice sound speed. The dimensionless form of the simplified BGK equation on a lattice takes the form

$$\frac{\partial f_i^{**}}{\partial \hat{t}} + \hat{\mathbf{v}}_i \cdot \hat{\nabla} f_i^{**} = \frac{c^2}{\nu}\left(f_i^{(e)} - f_i^{**}\right), \tag{5.1}$$

where $\hat{\mathbf{x}}$, $\hat{t}$, and $\hat{\mathbf{v}}_i$ are the (dimensionless) space coordinates, time, and molecular velocity components, respectively; f_i^{**} is the distribution function of gas molecules for the i-th velocity on the lattice; $f_i^{(e)}$ is the equilibrium distribution function. The distribution function f_i^{**} is defined at a discrete set[1] of spatial points $\hat{\mathbf{x}} = \mathbf{x}/\Delta x$, where Δx is the dimensionless mesh spacing, $\Delta x = \Delta x'/L$, with $\Delta x'$ the mesh spacing in physical units and L the characteristic length scale of the flow field. Similarly, time levels are defined as $\hat{t} = t/\Delta t$, where Δt is the dimensionless time step, $\Delta t = \Delta t'/(L/U)$,

[1] If not evident otherwise, we use "hat" notation for lattice quantities expressed by means of integer values and "prime" notation for quantities expressed in physical units.

with $\Delta t'$ the time step in physical units and U a characteristic flow speed. The Q lattice velocities $\hat{\mathbf{v}}_i$ are defined according to the considered scheme [90]. All points $\hat{\mathbf{x}}$ form a regular lattice such that $\hat{\mathbf{x}} - \hat{\mathbf{v}}_i$ belongs to the lattice, regardless of $\hat{\mathbf{x}}$ and $\hat{\mathbf{v}}_i$. The quantities $f_i^{(e)}$ are local functions of density $\rho = \sum_i f_i$ and momentum $\rho\mathbf{u} = \sum_i \hat{\mathbf{v}}_i f_i$ computed at $\hat{\mathbf{x}}$ and $\hat{t}$, namely $f_i^{(e)} = f_i^{(e)}(\rho, \mathbf{u})$. The quantities $f_i^{(e)}$ are designed in order to recover the incompressible isothermal fluid dynamics [90]. For sake of completeness, we report here the explicit expressions of the equilibrium functions for some popular lattices.

The D2Q9 lattice [90], suitable for two dimensional problems ($D = 2$), consists of the following discrete velocities ($Q = 9$): $\hat{\mathbf{v}}_0 = (0, 0)$, $\hat{\mathbf{v}}_i = (\pm 1, 0)$ and $(0, \pm 1)$, for $i = 1$–4, and $\hat{\mathbf{v}}_i = (\pm 1, \pm 1)$, for $i = 5$–8, where the i-th equilibrium distribution function $f_i^{(e)}$ reads

$$f_i^{(e)} = w_i \rho \left[1 + 3\hat{\mathbf{v}}_i \cdot \mathbf{u} + \frac{9}{2} (\hat{\mathbf{v}}_i \cdot \mathbf{u})^2 - \frac{3}{2}\mathbf{u}^2 \right], \tag{5.2}$$

with ρ the fluid density, and w_i the weights

$$w_i = \begin{cases} 4/9 & i = 0, \\ 1/9 & i = 1\text{–}4, \\ 1/36 & i = 5\text{–}8. \end{cases} \tag{5.3}$$

More explicitly, the complete set of equilibria takes the form:

$$f^{(e)} = \begin{bmatrix} 4/9\,\rho - 2/3\,\rho u^2 - 2/3\,\rho v^2, \\ 1/9\,\rho + 1/3\,\rho u + 1/3\,\rho u^2 - 1/6\,\rho v^2, \\ 1/9\,\rho + 1/3\,\rho v + 1/3\,\rho v^2 - 1/6\,\rho u^2, \\ 1/9\,\rho - 1/3\,\rho u + 1/3\,\rho u^2 - 1/6\,\rho v^2, \\ 1/9\,\rho - 1/3\,\rho v + 1/3\,\rho v^2 - 1/6\,\rho u^2, \\ 1/36\,\rho + 1/12\,\rho(u+v) + 1/8\,\rho(u+v)^2 - 1/24\,\rho(u^2+v^2), \\ 1/36\,\rho - 1/12\,\rho(u-v) + 1/8\,\rho(-u+v)^2 - 1/24\,\rho(u^2+v^2), \\ 1/36\,\rho - 1/12\,\rho(u+v) + 1/8\,\rho(-u-v)^2 - 1/24\,\rho(u^2+v^2), \\ 1/36\,\rho + 1/12\,\rho(u-v) + 1/8\,\rho(u-v)^2 - 1/24\,\rho(u^2+v^2) \end{bmatrix},$$

where u and v are the velocity components, i.e. $(u, v)^T = \mathbf{u}$, with pressure being $p = \rho/3$. The above equations (5.2) and (5.4) can be generalized as

follows [2]

$$f^{(g)}\left(\Pi_{xx},\Pi_{yy}\right)=\left[\begin{array}{c}\rho\left(1-\Pi_{xx}\right)\left(1-\Pi_{yy}\right),\\ \rho\left(\Pi_{xx}+u\right)\left(1-\Pi_{yy}\right)/2,\\ \rho\left(\Pi_{xx}-u\right)\left(1-\Pi_{yy}\right)/2,\\ \rho\left(1-\Pi_{xx}\right)\left(\Pi_{yy}+v\right)/2,\\ \rho\left(1-\Pi_{xx}\right)\left(\Pi_{yy}-v\right)/2,\\ \rho\left(\Pi_{xx}+u\right)\left(\Pi_{yy}+v\right)/4,\\ \rho\left(\Pi_{xx}-u\right)\left(\Pi_{yy}+v\right)/4,\\ \rho\left(\Pi_{xx}-u\right)\left(\Pi_{yy}-v\right)/4,\\ \rho\left(\Pi_{xx}+u\right)\left(\Pi_{yy}-v\right)/4,\end{array}\right] \tag{5.4}$$

with the equation (5.2) being a special case of (5.4): If one assumes $\Pi_{xx}=1/3+u^2$ and $\Pi_{yy}=1/3+v^2$, then $f^{(g)}\left(1/3+u^2,1/3+v^2\right)=f^{(e)}$ (if third order terms with respect to velocity components are neglected). However, it is possible to introduce more involved functions depending on additional parameters. For instance, a quasi-equilibrium function which is useful for tuning bulk viscosity of both lattice Boltzmann and link-wise ACM schemes can be expressed as

$$f^{(qe)}\left(\rho,\mathbf{u},\mathrm{Tr}\right)=f^{(g)}\left(\frac{\mathrm{Tr}+u^2-v^2}{2},\frac{\mathrm{Tr}-u^2+v^2}{2}\right), \tag{5.5}$$

where Tr is an additional tunable parameter (usually corresponding to the trace of the second order tensor $\mathbf{\Pi}=\sum_i \hat{\mathbf{v}}_i\hat{\mathbf{v}}_i f_i$ normalized by density (see also the Appendix D).

The D3Q19 lattice, which is suitable for three dimensional problems ($D=3$), consists of the following discrete velocities ($Q=19$): $\hat{\mathbf{v}}_0=(0,\,0,\,0)$; $\hat{\mathbf{v}}_i=(\pm1,\,0,\,0)$ and $(0,\,\pm1,\,0)$ and $(0,\,0,\,\pm1)$, for $i=1$–6; $\hat{\mathbf{v}}_i=(\pm1,\,\pm1,\,0)$ and $(\pm1,\,0,\,\pm1)$ and $(0,\,\pm1,\,\pm1)$, for $i=7$–18. Here, the the i-th function $f_i^{(e)}$ is formally identical to (5.2), with the following weights

$$w_i=\left\{\begin{array}{ll}1/3 & i=0,\\ 1/18 & i=1\text{–}6,\\ 1/36 & i=7\text{–}18.\end{array}\right. \tag{5.6}$$

Recovering incompressible Euler equations also requires that $\sum_i f_i^{(e)}=\rho$ and $\sum_i \hat{\mathbf{v}}_i f_i^{(e)}=\rho\mathbf{u}$, i.e. conservation of hydrodynamic moments, and $\sum_i \hat{\mathbf{v}}_i\hat{\mathbf{v}}_i f_i^{(e)}=\mathbf{\Pi}^{(e)}=\rho\mathbf{u}\mathbf{u}+p\,\mathbf{I}$, with p function of density only (isothermal case): $p=c^2\rho$. Further constraints can be found by asymptotic analysis (see Appendix C for details). However consistency leaves some degrees of freedom in designing these functions, which can be used for improving stability (one possible strategy is discussed in Appendix D). In the following, it will be convenient

to consider separately the odd parts of equilibria, namely the quantities $f_i^{(e,o)}$, defined as

$$f_i^{(e,o)}(\rho, \mathbf{u}) = \frac{1}{2}\left(f_i^{(e)}(\rho, \mathbf{u}) - f_i^{(e)}(\rho, -\mathbf{u})\right). \tag{5.7}$$

Let us suppose that $\nu \ll 1$: then it is possible to find an approximated solution of (5.1) by singular regular expansion, where:

$$f_i^{**} = f_i^{(e)} - \frac{\nu}{c^2}\,\hat{\mathbf{v}}_i \cdot \hat{\nabla} f_i^{(e)} + O(\nu^2). \tag{5.8}$$

Introducing the above approximation in the advection term of Eq. (5.1), it yields

$$\frac{\partial f_i^{**}}{\partial \hat{t}} = -\hat{\mathbf{v}}_i \cdot \hat{\nabla} f_i^{(e)} + \frac{\nu}{c^2}\,(\hat{\mathbf{v}}_i \cdot \hat{\nabla})^2 f_i^{(e)} + \frac{c^2}{\nu}\left(f_i^{(e)} - f_i^{**}\right) + O(\nu^2). \tag{5.9}$$

Here, the goal is to derive an algorithm formulated in terms of only hydrodynamic quantities, i.e. the statistical macroscopic moments of f_i^{**} corresponding to microscopic quantities conserved by the collisional operator (right hand side of Eq. (5.1)). In particular, the local equilibrium $f_i^{(e)}$ is defined such that it has the same hydrodynamic quantities of f_i^{**}. Hence, as far as the computation of the hydrodynamic quantities is concerned, the collisional operator in (5.9) is unessential. Removing the latter term determines a modification in the model equation, though there is no effect on the hydrodynamic quantities. Let us define a new model equation by removing the collisional term and neglecting terms $O(\nu^2)$ in (5.9), which can be re-formulated with respect to the new distribution function f_i^* as follows:

$$\frac{\partial f_i^*}{\partial \hat{t}} = -\hat{\mathbf{v}}_i \cdot \hat{\nabla} f_i^{(e)} + \frac{\nu}{c^2}\,(\hat{\mathbf{v}}_i \cdot \hat{\nabla})^2 f_i^{(e)}. \tag{5.10}$$

Clearly the previous one is the Fokker-Planck equation, with drift coefficient equal to 1 and diffusion coefficient equal to ν/c^2. The above model equation (5.10) can be recast in the equivalent form

$$\begin{aligned}\frac{\partial f_i^*}{\partial \hat{t}} = &-\eta_2\left(\hat{\mathbf{v}}_i \cdot \hat{\nabla} f_i^{(e,e)} - \eta_4/\eta_2\,(\hat{\mathbf{v}}_i \cdot \hat{\nabla})^2 f_i^{(e,e)}\right)\\ &-\eta_1\left(\hat{\mathbf{v}}_i \cdot \hat{\nabla} f_i^{(e,o)} - \eta_3/\eta_1\,(\hat{\mathbf{v}}_i \cdot \hat{\nabla})^2 f_i^{(e,o)}\right),\end{aligned} \tag{5.11}$$

where the odd part of the equilibrium distribution function is defined by (5.7), while the even part is $f_i^{(e,e)} = f_i^e - f_i^{(e,o)}$, $\eta_1 = \eta_2 = 1$ and $\eta_3 = \eta_4 = \nu/c^2$. Recalling that

$$\hat{\mathbf{v}}_i \cdot \hat{\nabla} f_i^{(e,o/e)} - \frac{1}{2}\,(\hat{\mathbf{v}}_i \cdot \hat{\nabla})^2 f_i^{(e,o/e)} \approx f_i^{(e,o/e)}(\hat{\mathbf{x}} - \hat{\mathbf{v}}_i, \hat{t}) - f_i^{(e,o/e)}(\hat{\mathbf{x}}, \hat{t}), \tag{5.12}$$

we modify once more the model equation by setting $\eta_1 = 2\nu/c^2$ and $\eta_4 = 1/2$ (while other parameters remain unchanged, namely $\eta_2 = 1$ and $\eta_3 = \nu/c^2$). By doing so, $\eta_4/\eta_2 = \eta_3/\eta_1 = 1/2$ which enables to use the approximation (5.12). By means of the above set of parameters, Eq. (5.11) becomes

$$\frac{\partial f_i^*}{\partial \hat{t}} = -\left(f_i^{(e,e)}(\hat{\mathbf{x}},\hat{t}) - f_i^{(e,e)}(\hat{\mathbf{x}}-\hat{\mathbf{v}}_i,\hat{t})\right) - 2\,\frac{\nu}{c^2}\left(f_i^{(e,o)}(\hat{\mathbf{x}},\hat{t}) - f_i^{(e,o)}(\hat{\mathbf{x}}-\hat{\mathbf{v}}_i,\hat{t})\right). \tag{5.13}$$

As common in LBM, we apply the forward Euler rule for approximating first order time derivatives:

$$\begin{aligned} f_i^*(\hat{\mathbf{x}},\hat{t}+1) = f_i^*(\hat{\mathbf{x}},\hat{t}) &- \left(f_i^{(e,e)}(\hat{\mathbf{x}},\hat{t}) - f_i^{(e,e)}(\hat{\mathbf{x}}-\hat{\mathbf{v}}_i,\hat{t})\right) \\ &-2\,\frac{\nu}{c^2}\left(f_i^{(e,o)}(\hat{\mathbf{x}},\hat{t}) - f_i^{(e,o)}(\hat{\mathbf{x}}-\hat{\mathbf{v}}_i,\hat{t})\right). \end{aligned} \tag{5.14}$$

As far as the computation of hydrodynamic quantities is concerned, the first term of the right hand side in (5.14) can be substituted by $f_i^{(e)}(\hat{\mathbf{x}},\hat{t})$ (they have same hydrodynamic moments). The final model equation can thus be re-formulated in terms of the distribution function f_i as follows

$$\begin{aligned} f_i(\hat{\mathbf{x}},\hat{t}+1) = f_i^{(e)}(\hat{\mathbf{x}},\hat{t}) &- \left(f_i^{(e,e)}(\hat{\mathbf{x}},\hat{t}) - f_i^{(e,e)}(\hat{\mathbf{x}}-\hat{\mathbf{v}}_i,\hat{t})\right) \\ &-2\,\frac{\nu}{c^2}\left(f_i^{(e,o)}(\hat{\mathbf{x}},\hat{t}) - f_i^{(e,o)}(\hat{\mathbf{x}}-\hat{\mathbf{v}}_i,\hat{t})\right), \end{aligned} \tag{5.15}$$

or equivalently

$$f_i(\hat{\mathbf{x}},\hat{t}+1) = f_i^{(e)}(\hat{\mathbf{x}}-\hat{\mathbf{v}}_i,\hat{t}) + \left(1-2\,\frac{\nu}{c^2}\right)\left(f_i^{(e,o)}(\hat{\mathbf{x}},\hat{t}) - f_i^{(e,o)}(\hat{\mathbf{x}}-\hat{\mathbf{v}}_i,\hat{t})\right). \tag{5.16}$$

In order to fix ideas, let us consider a local equilibrium such that $c^2 = 1/3$. Moreover, as common in LBM, the kinematic viscosity can be expressed in terms of the relaxation frequency ω of the numerical scheme (see Appendix C for details), namely

$$\nu = \frac{1}{3}\left(\frac{1}{\omega} - \frac{1}{2}\right). \tag{5.17}$$

Substituting Eq. (5.17) into Eq. (5.16) yields the Link-Wise re-formulation of the Artificial Compressibility Method (LW-ACM) for the incompressible isothermal fluid dynamics, expressed by the following system of algebraic equations

$$f_i(\hat{\mathbf{x}},\hat{t}+1) = f_i^{(e)}(\hat{\mathbf{x}}-\hat{\mathbf{v}}_i,\hat{t}) + 2\left(\frac{\omega-1}{\omega}\right)\left(f_i^{(e,o)}(\hat{\mathbf{x}},\hat{t}) - f_i^{(e,o)}(\hat{\mathbf{x}}-\hat{\mathbf{v}}_i,\hat{t})\right), \quad i = 0,\ldots,Q-1 \tag{5.18}$$

where Q is the number of lattice velocities. A clear advantage of the above scheme is that all quantities appearing in Eqs. (5.18) and (5.7) only depends on known (equilibrium) functions at a mesh node and its close neighbors. This introduces a significant simplification in the treatment of boundary conditions, which can be directly borrowed from finite-difference technology (see e.g. the isothermal Couette flow test case reported in Section 5.2.3). Similarly to LBM, the algebraic equations (5.18) can be implemented in three subsequent steps ("pull" formulation), namely pre-combining, streaming and post-combining,

$$f_i^*(\hat{\mathbf{x}} - \hat{\mathbf{v}}_i, \hat{t}) = f_i^{(e)}(\hat{\mathbf{x}} - \hat{\mathbf{v}}_i, \hat{t}) - 2\left(\frac{\omega - 1}{\omega}\right) f_i^{(e,o)}(\hat{\mathbf{x}} - \hat{\mathbf{v}}_i, \hat{t}), \tag{5.19a}$$

$$f_i^{**}(\hat{\mathbf{x}}, \hat{t} + 1) = f_i^*(\hat{\mathbf{x}} - \hat{\mathbf{v}}_i, \hat{t}), \tag{5.19b}$$

$$f_i(\hat{\mathbf{x}}, \hat{t} + 1) = f_i^{**}(\hat{\mathbf{x}}, \hat{t} + 1) + 2\left(\frac{\omega - 1}{\omega}\right) f_i^{(e,o)}(\hat{\mathbf{x}}, \hat{t}). \tag{5.19c}$$

Pre- and post-combining are local processes involving arithmetic operators, whereas streaming alone takes care of data exchange among the nearest neighbors of an arbitrary cell.

The implementation strategy given by Eqs. (5.19) admits a straightforward inclusion of external forcing, by considering the additional step

$$f_i^{\text{force}}(\hat{\mathbf{x}}, \hat{t} + 1) = f_i(\hat{\mathbf{x}}, \hat{t} + 1) + f_i^{(e,o)}\left(\rho(\hat{\mathbf{x}}, \hat{t}), \mathbf{g}(\hat{\mathbf{x}}, \hat{t})\right), \tag{5.20}$$

where $\mathbf{g} = (g_x, g_y)^T$ is the external acceleration. The previous correction is local: Similarly to finite-difference schemes, the external forcing is applied to the point where it is supposed to act. The functions $f_i^{(e,o)}$ are used for convenience (they are already known), for ensuring that the force only applies to the momentum equations.

We notice that, the same simple procedure cannot be applied to the lattice Boltzmann method, because a correction to the distribution function may affect the dynamics of the higher order moments as well. Consistent treatment of the forcing typically involves some special (non-trivial) techniques [41]. Details on the effects due to the correction (5.20), by asymptotic analysis, are reported in the Appendix C. Imposing a given physical acceleration $\bar{\mathbf{g}}$ within a flow, requires the tuning of numerical acceleration $\mathbf{g}$, namely $\mathbf{g} = \varepsilon^3\, \bar{\mathbf{g}}$ (in case of diffusive scaling). The same approach can be adopted to implement mass sources in the numerical scheme.

Finite difference formulation

Since the right hand side of Eq. (5.18) only depends on the equilibrium condition, which is in turn a function of the macroscopic quantities, it is

possible to provide a finite difference formula, expressed in terms of macroscopic quantities, which is fully equivalent to (5.18). As commonly done in the finite-difference literature, we denote by $\{P\}$ the set of computational points surrounding a generic point P (otherwise stated, the generic computational stencil). All the quantities are intended computed at the generic time level $\hat{t}$, while the superscript "+" denotes a quantity at the next time level $\hat{t}+1$. The unknown quantities are given by the velocity components $\mathbf{u} = (u, v)^T$ and the pressure p. Hence the equivalent finite-difference formulas must provide a way to compute u_P^+, v_P^+ and p_P^+ namely

$$u_P^+ = f_u\left(u_{\{P\}}, v_{\{P\}}, p_{\{P\}}; \omega\right), \tag{5.21a}$$

$$v_P^+ = f_v\left(u_{\{P\}}, v_{\{P\}}, p_{\{P\}}; \omega\right), \tag{5.21b}$$

$$p_P^+ = f_p\left(u_{\{P\}}, v_{\{P\}}, p_{\{P\}}; \omega\right). \tag{5.21c}$$

See Appendix E for a complete example based on the D2Q9 lattice [90]. The same finite-difference counterpart can be found for the Lattice Kinetic Scheme (LKS) [49], recovered in case $\omega = 1$, but Eq. (5.18) is also valid for tunable ω and consequently tunable viscosity ν (in particular, for high Reynolds number flows). Moreover, the same derivation can be done for the FD-LKSν proposed in [10], but Eq. (5.18) is formulated only along a particular lattice link and hence it can also take advantage of most of LBM technology (which is link-wise).

1. Availability of two alternative formulations of the same numerical scheme is very convenient. For example, it is possible to commute (even dynamically) between the formulation based on Eq. (5.18) and that based on Eqs. (5.21), depending on the best option in dealing with the local boundary conditions.

2. Similarly to conventional ACM [10, 81, 82], the formulation based on Eqs. (5.21) can be improved by introducing a semi-implicit step for updating the pressure field. Essentially the step in Eq. (5.21c) can be substituted by
$$p_P^+ = f_p\left(u_{\{P\}}^+, v_{\{P\}}^+, p_{\{P\}}; \omega\right), \tag{5.22}$$
using the already updated velocity field.

3. The finite-difference formulation allows to choose different relaxation parameters ω for different (macroscopic) equations. Let us define ω_u the relaxation frequency used in Eq. (5.21a) and (5.21b), while let us define $\omega_p \neq \omega_u$ the relaxation frequency used in Eq. (5.21c). Consequently two kinematic viscosities follow, namely $\nu = \nu(\omega)$ and $\nu_p = \nu(\omega_p)$, where the function $\nu = \nu(\omega)$ is given by Eq. (5.17). By

introducing these relaxation frequencies in Eqs. (5.21) and applying Taylor expansion to such novel expressions (see Appendix C for details), the equivalent system of macroscopic equations can be recovered in the continuum limit ($\varepsilon \to 0$). The momentum equation involves the kinematic viscosity ν (as previously), while the pseudo-compressibility term in the artificially compressible continuity equation, namely the first term in Eq. (C.16), becomes proportional to ε^2/ν_p, namely

$$\frac{\varepsilon^2}{6\rho_0\nu_p}\frac{\partial\bar{\rho}}{\partial t} + \nabla\cdot\bar{\mathbf{u}} = O(\varepsilon^4/\nu_p^2). \tag{5.23}$$

For high Reynolds number flows, where $\nu \ll 1$, replacing ν with ν_p in the previous equation helps to improve the accuracy in recovering the incompressible limit of Navier-Stokes equations. In fact ν_p can be chosen larger than ν such that the diverge-free condition for the velocity field can be accurately satisfied even on moderately refined meshes, i.e. meshes with moderately small grid spacing ε.

Let us assume $\Delta x = \varepsilon$ and $\Delta t = \varepsilon^2$ (diffusive scaling), with $\varepsilon = \Delta x/L = 1/N$ and N the number of mesh points. As reported in the Appendix C, asymptotic analysis [52] of (5.18) and (5.7) shows that, in the limit of vanishing grid spacing, $\varepsilon \ll 1$, the quantities $\bar{p} = (p - p_0)/\varepsilon^2 = (p' - p'_0)/U^2$ and $\bar{\mathbf{u}} = \mathbf{u}/\varepsilon = \mathbf{u}'/U$ satisfy the incompressible isothermal Navier-Stokes equations, with viscosity given by Eq. (5.17). The subscript 0 denotes mean value over the whole computational domain. Here, we stress that for a correct use of the proposed algorithm, it is important to consider a proper post-processing of the numerical results. To this respect, we notice that, for instance, the velocity field $\mathbf{u} = \sum_i \hat{\mathbf{v}}_i f_i / \sum_i f_i$ is mesh-dependent: $\mathbf{u} = \mathbf{u}(\varepsilon)$, with $\mathbf{u}$ going to zero as the mesh spacing ε vanishes. As a result, $\mathbf{u}$ is not the proper choice for describing the velocity field of incompressible flows: To this aim, instead, the quantity $\bar{\mathbf{u}} = \mathbf{u}/\varepsilon$ is adopted due to mesh-independence. Similar considerations apply also to other fields. For consistency with the LBM literature, in this work, the units of quantities directly based on f_i are referred to *lattice units*, while units of the corresponding mesh-independent quantities are termed *physical units*. We stress that finite-difference formulation of the proposed method can be carried out directly in physical units, thus avoiding the above post-processing. Nevertheless, here we prefer to keep the above post-processing for consistency with the Lattice Boltzmann community.

Finally, for consistency, accurate solution of INSE requires $\varepsilon^2/\nu \ll 1$, which is a criterion valid for the LBM as well (see Appendix C for details and the following discussion about the Minion & Brown flow in Section 5.2.3). On the other hand, for stability, numerical evidences suggest that LW-ACM is stable for $1 \leq \omega < 2$, which corresponds only to half of the stability

range for the relaxation frequency of the LBM. The attempts to overcome this limitation by considering also the local equilibrium in the down-wind computational node along the same link identified by the lattice velocity $\hat{\mathbf{v}}_i$, i.e. $\hat{\mathbf{x}} + \hat{\mathbf{v}}_i$, did not succeed so far. The reason may be due to the fact that, as far as only hydrodynamics is concerned, stability requires "up-wind" schemes, which discretize hyperbolic partial differential equations by using differencing biased in the direction of lattice velocities. In particular, the quantity $f_i(\hat{\mathbf{x}}, \cdot)$ streams along the link i-th with the lattice velocity $\hat{\mathbf{v}}_i$ and hence the corresponding up-wind node is $\hat{\mathbf{x}} - \hat{\mathbf{v}}_i$. Remarkably, Eq. (5.18) determines the dynamics of the quantity $f_i(\hat{\mathbf{x}}, \cdot)$ by only (equilibrium-based) information collected in the generic node $\hat{\mathbf{x}}$ and in the up-wind counterpart $\hat{\mathbf{x}} - \hat{\mathbf{v}}_i$.

In order to understand the consequences of the reduced stability range, let us introduce the Reynolds number $\mathrm{Re} = LU/\nu'$, namely

$$\mathrm{Re} = \frac{\mathrm{Ma}/\mathrm{Kn}}{1/3\ (1/\omega - 1/2)}, \tag{5.24}$$

where $\mathrm{Kn} \equiv \Delta x$ is the numerical Knudsen number, which is the dimensionless grid spacing, and $\mathrm{Ma} = U/(\Delta x'/\Delta t')$ is the numerical Mach number, which is the parameter controlling the magnitude of the artificial compressibility (see Appendix C for details). The Reynolds number is dictated by the physical problem under investigation, while the right hand side of the previous expression involves only numerical parameters, namely ω, Ma and Kn. In particular, as done also in LBM, for high Reynolds number flows in LW-ACM, it is convenient to chose $\omega \lesssim 2$ and $\mathrm{Ma} \sim \mathrm{Kn}$. On the other hand, the reduced stability range, i.e. $1 \leq \omega < 2$, induces a slight change in the parameters of LW-ACM for low Reynolds number flows. In fact, for soft-matter systems and/or in micro-scale flows solved by LW-ACM, it is convenient to chose $\omega \gtrsim 1$ and $\mathrm{Ma} \ll \mathrm{Kn}$ (fine time stepping). However it is important to point out that this drawback is a consequence of the link-wise formulation constraint: No such limitation appears in the original ACM [81, 82].

5.2.2 Optimized computer implementation

In the following, we discuss a few strategies useful for reducing the computational time, thanks to an optimized implementation of the algorithm (5.19) and (5.21). Similarly to LBM, the performance characteristics of single-processor implementations depends on the effect of different data layouts [108] (multi-processor optimization strategies are not considered in the present work, see Ref. [43]).

First of all, the streaming step should not overwrite data required for updating neighboring sites. A usual way to work around the resulting data dependencies owing to the propagation step is the use of two arrays (one

for the current and the other for the next time step), and toggling between them [108]. It is also possible (and even more efficient) using a single array, with proper ordering of the sequence of streamed lattice directions, though this may become cumbersome when dealing with wall boundary conditions. The best data layout requires that the distribution functions of the current cell are contiguously located in memory (e.g. by using the first index in Fortran, which addresses consecutive memory locations due to column major order [108]).

Secondly, to reduce the memory traffic, it is important that pre-combining, streaming and post-combining are executed in a single loop and not independently of each other in separate loops or routines, similarly to LBM [108]. This goal can be easily accomplished by reformulating Eqs. (5.19) in term of f_i^*: In fact, the hydrodynamic moments of f_i^* are not exactly equal to the hydrodynamic quantities, but the former are known functions of the latter. Hence it is convenient to compute directly f_i^*, which are ready to be streamed, and to extract the hydrodynamic quantities from f_i^*. This simplifies the implementation of a single updating loop through all computational sites at each time step.

Finally, it is important to reduce as much as possible the number of floating point operations and memory accesses per updated site. In LBM, the D3Q19 lattice with BGK collision operator requires about 180-200 floating point operations per cell and time step as well as reading 19 floating point values and writing to 19 different memory locations [108]. Roughly half of the floating point operations and half of the memory accesses are required by the D2Q9 lattice.

Let us considering the D2Q9 lattice and the LBM-style formulation of LW-ACM, as dictated by Eqs. (5.19), with the optimization tricks reviewed above. Such an implementation of LW-ACM requires 115 floating point operations (+28% compared to BGK-LBM) and 26 memory accesses (+44%) per cell. However, in the following, only the computational performances of LW-ACM in the FD formulation are further investigated, and its superior capabilities are demonstrated (compared to BGK-LBM). From a computational point of view, it may appear that formulas (5.21) are not suitable for an efficient implementation, since they involve many floating point operations. However, because they are derived from Eq. (5.18), it is possible to simplify them using (by-hand) common subexpression elimination (CSE) [43]. See Appendix E for a complete example based on the D2Q9 lattice [90]. Moreover, the same implementation tricks discussed above can be properly applied here.

First of all, the memory storage required by link-wise ACM is exactly one third of that of BGK-LBM (only hydrodynamic variables are needed). At

Table 5.1: Performance test of the link-wise ACM (by FD formulation) vs. BGK-LBM, based on the Minion & Brown flow [72] with Re $= 10,000$ in the time range $t \in [0,1]$, solved by a mesh with 512×512 nodes/sites and performing 12,800 iterations (Ma $= 0.04$). Both codes are serial and use double precision. The considered workstation has Intel® Core™ i7-920 (Bloomfield, 4 physical cores, 8MB L3) with clock rate 2.67GHz (due to TurboMode™ actually running at 2.80 GHz) and 12 GB of DDR3 memory (1333 MHz). The used Fortran compiler is Intel®version 11.1up8 (optimization level option "-O3") and the operative system is Ubuntu Linux i10.04 LTS (64 bit). The million fluid lattice cell updates per second (MLUPS) are reported for both methods.

Elementary stencil	Link-wise ACM by FD formulation	BGK-LBM
# of additions/subtractions	80	70
# of multiplications	60	40
# of floating point operations	140	110
# of actual data (t)	27	9
# of updated data ($t+1$)	3	9
external size of the stencil	$3\times3\times3$	$3\times3\times9$
MLUPS	29.43	27.28

each time step, it is enough to go through all computational cells/sites once and this can be done straightforwardly, because updating formulas are already expressed in terms of hydrodynamic variables. Finally, for locating the macroscopic quantities (p, u, v) contiguously in memory, it is possible to collect them in a single array and to use the first index for addressing them. This leads to an optimized FD-style implementation of Eqs. (5.21). On the D2Q9 lattice, a comparison between the FD-style implementation of link-wise ACM and BGK-LBM is reported in Table 5.1. Link-wise ACM requires more floating point operations but less memory accesses than BGK-LBM.

For clarity, let us analyze the updating process at each time. The external size of the stencil of LW-ACM is smaller than the one of LBM ($3\times3\times3$ instead of $3\times3\times9$ respectively, where 3×3 is due to the D2Q9 lattice, 3 is the number of hydrodynamic quantities and 9 the number of discrete distribution functions). During the generic updating process, if the cache is large enough to hold 3 "lines" (or 3 planes in 3D) of the computational domain, then updating the hydrodynamic quantities in a cell requires the loading of only the actual values of a further cell in the cache (3 loads). In the worst case, updating the hydrodynamic quantities in a cell requires the loading of the actual values of three additional cells in the cache: This amounts to 9 loads from actual array (3 physical quantities from the current, previous

and next "line"). In any case, 3 write-allocate transfers from main memory to cache and 3 stores to get the updated array from cache back to main memory are always required. This leads to 9–15 in total per nodal updates.

On the other hand, BGK-LBM requires 9 loads from the actual array (discrete distribution function), 9 write-allocate transfers and 9 stores to the updated array, leading to 27 memory transfers. For BGK-LBM, there is no reuse of data from cache because every discrete distribution function is only used once. As the number of memory transfers usually affects the performance more than the number of floating point operations, the performance of link-wise ACM is superior than that of BGK-LBM. Some performance data are reported in Table 5.1. FD-style implementation of link-wise ACM was able to achieve 29.43 million fluid lattice cell updates per second (MLUPS), which is the standard way to measure the performance of LBM implementations [108]. For the previous test, this value is roughly 8% faster than BGK-LBM.

Remark: In our opinion, there is still room for improvement according to the performance model (based on assuming either infinitely fast memory or infinitely fast compute units). For example, the numerical code for solving the 2D lid driven cavity test case achieved 32.3 MLUPS and this was essential for simulating very high Reynolds number flows. Importantly, with an efficient implementation, this algorithm may be one of the few which is compute-bound and not memory-bound. The latter observation is of particular interest for General-Purpose computing on Graphics Processing Units (GPGPU).

5.2.3 Simple boundary conditions

For sake of simplicity, numerical tests with simple boundary conditions are discussed first. Here, by simple boundary conditions, we mean either finite-difference boundary conditions (isothermal Couette flow) or periodic (generalized Green-Taylor vortex flow and Minion & Brown flow). More general boundary conditions taking advantage of the LBM technology will be discussed in Section 5.2.4.

Isothermal Couette flow

In this section, we consider the plane Couette flow where a viscous fluid is confined in a gap between two parallel plates, with the one moving in its own plane with respect to the other. Here, two configurations are simulated by the present LW-ACM method on several meshes: Couette flow without wall injection (referred to as Test 1), and Couette flow with wall injection (referred to as Test 2). In the latter configuration (Test 2) fluid is injected from the bottom wall into the gap and extracted from the top wall with a constant orthogonal velocity $\bar{v}_0$. At the stationary condition, the above

configurations admit the following exact solutions:

$$\bar{u}(y) = \frac{1}{2}\hat{u}_L\left(1+\frac{y}{L}\right)+\bar{u}_0\left(1-\frac{y^2}{L^2}\right), \qquad \text{(Test 1)}, \tag{5.25}$$

$$\bar{u}(y) = \bar{u}_L\left(\frac{\exp(y\,\mathrm{Re}/L)-1}{\exp(\mathrm{Re})-1}\right), \qquad \text{(Test 2)}, \tag{5.26}$$

where the Reynolds number Re is the main control parameter, L is a characteristic length depending on the considered test and ν is the kinematic viscosity.

For Test 1, L is half the gap height, while $\bar{u}_0$ represents a velocity based on the imposed pressure gradient $\nabla\bar{p}$:

$$\bar{u}_0 = \frac{L^2\nabla\bar{p}}{2\rho\nu},$$

$\bar{u}_L$ is the velocity of the top wall $\bar{u}_L = \bar{u}(y = L)$ and ρ is the density. The bottom wall is assumed stationary: $\bar{u}(y = -L) = 0$.

In case of wall injection (Test 2), L is the gap height, the Reynolds number Re in (5.25) is defined on the basis of the injection velocity $\bar{v}_0$, namely $\mathrm{Re} = \bar{v}_0 L/\nu$. Velocities at the top and bottom walls are: $\bar{u}(y = L) = \bar{u}_L$ and $\bar{u}(y = 0) = 0$, respectively. In all simulations, no-slip boundary conditions are applied along the wall by simply imposing the local equilibrium with the desired velocity, while periodic boundary conditions are adopted at the inlet and outlet.

First of all, diffusive scaling is considered: This strategy consists in scaling the velocity field on different meshes, keeping fixed the relaxation frequency (see Appendix C for details). This scaling ensures second order convergence in the accuracy, as reported in upper part of Table 5.2, where the L^2 norm of deviation of numerical results from exact solution (5.25) is shown. In addition, acoustic scaling is considered. This strategy consists in tuning the relaxation frequency on different meshes in order to keep constant the computed velocity field (see Appendix C for details). This scaling ensures first order convergence in the accuracy, as reported in the lower part of Table 5.2.

Generalized Green-Taylor vortex flow

In this section, some numerical results of the Taylor-Green vortex flow are reported. The latter problem is widely employed as a benchmark for various incompressible Navier-Stokes solvers, owing to the existence of a simple analytical solution. The original problem is characterized by the exponential decay in time due to viscous dissipation. However, here the original problem

Table 5.2: Convergence analysis for Couette flow without (Test 1) and with (Test 2) wall injection in case of both diffusive and acoustic scaling.

$\Delta t \propto \Delta x^2$ (diffusive scaling)				
			Error $L^2[\bar{u}]$	
$\varepsilon \equiv \Delta x$	Ma $\propto \Delta t/\Delta x$	$\nu \propto \mathrm{Re}^{-1}$	Test 1	Test 2
$1/10$	3.0×10^{-2}	3.0×10^{-2}	1.74×10^{-3}	4.59×10^{-4}
$1/20$	1.5×10^{-2}	3.0×10^{-2}	4.49×10^{-4}	1.21×10^{-4}
$1/40$	7.5×10^{-3}	3.0×10^{-2}	1.20×10^{-4}	3.11×10^{-5}
$\Delta t \propto \Delta x$ (acoustic scaling)				
			Error $L^2[\bar{u}]$	
$\varepsilon \equiv \Delta x$	Ma $\propto \Delta t/\Delta x =$ const.	$\nu \propto \mathrm{Re}^{-1}$	Test 1	Test 2
$1/10$	3.0×10^{-1}	3.0×10^{-3}	4.27×10^{-2}	1.05×10^{-2}
$1/20$	3.0×10^{-1}	1.5×10^{-3}	2.76×10^{-2}	5.19×10^{-3}
$1/40$	3.0×10^{-1}	7.5×10^{-4}	1.54×10^{-2}	2.66×10^{-3}

is modified such that it becomes periodic in time by the introduction of a proper external acceleration $\bar{\mathbf{g}} = (\bar{g}_x, \bar{g}_y)^T$ to Eq. (C.12), where

$$\begin{aligned} \bar{g}_x(t,x,y) &= \sin(x-\bar{u}_0 t)\cos(y-\bar{v}_0 t)(2\nu\cos t - \sin t), \\ \bar{g}_y(t,x,y) &= -\cos(x-\bar{u}_0 t)\sin(y-\bar{v}_0 t)(2\nu\cos t - \sin t), \end{aligned} \tag{5.28}$$

with $\bar{u}_0$ and $\bar{v}_0$ being constants aiming at preventing that the advection term balances with the pressure gradient. The modified problem admits the following analytical solution

$$\begin{aligned} \bar{u}(t,x,y) &= \bar{u}_0 + \sin(x-\bar{u}_0 t)\cos(y-\bar{v}_0 t)\cos t, \\ \bar{v}(t,x,y) &= \bar{v}_0 - \cos(x-\bar{u}_0 t)\sin(y-\bar{v}_0 t)\cos t, \\ \bar{p}(t,x,y) &= \frac{1}{4}[\cos 2(x-\bar{u}_0 t) + \cos 2(y-\bar{v}_0 t)]\cos^2 t. \end{aligned} \tag{5.29}$$

We solve the above modified problem numerically in the domain $\Omega = [0 \leq x \leq 2\pi] \times [0 \leq y \leq 2\pi]$ using periodic boundary condition, and $(\bar{u}_0, \bar{v}_0) = (0.3, 0.6)$. The kinematic viscosity is $\nu = 0.1$. Diffusive scaling is adopted for all simulations, namely Ma $= 2\pi\,$Kn or equivalently $\Delta t = \Delta x^2$ (see Appendix C for details).

The L^1 error data are reported in Table 5.3 at $t = 60$ for link-wise ACM, link-wise ACM with semi-implicit formulation (see the end of Section 5.2.1 where this formulation is presented), standard (second-order) ACM and multiple-relaxation-time (MRT) LBM. The standard ACM is described in Ref. [81].

Table 5.3: The L^1 norm of the error versus $\varepsilon \equiv \Delta x \equiv \mathrm{Ma}/2\pi$ at $t = 60$ in the problem of the generalized Taylor-Green vortex problem for $\nu = 0.1$.

Link-wise ACM			
$\varepsilon \equiv \Delta x$	Error $L^1[\bar{u}]$	Error $L^1[\bar{v}]$	Error $L^1[\bar{p}]$
$\pi/16$	1.69262×10^{-2}	1.96356×10^{-2}	3.45590×10^{-2}
$\pi/32$	4.38763×10^{-3}	4.70793×10^{-3}	7.91104×10^{-3}
$\pi/64$	1.41952×10^{-3}	1.50330×10^{-3}	2.21013×10^{-3}
Link-wise ACM (semi-implicit, see Section 5.2.1)			
$\varepsilon \equiv \Delta x$	Error $L^1[\bar{u}]$	Error $L^1[\bar{v}]$	Error $L^1[\bar{p}]$
$\pi/16$	1.70353×10^{-2}	2.02203×10^{-2}	3.09165×10^{-2}
$\pi/32$	4.41348×10^{-3}	4.70412×10^{-3}	6.11065×10^{-3}
$\pi/64$	1.41906×10^{-3}	1.50227×10^{-3}	1.73786×10^{-3}
ACM			
$\varepsilon \equiv \Delta x$	Error $L^1[\bar{u}]$	Error $L^1[\bar{v}]$	Error $L^1[\bar{p}]$
$\pi/16$	8.03750×10^{-3}	1.00313×10^{-2}	9.70682×10^{-3}
$\pi/32$	1.92844×10^{-3}	2.47186×10^{-3}	1.93893×10^{-3}
$\pi/64$	5.64682×10^{-4}	6.61285×10^{-4}	4.34911×10^{-4}
MRT-LBM			
$\varepsilon \equiv \Delta x$	Error $L^1[\bar{u}]$	Error $L^1[\bar{v}]$	Error $L^1[\bar{p}]$
$\pi/16$	7.67964×10^{-3}	8.90307×10^{-3}	1.67526×10^{-2}
$\pi/32$	1.84928×10^{-3}	2.17164×10^{-3}	3.63345×10^{-3}
$\pi/64$	6.12810×10^{-4}	6.81060×10^{-4}	1.11633×10^{-3}

In the MRT-LBM [31, 61], the consistent treatment of forcing is based on Ref. [41]. The time step employed in the LBM computation is the same as the one of ACM, i.e. $\mathrm{Ma} = 2\pi\,\mathrm{Kn}$ or equivalently $\Delta t = \varepsilon^2$, and the tuning parameters of MRT are $s_1 = s_4 = s_6 (= {\tau_\rho}^{-1} = {\tau_j}^{-1}) = 0$, $s_2 (= {\tau_e}^{-1}) = 1.63$, $s_3 (= {\tau_\varepsilon}^{-1}) = 1.14$, $s_5 = s_7 (= {\tau_q}^{-1}) = 1.92$ (see Refs. [61, 41]). All methods show nearly second-order convergence. Link-wise ACM shows larger numerical errors than ACM and MRT-LBM. However it must be stressed that the implementation of forcing in link-wise ACM is straightforward, while the consistent treatment of forcing in LBM is much more complicated [41]. Moreover in link-wise ACM, spatial operators (gradient and Laplace operator) do not need to be discretized individually (unlike ACM) but it is enough to discretize along the generic lattice direction: This makes much easier the treatment of three-dimensional cases.

Minion & Brown flow

LW-ACM and LBM are characterized by different values of artificial compressibility, leading to a different robustness with respect to under-resolved simulations. By referring to the pseudo-continuity equation for LW-ACM (see Eq. (C.16) in the Appendix C), it follows that accurate solution of divergence-free condition for the velocity field requires: $\varepsilon^2/\nu \ll 1$. This is even a more severe condition than the one of LBM, in case of high Reynolds number flows. In the following, we further explore this issue, by means of the Minion & Brown flow.

Minion & Brown [72] studied the performance of various numerical schemes for under-resolved simulations of the 2D incompressible Navier Stokes equations. The relevance of this flow for testing robustness and accuracy of LBM schemes was first pointed out by Dellar [29]. Minion & Brown considered initial conditions corresponding to the perturbed shear layer

$$\bar{u}(t,x,y) = \begin{cases} \tanh(k(y-1/4)), & y \leq 1/2, \\ \tanh(k(3/4-y)), & y > 1/2, \end{cases} \tag{5.30}$$

$$\bar{v}(t,x,y) = \delta \sin(2\pi(x+1/4)), \tag{5.31}$$

in the periodic domain $\Omega = [0 \leq x \leq 1] \times [0 \leq y \leq 1]$. The parameter k controls the shear layer width, while δ the magnitude of the initial perturbation. The shear layer is expected to roll up due to Kelvin-Helmholtz instability. With $k = 80$, $\delta = 0.05$, and Reynolds number $\mathrm{Re} = 1/\nu = 10000$, the thinning shear layer between the two rolling up vortices becomes under-resolved on a 128×128 grid. Minion & Brown [72] found that conventional numerical schemes using centered differences became unstable for this under-resolved flow, whereas "robust" or "upwind" schemes that actively suppress grid-scale oscillations all produce two spurious secondary vortices at the thinnest points of the two shear layers at $t = 1$. Dellar [29] found that, even though it is stable on the previous mesh, two spurious vortices are generated by the BGK LBM scheme based on the D2Q9 lattice and with unmodified bulk viscosity. The same author proposed a way to increase the bulk viscosity for overcoming this problem, and verified that the same result can be achieved by using MRT-LBM. Along the same idea, alternative formulations for modifying the dissipation of the LBM schemes have been proposed [8, 13].

Link-wise ACM is stable for the previous test, but the velocity field is not accurate enough due to numerical viscosity. For $\varepsilon = 1/128$ and $\nu = 1/10000$, indeed, the term that multiply the pressure time derivative in the pseudo-continuity equation (Eq. (C.16) in the Appendix C), namely ε^2/ν, reaches the value of 0.61, thus preventing an accurate fulfillment of the diverge-free condition for the velocity field. In the following, two improvements are worked out for circumventing the above problem.

First, we apply the strategy discussed at the end of Section 5.2.1, introducing a numerical fictitious viscosity $\nu_p = 170\,\nu$, with the corresponding relaxation frequency ω_p computed by means of (5.17). The relaxation frequency ω_p is used in the macroscopic updating rule (5.21c). Hence, the pseudo-compressibility term in the continuity equation, namely the first term in Eq. (C.16), becomes proportional to $\varepsilon^2/\nu_p = 0.0036 \ll \varepsilon^2/\nu$ and this improves the quality of the solution. The vorticity at $t = 1$ is reported in Figure 5.1, where the velocity field looks much better, but the two spurious secondary vortices at the thinnest points of the two shear layers are still present (similarly to BGK-LBM).

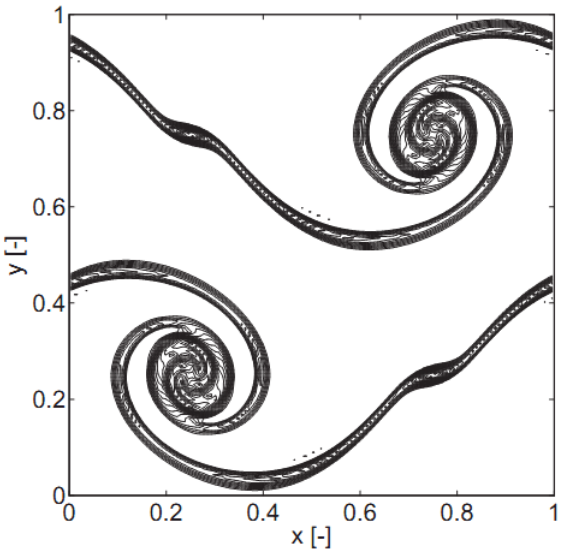

Figure 5.1: Contours of vorticity at $t = 1$ from the link-wise ACM with the first improvement ($\nu_p = 170\,\nu$, see Section 5.2.1) on a 128×128 grid with $\mathrm{Ma} = 0.04$ and $\mathrm{Re} = 10000$. See also Fig. 8 in [72].

The second improvement follows the idea to increase the bulk viscosity ξ, as suggested by Dellar [30]. As discussed in Appendix D, instead of the standard $f_i^{(e)}$, we consider a modified set of functions, namely $f_i^{(e*)} = f_i^{(e*)}(\gamma)$, where γ is a free parameter related to the bulk viscosity ξ: $\xi = 2\rho_0\nu\,(1+2\,\gamma)$. This strategy enables to increase the bulk viscosity and represents a valuable example, showing how to use moments of the updated distribution function for the local computation of derivatives (see the Appendix D for details). The above argument is a further confirmation that the present LW-ACM can easily incorporate technologies originally developed for LBM.

As a concluding remark, it is worth to point out that, even though LW-ACM can solve this under-resolved test case by means of previously discussed

improvements, the average and peak values of the velocity field divergence remain slightly larger than those computed by MRT-LBM. For sake of completeness, optimized ACM [82] yields much smaller values of velocity field divergence than those of MRT-LBM. However, it is important to keep in mind that the Minion & Brown flow is a very severe test due to the small initial perturbation δ, which realizes a very sharp boundary layer. Hence this test is a multi-scale problem and some of the regularity assumptions used in deriving the numerical schemes may not hold completely.

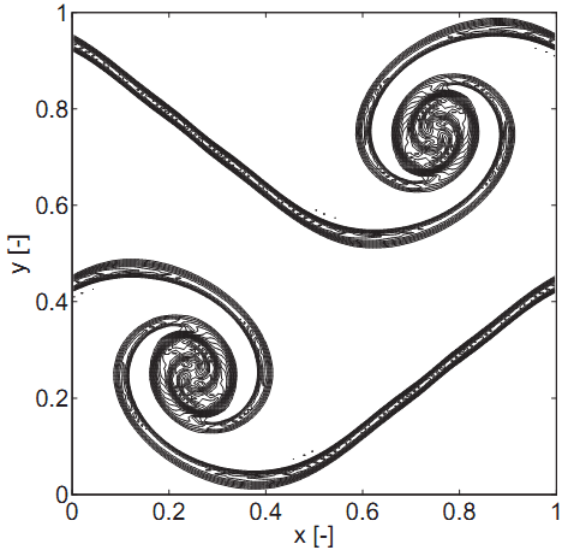

Figure 5.2: Contours of vorticity at $t = 1$ from the link-wise ACM with the both suggested improvements ($\nu_p = 170\,\nu$, see Section 5.2.1, and $\gamma = 0.4$, see Section D) on a 128×128 grid with Ma $= 0.04$ and Re $= 10000$.

5.2.4 Link-wise wall boundary conditions

The link-wise formulation of the proposed method offers significant advantages when dealing with wall boundary conditions. First, let us consider simple structured boundaries, where walls are aligned along the mesh (for general cases, the reader can refer to the next section). In particular, let us suppose that walls are located halfway between two consecutive nodes in an ideal step-wise geometry. Instead of using Eqs. (5.19), it proves convenient focusing on the quantities f_i^* (after pre-combining) streaming out of a single point $\mathbf{x}$ ("push" formulation)

$$f_i^*(\hat{\mathbf{x}}, \hat{t}) = f_i^{(e)}(\hat{\mathbf{x}}, \hat{t}) - 2\left(\frac{\omega - 1}{\omega}\right) f_i^{(e,o)}(\hat{\mathbf{x}}, \hat{t}). \tag{5.32}$$

Let us suppose that $\hat{\mathbf{x}}$ is a fluid node close to a complex wall boundary at rest

such that $\hat{\mathbf{x}} + \hat{\mathbf{v}}_i$ is a wall node. In an ideal step-wise geometry, the wall location is assumed halfway between $\hat{\mathbf{x}}$ and $\hat{\mathbf{x}} + \hat{\mathbf{v}}_i$. Hence, during the streaming step, the information stored in the discrete distribution function pointing towards the wall are reflected along the same link by the wall (according to the popular *bounce-back* rule), namely

$$f^{**}_{BB(i)}(\hat{\mathbf{x}}, \hat{t}+1) = f^{*}_{i}(\hat{\mathbf{x}}, \hat{t}), \tag{5.33}$$

where $BB(i)$ is the bounce-back operator giving the lattice link opposite to i-th. Finally the post-combining step can be performed in the usual way, namely

$$f_{BB(i)}(\hat{\mathbf{x}}, \hat{t}+1) = f^{**}_{BB(i)}(\hat{\mathbf{x}}, \hat{t}+1) + 2\left(\frac{\omega - 1}{\omega}\right) f^{(e,o)}_{BB(i)}(\hat{\mathbf{x}}, \hat{t}). \tag{5.34}$$

Considering that $\hat{\mathbf{v}}_i = -\hat{\mathbf{v}}_{BB(i)}$ and $f^{(e,o)}_{i} = -f^{(e,o)}_{BB(i)}$, the combination of previous steps yields

$$f_{BB(i)}(\hat{\mathbf{x}}, \hat{t}+1) = f^{(e)}_{i}(\hat{\mathbf{x}}, \hat{t}) + \left(2 - \frac{2}{\omega}\right) 2 f^{(e,o)}_{BB(i)}(\hat{\mathbf{x}}, \hat{t}). \tag{5.35}$$

In case of moving complex boundary with velocity $\mathbf{u}_w$, the procedure reported in [12] (here reformulated in terms of $f^{(e,o)}_{BB(i)}$) suggests the inclusion of the additional term

$$\delta f_{BB(i)}(\rho_0, \mathbf{u}_w) = 2 f^{(e,o)}_{BB(i)}(\rho_0, \mathbf{u}_w), \tag{5.36}$$

where $f^{(e,o)}_{BB(i)}$ is given by Eq. (5.7) and ρ_0 is the averaged density over the whole computational domain (see Appendix C for details). For sake of simplicity, let us consider the diffusive scaling: $\Delta x = \varepsilon \ll 1$, $\Delta t = \varepsilon^2$. Hence, the incompressible limit implies $\rho(\hat{\mathbf{x}}) = \rho_0 + O(\varepsilon^2)$. Moreover, the point $\hat{\mathbf{x}}$ is only $\varepsilon/2$ away from the moving wall. Combining the previous conditions, the following approximation holds $\mathbf{u}(\hat{\mathbf{x}}) = \mathbf{u}_w + O(\varepsilon^2)$ and

$$f^{(e,o)}_{BB(i)}(\hat{\mathbf{x}}, t) = f^{(e,o)}_{BB(i)}(\rho_0, \mathbf{u}_w) + O(\varepsilon^2),$$

meaning that the rightmost term of Eq. (5.35) produces a similar effect to the correction (5.36). Hence, the suggested correction for LBM will be multiplied by a scaling factor (complement to one of the factor multiplying the last term in Eq. (5.35)) in link-wise ACM, namely

$$f^{w}_{BB(i)}(\hat{\mathbf{x}}, \hat{t}+1) = f_{BB(i)}(\hat{\mathbf{x}}, \hat{t}+1) + \left(\frac{2}{\omega} - 1\right) \delta f_{BB(i)}(\rho_0, \mathbf{u}_w), \tag{5.38}$$

where $f^{w}_{BB(i)}$ is the proper boundary condition in case of moving boundary.

Link-wise formulation is also very useful in computing hydrodynamical forces acting on bodies. A popular approach in LBM literature is based on the so-called momentum exchange algorithm (MEA), originally proposed in [60] and lately improved in [66] (see [15] for a complete discussion). In LBM, at every time step, the momentum

$$\mathbf{p}_i = \hat{\mathbf{v}}_i f_i^{\text{post}}(\hat{\mathbf{x}}, \hat{t}) - \hat{\mathbf{v}}_{BB(i)} f_{BB(i)}(\hat{\mathbf{x}}, \hat{t}+1) = \hat{\mathbf{v}}_i \left[f_i^{\text{post}}(\hat{\mathbf{x}}, \hat{t}) + f_{BB(i)}(\hat{\mathbf{x}}, \hat{t}+1) \right], \tag{5.39}$$

is transferred from the fluid to the solid body (f_i^{post} is the post-collisional distribution function). For sake of simplicity, here we restrict ourselves on bodies at rest. In link-wise ACM, the quantity f_i^{post} is purposely defined in order to get rid of the last term in the post-combining step, namely

$$f_i^{\text{post}}(\hat{\mathbf{x}}, \hat{t}) = f_i^*(\hat{\mathbf{x}}, \hat{t}) - 2\left(\frac{\omega - 1}{\omega}\right) f_{BB(i)}^{(e,o)}(\hat{\mathbf{x}}, \hat{t}). \tag{5.40}$$

Introducing the previous definition in Eq. (5.39) yields

$$\mathbf{p}_i = \hat{\mathbf{v}}_i \left[f_i^*(\hat{\mathbf{x}}, \hat{t}) + f_{BB(i)}^{**}(\hat{\mathbf{x}}, \hat{t}+1) \right]. \tag{5.41}$$

The previous expression for link-wise ACM is general. In case of step-wise geometries (as those considered in this section), the expression (5.33) holds and Eq. (5.41) can be recast as: $\mathbf{p}_i = 2\hat{\mathbf{v}}_i f_i^*(\hat{\mathbf{x}}, \hat{t})$. The force exerted on a body is computed by a summation of the contributions (5.41) over all the boundary links surrounding its surface:

$$\mathcal{F} = \sum_{i \in \mathsf{S}} \mathbf{p}_i, \tag{5.42}$$

where S is the set of links starting from all surrounding nodes intersecting the body.

Conversion of the force (5.42) from lattice units to physical units requires substraction of the hydrostatic component $\mathcal{F}_0$ generated by the averaged density field ρ_0 (see also the Appendix C for details). Computing the hydrostatic force on partial boundaries of a body by Eq. (5.42 and 5.41) can be accomplished after exclusion of the velocity-dependent components of f_i^* and $f_{BB(i)}^{**}$. If the force is computed on the entire body surface, the hydrostatic force is null. The remaining quantity $\mathcal{F} - \mathcal{F}_0$ scales as the second order tensor: in case of diffusive scaling $\mathcal{F} - \mathcal{F}_0 \sim \varepsilon^2$. However the number of points in the set S increases proportionally to $1/\varepsilon$. Consequently the following scaling holds (see also Table 2.2)

$$\Delta\bar{\mathcal{F}} = (\mathcal{F} - \mathcal{F}_0)/\varepsilon^2 = \left(-\mathcal{F}_0/\varepsilon + \sum_{i \in \mathsf{S}(1/\varepsilon)} \mathbf{p}_i \right) / \varepsilon. \tag{5.43}$$

2D lid driven cavity flow

In this section, the effective enhanced stability of the present LW-ACM method is tested by means of the classical two-dimensional (2D) lid driven cavity problem (see also [14, 67, 95]). Such a benchmark has been considered owing to a singularity of the pressure in the lid corners, which makes it a severe test for robustness of numerical schemes, especially starting from moderately high Reynolds numbers. In all simulations, we consider a square domain $(x, y) \in [0, L] \times [0, L]$, with $L = 1$.
Such a domain is discretized by uniform collocated grid with $N \times N$ points. The boundaries are located half-cell away from the computational nodes. Let us denote $\hat{\mathbf{x}}_b$ the generic boundary computational node. In all inner nodes ($\hat{\mathbf{x}} \neq \hat{\mathbf{x}}_b$), Eq. (5.18) holds for any lattice velocity $\hat{\mathbf{v}}_i$. In an arbitrary boundary node $\hat{\mathbf{x}}_b$, Eq. (5.18) holds for any lattice velocity $\hat{\mathbf{v}}_i$ such that $\hat{\mathbf{x}}_b + \hat{\mathbf{v}}_i$ is still a computational node. In case $\hat{\mathbf{x}}_b + \hat{\mathbf{v}}_i$ falls out of the computational grid, the boundary condition (5.38) is applied, with $\mathbf{u}_w$ being the boundary velocity (imposed half-cell away from the boundary node $\hat{\mathbf{x}}_b$). In the following numerical simulations, $\mathbf{u}_w = (u_L, 0)^T$ at the lid wall, where u_L is the lid velocity, and $\mathbf{u}_w = 0$ for all the other walls. At the lid corners, the lid velocity is imposed, while for other corners the boundary conditions (5.38) are adopted. In Figs. 5.3 and 5.4, numerical results corresponding to several grids and methods are reported for Reynolds number $\mathrm{Re} = u_L L/\nu = 5000$. In this case, it is known that the flow is characterized by four main vortexes, whose actual *centers* can be found by searching for local extrema of the stream function ψ defined as:

$$u = \frac{\partial \psi}{\partial y}, \qquad v = -\frac{\partial \psi}{\partial x}, \tag{5.44}$$

with u and v being the horizontal and vertical component of the velocity field, respectively. For standard Lattice Boltzmann method [90] with BGK collisional operator and $D2Q9$ lattice, the coarsest grid which ensures numerical stability was found to be 250×250. On the other hand, the present LW-ACM method can be safely adopted with 125×125 grid, and reasonably accurate results are found as reported in Figs. 5.3 and 5.4. In addition, LW-ACM shows stability even with 50×50 grid ($1/25$ the total number of nodes needed by BGK-LBM method), where LW-ACM is still able to describe the main features of the 2D cavity flow at $\mathrm{Re} = 5000$.

In Fig. 5.4 the pressure contours for the same test are reported. As visible in the upper-left part of Fig. 5.4 the BGK solution shows some *checkerboard* pressure distribution at the top corners of the cavity. The mesh resolution is still enough to overcome the checkerboard instability mechanism: however this comes at the price of a very large computational domain (larger than 250×250). On the other hand, no such a problem was noticed with LW-ACM, even for quite coarse grids (down to 50×50). The absence of

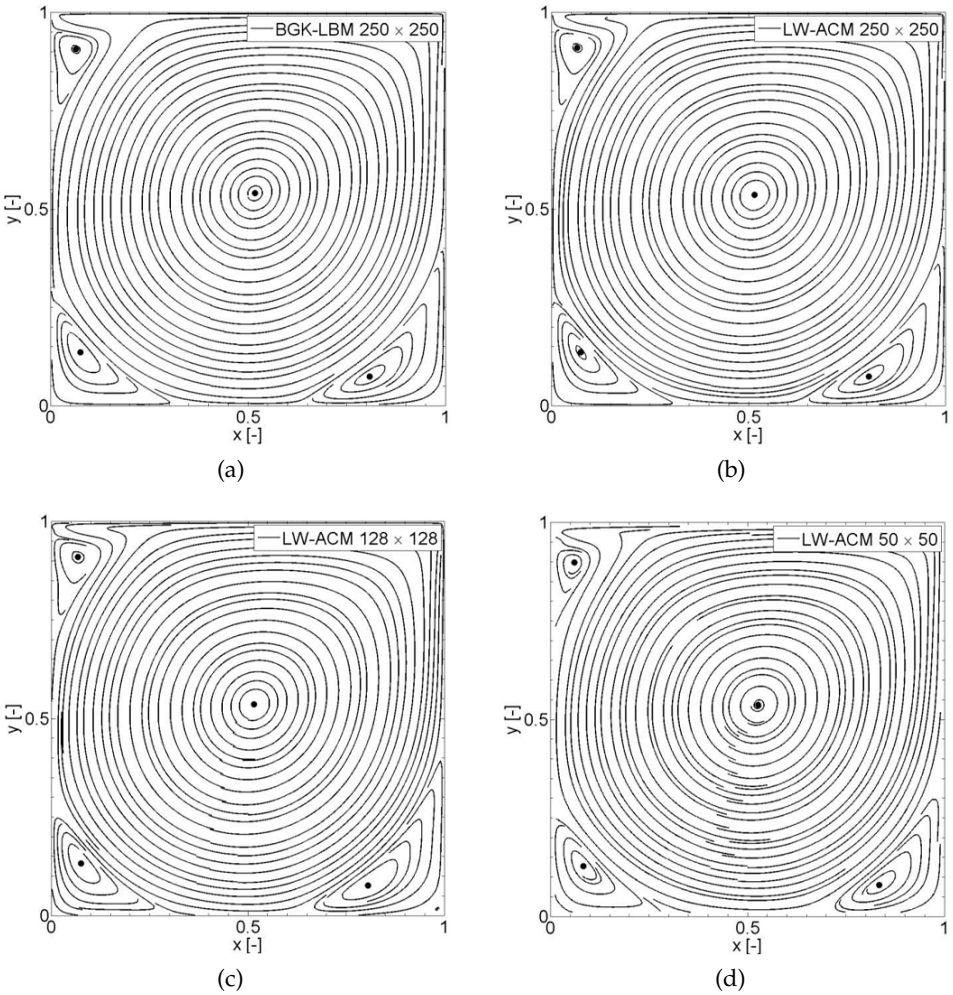

Figure 5.3: Streamlines for the lid driven cavity flow with Re = 5000. Different numerical methods and different meshes are compared. The location of the four minima of the stream-function is denoted by filled circles.

spurious oscillations in the numerical solutions by the artificial compressibility method (ACM) for this test case has been already pointed out [81]. Hence, the previous numerical evidences demonstrate that also the present link-wise formulation of ACM inherits the same feature.

It is worth stressing that numerical stability on coarse grids, yet with poor accuracy, is a highly desirable feature in several engineering problems, e.g. where a loose grid resolution of details of no interest (for the overall flow phenomena) should not prevent global convergence of the code. Clearly the numerical schemes should be compared in terms of the actual accuracy as well. From the very beginning, it is worth to point out that all considered

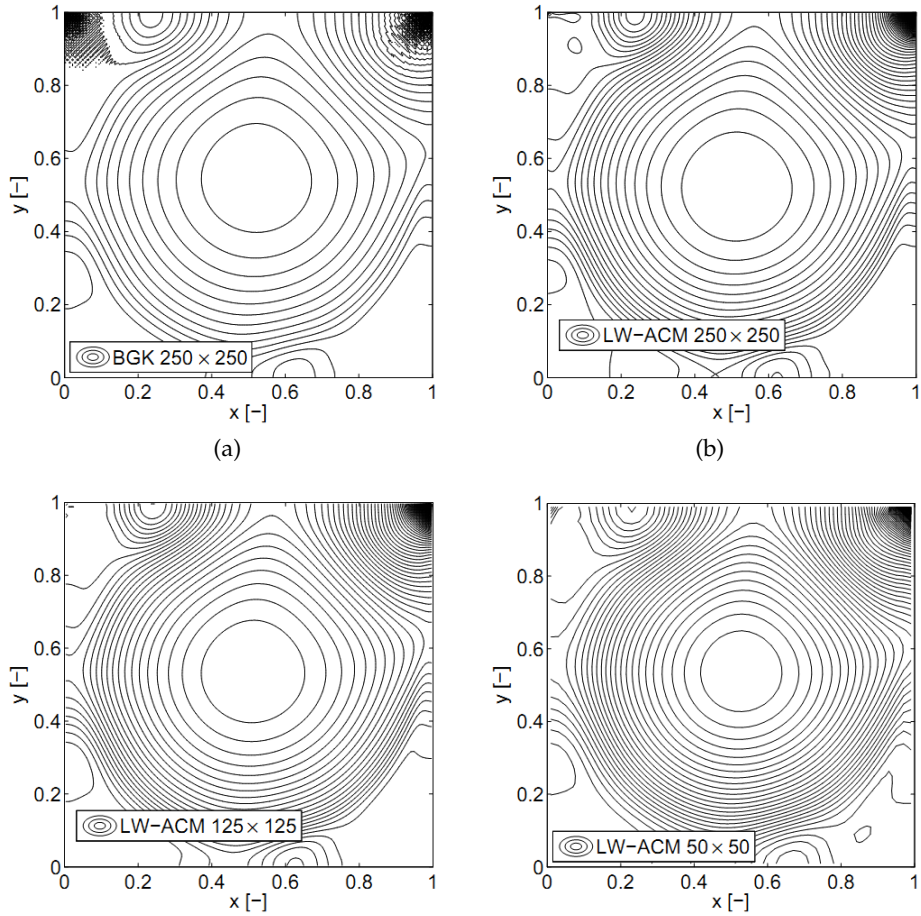

Figure 5.4: Pressure contours for the lid driven cavity flow with Re = 5000. Different numerical methods and different meshes are compared.

methods (i.e. BGK-LBM, MRT-LBM, ACM, LW-ACM) are based on artificial compressibility and even steady state solutions depend on the numerical Mach number (in particular, the pressure gradients depend on the Mach number, as well as the number of time steps). In particular, reducing the numerical Mach number improves the quality of the results. See Appendix C for details. Hence a fair comparison among different methods requires using the same numerical Mach number.

The flow fields of a 2D lid-driven cavity problem with Re = 5000 and 128×128 grid, as predicted by the optimized ACM method [81] and the present LW-ACM (with Mach number Ma = 0.2 and $\nu_p = \nu$), have been compared. Here optimized ACM means that (a) high wave numbers are damped for the suppression of the checkerboard instability and (b) the Richardson

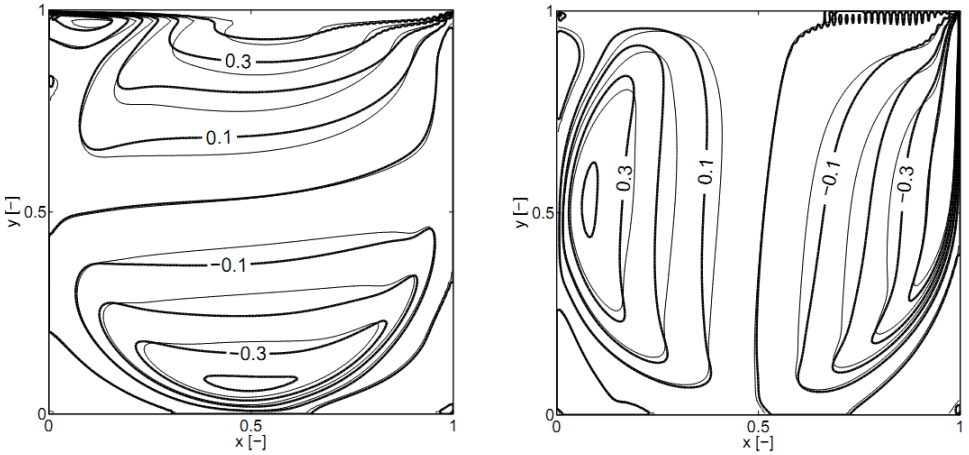

(a) (b)

Figure 5.5: Comparison of the velocity field for the lid driven cavity flow at Re $= 5000$ with 128×128 grids: horizontal component u and vertical component v are reported on the left and right hand side, respectively. Thin and bold lines denote the present LW-ACM (with $\nu_p = \nu$) and optimized ACM solution [81], respectively. The latter method is based on a second order accurate scheme in time, and fourth order accurate scheme in space (bulk fluid).

extrapolation in the Mach number (except around top singular corners) is employed [81]. As reported in Figs. 5.5 and 5.6, LW-ACM shows both a smoother and more accurate behavior (see also Table 5.4), beside a remarkably simpler implementation. Moreover, in Figs. 5.7 and 5.8, we report the flow fields of a 2D lid-driven cavity problem with Re $= 5000$ and 256×256 grid as predicted by the optimized ACM [81] and the present LW-ACM (with Mach number Ma $= 0.2$ and $\nu_p = \nu$), where a small mismatch between the two solutions is observed. This time the optimized ACM method is able to reproduce the reference results [14] with excellent accuracy (despite the use of a much coarser grid: 256^2 vs. 2048^2), although minor pressure oscillations are still visible at the lid corners and this affects, e.g., the prediction of entrophy (see Eq. (5.45) and Table 5.4). Differences between ACM and LW-ACM are mainly due to: 1) different accuracy of the two schemes (second and first order accuracy in time for ACM and the present LW-ACM respectively, whereas fourth and second order accuracy in space for ACM and the present LW-ACM respectively), and 2) slightly different treatment of boundaries. ACM imposes boundary conditions on the computational nodes, while in LW-ACM, analogously to LBM, the wall boundary conditions are imposed half cell away from the computational node. This allows one to avoid singularities, which appear in the top corners for this

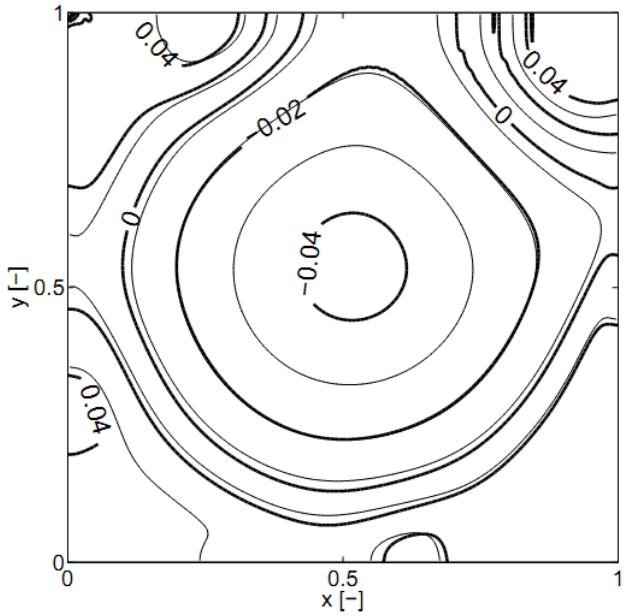

Figure 5.6: Comparison of the pressure field for the lid driven cavity flow at Re $= 5000$ with 128×128 grids. Thin and bold lines denote the present LW-ACM (with $\nu_p = \nu$) and optimized ACM solution [81], respectively. The latter method is based on a second order accurate scheme in time, and fourth order accurate scheme in space (bulk fluid).

test case. Despite all this, it is fair to say that the agreement between the above two solutions is quite good. In Figs. 5.9 and 5.10, the flow field computed by the LW-ACM with Re $= 5000$ and 256×256 grid is compared to a reference solution from the literature [14], where a state of the art code based on finite differences is used with a remarkably fine grid (2048×2048). Despite a significant disparity in the number of computational nodes (LW-ACM makes use of $1/64$ the nodes adopted for the reference solution), an excellent agreement is found. It is worth stressing that, the above problem was also simulated by the multiple relaxation time lattice Boltzmann method (MRT-LBM) with 256×256 grid. Comparison between MRT-LBM and the reference solution is also very good, however the issue of spurious pressure oscillations in the upper-left corner of the cavity could not be avoided. Further comparisons between the LW-ACM and other methods are proposed in Table 5.4. Here, coordinates of the primary vortex center (x_p, y_p), coordinates of the lower-right vortex center (x_{lr}, y_{lr}), total kinetic energy E and enstrophy Z are reported for several schemes and grids, where the latter

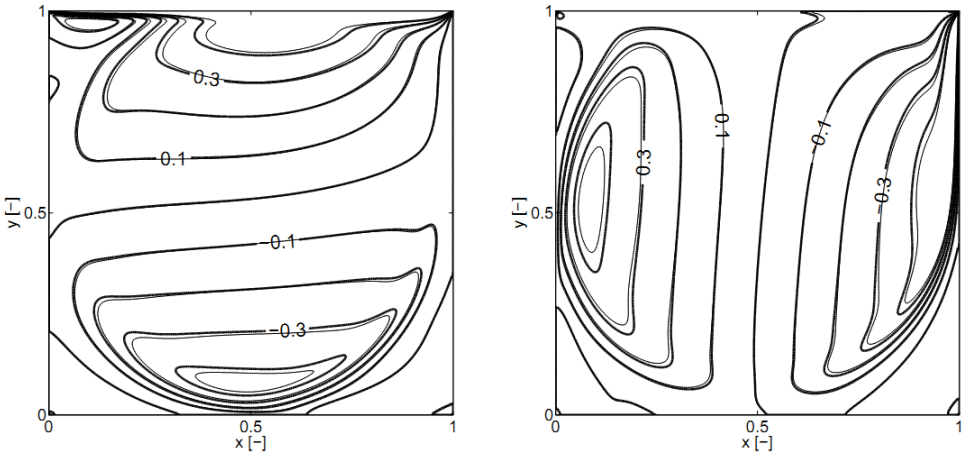

(a) (b)

Figure 5.7: Comparison of the velocity field for the lid driven cavity flow at Re $= 5000$ with 256×256 grids: horizontal component u and vertical component v are reported on the left and right hand side, respectively. Thin and bold lines denote the present LW-ACM (with $\nu_p = \nu$) and ACM solution [81], respectively. The latter method is based on a second order accurate scheme in time, and fourth order accurate scheme in space.

two quantities are computed as follows:

$$\begin{aligned} E &= \frac{1}{2}\int_{\Omega} \|\mathbf{u}\|^2 \, d\Omega \approx \frac{1}{2}\Delta x \Delta y \sum_{i,j} \left(u_{i,j}^2 + v_{i,j}^2\right), \\ Z &= \frac{1}{2}\int_{\Omega} \|\omega\|^2 \, d\Omega \approx \frac{1}{2}\Delta x \Delta y \sum_{i,j} \omega_{i,j}^2, \end{aligned} \tag{5.45}$$

with $\omega = \partial_x v - \partial_y u$, Δx and Δy being the vorticity and the grid spacings respectively. In our study, we notice that one consequence of spurious pressure oscillations in the solution of classical lattice Boltzmann schemes is that both BGK-LBM and MRT-LBM show remarkable inaccuracy in recovering the enstrophy value predicted by the reference [14], whereas the present LW-ACM overcomes the above issue.

Finally, based on Figs. 5.3-5.10, on comparisons of local and global quantities proposed in Table 5.4, we can conclude that LW-ACM represents an excellent alternative in terms of simplicity, stability and accuracy.

Remark-In this study, towards the end of making an extensive comparison among state of the art INSE solvers, simulations are performed by different methods and grids as reported in Table 5.4. Since boundaries may be located

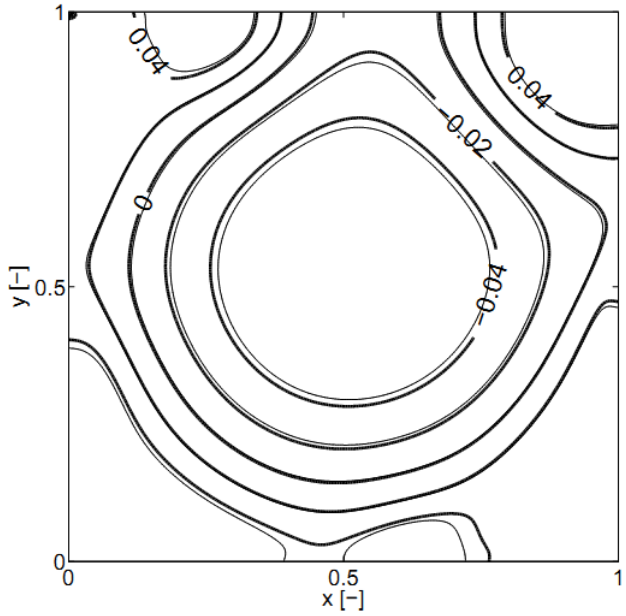

Figure 5.8: Comparison of the pressure field for the lid driven cavity flow at Re = 5000 with 256×256 grids. Thin and bold lines denote the present LW-ACM (with $\nu_p = \nu$) and ACM solution [81], respectively. The latter method is based on a second order accurate scheme in time, and fourth order accurate scheme in space.

differently for different methods (e.g. unlike ACM [81] where boundaries coincide with computational nodes, in LW-ACM boundaries are half cell away from computational nodes), upon convergence, all the fields are first interpolated (by cubic spline interpolation) on a shifted grid (same size as the one used for fluid dynamic computations) having the boundaries located on the computational nodes. The values of global kinetic energy and enstrophy given by Eq. (5.45) are based on the latter shifted grids.

Moreover, if one performs the calculation of streamlines and vortex locations on the basis of the same nodes of the fluid dynamic grid, the final accuracy will depends on both the accuracy of the numerical solution and the grid itself. Hence, results on coarse grids are penalized twice. Therefore, towards the end of computing the coordinates (x_p, y_p) and (x_{lr}, y_{lr}), all the hydrodynamic fields (as computed by the several schemes and different meshes) are first interpolated (by cubic spline interpolation) on a larger mesh, and thereafter the stream function and the vortex locations are computed. The latter post-processing procedure is composed of the following subsequent steps: 1) interpolation of the results on fixed fine grid (1000^2 in Table 5.4); 2) computation of the stream function and its local extrema denoting the vortex centers.

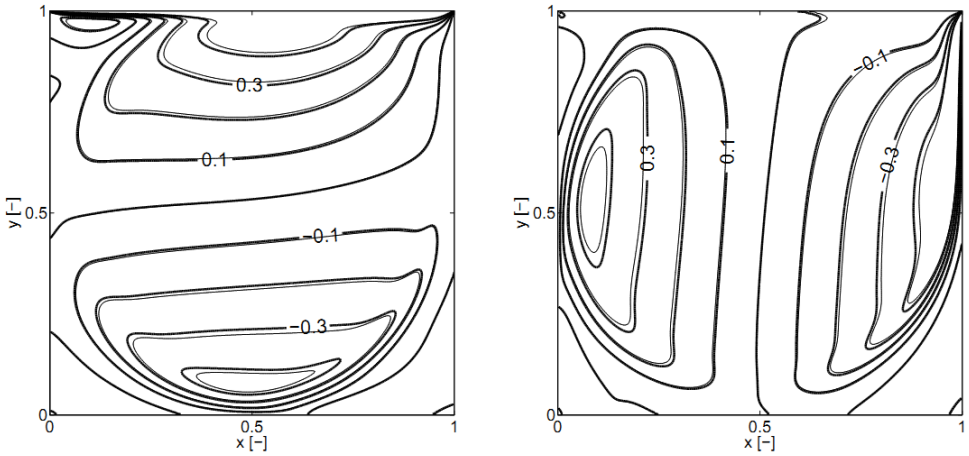

(a) (b)

Figure 5.9: Comparison of the velocity field for the lid driven cavity flow at Re $= 5000$: (a) horizontal component u and (b) vertical component v are reported. Thin and bold lines denote the present LW-ACM (256×256 grid, with $\nu_p = \nu$) and the reference solution [14] (2048×2048 grid), respectively.

3D diagonally driven cavity flow

One of the main advantage of the proposed link-wise formulation of ACM consists in its independence on the space dimensionality (as far as the considered equilibrium satisfies the constraints required by the target equations: see Appendix C for details). As a result, the extension of LW-ACM to three-dimensional flows is straightforward. In the following calculations, the D3Q19 lattice [90] will be used: even though that is not a Hermitian lattice (such as D3Q27), the former lattice allows to satisfy the constraints required by the Navier-Stokes equations (in particular Eq. (C.10)).

Here, we have chosen the three-dimensional (3D) diagonally lid-driven cavity flow, which is a classical benchmark for numerical solvers of the incompressible Navier-Stokes equations (see also [32, 86, 87]). The cavity is a cubic box with unit edge as schematically sketched in Fig. 5.11. The boundary condition at the top plane $(x, y, 1)$ is $\mathbf{u}_L = (\sqrt{2}, \sqrt{2}, 0)/2$ so that $u_L = \|\mathbf{u}_L\| = 1$, whereas the remaining five walls are subject to no-slip boundary conditions. The computational domain is discretized by a uniform collocated grid with N^3 nodes, with boundaries located half-cell away from the computational nodes. Towards the end of making a comparison with data from literature, calculations have been performed by the LW-ACM at two Reynolds numbers studied in [86, 87] and [32] (Re $= 700$, Re $= 2000$), and two grids: $N = 48$ and $N = 60$. Let us denote $\hat{\mathbf{x}}_w$ the generic boundary computational node. In all inner computational nodes ($\hat{\mathbf{x}} \neq \hat{\mathbf{x}}_w$), Eq. (5.18) holds for any lattice

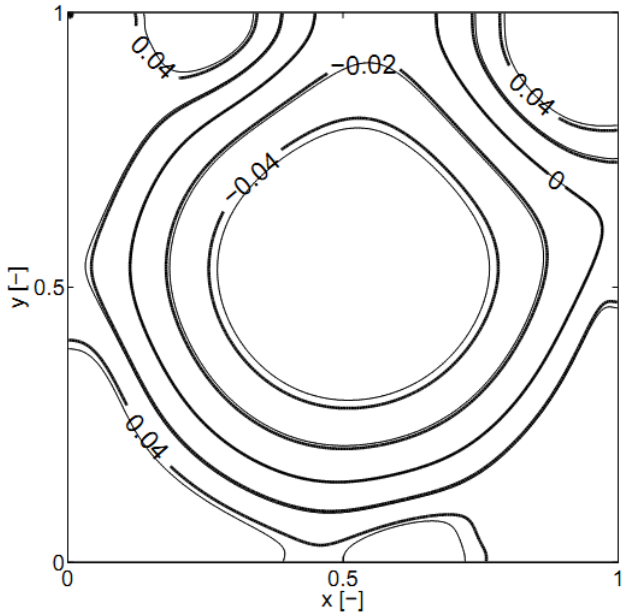

Figure 5.10: Comparison of the pressure field for the lid driven cavity flow at Re $= 5000$. Thin and bold lines denote the present LW-ACM (256×256 grid) and the reference solution [14] (2048×2048 grid), respectively.

velocity $\hat{\mathbf{v}}_i$.

In this test case, numerical stability is significantly affected by boundary conditions. For that reason, in Ref. [32], Authors suggest to use equilibrium-based boundary conditions for the sliding wall at relatively high Reynolds numbers on small computational grids. Nevertheless, as pointed out [32], this implementation imposes an incorrect constant pressure at the boundary, with the momentum transfer significantly weakened in the direction perpendicular to the lid. Moreover, in Ref. [32], the "node" bounce-back boundary conditions are applied to the remaining five walls for imposing no-slip boundary conditions. Although such an approach reduces oscillations caused by the parity invariance and thus enhances the numerical stability, the several simplifications discussed above were necessary to simulate the 3D cavity flow with Re $= 2000$, $D3Q15$ lattice and 52^3 grid.

On the contrary, the present LW-ACM method does not need to resort to the above simplifications any longer. At an arbitrary boundary node $\hat{\mathbf{x}}_w$ Eq. (5.38) holds, with $\mathbf{u}_w$ being the boundary velocity (imposed half-cell away from the boundary computational node $\hat{\mathbf{x}}_w$). This increases the accuracy in treating the boundaries (compared to [32]) and, most importantly, it makes problems in three-dimensions just a straightforward extension of the ones in two-dimensions (see previous section). In Figs. 5.12, 5.13 and 5.14 we report a comparison between the velocity fields (in the MP, CP and PP planes of Fig.

Table 5.4: 2D lid driven cavity flow at Re = 5000: Comparison between the present LW-ACM (with Mach number Ma = 0.2, $\nu = \nu_p$) and alternative solvers for INSE from literature [81, 14, 31]. In artificial compressibility methods (LW-ACM, BGK-LBM, MRT-LBM), even steady state solutions depend on the numerical Mach number: Hence a fair comparison among different methods requires using the same numerical Mach number (Ma = 0.2 in this case). †This is the optimized version of the ACM method proposed in [81] where (a) high wave numbers are damped for the suppression of the checkerboard instability and (b) the Richardson extrapolation in the Mach number (except around top singular corners) is employed. *Owing to both the accuracy of the scheme and the size of meshes adopted, these results are considered as a reference for the present study. However, since enstrophy Z for 2D lid-driven cavity goes to infinity as the grid spacing goes to zero [14], a meaningful comparison for Z is among similar grids.

Scheme	Grid	(x_p, y_p)	(x_{lr}, y_{lr})	Energy	Enstrophy
Present	128×128	$(0.51652, 0.53754)$	$(0.81081, 0.079079)$	0.039845	29.247
[81]	128×128	$(0.52052, 0.53954)$	$(0.82883, 0.071071)$	0.027430	41.249
[81]†	128×128	$(0.51652, 0.53854)$	$(0.80981, 0.072072)$	0.038371	37.704
BGK-LBM	128×128	unstable	unstable	unstable	unstable
MRT-LBM	128×128	$(0.51652, 0.53554)$	$(0.80881, 0.075075)$	0.043600	37.404
[14]*	128×128	$(0.51562, 0.53906)$	$(0.80469, 0.070313)$	0.043566	30.861
Present	256×256	$(0.51552, 0.53554)$	$(0.80581, 0.074074)$	0.044391	34.821
[81]	256×256	$(0.51652, 0.53654)$	$(0.80881, 0.072072)$	0.040896	43.198
[81]†	256×256	$(0.51451, 0.53654)$	$(0.80380, 0.072072)$	0.048114	42.290
BGK-LBM	250×250	$(0.51752, 0.54054)$	$(0.80781, 0.074074)$	0.041614	40.455
MRT-LBM	256×256	$(0.51552, 0.53554)$	$(0.80681, 0.074074)$	0.045222	40.833
[14]*	256×256	$(0.51562, 0.53516)$	$(0.80859, 0.074219)$	0.046204	34.368
[14]*	2048×2048	$(0.51465, 0.53516)$	$(0.80566, 0.073242)$	0.047290	40.261

5.11) by both the commercial code FLUENT (non-uniform 68^3 grid) [86, 87], here considered as a reference, and the present LW-ACM (60^3 uniform grid) at Reynolds Re = 700: All the flow structures are correctly reproduced by LW-ACM. Due to a lack of local quantities in Ref. [86] for Re = 2000, we solved the latter case by the commercial code FLUENT on our own and we included these results as well in the following comparison. It is important to point out (as reported in Ref. [86]) that commercial code FLUENT did not converge with uniform mesh, i.e. without wall mesh refinement. On the other hand, no such problem was found by LW-ACM. Based on a comparison of local quantities in Fig. 5.15 for Re = 700, in Fig. 5.16 for Re = 2000

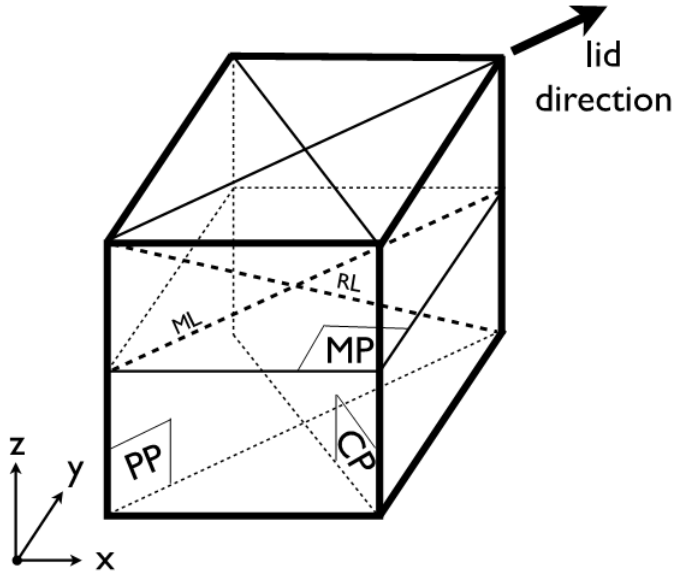

Figure 5.11: Cavity flow with the lid moving along its diagonal. Velocity components along axes x, y and z are denoted u, v and w respectively.

and parallel/perpendicular global momenta $M_{\parallel}$, $M_{\perp}$:

$$\begin{aligned} M_{\parallel} &= \frac{1}{2}\int_V (u+w)^2 dV \approx \frac{1}{2}\Delta x\Delta y\Delta z \sum_{i,j,k} \left(u_{i,j,k}+w_{i,j,k}\right)^2, \\ M_{\perp} &= \frac{1}{2}\int_V (u-w)^2 dV \approx \frac{1}{2}\Delta x\Delta y\Delta z \sum_{i,j,k} \left(u_{i,j,k}-w_{i,j,k}\right)^2 \end{aligned} \tag{5.46}$$

reported in Table 5.5, we can conclude that the present LW-ACM is indeed able to recover the reference solution with significant accuracy.

In Fig. 5.17, results of the 3D lid-driven cavity flow at higher Reynolds number, $\mathrm{Re} = 2000$, are reported. It is worth stressing that, here all the main structures of the flow are correctly described by LW-ACM even with grids coarser than the one adopted in the reference solution [86, 87]. We stress that, describing secondary vortexes in this case is known to be a severe test for numerical schemes (in particular catching top-left and bottom-right secondary vortexes).

For the sake of completeness, we also notice as the Reynolds number increases larger deviations of the LW-ACM solution from the reference are observed in terms of the parallel/perpendicular global momenta $M_{\parallel}$, $M_{\perp}$ (see Table 5.5).

Finally, in Fig. 5.18 the numerical results obtained by both LW-ACM and the MRT-LBM [32] are shown. These two simulations are not perfectly comparable each other. In fact, Authors in Ref. [32] were forced by stability issues

to implement some simplifications when dealing with the boundary conditions (mainly, equilibrium-based boundary conditions for imposing the lid velocity and "node" bounce-back for the no-slip boundary conditions). Those simplifications reduce the accuracy with regards to that recovered by Eq. (5.38).

Other minor difference is that [32] and the present study were obtained by the D3Q15 lattice with 52^3 grid, and D3Q19 lattice with 48^3 grid respectively. We notice that, in this case, MRT-LBM makes use of a larger number of degrees of freedom compared to LW-ACM: $52^3 \times 15 > 48^3 \times 19$. In spite of this, it is quite clear by Fig. 5.18 that the pressure field recovered by the present LW-ACM is remarkably smoother than the one obtained by MRT-LBM. More specifically, a crucial difference is that LW-ACM predicts smooth pressure increase at the top-right corner, while the MRT-LBM results are affected by oscillations around the imposed constant pressure at the top plane.

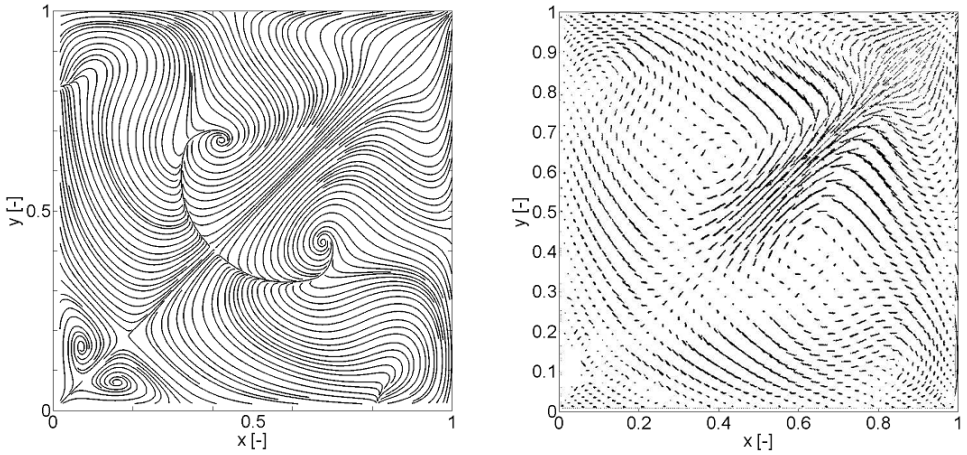

(a) (b)

Figure 5.12: Flow in the middle plane $z = 0.5$ of the 3D diagonally driven cavity (MP plane in Fig. 5.11) at $\mathrm{Re} = 700$. Comparison between the LW-ACM with 60^3 grid (a) and a reference solution [86] obtained by the commercial code FLUENT (b) with 68^3 total number of grid nodes.

Circular Couette flow

Dealing with moving complex boundaries is very important in many applications: for example, particle suspensions, granular flows and active (bio-) agents immersed in the flow. In these cases, the essential issue is to reduce

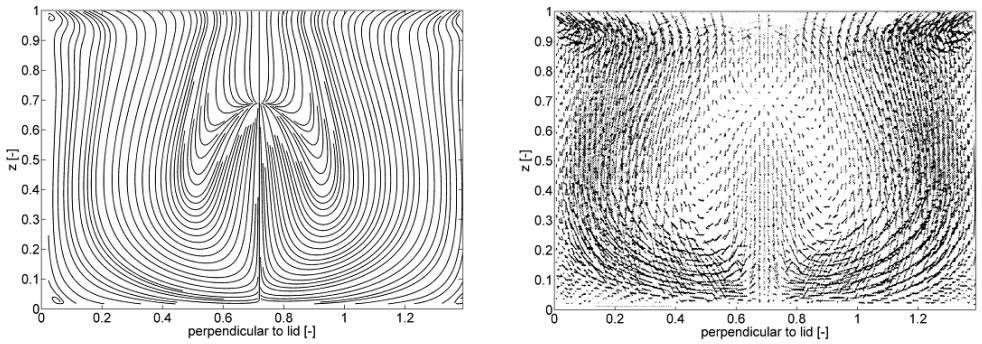

(a) (b)

Figure 5.13: Flow in the plane perpendicular to the direction of the lid (CP plane in Fig. 5.11) at Re $= 700$. Comparison between the LW-ACM with 60^3 Cartesian grid (a) and a reference solution [86] obtained by the commercial code FLUENT (b) with 68^3 total number of grid nodes. At the centerline, a stagnation point is observed at $z = 0.68$ (present), and $z = 0.74$ (FLUENT).

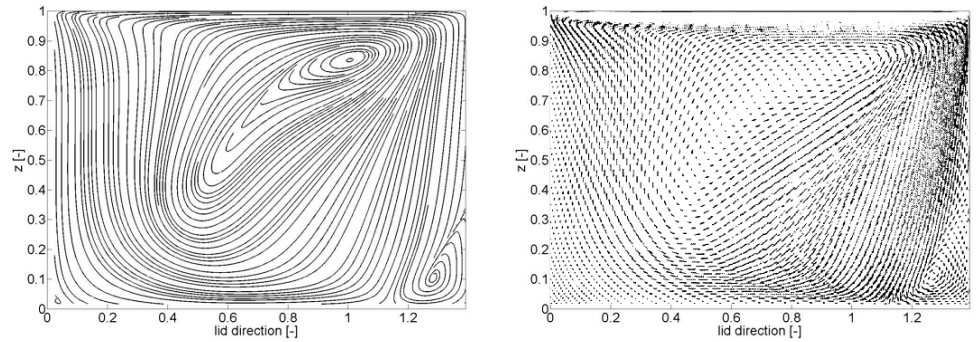

(a) (b)

Figure 5.14: Flow in the plane parallel to the direction of the lid (PP plane in Fig. 5.11) at Re $= 700$. Comparison between the LW-ACM with 60^3 Cartesian grid (a) and a reference solution [86] obtained by the commercial code FLUENT (b) with 68^3 total number of grid nodes.

as much as possible the computational demand by avoiding re-meshing every time that the considered objects move in the flow. Taking into account moving objects is also complicated by the need of re-initializing the portions of the flow field which are filled again by the fluid after the motion of the objects. The latter feature is neglected here, because it is a general issue, not peculiar of the link-wise methods.

First of all, we extend the wall boundary treatment discussed in the previous sections. Let us suppose that $\hat{\mathbf{x}}$ is a fluid node close to a complex wall

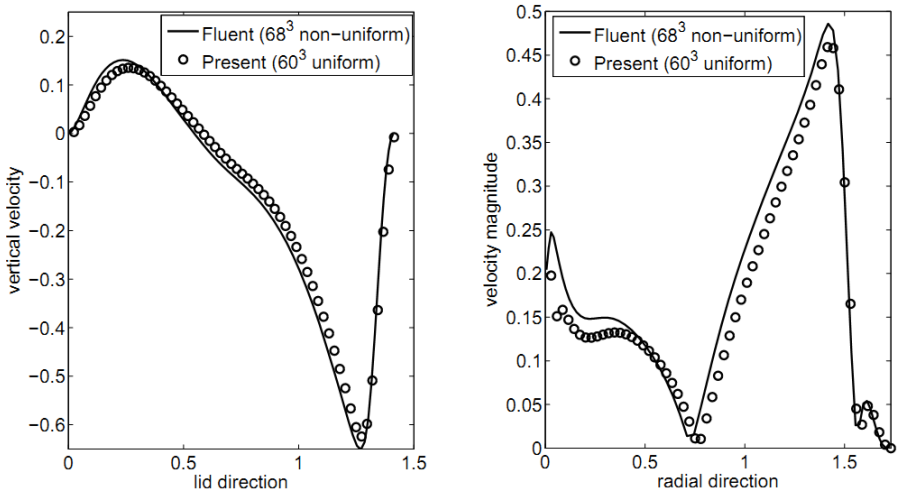

(a) (b)

Figure 5.15: Velocity profile along the line ML (a) and the line RL (b) at Re = 700 (see also Fig. 5.11). Comparison between the present LW-ACM with uniform 60^3 Cartesian grid and a reference solution (consistent with [86]) obtained by the commercial code FLUENT with non-uniform 68^3 total number of grid nodes.

Table 5.5: 3D diagonally driven cavity: Volume integral of momentum flux. Comparisons are carried out between the present LW-ACM method and the reference solution in [86] adopting 60^3 and 68^3 total number of grid nodes, respectively.

	Present, Re = 700	[86, 87], Re = 700	Present, Re = 2000	[86, 87], Re = 2000
$\int_V M_{\parallel}$	0.203×10^{-1}	0.216×10^{-1}	0.134×10^{-1}	0.163×10^{-1}
$\int_V M_{\perp}$	0.232×10^{-2}	0.283×10^{-2}	0.174×10^{-2}	0.239×10^{-2}

boundary at rest such that $\hat{\mathbf{x}} + \hat{\mathbf{v}}_i$ is a wall node. Let us focus on the intersection between the i-th lattice link and the wall. The distance between the latter intersection and the fluid node, divided by the mesh spacing Δx, gives the normalized distance $0 \leq q \leq 1$ (above we considered only the case: $q = 1/2$). In this case, the streaming step can be performed following the same procedure provided for LBM in [12] (instead of using Eq. (5.34)), namely

$$f^{**}_{BB(i)}(\hat{\mathbf{x}}, \hat{t}+1) = \begin{cases} 2q f^{*}_{i}(\hat{\mathbf{x}}, \hat{t}) + (1-2q) f^{*}_{i}(\hat{\mathbf{x}} - \varepsilon\, \hat{\mathbf{v}}_i, \hat{t}), & q < 1/2, \\ \dfrac{1}{2q} f^{*}_{i}(\hat{\mathbf{x}}, \hat{t}) + \left(1 - \dfrac{1}{2q}\right) f^{*}_{BB(i)}(\hat{\mathbf{x}}, \hat{t}), & q \geq 1/2, \end{cases}$$

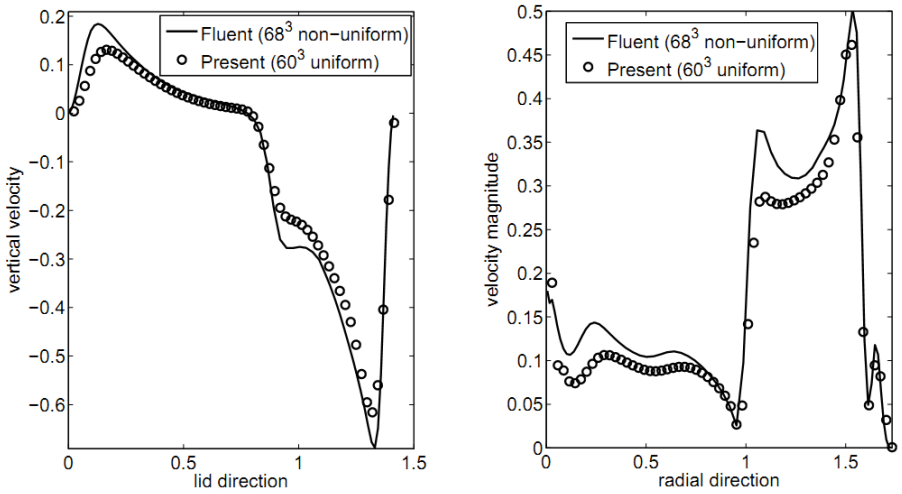

(a) (b)

Figure 5.16: Velocity profile along the line ML (a) and the line RL (b) at Re = 2000 (see also Fig. 5.11). Comparison between the present LW-ACM with uniform 60^3 Cartesian grid and a reference solution obtained by the commercial code FLUENT with non-uniform 68^3 total number of grid nodes.

where $BB(i)$ is the bounce-back operator giving the lattice link opposite to i-th. Finally the post-combining step can be performed in the usual way, namely by means of Eq. (5.34).

In case of moving complex boundary with velocity $\mathbf{u}_w$, the procedure reported in [12] suggests to consider an additional term, namely

$$\delta f_{BB(i)}(\rho_0, \mathbf{u}_w) = \begin{cases} 2f^{(e,o)}_{BB(i)}(\rho_0, \mathbf{u}_w), & q < 1/2, \\ \dfrac{1}{q} f^{(e,o)}_{BB(i)}(\rho_0, \mathbf{u}_w), & q \geq 1/2, \end{cases} \tag{5.47}$$

where $f^{(e,o)}_{BB(i)}$ is given by Eq. (5.7) and ρ_0 is the average value of the density over the whole computational domain (see Appendix C for details). Similarly to what we did in the previous sections, in case of diffusive scaling, the suggested correction for LBM will be multiplied by a scaling factor in link-wise ACM. Hence $f^{w}_{BB(i)}$ given by Eq. (5.38) is the proper boundary condition in case of moving complex boundary. In this section, numerical results are reported for the circular Couette flow, where a viscous fluid is confined in the gap between two concentric rotating cylinders. In our study, we assume the inner cylinder (with radius r_i) at rest while the outer cylinder (with radius r_e) rotates at a constant angular velocity $1/r_e$. The latter flow

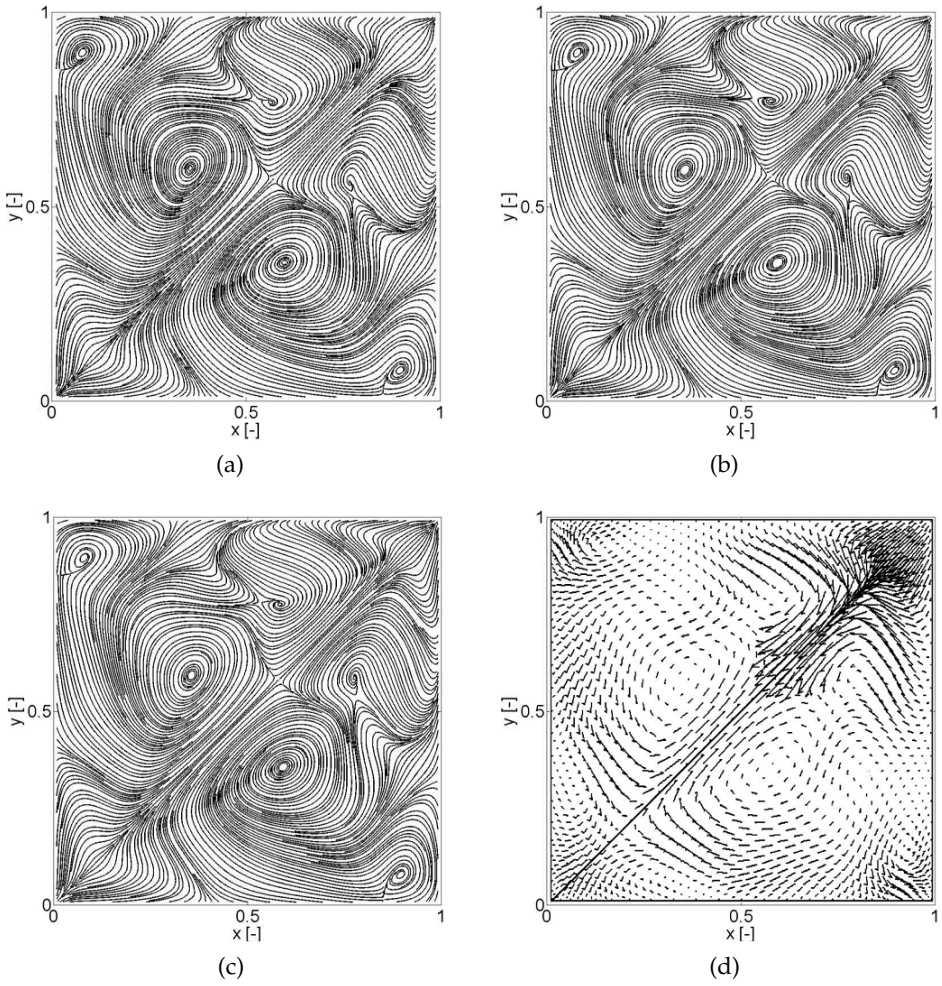

Figure 5.17: Flow in the middle plane $z = 0.5$ of the 3D diagonally driven cavity (MP plane in Fig. 5.11) at $\mathrm{Re} = 2000$. a) LW-ACM with 48^3 uniform grid. b) LW-ACM with 60^3 uniform grid. c) LW-ACM with 68^3 uniform grid. d) Reference solution by the commercial code FLUENT with 68^3 non-uniform grid [87].

admits the following exact solution:

$$\bar{u}(t,r,\theta) = -C\left(\frac{r}{r_i} - \frac{r_i}{r}\right)\sin(\theta), \tag{5.48}$$

$$\bar{v}(t,r,\theta) = C\left(\frac{r}{r_i} - \frac{r_i}{r}\right)\cos(\theta), \tag{5.49}$$

$$\bar{p}(t,r,\theta) = \bar{p}_i + C^2 \ln\left(\frac{r_i^2}{r^2}\right) - \frac{C^2}{2}\left(\frac{r_i^2}{r^2} - \frac{r^2}{r_i^2}\right), \tag{5.50}$$

$$\bar{\mathcal{T}} = 4\pi C\,\nu\, r_i, \tag{5.51}$$

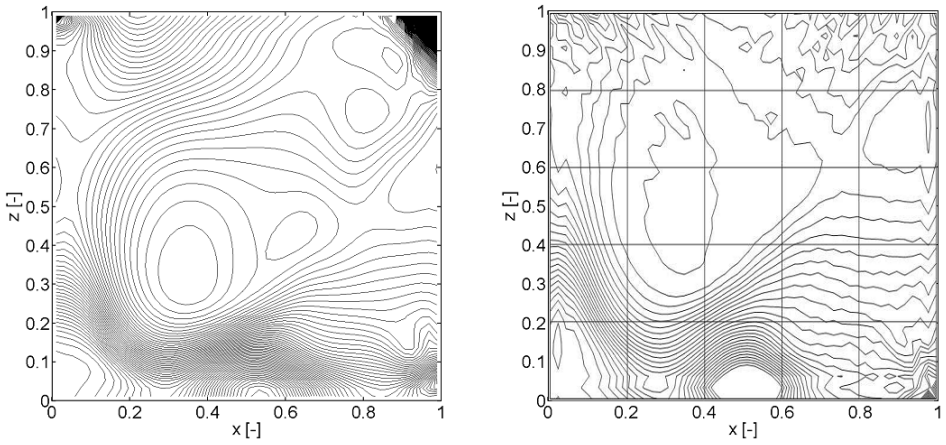

(a) (b)

Figure 5.18: Pressure contours for the diagonally driven cavity flow for Re = 2000 at the lateral mid-plane ($y = 0.5$): Solution obtained by present LW-ACM with 48^3 uniform grid and $D3Q19$ lattice (a), and MRT-LBM method with 52^3 uniform grid and $D3Q15$ lattice [32] (b).

where

$$C = \frac{1}{r_e/r_i - r_i/r_e}. \tag{5.52}$$

Here, $\bar{u}$, $\bar{v}$, $\bar{p}$ and $\bar{\mathcal{T}}$ denote horizontal velocity, vertical velocity, pressure and the torque on the inner cylinder respectively, with θ being the angle between radial direction and the horizontal axis. A schematic representation of this setup is reported in Figure 5.19. Diffusive scaling is considered for this test case, where the velocity field is scaled on meshes with different sizes, keeping fixed the relaxation frequency (see Appendix C for details). The latter scaling ensures second order convergence in the accuracy, as reported in Table 5.6. Moreover, the torque exerted by the fluid on the inner cylinder is computed. To this end, Eq. (5.41) is applied in combination with the boundary conditions provided by (5.47). The computation of $\bar{\mathcal{T}}$ was finally performed by a summation of the contributions (5.41) over all the boundary links around its surface, namely

$$\mathcal{T} = \sum_{i \in \mathsf{S}} (\hat{\mathbf{x}} - \hat{\mathbf{x}}_c) \times \mathbf{p}_i, \tag{5.53}$$

where $\hat{\mathbf{x}}_c$ is the center of the cylinders and S is the set of links starting from all nodes surrounding the body and intersecting the body itself. Similarly to what has been done for scaling the force exerted on a body, the above torque (assumed acting on the whole inner cylinder) must be converted from lattice units to physical units (see Table 2.2 for details). More specifically, the

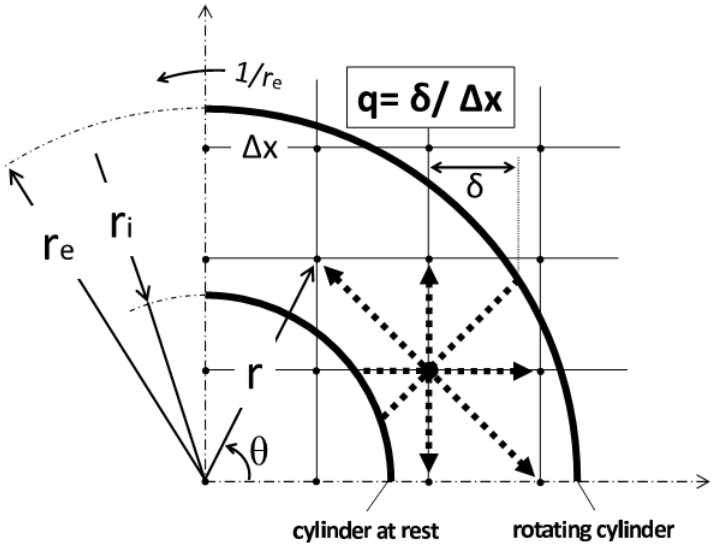

Figure 5.19: Set-up of the circular Couette flow, where one quarter of the domain is reported. For the sake of clarity, a significantly coarse grid is represented.

formula is the following

$$\bar{\mathcal{T}} = \sum_{i \in \mathsf{S}(1/\varepsilon)} (\hat{\mathbf{x}} - \hat{\mathbf{x}}_c) \times \mathbf{p}_i, \tag{5.54}$$

because $|\hat{\mathbf{x}} - \hat{\mathbf{x}}_c| \sim 1/\varepsilon$ and this automatically takes into account the force scaling reported in Eq. (5.43). In Table 5.6, the numerical results for the

circular Couette flow are reported. As expected, the numerical solution in terms of velocity and pressure shows almost second order convergence rate. On the other hand, the modified MEA for link-wise ACM in computing $|\bar{\mathcal{T}}|$ shows first order convergence rate (similarly to the original MEA for LBM). The torque is a global quantity and hence it may hide some error compensation. In order to report a quantitative and detailed assessment of the local stresses, we consider the local wall shear stress on the inner cylinder surface, namely

$$\bar{\tau}_i = \nu \left. \frac{d\bar{w}}{dr} \right|_i = \frac{\bar{\mathcal{T}}}{2\pi r_i^2}, \tag{5.55}$$

where $\bar{w} = \sqrt{\bar{u}^2 + \bar{v}^2}$. In particular, in Figs. 5.20a and 5.20b the pressure and the wall shear stress absolute error are reported respectively, as a function of the intersection angle (in the interval $\theta \in [0, \pi/2]$) between the versor normal to the inner cylinder (radial direction) and the horizontal axis of the Cartesian grid. In both cases, the errors are computed by the absolute value

Table 5.6: The L^1 norm of the error versus $\varepsilon \equiv \Delta x \equiv \mathrm{Ma}$ at $t = 20$ in the problem of the circular Couette flow for $\nu = 0.07$.

Link-wise ACM			
$\varepsilon \equiv \Delta x$	Error $L^1[\bar{u}_\theta]$	Error $L^1[\bar{p}]$	Error $L^1[\lvert\bar{\mathcal{T}}\rvert]$
1/20	1.53627×10^{-3}	8.81208×10^{-4}	4.20562×10^{-4}
1/40	3.50537×10^{-4}	3.58432×10^{-4}	1.98687×10^{-4}
1/80	1.77257×10^{-4}	1.97650×10^{-4}	9.13289×10^{-5}
1/160	3.42570×10^{-5}	6.16474×10^{-5}	3.66160×10^{-5}
MRT-LBM			
$\varepsilon \equiv \Delta x$	Error $L^1[\bar{u}_\theta]$	Error $L^1[\bar{p}]$	Error $L^1[\lvert\bar{\mathcal{T}}\rvert]$
1/20	4.66795×10^{-3}	2.52316×10^{-3}	7.58091×10^{-5}
1/40	1.52864×10^{-3}	8.47929×10^{-4}	1.39351×10^{-4}
1/80	3.08607×10^{-4}	2.99584×10^{-4}	6.98541×10^{-5}
1/160	7.99695×10^{-5}	1.09817×10^{-4}	3.39760×10^{-5}

of the discrepancy between the computed quantities and the analytical solutions. Different meshes are considered, namely $\varepsilon = 1/40$, $1/80$ and $1/160$. The numerical results show that, for both pressure values and wall shear stresses, the LW-ACM produces numerical results which are systematically more accurate than those by LBM, even though the two methods are using the same boundary conditions. On finer meshes, the numerical errors are more scattered due to amplification by the logarithmic scale.

In this section, we reported evidences about the possibility to use boundary conditions, originally formulated for LBM, also in the context of LW-ACM. The drawback is that these boundary conditions are less intuitive than those commonly used in FD and this is particularly strident for LW-ACM, which has a FD formulation indeed. As a concluding remark, it is important to recall that the formulation of the boundary condition is very transparent in the original ACM, e.g. no slip wall velocity and zero pressure gradient normal to the wall. Moreover, by taking into account the curvature correctly (e.g. by finite-volume ACM using body-fitted cell system), the accuracy is dramatically improved. The reason is that, in link-wise ACM and in LBM, the boundary condition for curved wall is based on one dimensional interpolation, but this method is not very accurate for computing stresses (depending on local spatial derivatives). Hence for accurate solving boundary layers, the finite-volume ACM using body-fitted cell system is preferable. However, in the present paper, we used link-wise boundary conditions because they are extremely simple to be generalized in three dimensions and they have potential when dealing with moving complex objects (e.g. particles).

5.2.5 Energy equation

Under the assumption of negligible viscous heating and conservation of internal energy, in the incompressible limit, the temperature field is governed by an advection-diffusion equation. Let us call T the normalized temperature field such that $T \leq 1$ in all the domain of interest, with the quantities $f_i^{(e)}$ defined such that $p = \rho\, T/3$.

There were a number of suggestions aiming at enabling thermal fluid-dynamic simulations with the lattice Boltzmann method [62]. Among the most interesting ones, we remind: (a) Increase of the number of velocities and inclusion of higher-order nonlinear terms (in flow velocity) in the equilibrium distribution functions; (b) inclusion of finite difference corrections aiming at the fulfillment of energy conservation on standard lattices [88] and, (c) use of two sets of distribution functions for particle number density (f_i), and energy density (g_i), doubling the number of discrete velocities. Even though the first and the second approaches are preferable from the theoretical point of view, the last one is characterized by a much simpler implementation. When dealing with the incompressible limit, the pressure field is characterized by small variations. However, cases may be experienced where large temperature and density gradients compensate each other. If both pressure gradients and temperature gradients are small, a weak coupling between fluid dynamic and energy equations is realized and the simplified approach (c) discussed above can be adopted. This approach will be further extended below in the framework of the present LW-ACM. Extensions of the approach (b) in the framework of LW-ACM are currently under investigation as well.

Table 5.7: Convergence analysis for thermal Couette flow in case of diffusive scaling, with Prandtl number $\mathrm{Pr} = 0.71$.

Link-wise ACM					
$\varepsilon \equiv \Delta x$	$\mathrm{Ma} \propto \Delta t/\Delta x$	$\nu \propto \mathrm{Re}^{-1}$	$\alpha \propto \mathrm{Pe}^{-1}$	Error $L^2[\bar{u}]$	Error $L^2[T]$
$1/5$	1.11×10^{-2}	5.55×10^{-2}	1.11×10^{-2}	3.10×10^{-3}	1.61×10^{-6}
$1/10$	5.55×10^{-2}	5.55×10^{-2}	1.11×10^{-2}	8.25×10^{-4}	4.28×10^{-7}
$1/20$	2.78×10^{-3}	5.55×10^{-2}	1.11×10^{-2}	2.12×10^{-4}	1.01×10^{-7}

The LW-ACM approach for (weak) thermal fluid dynamic simulations makes

use of the following system of algebraic equations

$$g_i(\hat{\mathbf{x}}, \hat{t}+1) = g_i^{(e)}(\hat{\mathbf{x}} - \hat{\mathbf{v}}_i, \hat{t}) + 2\left(\frac{\omega_t - 1}{\omega_t}\right)\left(g_i^{(e,e)}(\hat{\mathbf{x}}, \hat{t}) - g_i^{(e,e)}(\hat{\mathbf{x}} - \hat{\mathbf{v}}_i, \hat{t})\right), \tag{5.56}$$

for $i = 0, \ldots, Q_t - 1$ (the number of lattice velocities for solving the thermal field can be different from that used for solving the velocity field, i.e. $Q_t \neq Q$). The quantities $g_i^{(e)}$ are local functions of $T = \sum_i g_i$ and $T\mathbf{u} = \sum_i \hat{\mathbf{v}}_i g_i$ at the same point $\hat{\mathbf{x}}$ and time $\hat{t}$. The quantities $g_i^{(e)}$ are designed in order to recover the advection-diffusion equation, according to the constraints discussed below. In particular, recovering the advection-diffusion equation requires : $\sum_i g_i^{(e)} = T$ and $\sum_i \hat{\mathbf{v}}_i g_i^{(e)} = T\mathbf{u}$, i.e. the conservation of hydrodynamic moments, and $\sum_i \hat{\mathbf{v}}_i \hat{\mathbf{v}}_i g_i^{(e)} = \mathbf{\Pi}_t^{(e)} = \mathbf{u}\mathbf{u} + T/3\,\mathbf{I}$. On the other hand, the even parts of equilibria $g_i^{(e,e)}$ are defined as

$$g_i^{(e,e)}(T, \mathbf{u}) = \frac{1}{2}\left(g_i^{(e)}(T, \mathbf{u}) + g_i^{(e)}(T, -\mathbf{u})\right). \tag{5.57}$$

Here, a few numerical results are reported for the thermal Couette problem, which is realized by confining a viscous fluid in a gap between two parallel plates. Assuming that the one plate (hot wall located at $y = 0$ and with temperature $\bar{T}_N$) moves in its own plane, whereas the other (cold wall located at $y = 2L$ and with temperature $\bar{T}_S$) is at rest, the controlling parameters are the Prandtl number $\mathrm{Pr} = \nu/\alpha$ (measuring the momentum diffusivity: ν, to heat diffusivity: α) and the Eckert number $\mathrm{Ec} = \bar{u}^2/c_v\Delta\bar{T}$ (measuring the kinetic energy: $\rho\bar{u}^2/2$, to internal energy: $\rho c_v \Delta\bar{T}$). Thermal Couette flow admits the following analytical solution of the temperature field:

$$\bar{T}(y) = \bar{T}_S + \frac{y}{2L}\Delta\bar{T} + \frac{\mathrm{Br}\Delta\bar{T}}{2}\frac{y}{2L}\left(1 - \frac{y}{2L}\right), \tag{5.58}$$

with $\Delta\bar{T} = (\bar{T}_N - \bar{T}_S)$, and the Brinkman number $\mathrm{Br} = \mathrm{Pr}\,\mathrm{Ec}$.
Diffusive scaling was considered in our simulations, where the velocity field is scaled on meshes with different sizes, keeping fixed the relaxation frequency (see the Appendix C for details). Some preliminary numerical results are reported in Table 5.7 for $\mathrm{Pr} = \nu/\alpha = 0.71$

5.3 Conclusions

In the present chapter, a novel method for low Mach number fluid dynamic simulations is proposed, taking inspiration from the best features of both the Lattice Boltzmann Method (LBM) and more classical computational fluid dynamic (CFD) techniques such as the Artificial Compressibility Method (ACM). The main advantage is the possibility of exploiting well established

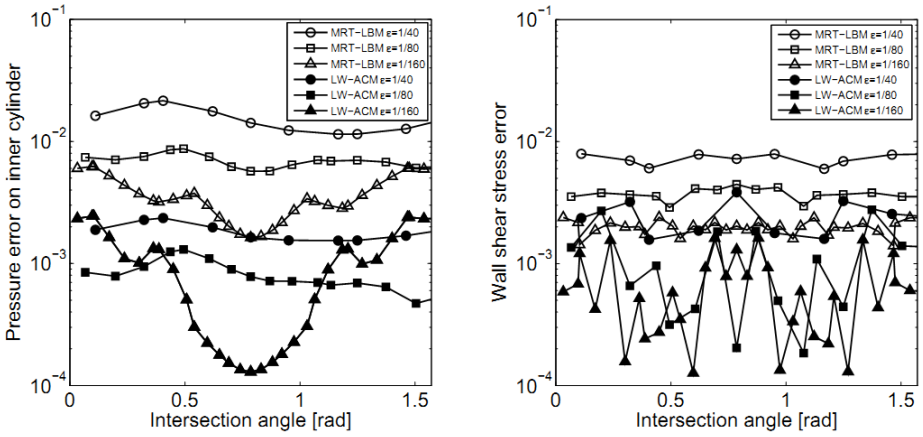

(a) (b)

Figure 5.20: Circular Couette flow: (a) pressure error (absolute value of the discrepancy with respect to the analytical solution) of the pressure solution interpolated on the inner cylinder surface as a function of the intersection angle (in the interval $\theta \in [0, \pi/2]$), between the versor normal to the inner cylinder (radial direction) and the horizontal axis of the Cartesian grid; (b) wall shear stress error (absolute value of the discrepancy with regards to the analytical solution) calculated by means of the local solution gradient on the inner cylinder surface as a function of the intersection angle (in the interval $\theta \in [0, \pi/2]$), between the versor normal to the inner cylinder (radial direction) and the horizontal axis of the Cartesian grid.

technologies originally developed for LBM and classical CFD, with special emphasis on finite differences (at least in the present paper), at the cost of minor changes. For instance, like LBM, it is possible to use simple Cartesian structured meshes, eventually recursively refined in the vicinity of solid walls, and there is no need of solving Poisson equations for pressure. On the other hand, any boundary condition designed for finite difference schemes can be easily included.

As far as solving incompressible Navier-Stokes equations - INSE - (by minimal amount of unknowns) is the only concern, the pseudo-kinetic heritages of LBM represent a severe limitation to several aspects such as designing flexible boundary conditions, introducing tunable forcing terms and analyzing consistency of the numerical scheme (asymptotics). On the contrary, the suggested method has no such pseudo-kinetic heritages. Or in other words, following the standard LBM nomenclature, the present LW-ACM requires no high-order moments beyond hydrodynamics (often referred to as *ghost moments*) and no kinetic expansion such as Chapman-Enskog, Hilbert, van Kampen. Like finite difference schemes, only standard Taylor expansion

is needed for analyzing consistency. Beside the above aspects, numerical evidences reported in this work suggest that LW-ACM represents an excellent alternative in terms of simplicity, stability and accuracy. Hence, in this framework (solving INSE by minimal amount of unknowns), the utility of high-order moments is questionable.

Finally, preliminary efforts towards optimal implementations have shown that LW-ACM is capable of similar computational speed as optimized (BGK-) LBM. In addition, the memory demand is significantly smaller than (BGK-) LBM. In our opinion, there is still room for improvement according to the performance model (based on assuming either infinitely fast memory or infinitely fast compute units). Importantly, with an efficient implementation, this algorithm may be one of the few which is compute-bound and not memory-bound. The latter observation is of particular interest for General-Purpose computing on Graphics Processing Units (GPGPU).

With respect to reactive flows, the formulation of LW-ACM discussed in this chapter corresponds to the model in [110]. It can be used only for combustion at the low Mach number limit, if the flow field is assumed not to be affected by chemical reaction. In other words, continuity and momentum equations are decoupled from the energy and species equations. In this case results agree with the solution of an incompressible macroscopic model, but, clearly, deviations appear if compressibility is taken into account. However, this limitation does not diminish the validity of LW-ACM. It simply represents the starting point for future improvements of the model towards combustion applications.

Chapter 6

Conclusions

> We shall not cease from exploration and the end of all our exploring will be to arrive where we started and know the place for the first time.
>
> *Thomas Stearns Eliot (1888-1965)*

In this thesis, we focus on the formulation and testing of lattice Boltzmann method (LBM) for combustion problems. To this end, new numerical schemes for reactive flows have been elaborated and validated, so to broaden the range of applicability of LBM.

A general LBM scheme for simulating reactive flows at the low Mach number limit has been proposed. A recent model for compressible thermal flows has been extended to this purpose. With respect to combustion applications, major advantages of this model are listed below:

a. Coupling of continuity, momentum and energy equations by means of one distribution function only. This comes with a significant saving in terms of memory storage and computational time;

b. Significant density variation and mass concentration gradient are handled without loss of numerical stability and without loss of accuracy.

Compressibility effects need to be accounted for also in the equations for the chemical species. It turned out that the existing models available in literature are not suitable to accomodate large density variation in the species mass concentrations. This is due to the fact that classical models recover the species equation with a deviation term which stems from the second-order moment and is proportional to the density gradient. In order to remove

it, the equilibrium population of standard LBM is modified by introducing a dimensionless parameter relating the local value of the density field to the minimum one and by redefining the relaxation frequency in the BGK collision term. This extension allows to apply LBM to a wide range of combustion phenomena, which were not properly addressed so far. With this new scheme the incompressible limit is readily available and classical models are recovered. Furthemore, the proposed scheme can be extended also to other models, where an advection-diffusion equation needs to be solved and compressibility effects have to be taken into account (e.g. [105]). For validation purposes, the proposed reactive LBM model has been validated against reference solution in the continuumm limit. The agreement between the solutions has been found to be very satisfactory. Without any lack of generality, we considered a global chemical step with only three reactive species, instead of a detailed mechanism. In fact, simulating reactive flows with detailed chemistry by means of lattice Boltzmann method, poses a challenge due to large number of fields to store in memory (compared to conventional method). Moreover, stiffness restricts one to chose small time step, making the computational time even more demanding. From this point of view, model reduction techniques represent a possible solution, where both stiffness and the number of fields involved in the computations are drastically reduced [23, 24, 25]. Application of such techniques to the present model is under investigation.

Numerical models for combustion simulations require also an adequate treatment of thermal radiation. LBM can be extended to solve radiative problems in an absorbing, emitting and participating medium. In this thesis, improvements to the model proposed by Asinari et al. [9] have been presented. As in [9] the azimuthal angle is discretized according to the lattice velocities on the computational plane. Uniform discretization of the polar angle is achieved by enlarging the set of lattice velocities: an additional component along the normal axis is introduced. The projection of the total discrete velocity still belongs to the original computational lattice. Validation of the model is carried out by solving a 2D benchmark problem. Results are found in good agreement with reference solutions computed by means of standard Finite Volume Method. Extensive error analysis is also reported for different values of the spatial and angular discretizations, and extinction coefficients. The proposed radiative LBM scheme is found to be (at most) first oder accurate, in case of standard lattices, which ensures enough accuray in the advection of radiation information. It also turned out that large subvisions of the polar angle spoils the numerical accuracy, because of a larger (fictitious) mean free path. A *thermalization* procedure seems to improve the accuracy in case of large subdivions of the polar angle. Major feature of radiative LBM is represented by the possibility to make use of the same data structures of the flow solver. Thus, the coupling between ra-

diative and reactive LBM can be done, at a cost of minor changes: scattering can be neglected as long as suspended particles (e.g. soot) are not considered and radiative equilibrium condition no longer holds. In the latter case, the volumetric absorption is not equal to the volumetric emission anymore and it has to be computed as an higher-order moment of the intensity.

Even if it provides a viable solution for simulating reactive flows in LBM, the combustion model presented in this thesis suffers from the same limitations of standard lattice Boltzmann models. Due to the pseudo-kinetic origins, LBM deals with a larger set of unknowns than hydrodynamics. The ghost moments, which are unessential if one is interested only in the continuum limit, can lead to numerical instabilities. Moreover, there is no recipe to optimally design such moments. This limitation also affects the way LBM deals with general boundaries. The desired values of the macroscopic moments needs to be converted in terms of constraints for the distribution function. This implies that also boundary conditions on ghost moments must be provided as well, leading to the development of suitable models also in case of simple boundaries, such as inlet and outlet. Thus, possible improvements would be to remove these limitations and retain the main feature of LBM. For this reason, we proposed a novel method for the simulation of low Mach number fluid-dynamics that can borrow well established techniques from both LBM and classical computational fluid-dynamics (CFD) methods, such the Artificial Compressibility Method (ACM). From the LBM side, all the methodologies developed for complex boundaries are automatically available. For simple geometries, CFD techniques can be used, avoiding any reconstruction of the distribution function on the boundary nodes, like in standard LBM. The kinetic heritage of LBM is removed, or in other words, the LW-ACM does not require *ghost* moments or kinetic expansions like Chapman-Enskog. Several two- and three-dimensional benchmark problems have been solved, for validation purposes. Results are in good agreement with reference solutions. The method is second order accurate (diffusive scaling) as standard LBM models. Due to its simplicity, stability and accuracy, the LW-ACM can be regarded as an attractive alternative to classical CFD tools, as far as incompressible or weak-compressible flows are the main concern. LW-ACM also represents the first step towards the development of models for reactive flows. The present formulation is equivalent to the model in [110]. Since compressibility effects cannot be taken into account, its validity is limited only to incompressible flows. However, it may still be useful for understanding some phenomena occurring in combustion. For instance, with respect to the mesochannel, LW-ACM can be used to examine the dynamics of premixed flame by means of a simplified model, as in [59]. Clearly, in this case only qualitative informations can be extracted by the model. Quantitative results can be obtained only if compressibility effects are properly taken into account. Thus, possible extensions of the pro-

posed method to compressible flows, and hence to reactive flows, will be considered in the near future.

Appendix A

Standard FVM for radiative heat transfer

For the i-th discrete solid angle Ω_i, under the assumption of isotropic scattering and radiative equilibrium, RTE becomes:

$$\frac{dI}{ds} = \mathbf{s}_i \cdot \nabla I_i = \beta \left(S_i - I_i \right), \tag{A.1}$$

where, the radiative source function $S_i = I_b$ and

$$\mathbf{s}_i = \left(\mathbf{s}_i \cdot \mathbf{i} \right) \mathbf{i} + \left(\mathbf{s}_i \cdot \mathbf{j} \right) \mathbf{j} + \left(\mathbf{s}_i \cdot \mathbf{k} \right) \mathbf{k} = \xi_i \mathbf{i} + \eta_i \mathbf{j} + \mu_i \mathbf{k}. \tag{A.2}$$

For a 2-D problem. Eq. (A.1) can be rewritten as:

$$\xi_i \frac{\partial I_i}{\partial x} + \eta_i \frac{\partial I_i}{\partial y} = \beta \left(S_i - I_i \right). \tag{A.3}$$

The finite volume formulation is obtained by integrating Eq. (A.3) over the volume element V. For instance, the term $\partial I_i / \partial x$ becomes:

$$\int_V \frac{\partial I_i}{\partial x} dV = \int_{A_E} I_i dA_E - \int_{A_W} I_i dA_W = I_{E_i} A_E - I_{W_i} A_W, \tag{A.4}$$

where I_{E_i} and I_{W_i} are average value of the discrete intensity I_i over the faces A_E and A_W, respectively (see Fig. A.1). Integrating Eq. (A.3) over the volume element yields:

$$\xi_i \left(A_E I_{E_i} - A_W I_{W_i} \right) + \eta_i \left(A_N I_{N_i} - A_S I_{S_i} \right) = -\beta V I_{P_i} + \beta V S_{P_i}, \tag{A.5}$$

where I_{P_i} and S_{P_i} are volume averages. In Eq. (A.5), cell-edge intensities are related to volume-averaged intensities by means of linear relationship:

$$I_{P_i} = \gamma_y I_{N_i} + \left(1 - \gamma_y \right) I_{S_i} = \gamma_x I_{E_i} + \left(1 - \gamma_x \right) I_{W_i}, \tag{A.6}$$

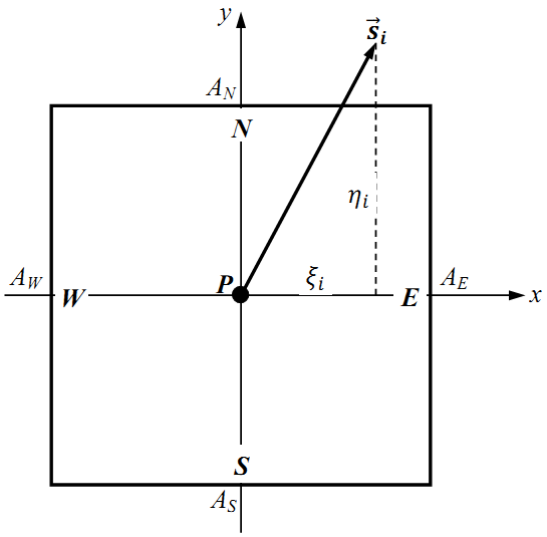

Figure A.1: A general 2D control volume.

where γ_x and γ_y are constants. A common choice is $\gamma_x = \gamma_y = 1/2$, usually known as the *diamond scheme*. In the finite volume formulation, intensities are assumed to be constant over the discrete solid angle Ω_i and integrating Eq. (A.5) over the solid angle, yields:

$$W_x \left(A_E I_{E_i} - A_W I_{W_i}\right) + W_y \left(A_N I_{N_i} - A_S I_{S_i}\right) = W_G \left(-\beta V I_{P_i} + \beta V S_{P_i}\right), \quad \text{(A.7)}$$

where:

$$\begin{aligned} W_x &= \int_{\Omega_i} \eta_i d\Omega_i = \int_{\delta_i - \frac{\Delta\delta_i}{2}}^{\delta_i + \frac{\Delta\delta_i}{2}} \cos\delta d\delta \int_{\gamma_j - \frac{\Delta\gamma_j}{2}}^{\gamma_j + \frac{\Delta\gamma_j}{2}} \sin^2\gamma d\gamma, \\ W_y &= \int_{\Omega_i} \eta_i d\Omega_i = \int_{\delta_i - \frac{\Delta\delta_i}{2}}^{\delta_i + \frac{\Delta\delta_i}{2}} \sin\delta d\delta \int_{\gamma_j - \frac{\Delta\gamma_j}{2}}^{\gamma_j + \frac{\Delta\gamma_j}{2}} \sin^2\gamma d\gamma, \\ W_G &= \frac{1}{4\pi} \int_{\delta_i - \frac{\Delta\delta_i}{2}}^{\delta_i + \frac{\Delta\delta_i}{2}} \int_{\gamma_j - \frac{\Delta\gamma_j}{2}}^{\gamma_j + \frac{\Delta\gamma_j}{2}} \sin\gamma d\delta d\gamma. \end{aligned} \quad \text{(A.8)}$$

In the implementation of the radiative FVM, usually the lower left corner is chosen as the starting point; the south and west walls are part of the boundaries and the intensities coming from these walls are known from the boundary conditions. Combining Eqs. (A.6) and (A.9) and using the diamond scheme, the first quadrant ($\xi_i > 0$ and $\eta_i > 0$) intensity at the center of the control volume P becomes:

$$I_{P_i} = \frac{2\left|W_x\right| I_{W_i} A_W + 2\left|W_y\right| I_{S_i} A_S + W_G \beta S_{P_i} V}{2\left|W_x\right| A_W + 2\left|W_y\right| A_S + W_G \beta V}. \quad \text{(A.9)}$$

Table A.1: Mean temperature of the medium inside the enclosure computed through standard FVM.

		$\beta = 2.0$			$\beta = 5.0$		
		$N_x = 40$	$N_x = 80$	$N_x = 160$	$N_x = 100$	$N_x = 200$	$N_x = 400$
$N_\delta = 8$	$N_\gamma = 1$	0.64448	0.65976	0.66749	0.64674	0.65261	0.65554
	$N_\gamma = 4$	0.64461	0.65989	0.66759	0.64764	0.65349	0.65641
	$N_\gamma = 8$	0.64477	0.66004	0.66775	0.64790	0.65375	0.65667
	$N_\gamma = 16$	0.64483	0.66009	0.66780	0.64799	0.65383	0.65675
$N_\delta = 16$	$N_\gamma = 1$	0.64627	0.66163	0.66938	0.64802	0.65390	0.65684
	$N_\gamma = 4$	0.64638	0.66173	0.66947	0.64893	0.65480	0.65773
	$N_\gamma = 8$	0.64655	0.66190	0.66964	0.64920	0.65507	0.65800
	$N_\gamma = 16$	0.64661	0.66195	0.66969	0.64929	0.65515	0.65808
$N_\delta = 32$	$N_\gamma = 1$	0.64665	0.66207	0.66984	0.64830	0.65420	0.65714
	$N_\gamma = 4$	0.64677	0.66218	0.66993	0.64922	0.65510	0.65804
	$N_\gamma = 8$	0.64693	0.66234	0.97010	0.64949	0.65537	0.65830
	$N_\gamma = 16$	0.64699	0.66239	0.67015	0.64957	0.65545	0.65839

Intensities I_{E_i} and I_{N_i} are then evaluated by applying Eq. (A.6). When all the first-quadrant cell-centered intensities are computed, the same procedure is applied for the other three quadrants, starting from the remaining three corners of the enclosure. For the other three quadrants, Eq. (A.9) is rewritten as follows:

- 2^{nd} quadrant ($\xi_i < 0$ and $\eta_i > 0$):

$$I_{P_i} = \frac{2\left|W_x\right| I_{E_i} A_E + 2\left|W_y\right| I_{S_i} A_S + W_G \beta S_{P_i} V}{2\left|W_x\right| A_E + 2\left|W_y\right| A_S + W_G \beta V}. \tag{A.10}$$

- 3^{rd} quadrant ($\xi_i < 0$ and $\eta_i < 0$):

$$I_{P_i} = \frac{2\left|W_x\right| I_{E_i} A_E + 2\left|W_y\right| I_{N_i} A_N + W_G \beta S_{P_i} V}{2\left|W_x\right| A_E + 2\left|W_y\right| A_N + W_G \beta V}. \tag{A.11}$$

- 4^{th} quadrant ($\xi_i > 0$ and $\eta_i < 0$):

$$I_{P_i} = \frac{2\left|W_x\right| I_{W_i} A_W + 2\left|W_y\right| I_{N_i} A_N + W_G \beta S_{P_i} V}{2\left|W_x\right| A_W + 2\left|W_y\right| A_N + W_G \beta V}. \tag{A.12}$$

The numerical results obtained by means of a standard FVM solver are reported in the following for sake of completeness.

Table A.2: Dimensionless total heat flux along the south wall computed through standard FVM.

		$\beta = 2.0$			$\beta = 5.0$		
		$N_x = 40$	$N_x = 80$	$N_x = 160$	$N_x = 100$	$N_x = 200$	$N_x = 400$
$N_\delta = 8$	$N_\gamma = 1$	0.65157	0.65246	0.65288	0.45370	0.45413	0.45434
	$N_\gamma = 4$	0.65768	0.65855	0.65899	0.46249	0.46293	0.46315
	$N_\gamma = 8$	0.66000	0.66088	0.66131	0.46520	0.46565	0.46587
	$N_\gamma = 16$	0.66075	0.66163	0.66206	0.46605	0.46650	0.46672
$N_\delta = 16$	$N_\gamma = 1$	0.66101	0.66191	0.66236	0.46355	0.46400	0.46421
	$N_\gamma = 4$	0.66695	0.66783	0.66829	0.47236	0.47281	0.47303
	$N_\gamma = 8$	0.66923	0.67012	0.67057	0.47508	0.47553	0.47576
	$N_\gamma = 16$	0.66996	0.67085	0.67131	0.47594	0.47639	0.47662
$N_\delta = 32$	$N_\gamma = 1$	0.66352	0.66437	0.66483	0.46613	0.46654	0.46676
	$N_\gamma = 4$	0.66940	0.67027	0.67072	0.47495	0.47537	0.47560
	$N_\gamma = 8$	0.67168	0.67254	0.67300	0.47767	0.47810	0.47833
	$N_\gamma = 16$	0.67241	0.67238	0.67373	0.47853	0.47896	0.47919

Appendix B

Coupling radiation and combustion

In Chapter 4, the lattice Boltzmann model for radiative heat transfer in an absorbing, emitting and scattering medium is described. However, when taking into account radiation in Eq. (3.2), some preliminary consideration need to be done. Coefficients κ_a and σ_s in Eq. (4.1) depends on the reactive gas mixture. For this participating medium, the atoms, which are the only responsible of scattering, are very small compared with the wavelength and thus, scattering coefficient becomes negligible. This simplifies the radiative transfer equations, since the in-scattering term is no longer taken into account.

The interaction between electromagnetic waves and particles is determined by the relative size of the particles compared with the wavelength of the radiation. In order to quantify this interaction, the size parameter x is defined as:

$$x = \frac{2\pi a}{\lambda} \ll 1, \tag{B.1}$$

where a is the radius of the particle. In our case the particles of the medium are represented by the atoms (molecular gas), whose radius is the order of the Angstrom ($\approx 10^{-10}$m), while the wavelength is the order of 10^{-6}m. Thus, for reactive gas mixtures $x \ll 1$. In the limit of $x \to 0$, Rayleigh scattering theory can be considered and the scattering efficiency factor, to which σ_s is related, can be defined as:

$$Q_{sca} = \frac{8}{3} \left| \frac{m^2 - 1}{m^2 + 2} \right|^2 x^4, \tag{B.2}$$

where $m = n + i\beta$ is the complex index of refraction and n is the refractive index. Since $x \ll 1$ and $x^4 \ll x$, scattering can be neglected as compared with absorption. Thus, Eq.(4.1) reduces to radiative transfer equation in an absorbing and emitting medium:

$$\frac{dI}{ds} = \mathbf{s} \cdot \nabla I = \kappa_a \left(I_b - I \right), \tag{B.3}$$

where the quantity $\kappa_a I_b$ accounts for energy emission and $\kappa_a I$ accounts for energy absorption.

The lattice Boltzmann numerical scheme corresponding to Eq. (B.3) can be derived following the same procedure described in Chapter 4. Hence, the 2D radiative LB scheme in case of absorbing and emitting participating medium reads:

$$\frac{I_{ij}\left(\mathbf{x}+\mathbf{v}_i\Delta t, t+\Delta t\right) - I_{ij}\left(\mathbf{x}, t\right)}{\Delta t} = \frac{1}{\tau_{ij}}\left[I_b\left(\mathbf{x}, t\right) - I_{ij}\left(\mathbf{x}, t\right)\right], \tag{B.4}$$

where the relaxation time $\tau_{ij} = 1/\left(\kappa_a \mathrm{V}_{ij}\right)$. The equilibrium distribution function concur with the blackbody intensity I_b and hence is function of the temperature only.

Eq.(B.4) has to be solved in order to compute the radiative heat flux $\mathbf{q}_{rad}$ in Eq. (3.2):

$$\mathbf{q}_{rad} = \nabla \cdot \mathbf{q}_R = \kappa_a\left(4\pi I_b - G\right), \tag{B.5}$$

where G is the incident radiation and is computed as an higher order moment of the intensity:

$$G = \int_{\Omega=0}^{4\pi} I\left(\mathbf{x}, \delta, \gamma\right)\, d\Omega = \int_{\delta=0}^{2\pi}\int_{\gamma=0}^{\pi} I\left(\mathbf{x}, \delta, \gamma\right)\, \sin\gamma\, d\delta d\gamma. \tag{B.6}$$

Applying quadrature schemes as in Chapter 4, the incident radiation is then evaluated as follows:

$$G \approx \sum_{i=1}^{N_\delta}\sum_{j=1}^{N_\gamma}\left[I_{ij}\int_{\delta_i-\frac{\Delta\delta_i}{2}}^{\delta_i+\frac{\Delta\delta_i}{2}}\int_{\gamma_j-\frac{\Delta\gamma_j}{2}}^{\gamma_j+\frac{\Delta\gamma_j}{2}} \sin\gamma\, d\delta d\gamma\right] = \sum_{i=1}^{N_\delta}\sum_{j=1}^{N_\gamma} W_{ij} I_{ij}, \tag{B.7}$$

In order to evaluate the intensity from Eq.(B.4) and the divergence of the radiative heat flux from Eq.(B.5), the absorption coefficient of the gas mixture has to be defined. Due to its spectral variation, evaluation of the radiative absorption coefficient may turn out to be complicated. Models such as the Narrow Band Models (the Elsasser Model and the Statistical Model) or the Wide Band Models (the Box Model and the Exponential Wide Band Model) have the merit to describe very rigorously absorption of molecular gases, but their main drawback is that they may result much more time consuming than the solution of RTE itself. In practical engineering problems, less sophisticated and time demanding models are usually sufficient to evaluate the absorption coefficient of the medium. A reasonable choice could be to use mean absorption coefficients and to incorptorate them in the numerical scheme for the solution of Eq.(4.1). The most important is the Planck mean absorption coefficient, which describes the total emission from a medium,

and accurately describes radiative heat loss from optically thin gas. It is defined as:

$$\kappa_P = \frac{\int_0^\infty I_{b\lambda}\kappa_\lambda \, d\lambda}{\int_0^\infty I_{b\lambda} \, d\lambda} = \frac{\pi}{\sigma T^4} \int_0^\infty I_{b\lambda}\kappa_\lambda \, d\lambda, \tag{B.8}$$

where $I_{b\lambda}$ and κ_λ are the blackbody intesity and the absorption coefficient at wavenumber λ, respectively. Eq.(B.8) defines a pressure absorption coefficient κ_P as the mean value of the spectral absorption coefficient κ_λ over the whole range of wavelenths. Neverthless, the pressure absorption coefficient strongly varies over the wavelenghts range and there exist windows in the spectrum where the medium does not absorb. Eq.(B.8) actually does not account for non-absorbing window regions.

The absorption coefficient κ_{ak} dependes on the temperature of the mixture and on the concentration of the k-th chemical species as:

$$\kappa_{ak} = \kappa_P p_{tot} Y_k, \tag{B.9}$$

where p_{tot} and Y_k are the total pressure of the mixture and the mass concentration of the k-th species, respectively.

Values of the Planck mean absorption coefficient are available for several molecular gases from Tien [104]. These values have been obtained by integrating exponential wide band data across the spectrum, based on correlations of low resolution experiments. The accuracy of experimental wide band parameters is known to be rather poor and, therefore, the validity of the Planck mean absorption coefficient as given by Tien has been questioned in recent years. As an alternative the Planck mean absorption coefficient can also be obtained from high resolution databases, such as HITRAN96 [93] and HITEMP [92]. The HITRAN and HITEMP databases provide spectral line information for different radiating gases. Since absorption coefficient are additive, the Planck mean absorption coefficient consists of individual contributions from all spectral lines , or

$$\kappa_P = \frac{\pi}{\sigma T^4} \sum_i \int_0^\infty \kappa_{i\lambda} I_{b\lambda} d\lambda, \tag{B.10}$$

where the sum is over all the spectral lines and $\kappa_{i\lambda}$ is the absorption coefficient contributed by the i-th spectral line centered at λ_i. Since the Palnck functions varies a little across each spectral line, Eq. (B.10) may be restated as

$$\kappa_P = \frac{\pi}{\sigma T^4} \sum_i I_{b\lambda i} \int_0^\infty \kappa_{i\lambda} d\lambda = \sum_i \frac{\pi}{\sigma T^4} I_{b\lambda i} S_i, \tag{B.11}$$

where S_i is the line-integrated absorption coefficient or line strength, defines as $S_i = \int_0^\infty \kappa_{i\lambda} d\lambda$. Thus, the Planck mean absorption coefficient is the Planck function weighted sum of the line strenghts of all spectral lines, which are

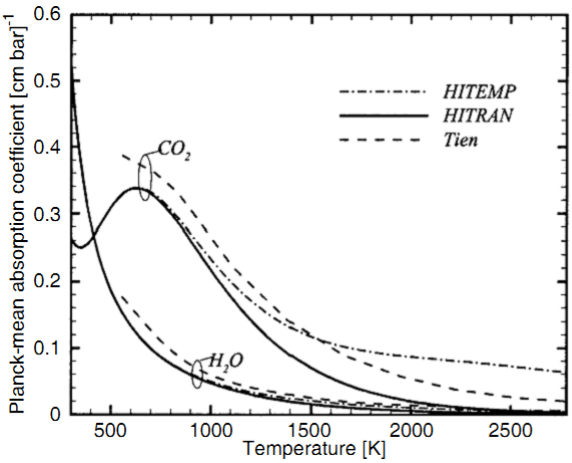

(a)

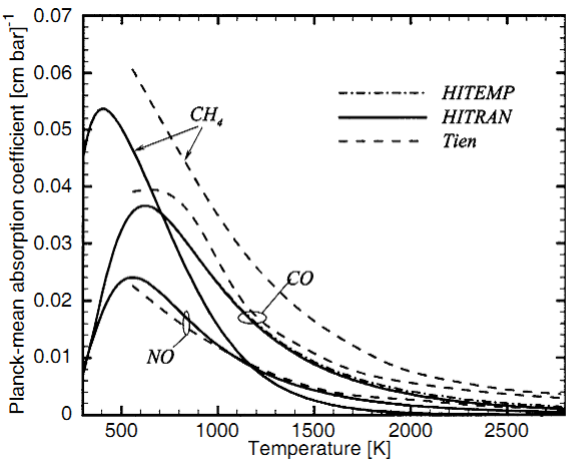

(b)

Figure B.1: Planck mean absorption coefficient for CO_2 and H_2O (a) and CH_4, CO and NO (b) [48]

listed in the HITRAN and HITEMP databases. Planck mean absorption coefficient for some chemical species are reported in Figs B.1. It is worth to stress out that Planck-means absorption coefficient is appropriate if the medium is optically thin. Optical thickness may change along a given path and for this reason the Rosseland-mean absorption coefficient has been defined for an optically thick medium. Rosseland-mean absorption coefficient is defined as:

$$\frac{1}{\kappa_R} = \int_0^\infty \frac{1}{\kappa_\lambda}\frac{dI_{b\lambda}}{dT}\,d\lambda \Bigg/ \int_0^\infty \frac{dI_{b\lambda}}{dT}\,d\lambda = \frac{\pi}{4\sigma T^3}\int_0^\infty \frac{1}{\kappa_\lambda}\frac{dI_{b\lambda}}{dT}\,d\lambda. \tag{B.12}$$

Several authors attempted to evaluate Rosseland-mean absorption coefficient, but results are regarded as very dubiuos.

Appendix C

LW-ACM: Asympthotic analysis of Link-wise Artificial Compressibity Method

In (5.18), with $\hat{\mathbf{x}} = \mathbf{x}/\Delta x$ and $\hat{t} = t/\Delta t$, both Δt and Δx must approach zero, though it is not clear the value of the limit: $\lim_{\Delta x \to 0} \Delta t/\Delta x$. In order to clarify this point, we apply Taylor expansion to (5.18)

$$\begin{aligned} f_i(t+\Delta t) \quad &= f_i^{(e)} - \Delta x\, \hat{\mathbf{v}}_i \cdot \nabla f_i^{(e)} + \frac{\Delta x^2}{2}(\hat{\mathbf{v}}_i \cdot \nabla)^2 f_i^{(e)} - \frac{\Delta x^3}{6}(\hat{\mathbf{v}}_i \cdot \nabla)^3 f_i^{(e)} + \dots \\ &+ \left(2 - \frac{2}{\omega}\right)\left(\Delta x\, \hat{\mathbf{v}}_i \cdot \nabla f_i^{(e,o)} - \frac{\Delta x^2}{2}(\hat{\mathbf{v}}_i \cdot \nabla)^2 f_i^{(e,o)} + \frac{\Delta x^3}{6}(\hat{\mathbf{v}}_i \cdot \nabla)^3 f_i^{(e,o)}\right) + \dots, \end{aligned} \tag{C.1}$$

where all the quantities are computed in the same point $\mathbf{x}$ and hence this is no more explicitly reported. A summation of Eqs. (C.1) over i yields:

$$\begin{aligned} \frac{\partial \rho}{\partial t} + \left(\frac{2}{\omega} - 1\right)\frac{\Delta x}{\Delta t}\nabla \cdot (\rho \mathbf{u}) \quad + \quad & \frac{1}{6}\left(\frac{2}{\omega} - 1\right)\frac{\Delta x^3}{\Delta t}(\nabla\cdot)^3 \mathsf{Q}^{(e)} = \\ & \frac{\Delta x^2}{2\,\Delta t}(\nabla\cdot)^2 \mathbf{\Pi}^{(e)} + O\left(\frac{\Delta x^4}{\Delta t}(\nabla\cdot)^2 \mathbf{\Pi}^{(e)}\right) \end{aligned} \tag{C.2}$$

with $\mathsf{Q}^{(e)} = \sum_i \hat{\mathbf{v}}_i \hat{\mathbf{v}}_i \hat{\mathbf{v}}_i f_i^{(e)}$. In the rightmost term of the above expression (C.2), we rely upon the fact that spatial derivatives of the fourth-order moments have the same growth rate of spatial derivatives of the second-order moments. Moreover, the diverge is raised to a power which is selected for consistency with the units of other terms. This is unessential, as far as the order of magnitude of the term is concerned. Multiplying (C.1) by $\hat{\mathbf{v}}_i$ and summing over i, it yields

$$\frac{\partial(\rho \mathbf{u})}{\partial t} + \frac{\Delta x}{\Delta t}\nabla \cdot \mathbf{\Pi}^{(e)} = \frac{\Delta x^2}{\Delta t}\left(\frac{1}{\omega} - \frac{1}{2}\right)(\nabla\cdot)^2 \mathsf{Q}^{(e)} + O\left(\frac{\Delta x^3}{\Delta t}\nabla \cdot \mathbf{\Pi}^{(e)}\right). \tag{C.3}$$

Similar considerations as Eq. (C.2) apply to the rightmost term in the above equation (C.3). Concerning the relationship between Δt and Δx, (C.3) suggests two possible strategies:

$$\Delta t \propto \Delta x, \qquad \text{acoustic scaling,} \tag{C.4a}$$

$$\Delta t \propto \Delta x^2, \qquad \text{diffusive scaling.} \tag{C.4b}$$

Sometimes, the dimensionless mesh spacing $\Delta x = \Delta x'/L$ is referred to as spacing ($\Delta x \equiv h$) in the literature on finite difference method or even numerical Knudsen number ($\Delta x \equiv \mathrm{Kn}$) in the Lattice Boltzmann literature. Similarly, it is possible to introduce a numerical Mach number: $\mathrm{Ma} = U/(\Delta x'/\Delta t')$. In this way, the dimensionless time step $\Delta t = \Delta t'/(L/U)$ can be expressed as $\Delta t \equiv \mathrm{Kn}\,\mathrm{Ma}$. Hence, the acoustic scaling corresponds to constant Ma, while the diffusive scaling to $\mathrm{Ma} \propto \Delta x$. Regardless of the adopted strategy, the numerical scheme must converge towards the physical solution of the incompressible Navier-Stokes equations. The physical solution is identified by the Reynolds number, which is the reciprocal of the factor multiplying the second-order spatial derivatives in Eq. (C.3), namely

$$\frac{\Delta x^2}{\Delta t}\left(\frac{1}{\omega} - \frac{1}{2}\right) \propto \frac{1}{\mathrm{Re}}. \tag{C.5}$$

Hence, according to (C.5), in acoustic scaling ω needs to be tuned in order to guarantee a constant Reynolds number, while in diffusive scaling a fixed ω already ensures a constant Reynolds number. Moreover, in acoustic scaling, the smaller Δx the smaller ω for keeping fixed the Reynolds number. The latter case can be problematic in the present LW-ACM due to the heuristic stability domain, $1 \leq \omega < 2$, thus diffusive scaling is generally preferable.

Similarly to standard LBM, in LW-ACM, the definition of Δt and Δx is implicit (and this is sometimes a source of confusion). In fact, the end-user can select both $\mathrm{Kn} \propto 1/N$ (with N the number of mesh points along the flow characteristic length) and Ma by a scaling factor for the velocity field. Hence, the acoustic scaling requires the tuning of the relaxation frequency ω on different meshes, keeping constant the computed velocity field. On the other hand, the diffusive scaling corresponds to a scaling of the velocity field (see also the section below) on different meshes, keeping fixed the relaxation frequency.

C.1 Diffusive scaling

Substituting $\Delta x = \varepsilon \ll 1$ and $\Delta t = \varepsilon^2$ into (C.3), it yields

$$\frac{\partial(\rho \mathbf{u})}{\partial t} + \frac{1}{\varepsilon}\nabla \cdot \mathbf{\Pi}^{(e)} = \left(\frac{1}{\omega} - \frac{1}{2}\right)(\nabla\cdot)^2 \mathrm{Q}^{(e)} + O\left(\varepsilon \nabla \cdot \mathbf{\Pi}^{(e)}\right). \tag{C.6}$$

Due to the presence of a mesh-dependent parameter in (C.6), upon convergence, all moments need to be scaled via the following post-process:

$$\bar{\mathbf{u}} = (\mathbf{u} - \mathbf{u}_0)/\varepsilon, \qquad \bar{\mathbf{\Pi}}^{(e)} = (\mathbf{\Pi}^{(e)} - \mathbf{\Pi}_0)/\varepsilon^2, \qquad \bar{\mathrm{Q}}^{(e)} = (\mathrm{Q}^{(e)} - \mathbf{Q}_0)/\varepsilon, \tag{C.7}$$

where $\mathbf{u}_0$, $\mathbf{\Pi}_0$ and $\mathbf{Q}_0$ are constants, with the odd quantities $\mathbf{u}_0$ and $\mathbf{Q}_0$ equal to zero. On the contrary, the even quantity $\mathbf{\Pi}_0 = p_0\mathbf{I}$, where p_0 is the average pressure over the whole computational domain (the average even moment $\mathbf{\Pi}^{(e)}$ over the whole computational domain depends mainly on the amount of mass and only slightly on the flow field).

As a result, the normalized pressure field is defined as $\bar{p} = (p - p_0)/\varepsilon^2$ and the normalized density field as $\bar{\rho} = (\rho - \rho_0)/\varepsilon^2$ or equivalently $\rho = \rho_0 + \varepsilon^2\,\bar{\rho}$. Upon substitution of the latter quantities into (C.2), it follows

$$\nabla \cdot \bar{\mathbf{u}} = O(\varepsilon^2). \tag{C.8}$$

Recalling that $\mathbf{\Pi}^{(e)} = \rho\mathbf{u}\mathbf{u} + p\,\mathbf{I}$ and introducing the scaled quantities, we obtain

$$\rho_0 \frac{\partial \bar{\mathbf{u}}}{\partial t} + \rho_0 \bar{\mathbf{u}} \cdot \nabla \bar{\mathbf{u}} + \nabla \bar{p} = \left(\frac{1}{\omega} - \frac{1}{2}\right) (\nabla\cdot)^2 \bar{\mathrm{Q}}^{(e)} + O(\varepsilon^2). \tag{C.9}$$

In order to recover the incompressible isothermal fluid dynamics, the quantities $f_i^{(e)}$ are designed [90] such that

$$Q_{ijk}^{(e)} = \frac{\rho}{3}\left(u_i\delta_{jk} + u_j\delta_{ik} + u_k\delta_{ij}\right). \tag{C.10}$$

Consequently

$$\nabla \cdot \nabla \cdot \bar{\mathrm{Q}}^{(e)} = \frac{\rho_0}{3}\nabla^2\bar{\mathbf{u}} + \frac{2\,\rho_0}{3}\nabla\,\nabla\cdot\bar{\mathbf{u}} + O(\varepsilon^2) = \frac{\rho_0}{3}\nabla^2\bar{\mathbf{u}} + O(\varepsilon^2), \tag{C.11}$$

where the last result is due to Eq. (C.8). Introducing the previous assumption in Eq. (C.9), it yields

$$\boxed{\frac{\partial \bar{\mathbf{u}}}{\partial t} + \bar{\mathbf{u}} \cdot \nabla \bar{\mathbf{u}} + \frac{1}{\rho_0}\nabla \bar{p} = \nu\nabla^2\bar{\mathbf{u}} + O(\varepsilon^2)}. \tag{C.12}$$

where

$$\nu = \frac{1}{3}\left(\frac{1}{\omega} - \frac{1}{2}\right). \tag{C.13}$$

Introducing the previous expression into Eq. (C.2), it yields

$$\frac{\varepsilon^2}{\rho_0}\frac{\partial \bar{\rho}}{\partial t} + 6\nu\nabla\cdot\bar{\mathbf{u}} = \frac{\varepsilon^2}{2}\nabla\cdot\left(\bar{\mathbf{u}}\cdot\nabla\bar{\mathbf{u}} + \frac{1}{\rho_0}\nabla\bar{p}\right) + O(\varepsilon^4). \tag{C.14}$$

Taking into account the new definition given by (C.13), Eq. (C.8) should be expressed more rigorously as $\nabla \cdot \bar{\mathbf{u}} = O(\varepsilon^2/\nu)$. Combining the latter equation and Eq. (C.12), it follows

$$\nabla \cdot \left(\bar{\mathbf{u}} \cdot \nabla \bar{\mathbf{u}} + \frac{1}{\rho_0} \nabla \bar{p} \right) = O(\varepsilon^2/\nu). \tag{C.15}$$

Introducing the above expression into Eq. (C.14), it yields

$$\boxed{\frac{\varepsilon^2}{6\rho_0 \nu} \frac{\partial \bar{\rho}}{\partial t} + \nabla \cdot \bar{\mathbf{u}} = O(\varepsilon^4/\nu^2)}. \tag{C.16}$$

The divergence-free condition for the velocity field requires that $\varepsilon^2/\nu \ll 1$, which is consistent with (C.12) as well.

C.2 Acoustic scaling

Assuming $\Delta x = \varepsilon \ll 1$ and $\Delta t = \varepsilon$, Eq. (C.3) yields

$$\frac{\partial(\rho \mathbf{u})}{\partial t} + \nabla \cdot \mathbf{\Pi}^{(e)} = \varepsilon \left(\frac{1}{\omega} - \frac{1}{2} \right) (\nabla \cdot)^2 \mathbf{Q}^{(e)} + O(\varepsilon^2). \tag{C.17}$$

This time, there is no need to scale all the moments and a proper tuning of ω is sufficient instead (see below). Leaving the moments unscaled and substituting the above assumptions in Eq. (C.2), we obtain

$$\frac{\partial \rho}{\partial t} + \left(\frac{2}{\omega} - 1 \right) \nabla \cdot (\rho \mathbf{u}) = O(\varepsilon). \tag{C.18}$$

The above equation (C.18) proves that acoustic scaling should not be used in link-wise ACM, when dealing with transient simulations, while for steady state flows we get:

$$\nabla \cdot (\rho \mathbf{u}) = O(\varepsilon/\nu), \tag{C.19}$$

showing that, if the density (pressure) gradients are small (consistently with the incompressible limit), the above equation provides indeed an accurate divergence-free velocity field. However, in acoustic (unlike diffusive scaling) the compressibility error cannot be reduced by mesh refinement. Taking into account Eq. (C.10) and Eq. (C.19), we get

$$\nabla \cdot \nabla \cdot \mathbf{Q}^{(e)} = \frac{1}{3} \nabla^2 (\rho \mathbf{u}) + O(\varepsilon/\nu), \tag{C.20}$$

hence

$$\frac{\partial(\rho \mathbf{u})}{\partial t} + \nabla \cdot (\rho \mathbf{u}\mathbf{u}) + \nabla p = \bar{\nu} \nabla^2 (\rho \mathbf{u}) + O(\varepsilon), \tag{C.21}$$

where $\bar{\nu} = \varepsilon\,\nu$. If the density (and pressure) gradients are small, the solution to the system formed by (C.19) and (C.21) provides a reasonable approximation of the Navier-Stokes solution in the incompressible limit. However, the latter system does not asymptotically converge towards the incompressible Navier-Stokes solution, as the mesh get finer and finer (at least, as far as the discretization error is smaller than the compressibility error). This is the main reason why the diffusive scaling is preferred in this work.

C.3 Forcing

Let us consider the forcing step described by Eq. (5.20), with $\Delta x = \varepsilon \ll 1$, $\Delta t = \varepsilon^{\beta+1}$ (or equivalently $\mathrm{Ma} = \mathrm{Kn}^{\beta}$) where β is a free parameter ($\beta = 0$ and $\beta = 1$ denote acoustic and diffusive scaling, respectively). The correction due to (5.20) leads to an additional term in (C.3):

$$\frac{\partial(\rho\mathbf{u})}{\partial t} + \frac{\Delta x}{\Delta t}\,\nabla\cdot\boldsymbol{\Pi}^{(e)} = \frac{\Delta x^2}{\Delta t}\left(\frac{1}{\omega} - \frac{1}{2}\right)(\nabla\cdot)^2\mathrm{Q}^{(e)} + O\left(\frac{\Delta x^3}{\Delta t}\nabla\cdot\boldsymbol{\Pi}^{(e)}\right) + \frac{1}{\Delta t}\,\rho\mathbf{g}. \tag{C.22}$$

From the definition $\Delta t \equiv \mathrm{Kn}\,\mathrm{Ma}$ and $\mathbf{u} = \mathrm{Ma}\,\bar{\mathbf{u}}$ (see the previous section), the proper scaling for the forcing term follows:

$$\bar{\mathbf{g}} = \frac{1}{\mathrm{Kn}\,\mathrm{Ma}^2}\,\mathbf{g} = \frac{1}{\varepsilon^{2\beta+1}}\,\mathbf{g}. \tag{C.23}$$

A certain physical acceleration $\bar{\mathbf{g}}$ (fixed for a given problem), can be imposed in the numerical code through the mesh-dependent acceleration $\mathbf{g} = \varepsilon^{2\beta+1}\,\bar{\mathbf{g}}$.

C.4 Energy equation

Eq. (5.56) is formulated in terms of $\hat{\mathbf{x}} = \mathbf{x}/\Delta x$ and $\hat{t} = t/\Delta t$. In the following, let us consider the diffusive scaling, namely $\Delta x = \varepsilon \ll 1$ and $\Delta t = \varepsilon^2$. Taylor expansion of Eq. (5.56) yields

$$\begin{aligned} g_i(t+\varepsilon^2) \;=\; & g_i^{(e)} - \varepsilon\,\hat{\mathbf{v}}_i\cdot\nabla g_i^{(e)} + \frac{\varepsilon^2}{2}(\hat{\mathbf{v}}_i\cdot\nabla)^2 g_i^{(e)} \\ & + \left(2 - \frac{2}{\omega_t}\right)\left(\varepsilon\,\hat{\mathbf{v}}_i\cdot\nabla g_i^{(e,e)} - \frac{\varepsilon^2}{2}(\hat{\mathbf{v}}_i\cdot\nabla)^2 g_i^{(e,e)}\right) + \ldots \end{aligned} \tag{C.24}$$

where all the quantities are computed in the same point $\mathbf{x}$ and time t and hence this is no more explicitly reported. Summation over i of the equations (C.24) yields

$$\frac{\partial T}{\partial t} + \frac{1}{\varepsilon}\,\nabla\cdot(T\mathbf{u}) + \frac{\varepsilon}{6}\,(\nabla\cdot)^3\mathbf{Q}_t^{(e)} = \left(\frac{1}{\omega_t} - \frac{1}{2}\right)(\nabla\cdot)^2\boldsymbol{\Pi}_t^{(e)} + O\left(\varepsilon^2(\nabla\cdot)^2\boldsymbol{\Pi}_t^{(e)}\right), \tag{C.25}$$

with $\mathbf{Q}_t^{(e)} = \sum_i \hat{\mathbf{v}}_i \hat{\mathbf{v}}_i \hat{\mathbf{v}}_i g_i^{(e)}$. In the rightmost term of the expression (C.25), we rely upon the fact that spatial derivatives of the fourth-order moments have the same growth rate of spatial derivatives of the second-order moments. Moreover, in the same term, the diverge is raised to a power which is selected for consistency with the units of other terms. This is unessential, as far as the order of magnitude of the term is concerned.

Similarly to the fluid dynamic equations (see the Appendix C), we apply the following post-processing for scaling all moments (arbitrary constants have been already omitted):

$$\bar{\mathbf{u}} = \mathbf{u}/\varepsilon, \qquad \bar{\mathbf{\Pi}}_t^{(e)} = \mathbf{\Pi}_t^{(e)}, \qquad \bar{\mathrm{Q}}_t^{(e)} = \mathrm{Q}_t^{(e)}/\varepsilon. \tag{C.26}$$

One possibility for automatic implementation of the latter scaling is to assume

$$(\bar{\mathrm{Q}}_t^{(e)})_{ijk} = \frac{1}{3}\left(\bar{u}_i\delta_{jk} + \bar{u}_j\delta_{ik} + \bar{u}_k\delta_{ij}\right), \tag{C.27}$$

similarly to Eq. (C.10), because thus all terms in $\mathrm{Q}_t^{(e)}$ become proportional to the velocity field (and they are automatically scaled by means of the first of the above scalings).

Moreover, taking into account the second scaling and the definition of $\mathbf{\Pi}_t^{(e)}$ reported in the main text, we conclude that $\bar{\mathbf{\Pi}}_t^{(e)} = \varepsilon^2 \bar{\mathbf{u}}\bar{\mathbf{u}} + T/3\,\mathbf{I}$, where T does not need to be scaled (or equivalently $\bar{T} = T$). Substituting the previous scalings into (C.24), and taking into account (C.8), we obtain

$$\boxed{\frac{\partial \bar{T}}{\partial t} + \bar{\mathbf{u}} \cdot \nabla \bar{T} = \alpha \nabla^2 \bar{T} + O(\varepsilon^2)}, \tag{C.28}$$

where

$$\alpha = \frac{1}{3}\left(\frac{1}{\omega_t} - \frac{1}{2}\right). \tag{C.29}$$

Appendix D

LW-ACM: Computing derivatives locally

LW-ACM allows a straightforward local computation of spatial derivatives. In this respect, a good example is provided by the following strategy for tuning bulk viscosity. Since the LW-ACM (like LBM and ACM) is an artificial compressibility scheme, bulk viscosity can be regarded as a free parameter (if the incompressible limit is the only concern).

One possible strategy for tuning the bulk viscosity is described below. Instead of standard $f_i^{(e)}$ (see Eq. (5.2)) in Eq. (5.18), we consider a modified set of functions, namely $f_i^{(e*)}$, defined as

$$f_i^{(e*)} = f_i^{(qe)} \left(\rho, \mathbf{u}, \mathrm{Tr}^{(e)} + \gamma \left(\mathrm{Tr}^{(+)} - \mathrm{Tr}^{(e)} \right) \right), \tag{D.1}$$

where $f^{(qe)}\left(\rho, \mathbf{u}, \mathrm{Tr}\right)$ is given by Eq. (5.5), γ is a free parameter, $\mathrm{Tr}^{(e)}$ is the trace of the tensor $\mathbf{\Pi}^{(e)}$ normalized by the density and $\mathrm{Tr}^{(+)}$ is the trace of the tensor $\mathbf{\Pi}^{(+)} = \sum_i \hat{\mathbf{v}}_i \hat{\mathbf{v}}_i f_i(t + \Delta t)$ normalized again by the density. Let us consider the two dimensional case ($D = 2$): by definition, $\mathrm{Tr}^{(e)} = 2/3 + \mathbf{u}^2$. Substituting the latter into Eq. (D.1) and taking into account the definition of $f_i^{(qe)}$ given by Eq. (5.5), it is possible to compute the second order tensor of $f_i^{(e*)}$, namely

$$\mathbf{\Pi}^{(e*)} = \mathbf{\Pi}^{(e)} + \frac{\gamma}{2} \left(\mathrm{Tr}^{(+)} - \mathrm{Tr}^{(e)} \right) \mathbf{I}. \tag{D.2}$$

At the leading order, the modified equilibrium differs from the standard one only due to even moments.

In order to simplify the last term of the Eq. (D.2), by Eqs. (C.1), we compute the following quantities

$$\mathbf{\Pi}^{(+)} = \mathbf{\Pi}^{(e)} - 6\nu \, \Delta x \, \nabla \cdot \mathbb{Q}^{(e)} + O\left(\Delta x^2 (\nabla \cdot)^2 \mathbf{\Pi}^{(e)} \right), \tag{D.3}$$

where $\mathbf{\Pi}^{(+)} = \sum_i \hat{\mathbf{v}}_i \hat{\mathbf{v}}_i f_i(t + \Delta t)$. Recalling the definition in (C.10), it yields

$$\mathbf{\Pi}^{(+)} = \mathbf{\Pi}^{(e)} - 2\nu\,\Delta x\,\left(\nabla(\rho\mathbf{u}) + \nabla(\rho\mathbf{u})^T + \nabla\cdot(\rho\mathbf{u})\,\mathbf{I}\right) + O\left(\Delta x^2(\nabla\cdot)^2\mathbf{\Pi}^{(e)}\right). \tag{D.4}$$

with its trace taking the form:

$$\mathrm{Tr}^{(+)} = \mathrm{Tr}^{(e)} - 8\nu\,\Delta x\,\nabla\cdot(\rho\mathbf{u}) + O\left(\Delta x^2(\nabla\cdot)^2\mathbf{\Pi}^{(e)}\right). \tag{D.5}$$

Considering the diffusive scaling, namely $\Delta x = \varepsilon \ll 1$ and $\Delta t = \varepsilon^2$ (see Appendix C for further details about the diffusive scaling), the previous expression can be recast as:

$$\bar{\mathrm{Tr}}^{(+)} = \bar{\mathrm{Tr}}^{(e)} - 8\rho_0\nu\,\nabla\cdot\bar{\mathbf{u}} + O(\varepsilon^2). \tag{D.6}$$

Introducing the previous expression into Eq. (D.2) and applying the scaling to the remaining terms, it reads:

$$\bar{\mathbf{\Pi}}^{(e*)} = \bar{\mathbf{\Pi}}^{(e)} - 4\rho_0\nu\,\gamma\,\nabla\cdot\bar{\mathbf{u}}\,\mathbf{I} + O(\varepsilon^2). \tag{D.7}$$

Substituting $\bar{\mathbf{\Pi}}^{(e*)}$ instead of $\bar{\mathbf{\Pi}}^{(e)}$ into Eq. (C.9) and taking into account Eq. (C.11), it yields

$$\rho_0\frac{\partial\bar{\mathbf{u}}}{\partial t} + \rho_0\bar{\mathbf{u}}\cdot\nabla\bar{\mathbf{u}} + \nabla\bar{p} = \nu\,\nabla^2\bar{\mathbf{u}} + \xi\,\nabla\,\nabla\cdot\bar{\mathbf{u}} + O(\varepsilon^2), \tag{D.8}$$

where $\xi = 2\rho_0\nu\,(1 + 2\,\gamma)$ is related to the bulk viscosity. The previous equation is consistent with Eq. (C.12), because the gradient of the divergence of the velocity field is as large as the leading error (hence it is not spoiling the consistency). However, the range $\gamma \geq 0$ is usually beneficial to numerical stability. This strategy enables to increase the bulk viscosity by using the updated distribution function for computing locally all required derivatives (involved in the divergence of the velocity field).

Appendix E

LW-ACM: Equivalent finite-difference formulas

Here, we provide some finite-difference formulas fully equivalent to Eq. (5.18) for a chosen lattice. Let us consider the popular D2Q9 lattice [90] for two dimensional problems ($D = 2$), and consisting of nine discrete velocities ($Q = 9$). The quantities $f_i^{(e)}$ can be explicitly defined for this lattice [90]. They allow to recover the incompressible Euler equations (with $p = \rho/3$), and they are consistent with the property given by (C.11), which is essential for recovering Navier-Stokes equations. The numerical algorithm is fully defined, upon substitution of $f_i^{(e)}$ into the Eq. (5.18).

According to the finite-difference literature, we define the generic computational stencil by means of cardinal directions. The generic point P with a position vector $\hat{\mathbf{x}} = (n, m)^T$ (the superscript T denotes transposition) is identified by a pair of integers n and m. By means of the subscripts E and W, we denote the neighboring points $(n \pm 1, m)^T$, respectively. Similarly, by means of the subscripts N and S, we mean the neighboring points $(n, m \pm 1)^T$, respectively. Two types of subscripts may be used concurrently for identifying the diagonal points.

Concerning time levels, if not otherwise stated, all quantities are intended as computed at the generic time level $\hat{t}$, with the superscript "$+$" meaning a quantity at the new time level $\hat{t} + 1$. The unknown quantities are given by the velocity components $\mathbf{u} = (u, v)^T$ and the pressure p (the density for this model is given by $\rho = 3\,p$). Hence the equivalent finite-difference formulas must provide a way to compute u_P^+, v_P^+ and p_P^+.

Applying the definitions of hydrodynamic quantities to Eq. (5.18), it follows:

$$\begin{aligned} p_P^+ u_P^+ &= p_E(-6u_E^2 + 6u_E + 3v_E^2 - 2)/18 + p_W(6u_W^2 + 6u_W - 3v_W^2 + 2)/18 \\ &\quad - p_{NE}(3u_{NE}^2 + 9u_{NE}v_{NE} - 3u_{NE} + 3v_{NE}^2 - 3v_{NE} + 1)/36 \\ &\quad + p_{NW}(3u_{NW}^2 - 9u_{NW}v_{NW} + 3u_{NW} + 3v_{NW}^2 - 3v_{NW} + 1)/36 \\ &\quad - p_{SE}(3u_{SE}^2 - 9u_{SE}v_{SE} - 3u_{SE} + 3v_{SE}^2 + 3v_{SE} + 1)/36 \\ &\quad + p_{SW}(3u_{SW}^2 + 9u_{SW}v_{SW} + 3u_{SW} + 3v_{SW}^2 + 3v_{SW} + 1)/36 \\ &\quad + 2/3(1/\omega - 1)\,[p_E u_E - 3p_P u_P + p_W u_W \\ &\quad + (p_{NE}u_{NE} + p_{NW}u_{NW} + p_{SE}u_{SE} + p_{SW}u_{SW})/4 \\ &\quad + (p_{NE}v_{NE} - p_{NW}v_{NW} - p_{SE}v_{SE} + p_{SW}v_{SW})/4]\,, \end{aligned} \tag{E.1}$$

$$\begin{aligned} p_P^+ v_P^+ &= p_N(3u_N^2 - 6v_N^2 + 6v_N - 2)/18 + p_S(-3u_S^2 + 6v_S^2 + 6v_S + 2)/18 \\ &\quad - p_{NE}(3u_{NE}^2 + 9u_{NE}v_{NE} - 3u_{NE} + 3v_{NE}^2 - 3v_{NE} + 1)/36 \\ &\quad - p_{NW}(3u_{NW}^2 - 9u_{NW}v_{NW} + 3u_{NW} + 3v_{NW}^2 - 3v_{NW} + 1)/36 \\ &\quad + p_{SE}(3u_{SE}^2 - 9u_{SE}v_{SE} - 3u_{SE} + 3v_{SE}^2 + 3v_{SE} + 1)/36 \\ &\quad + p_{SW}(3u_{SW}^2 + 9u_{SW}v_{SW} + 3u_{SW} + 3v_{SW}^2 + 3v_{SW} + 1)/36 \\ &\quad 2/3(1/\omega - 1)\,[p_N v_N - 3p_P v_P + p_S v_S \\ &\quad + (p_{NE}u_{NE} - p_{NW}u_{NW} - p_{SE}u_{SE} + p_{SW}u_{SW})/4 \\ &\quad + (p_{NE}v_{NE} + p_{NW}v_{NW} + p_{SE}v_{SE} + p_{SW}v_{SW})/4]\,. \end{aligned} \tag{E.2}$$

$$\begin{aligned} p_P^+ &= -2p_P(3u_P^2 + 3v_P^2 - 2)/9 \\ &\quad - p_E(-6u_E^2 + 6u_E + 3v_E^2 - 2)/18 + p_W(6u_W^2 + 6u_W - 3v_W^2 + 2)/18 \\ &\quad - p_N(3u_N^2 - 6v_N^2 + 6v_N - 2)/18 + p_S(-3u_S^2 + 6v_S^2 + 6v_S + 2)/18 \\ &\quad + p_{NE}(3u_{NE}^2 + 9u_{NE}v_{NE} - 3u_{NE} + 3v_{NE}^2 - 3v_{NE} + 1)/36 \\ &\quad + p_{NW}(3u_{NW}^2 - 9u_{NW}v_{NW} + 3u_{NW} + 3v_{NW}^2 - 3v_{NW} + 1)/36 \\ &\quad + p_{SE}(3u_{SE}^2 - 9u_{SE}v_{SE} - 3u_{SE} + 3v_{SE}^2 + 3v_{SE} + 1)/36 \\ &\quad + p_{SW}(3u_{SW}^2 + 9u_{SW}v_{SW} + 3u_{SW} + 3v_{SW}^2 + 3v_{SW} + 1)/36 \\ &\quad + 2/3(1/\omega - 1)\,[-p_E u_E + p_S v_S + p_W u_W - p_N v_N \\ &\quad + (p_{SW}u_{SW} + p_{NW}u_{NW} - p_{NE}u_{NE} - p_{SE}u_{SE})/4 \\ &\quad + (p_{SW}v_{SW} - p_{NW}v_{NW} - p_{NE}v_{NE} + p_{SE}v_{SE})/4]\,, \end{aligned} \tag{E.3}$$

It is important to stress that the above expressions (E.1), (E.2), (E.3) for the considered lattice model are fully equivalent to (5.18) up to machine precision, since no asymptotic analysis is requested in their derivation.

From a computational perspective, optimal implementation requires that the number of floating point operations are reduced as much as possible by common subexpression elimination (CSE) [43]. Moreover, for locating the macroscopic quantities (p, u, v) contiguously in the memory, it is possible to

collect them in a single array and to use the first index for addressing them, namely $\mathsf{M}(1:3, 1:\mathsf{N_x}, 1:\mathsf{N_y})$ where $\mathsf{N_x} \times \mathsf{N_y}$ is the generic mesh. This leads to an optimized FD-style implementation. First of all, let us compute the following auxiliary quantities

$$
\begin{aligned}
pu_P &= \mathsf{M}(1,\mathsf{i},\mathsf{j})\,\mathsf{M}(2,\mathsf{i},\mathsf{j}), \qquad \varphi u_P = 2\,pu_P,\\
pv_P &= \mathsf{M}(1,\mathsf{i},\mathsf{j})\,\mathsf{M}(3,\mathsf{i},\mathsf{j}), \qquad \varphi v_P = 2\,pv_P,\\
pv_N &= \mathsf{M}(1,\mathsf{i},\mathsf{j}+1)\,\mathsf{M}(3,\mathsf{i},\mathsf{j}+1), \qquad pv_S = \mathsf{M}(1,\mathsf{i},\mathsf{j}-1)\,\mathsf{M}(3,\mathsf{i},\mathsf{j}-1),\\
pu_E &= \mathsf{M}(1,\mathsf{i}+1,\mathsf{j})\,\mathsf{M}(2,\mathsf{i}+1,\mathsf{j}), \qquad pu_W = \mathsf{M}(1,\mathsf{i}-1,\mathsf{j})\,\mathsf{M}(2,\mathsf{i}-1,\mathsf{j}),\\
pu_{NE} &= \mathsf{M}(1,\mathsf{i}+1,\mathsf{j}+1)\,\mathsf{M}(2,\mathsf{i}+1,\mathsf{j}+1),\\
pu_{NW} &= \mathsf{M}(1,\mathsf{i}-1,\mathsf{j}+1)\,\mathsf{M}(2,\mathsf{i}-1,\mathsf{j}+1),\\
pu_{SE} &= \mathsf{M}(1,\mathsf{i}+1,\mathsf{j}-1)\,\mathsf{M}(2,\mathsf{i}+1,\mathsf{j}-1),\\
pu_{SW} &= \mathsf{M}(1,\mathsf{i}-1,\mathsf{j}-1)\,\mathsf{M}(2,\mathsf{i}-1,\mathsf{j}-1),\\
pv_{NE} &= \mathsf{M}(1,\mathsf{i}+1,\mathsf{j}+1)\,\mathsf{M}(3,\mathsf{i}+1,\mathsf{j}+1),\\
pv_{NW} &= \mathsf{M}(1,\mathsf{i}-1,\mathsf{j}+1)\,\mathsf{M}(3,\mathsf{i}-1,\mathsf{j}+1),\\
pv_{SE} &= \mathsf{M}(1,\mathsf{i}+1,\mathsf{j}-1)\,\mathsf{M}(3,\mathsf{i}+1,\mathsf{j}-1),\\
pv_{SW} &= \mathsf{M}(1,\mathsf{i}-1,\mathsf{j}-1)\,\mathsf{M}(3,\mathsf{i}-1,\mathsf{j}-1),
\end{aligned}
\tag{E.4}
$$

and

$$
\begin{aligned}
\varphi_1 &= pu_E\,(-\mathsf{M}(2,\mathsf{i}+1,\mathsf{j})+1) + \mathsf{M}(1,\mathsf{i}+1,\mathsf{j})\,(\mathsf{M}(3,\mathsf{i}+1,\mathsf{j})^2/2 - r_{13}),\\
\varphi_2 &= pu_W\,(\mathsf{M}(2,\mathsf{i}-1,\mathsf{j})+1) - \mathsf{M}(1,\mathsf{i}-1,\mathsf{j})\,(\mathsf{M}(3,\mathsf{i}-1,\mathsf{j})^2/2 - r_{13}),\\
\varphi_3 &= pv_N\,(-\mathsf{M}(3,\mathsf{i},\mathsf{j}+1)+1) + \mathsf{M}(1,\mathsf{i},\mathsf{j}+1)\,(\mathsf{M}(2,\mathsf{i},\mathsf{j}+1)^2/2 - r_{13}),\\
\varphi_4 &= pv_S\,(\mathsf{M}(3,\mathsf{i},\mathsf{j}-1)+1) - \mathsf{M}(1,\mathsf{i},\mathsf{j}-1)\,(\mathsf{M}(2,\mathsf{i},\mathsf{j}-1)^2/2 - r_{13}),\\
\varphi_5 &= pu_{NE}\,(\mathsf{M}(2,\mathsf{i}+1,\mathsf{j}+1) + 3\,\mathsf{M}(3,\mathsf{i}+1,\mathsf{j}+1) - 1) + \ldots\\
&\quad \cdots + pv_{NE}\,(\mathsf{M}(3,\mathsf{i}+1,\mathsf{j}+1) - 1) + \mathsf{M}(1,\mathsf{i}+1,\mathsf{j}+1)\,r_{13},\\
\varphi_6 &= pu_{NW}\,(\mathsf{M}(2,\mathsf{i}-1,\mathsf{j}+1) - 3\,\mathsf{M}(3,\mathsf{i}-1,\mathsf{j}+1) + 1) + \ldots\\
&\quad \cdots + pv_{NW}\,(\mathsf{M}(3,\mathsf{i}-1,\mathsf{j}+1) - 1) + \mathsf{M}(1,\mathsf{i}-1,\mathsf{j}+1)\,r_{13},\\
\varphi_7 &= pu_{SE}\,(\mathsf{M}(2,\mathsf{i}+1,\mathsf{j}-1) - 3\,\mathsf{M}(3,\mathsf{i}+1,\mathsf{j}-1) - 1) + \ldots\\
&\quad \cdots + pv_{SE}\,(\mathsf{M}(3,\mathsf{i}+1,\mathsf{j}-1) + 1) + \mathsf{M}(1,\mathsf{i}+1,\mathsf{j}-1)\,r_{13},\\
\varphi_8 &= pu_{SW}\,(\mathsf{M}(2,\mathsf{i}-1,\mathsf{j}-1) + 3\,\mathsf{M}(3,\mathsf{i}-1,\mathsf{j}-1) + 1) + \ldots\\
&\quad \cdots + pv_{SW}\,(\mathsf{M}(3,\mathsf{i}-1,\mathsf{j}-1) + 1) + \mathsf{M}(1,\mathsf{i}-1,\mathsf{j}-1)\,r_{13},
\end{aligned}
\tag{E.5}
$$

where $r_{13} = 1/3$. By means of the quantities (E.4) and (E.5), it is possible to

compute the following additional quantities

$$\begin{aligned}
\varphi_{Pp} &= pu_P + pv_P, & \varphi_{Pm} &= pu_P - pv_P,\\
\varphi_{NEp} &= pu_{NE} + pv_{NE}, & \varphi_{SWp} &= pu_{SW} + pv_{SW},\\
\varphi_{NWm} &= pu_{NW} - pv_{NW}, & \varphi_{SEm} &= pu_{SE} - pv_{SE},\\
\Phi_{NE} &= \varphi_{NEp} - \varphi_{Pp}, & \Phi_{SW} &= \varphi_{Pp} - \varphi_{SWp},\\
\Phi_{NW} &= \varphi_{NWm} - \varphi_{Pm}, & \Phi_{SE} &= \varphi_{Pm} - \varphi_{SEm},\\
\Phi_{NWSE} &= \Phi_{NW} - \Phi_{SE}, & \Phi_{NESW} &= \Phi_{NE} - \Phi_{SW}.
\end{aligned} \tag{E.6}$$

Finally, auxiliary quantities are used in computing the updating formulas:

$$\begin{aligned}
\rho_P^+ &= \mathsf{M}(1,\mathsf{i},\mathsf{j})\, r_{43} - \varphi u_P\, \mathsf{M}(2,\mathsf{i},\mathsf{j}) - \varphi v_P\, \mathsf{M}(3,\mathsf{i},\mathsf{j}) + \varphi_2 - \varphi_1 + \varphi_4 - \varphi_3 + \dots\\
&\quad \cdots + (\varphi_5 + \varphi_6 + \varphi_7 + \varphi_8)/4 - b_4\,(\Phi_{NW} + \Phi_{SE} - \Phi_{NE} - \Phi_{SW}) + \dots\\
&\quad \cdots + b\,(pu_E - pu_W + pv_N - pv_S),\\
p_P^+ &\equiv \mathsf{M}^+(1,\mathsf{i},\mathsf{j}) = \rho_P^+/3,
\end{aligned} \tag{E.7}$$

$$\begin{aligned}
u_P^+ &\equiv \mathsf{M}^+(2,\mathsf{i},\mathsf{j}) = (\varphi_1 + \varphi_2 + (\varphi_6 - \varphi_5 - \varphi_7 + \varphi_8)/4 + \dots\\
&\quad \cdots - a\,(pu_E - \varphi u_P + pu_W) - b_4\,(\Phi_{NESW} + \Phi_{NWSE}))/\rho_P^+,
\end{aligned} \tag{E.8}$$

$$\begin{aligned}
v_P^+ &\equiv \mathsf{M}^+(3,\mathsf{i},\mathsf{j}) = (\varphi_3 + \varphi_4 + (\varphi_7 + \varphi_8 - \varphi_5 - \varphi_6)/4 + \dots\\
&\quad \cdots - a\,(pv_N - \varphi v_P + pv_S) - a_4\,(\Phi_{NESW} - \Phi_{NWSE}))/\rho_P^+,
\end{aligned} \tag{E.9}$$

where $r_{43} = 4/3$, $b = 2 - 2/\omega$, $a_4 = a/4$, $b = 2 - 2/\omega_p$ and $b_4 = b/4$. The previous optimized formulas are consistent with Eqs. (E.1-E.3) in case $\omega_p = \omega$, $b = a$ and $b_4 = a_4$. Kinematic viscosity is controlled via the parameter ω according to (5.17), whereas the parameter ω_p is responsible of the artificial compressibility. In particular, if $\omega_p \neq \omega$, the first term in Eq. (C.16) becomes proportional to ε^2/ν_p, where ν_p is the value obtained by using ω_p in Eq. (5.17). Without additional computational costs, a proper choice of $\nu_p > \nu$ allows to reduce the compressibility error in case of under-resolved simulations.

Bibliography

[1] N. Anand and S. C. Mishra. The discrete transfer method applied to the radiative heat transfer in a variable refractive index semitransparent medium. *J. Quant. Spectrosc. Radiat. Transfer*, 102:432–440, 2006.

[2] S. Ansumali and I. V. Karlin. Kinetic boundary condition for the lattice boltzmann method. *Phys. Rev. E*, 66:026311, 2002.

[3] S. Ansumali and I. V. Karlin. Consistent lattice boltzmann method. *Phys. Rev. Lett.*, 95:260605, 2005.

[4] P. Asinari. *Multi-Scale Analysis of Heat andMass Transfer in Mini/Micro-Structures*. PhD thesis, Politecnico di Torino, 2005.

[5] P. Asinari. Multiple-relaxation-time lattice boltzmann scheme for homogeneous mixture flows with external force. *Phys. Rev. E*, 77:056706, 2008.

[6] P. Asinari. Lattice boltzmann scheme for reactive mixture modelling: Analysis of the continuum diffusion regimes recovering maxwell-stefan model and incompressible navier-stokes equations. *Phys. Rev. E*, 80:056701, 2009.

[7] P. Asinari. Nonlinear boltzmann equation for the hommogeneous isotropic case: Minimal deterministic matlab program. *Comp. Phys. Comm.*, 181:1776–1788, 2010.

[8] P. Asinari and I. V. Karlin. Quasiequilibrium lattice boltzmann models with tunable bulk viscosity for enhancing stability. *Phys. Rev. E*, 81:016702, 2010.

[9] P. Asinari, S. C. Mishra, and R. Borchiellini. A lattice boltzmann formulation to the analysis of radiative heat transfer problems in a participating medium. *Numer. Heat Transfer B*, 57:1–21, 2010.

[10] P. Asinari and T. Ohwada. Connection between kinetic methods for fluid-dynamic equations and macroscopic finite-difference schemes. *Comput. Math. Appl.*, 58:841–861, 2009.

[11] P. L. Bhatnagar, E. P. Gross, and M. Krook. A model for collision processes in gases. i. small amplitude processes in charged and neutral one-component systems. *Phys. Rev*, 94:511–525, 1954.

[12] M. Bouzidi, M. Firdaouss, and P. Lallemand. Momentum transfer of boltzmann-lattice fluid with boundaries. *Phys. Fluids*, 13:3452–3459, 2001.

[13] R. A. Brownlee, A. N. Gorban, and J. Levesley. Nonequilibrium entropy limiters in lattice boltzmann methods. *Physica A: Statistical Mechanics and its Applications*, 387:385–406, 2008.

[14] C. H. Bruneau and M. Saad. The 2d lid-driven cavity problem revisited. *Computers & Fluids*, 35:326–348, 2006.

[15] A. Caiazzo. PhD thesis, Scuola Normale Superiore, Pisa, Italy, and Technische Universität Kaiserslautern, 2007.

[16] C. Cercignani. *The Boltzmann equation and its application*. Springer, 1988. New York.

[17] C. Cercignani. *Mathematical Methods in Kinetic Theory*. Plenum, 1990.

[18] J. C. Chai and S. V. Patankar. Finite volume method for radiation heat transfer. *Adv. Numerical Heat Transfer*, 2:110–135, 2000.

[19] S. Chapman. On the law of distribution of molecular velocities, and on the theory of viscosity and thermal conduction, in a non-uniform simple monatomic gas. *Phil. Trans. Roy. Soc. A*, 216:279–348, 1916.

[20] S. Chapman. On the kinetic theory of a gas. part ii. - a composite monatomic gas: Diffusion, viscosity, and thermal conduction. *Phil. Trans. Roy. Soc. A*, 217:115–197, 1918.

[21] H. Chen, S. Chen, and H. W. Matthaeus. Recovery the navier-stokes equations using lattice gas boltzmann method. *Phys. Rev. A*, 45:R5339, 1992.

[22] S. Chen, Z. Liu, Z. Tian, B. Shi Shi, and C. Zheng. A simple lattice boltzmann scheme for combustion simulation. *Comp. Math. Appl.*, 55:1424–1432, 2008.

[23] E. Chiavazzo. *Invariant Manifolds and Lattice Boltzmann method for Combustion*. PhD thesis, ETH Zürich, 2009. Diss. No. 18233.

[24] E. Chiavazzo, I. V. Karlin, A. N. Gorban, and K. Boulouchos. Combustion simulation via lattice boltzmann and reduced chemical kinetics. *J. Stat. Mech.*, 66:P06013, 2009.

[25] E. Chiavazzo, I. V. Karlin, A. N. Gorban, and K. Boulouchos. Coupling of the model reduction technique with the lattice boltzmann method for combustion simulations. *Comb. Flame*, 157:1833–1849, 2010.

[26] A. J. Chorin. A numerical method for solving incompressible viscous flow problems. *J. Comput. Phys.*, 2:12–26, 1976.

[27] P. S. Cumber and M. Fairweather. Devaluation of flame emission models combined with the discrete transfer method for combustion system simulation. *Int. J. Heat Mass Transfer*, 102:5221–5239, 2005.

[28] R. Das, S. C. Mishra, M. Ajith, and R. Uppaluri. An inverse analysis of a transient 2-d conduction-radiation problem using the lattice boltzmann method and the finite volume method coupled with the genetic algorithm. *J. Quant. Spectrosc. Radiat. Transfer*, 109:2060–2077, 2008.

[29] P. J. Dellar. Bulk and shear viscosities in lattice boltzmann equations. *Phys. Rev. E*, 64:031203, 2001.

[30] P. J. Dellar. Nonhydrodynamic modes and a priori construction of shallow water lattice boltzmann equations. *Phys. Rev. E*, 65:036309, 2002.

[31] D. d'Humières. *Generalized lattice Boltzmann equations*, volume Prog. Astronaut. Aeronaut. B.D. Shizgal, D.P. Weaver (Eds.), 1992. Rarefied Gas Dynamics: Theory and Simulations.

[32] D. d'Humières, M. Krafczyk, I. Ginzburg, P. Lallemand, and L. S. Luo. Multiple-relaxation-time lattice boltzmann models in three dimensions. *Phil. Trans. R. Soc. Lond. A*, 360:437–451, 2002.

[33] J. G. M. Eggels and J. A. Sommers. Numerical simulation of free convective flow using the lattice-boltzmann scheme. *Int. J. Heat Fluid Flow*, 16:357–364, 1995.

[34] D. Enskog. *Kinetische Theorie der Vorgänge in mässig verdünnten Gasen*. PhD thesis, Uppsala, 1917.

[35] O. Filippova and D. Hänel. A novel lattice bgk approah for low mah number combustion. *J. Stat. Phys*, 158:139–160, 2000.

[36] O. Filippova and D. Hänel. A novel numerical scheme for reactive flows at low mach numbers. *Comp. Phys. Comm*, 129:267–274, 2000.

[37] W. A. Fiveland. Discrete-ordinates solution of the radiative transport equation for rectangular enclosures. *J. Heat Transfer*, 106:699–706, 1984.

[38] Inc. Fluent. *Fluent Release 6.3 User Guide*, 2006.

[39] C. E. Frouzakis. *Lattice Boltzmann Methods for Reactive and Other Flows*, volume 95. Fluid Mechanics and Its Applications, 2011. edited by T. Echekki and E. Mastorakos, Part 4.

[40] W. W. Grabowski. Impact of cloud microphysics on convective-radiative quasi equilibrium revealed by cloud-resolving convection parameterization. *J. Clim.*, 16:3463–3475, 2003.

[41] Z. Guo, C. Zheng, and B. Shi. Lattice boltzmann equation with multiple effective relaxation times for gaseous microscale flow. *Phys. Rev. E*, 77:036707, 2008.

[42] Z. L. Guo, B. C. Shi, and N. C. Wang. Lattice bgk model for incompressible navier–stokes equation. *J. Comp. Phys.*, 165:288–306, 2000.

[43] G. Hager, G. Wellein, T. Zeiser, S. Donath, and G. Hager. *Introduction to High Performance Computing for Scientists and Engineers*, volume 95. CRC Press, 2010.

[44] X. He, S. Chen, and G. D. Doolen. A novel thermal model for the lattice boltzmann method in incompressible limit. *J. Comp. Physics*, 146:282–30, 1998.

[45] X. He and L. S. Luo. Theory of lattice boltzmann method: from the boltzmann equation to the lattice boltzmann equation. *Phys. Rev. E*, 56:6811, 1997.

[46] F. J. Higuera and J. Jimenez. Boltzmann approach to lattice gas simulations. *EuroPhys. Lett.*, 9:663–668, 1989.

[47] F. J. Higuera, S. Succi, and R. Benzi. Lattice gas dynamics with enhanced collisions. *EuroPhys. Lett.*, 9:345–349, 1989.

[48] Z. Hongmei and M. F. Modest. Evaluation of the planck-mean absorption coefficient from hitran and hitemp databases. *JQSRT*, 73:649–653, 2002.

[49] T. Inamuro. A lattice kinetic scheme for incompressible viscous flows with heat transfer. *Proc. R. Soc. Lond. A*, 360:477–484, 2002.

[50] D. M. Ingram, D. M Causon, and C. G. Mingham. Developments in cartesian cut cell methods. *Math. Comp. Simul.*, 61:561–572, 2003.

[51] M. Junk. A finite difference interpretation of the lattice boltzmann method. *Numer. Methods Part. Diff. Eq.*, 17:383–402, 2001.

[52] M. Junk, A. Klar, and L. S. Luo. Asymptotic analysis of the lattice boltzmann equation. *J. Comput. Phys.*, 210:676–704, 2005.

[53] Q. Kang, P. C. Lichtner, and D. R. Janecky. Lattice boltzmann method for reacting flows in porous media. *Phys. Rev. E*, 2:545–563, 2010.

[54] I. V. Karlin, A. Ferrante, and H. C. Ottinger. Perfect entropy functions of the lattice boltzmann method. *Europhys. Lett.*, 47:182–188, 1999.

[55] R. J. Kee, M. E. Coltrin, and P. Glarborg. *Chemically Reacting Flow: Theory and Practice*. Wiley-Interscience, 2003. New Jersey.

[56] K. Kim and Z. Guo. Ultrafast radiation heat transfer in laser tissue welding and soldering. *Numer. Heat Transfer A*, 46:23–40, 2004.

[57] M. Y. Kim, S. W. Baek, and C. Y. Lee. Prediction of radiative heat transfer between two concentric spherical enclosures with the finite volume method. *Int. J. Heat Mass Transfer*, 51:4820–4828, 2000.

[58] M. P.. Kirkpatrick, S. W. Armfield, and J. H. Kent. A representation of curved boundaries for the solution of the navier stokes equations on a staggered three-dimensional cartesian grid. *J. Comput. Phys.*, 184:1–36, 2003.

[59] V. N. Kurdyumov, G. Pizza, C. E. Frouzakis, and J. Mantzaras. Dynamics of premixed flames in a narrow channel with step-wise wall temperature. *Comb. Flames*, 156:2190–2200, 2009.

[60] A. J. C. Ladd. Numerical simulations of particular suspensions via a discretized boltzmann equation - part 1. *J. Fluid Mech.*, 271:285–310, 1994.

[61] P. Lallemand and L. S. Luo. Theory of the lattice boltzmann method: dispersion, dissipation, isotropy, galilean invariance, and stability. *Phys. Rev. E*, 61:6546, 2000.

[62] P. Lallemand and L. S. Luo. Theory of the lattice boltzmann method: Acoustic and thermal properties in two and three dimensions. *Phys. Rev. E*, 68:036706, 2003.

[63] C. K. Law. *Combustion Physics*. Cambridge University Press, 2006.

[64] V. D. Liseikin. *Grid Generation Methods*, volume 95. Springer, 2010. second ed., Series: Scientific Computation.

[65] F. C. Lockwood and N. G. Shah. A new radiation solution method for incorporation in general combustion prediction procedures. In *Eighteenth Symposium (Int.) on Combustion*, pages 1405–1414, Pittsburgh, 1981. The Combustion Institute.

[66] E. Lorenz, A. Caiazzo, and A. G. Hoekstra. Corrected momentum exchange method for lattice boltzmann simulations of suspension flow. *Phys. Rev. E*, 79:036705, 2009.

[67] L. S. Luo, W. Liao, X. Chen, Y. Peng, and W. Zhang. Numerics of the lattice boltzmann method: Effects of collision models on the lattice boltzmann simulations. *Phys. Rev. E*, 83:056710, 2011.

[68] X. L. Luo, Z. L. Gu, K. B. Lei, S. Wang, and K. Kase. A three-dimensional cartesian cut cell method for incompressible viscous flow with irregular domains. *Int. J. Numer. Meth. Fluids*, 2011. in press.

[69] F. J. Marakis, C. Papapavlou, and E. Kakaras. A parametric study of radiative heat transfer in pulverised coal furnaces. *Int. J. Heat Mass Transfer*, 43:2961–2971, 2000.

[70] N. M. Marinov, C. K. Westbrook, and W. J. Pitz. Detailed global chemical kinetics model for hydrogen. In *8th Int. Symp. on Transport Properties*, 1995. San Francisco, CA.

[71] F. Massaioli, R. Benzi, and S. Succi. Exponential tails in rayleigh-benard convection. *Europhys. Lett.*, 21:305–310, 1993.

[72] M. L. Minion and D. L. Brown. Performance of underresolved two-dimensional incompressible flow simulations ii. *J. Comput. Phys.*, 138:734, 1997.

[73] S. C. Mishra, A. Lankadasu, and K. Beronov. Application of the lattice boltzmann method for solving the energy equation of a 2-d transient conduction-radiation problem. *Int. J. Heat Mass Transfer*, 48:3648–3659, 2005.

[74] S. C. Mishra, T. B. Pavan Kumar, and B. Mondal. Lattice boltzmann method applied to the solution of energy equation of a radiation and non-fourier heat conduction problem. *Numer. Heat Transfer A*, 54:798–818, 2008.

[75] S. C. Mishra and M. Prasad. Radiative heat transfer in absorbing-emitting-scattering gray media inside 1-d gray cartesian enclosure using the collapsed dimension method. *Int. J. Heat Mass Transfer*, 45:697–700, 2002.

[76] S. C. Mishra and H. K. Roy. Solving transient conduction-radiation problems using the lattice boltzmann method and the finite volume method. *J. Comput. Physics*, 223:2007, 2007.

[77] S. C. Mishra, H. K. Roy, and N. Misra. Discrete ordinate method with a new and a simple quadrature scheme. *J. Quant. Spectrosc. Radiat. Transfer*, 101:249–262, 2006.

[78] M. F. Modest. *Radiative Heat Transfer*. Academic Press, 2003. second ed., New York.

[79] B. Mondal and S. C. Mishra. Simulation of natural convection in the presence of volumetric radiation using the lattice boltzmann method. *Numer. Heat Transfer A*, 55:18–41, 2009.

[80] M. A. Mujeebu, M. Z. Abdullah, A. A. Mohamad, and M. Z. Abu Bakar. Trends in modeling of porous media combustion. *Prog. Energy Combust. Sci.*, 36:627–650, 2010.

[81] T. Ohwada and P. Asinari. Artificial compressibility method revisited: asymptotic numerical method for incompressible navier-stokes equations. *J. Comp. Physics*, 229:1698–1723, 2010.

[82] T. Ohwada, P. Asinari, and D. Yabusaki. Artificial compressibility method and lattice boltzmann method: Similarities and differences. *Comput. Math. Appl.*, in press:3452–3459, 2011.

[83] G. Pal, S. Basu, K. Mitra, and S. Kumar. Bioheat transfer in layered skin model subjected to short pulse laser irradiation. *Laser Surg. Med.*, 13:12–37, 2005.

[84] A. Parmigiani. *Lattice Boltzmann calculations of reactive multiphase flows in porous media*. PhD thesis, Univ. Geneva, 2011. Diss. No. 4287.

[85] G. Pizza, C. E. Frouzakis, J. Mantzaras, A. G. Tomboulides, and K. Boulouchos. Dynamics of premixed hydrogen/air flames in mesoscale channels. *Comb. Flame*, 155:2–20, 2008.

[86] A. Povitsky. High-incidence 3-d lid-driven cavity flow. *American Institute of Aeronautics and Astronautics*, 01-2847:1–7, 2001.

[87] A. Povitsky. Three-dimensional flow in cavity at yaw. *Nonlinear Analysis*, 63:e1573–e1584, 2005.

[88] N. I. Prasianakis and I. V. Karlin. Lattice boltzmann method for thermal flow simulation on standard lattices. *Phys. Rev. E*, 76:016702, 2007.

[89] N. I. Prasianakis and I. V. Karlin. Lattice boltzmann method for simulation of compressible flows on standard lattices. *Phys. Rev. E*, 78:016704, 2008.

[90] Y. Qian, D. d'Humieres, and P. Lallemand. Lattice bgk models for navier-stokes equation. *Europhys. Lett.*, 17:479–484, 1992.

[91] R. Raj, A. Prasad, P. R. Parida, and S. C. Mishra. Analysis of solidification of a semitransparent planar layer using the lattice boltzmann method and the discrete transfer method. *Numer. Heat Transfer A*, 49:279–299, 2006.

[92] L.S. Rothman, C. Camy-Peyret, J. M. Flaud, R. R. Gamache, A. Goldman, D. Goorvitch, R. L. Hawkins, J. Schroeder, J. E. A. Selby, and R. B. Wattson. Hitemp, the high-temperature molecular spectroscopic database. *JQSRT*, 2002.

[93] L.S. Rothman, C. P. Rinsland, A. Goldman, S. T. Massie, D. P. Edwards, J. M. Flaud, A. Perrin, C. Camy-Peyret, V. Dana, J. Y. Mandin, J. Schroeder, A. McCann, R. R. Gamache, R. B. Wattson, K. Yoshino, K. V. Chance, K. W. Jucks, L. R. Brown, V. Nemtchinov, and P. Varanasi. The hitran molecular spectroscopic database and hawks (hitran atmospheric workstation): 1996 edition. *JQSRT*, 60:665–710, 1998.

[94] P. Sadooghi. Transient coupled radiative and conductive heat transfer in a semitransparent layer of ceramic. *J. Quant. Spectros. Radiat. Transfer*, 92:403–416, 2005.

[95] M. Sahin and R. G Owens. A novel fully-implicit finite volume method applied to the lid-driven cavity problem. part i and ii. *Int. J. Numer. Methods. Fluids*, 42:326–348, 2003.

[96] M. Sbragaglia and S. Succi. A note on the lattice boltzmann method beyond the chapman-enskog limits. *Europhys. Lett.*, 73:370–376, 2006.

[97] X. Shan. Simulation of rayleigh-bénard convection using a lattice boltzmann method. *Phys. Rev. E*, 55:2780–2788, 1997.

[98] Y. Shu, B. Q. Al, and K. G. Lynn. Numerical modeling of internal radiation and solidification in semitransparent melts in magnetic fields. *Numer. Heat Transfer B*, 45:957–976, 2004.

[99] R. Siegel and J. R. Howell. *Thermal Radiation Heat Transfer*. Taylor & Francis, 2002. fourth ed., New York.

[100] M. Spinnler, F. Winter, E. R, and R. Viskanta. Studies on high-temperature multilayer thermal insulations. *Int. J. Heat Mass Transfer*, 47:1305–1312, 2004.

[101] J. D. Sterling and S. Chen. Stability analysis of the lattice boltzmann methods. *J. Comp. Phys.*, 123:196–206, 1996.

[102] S. Succi. *The lattice Boltzmann equation for fluid dynamics and beyond*. Oxford University Press, 2001. second ed., New York.

[103] S. Succi, G. Bella, and F. Papetti. Lattice kinetic theory for numerical combustion. *J. Sci. Comp.*, 12:395–408, 1997.

[104] C. L. Tien. *Thermal radiation properties of gases, Advances in heat transfer*, volume 5. Academic Press, 2011. New York.

[105] J. Tölke. A thermal model based on the lattice boltzmann method for low mach number compressible flows. *J. Comp. Theor. Nanoscience*, 3:1–9, 2006.

[106] A. G. Tomboulides and S. A. Orzag. A quasi-two dimensional benchmark problem for low mach number compressible codes. *J. Comp. Phys.*, 146:691–706, 1998.

[107] R. G. M. van der Sman, M. H. Ernst, and A. C. Berkenbosch. Lattice boltzmann scheme for cooling of packed cut flowers. *Int. J. Heat Mass Transfer*, 43:577–587, 2000.

[108] G. Wellein, T. Zeiser, S. Donath, and G. Hager. On the single processor performance of simple lattice boltzmann kernels. *Comp. Fluids*, 35:910–919, 2006.

[109] D. A. Wolf-Gradow. *Lattice-gas cellular automata and lattice Boltzmann models*. Springer, 2000. Berlin.

[110] K. Yamamoto, X. He, and G. D. Doolen. Simulation of combustion field with lattice boltzmann method. *J. Stat. Phys.*, 107:367–383, 2002.

[111] C. Yao, G. X. Wang, and B. T. F. Chung. Nonequilibrium planar interface model for solidification of semitransparent radiating materials. *J. Thermophys Heat Transfer*, 14:297–304, 2000.

[112] T. Ye, R. Mittal, H. S. Udaykumar, and W. Shyyy. An accurate cartesian grid method for viscous incompressible flows with complex immersed boundaries. *J. Comput. Phys.*, 156:209–240, 1999.

[113] D. P. Young, R. G. Melvin, M. B. Bieterman, F. T. Johnson, and J. E. Samant, S. S.and Bussoletti. A locally refined rectangular grid finite element method: application to computational fluid dynamics and computational physics. *J. Comput. Phys.*, 92:1–66, 1991.

[114] D. D. Zeeuw and K. G. Powell. An adaptively refine cartesian mesh solver for the euler equation. *J. Comput. Phys.*, 104:56–68, 1993.

[115] D. P. Ziegler. Boundary conditions for the lattice boltzmann simulations. *Jour. Stat. Phys.*, 71:1171–1177, 2003.

[116] Q. Zou and X. He. On pressure and velocity boundary conditions for the lattice boltzmann bgk model. *Phys. Fluids*, 9:1591–1598, 1997.

[117] Q. Zou, S. Hou, S. Chen, and G. D. Doolen. An improved incompressible lattice boltzmann model for time-independent flows. *J. Stat. Phys*, 81:35–48, 1995.